NTNU

Norwegian University of
Science and Technology

Minimizing Ski Friction through Nanostructured Hydrophobic Surfaces

Tone Hjort Madsen

Master of Science in Mechanical Engineering
Submission date: June 2018
Supervisor: Jan Torgersen, MTP
Co-supervisor: Martin Steinert, MTP
Alex Klein-Paste, IBM

Norwegian University of Science and Technology
Department of Mechanical and Industrial Engineering

Preface

This thesis is submitted as a closing part of a Master's degree in Product Development and Production at the Department of Mechanical and Industrial Engineering (MTP) at the Norwegian University of Science and Technology (NTNU). The work was conducted in the period January-June 2018. Associate Professor Jan Torgersen was the main supervisor. Professor Martin Steinert and Professor Alex Klein-Paste were co-supervisors for the project.

The work counted for 30 credits and is a continuation of a specialization project conducted during fall 2017, which counted for 15 credits. The project is given by and defined in cooperation with Olympiatoppen as part of the more extensive project, Forsprang 2018. This is a research project in which innovation and new technologies are used with the aim of a better understanding of friction, with skis as the primary focus.

Abstract

The correlation between ski friction and a ski base surface that can enhance hydrophobicity by geometry has been investigated. A review is given of existing knowledge about the linkage between ski friction mechanisms, generation of a water film between ski-and snow base, and wettability. The effect of roughness induced wettability is explained, and forms the basis of examining nanostructuring techniques to obtain a hydrophobic ski base. The fabrication of an anodic aluminum oxide (AAO) miniature ski prototype is reported, conducted with a simple and low-cost setup. Anodization is performed in a single step procedure with a constant current of 5.18 A for 40 minutes, and an electrolyte consisting of sulfuric acid, oxalic acid, and sodium chloride. The resulting porous surface structure was analyzed with SEM, and pore diameters measured to 20-33 nm. The contact angle (CA) was measured to 130° for the anodized sample when coated with PTFE. A reference sample with identical dimensions, but with a longitudinally milled surface, was fabricated and measured a CA of 92°, also when PTFE coated. Friction tests were performed with a Linear Analyzer of Road Surface (LARS) apparatus in which the samples were accelerated on a linear snow track at an indoor facility. The coefficient of friction (COF) was measured at a constant velocity of 2 m/s. Measurements were conducted on both anodized and reference sample at snow temperatures of -10 °C and -4.6 °C. The surfaces were analyzed with an optical profilometer (OP) and CA measured, both before and after friction tests. The results from the friction tests state that the anodized sample holds lowest COF at -10 °C, but the reference sample has lowest values at -4.6 °C. However, it is believed that the observed wear of PTFE is more critical for the AAO sample, and hence a clear conclusion cannot be stated on whether the nanoporous hydrophobic surface yields reduced friction compared to the reference sample.

Sammendrag

Korrelasjonen mellom skifriksjon og en skibase-overflate som kan forbedre hydrofobisitet geometrisk har blitt undersøkt. En oppsummering er gitt av eksisterende kunnskap om forholdet mellom ski-friksjonsmekanismer, generering av en vannfilm mellom ski-og snøbase, og fukting. Effekten av ruhetsindusert fukting forklares og former et grunnlag for å undersøke nanostruktureringsteknikker for å oppnå en hydrofobisk skibase. Fabrikasjonen av anodisk aluminiumsoksid (AAO) på en miniatyr skiprototype rapporteres, utført med et enkelt og rimelig oppsett. Anodiseringen er utført med en ett-stegs prosedyre med konstant strøm på 5.18 A i 40 minutter, hvor elektrolytten besto av svovelsyre, oksalsyre, og natriumklorid. Resulterende porøs overflatestruktur ble analysert med SEM, og porediametere målt til 20-33 nm. Kontaktvinkelen (CA) ble målt til 130° for den anodiserte prøven når belagt med PTFE. En referanseprøve med identiske dimensjoner, men med langsgående fresespor, ble fabrikkert og målte en CA på 92°, også når belagt med PTFE. Friksjonstester ble gjennomført med en Linear Analyzer of Road Surface (LARS), hvor prøvene ble akselerert på en lineær snøbane i en innendørs fasilitet. Målinger ble gjort på både anodisert- og referanseprøve ved snøtemperaturer på -10 °C og -4.6 °C. Overflatene ble analysert med et optisk profilometer (OP) og CA målt, begge både før og etter friksjonstester. Resultatene fra friksjonstestene tilsier at den anodiserte prøver har lavest COF ved -10 °C, men at referanseprøven har lavest COF ved -4.6 °C. Det antas likevel at den observerte slitasjen av PTFE er mer kritisk for AAO-prøven, og at det derfor ikke kan konkluderes om hvorvidt den nanoporøse hydrofobiske overflaten viser redusert friksjon sammenlignet med referanseprøven.

Acknowledgment

I would like to express appreciation to my supervisor, Jan Torgersen, for professional support and availability throughout the work. Thank you for offering the perfect balance between proposing new ideas and letting me develop my own. I would also like to thank my co-supervisor, Martin Steinert, for innovative ideas for the next steps, and for welcoming me into the TrollLABS community. To my second co-supervisor Alex Klein-Paste, who came to rescue with a brand new high-tech snow lab at the Department of Civil and Environmental Engineering, and for numerous ideas on how to test my samples. To Olympiatoppen and my company contact Felix Breitschädel, for providing an interesting project, and for giving access to knowledge and observations during a visit to Beitostølen in November.

Thank you to Ph.D. student Mathis Dahl Fenre for his enormous dedication to helping me perform friction tests in the snow lab. To Ph.D. student Christian Torres Rodriguez for the great training in the Corrosion Lab, and for his patience and helpful inputs when my chemistry knowledge came short. Thank you to all the fellow Master's students and Ph.D.s at TrollLABS and in the Materials Design and Compliance group for help and feedback. Also, thanks to the fellow students at the department for the collaboration and for building a such an incredible study environment throughout the years at NTNU.

Thank you to John Erik Lein at SINTEF for letting me borrow equipment for anodizing, and for guidance through the process. To everyone at the Realization Lab; thank you for your availability and service. Thank you to senior engineer Gaute Stenerud for providing assistance with SEM imaging at NTNU Nanomechanical Lab. The Research Council of Norway is acknowledged for the support to the Norwegian Micro- and Nano-Fabrication Facility, NorFab. Thank you to higher executive officer Natalia Trotsenko for always managing extremely quick product orders so I could conduct my work as fast as possible.

Abbreviations

AAO	Anodic aluminum oxide
ACA	Advancing contact angle
ACCA	Actual contact angle
APCA	Apparent contact angle
AR	Aspect ratio
BL	Boundary Lubrication
BSE	Backscattered electrons
CA	Contact angle
CAD	Computer-aided design
CAH	Contact angle hysteresis
CCD	Charge-coupled device
COF	Coefficient of friction
FIS	Fédération Internationale de Ski
GIMP	GNU Image Manipulation Program
HL	Hydrodynamic Lubrication
IFT	Interfacial tension
IMU	Inertial measurement unit
LARS	Linear Analyzer of Road Surface
ML	Mixed Lubrication
MLA	Maskless aligner
MSA	Mobile Surface Analyzer
NIL	Nanoimprint lithography
NTNU	Norwegian University of Science and Technology
OM	Optical microscope
OP	Optical profilometer
OWRK	Owens, Wendt, Rabel, and Kalble
PDMS	Polydimethylsiloxane
PE	Polyethylene
PFOA	Perfluorooctanoic
PL	Photolithography
PMMA	Poly(methyl methacrylate)
PSI	Phase Shifting Interferometry
PTFE	Polytetrafluorethylene
PUA	Polyurethane acrylate
RCA	Receding contact angle
RH	Relative humidity

SC	Snow compactor
SCIL	Substrate conformal imprint lithography
SE	Secondary electrons
SEM	Scanning electron microscope
SFE	Surface free energy
SFT	Surface tension
TA	Tilting angle
UHMWPE	Ultra-high molecular weight polyethylene
VSI	Vertical Scanning Interferometry
XC	Cross-country

List of Symbols

F_{snow}	Friction force on ice/snow
F_{air}	Air drag
W	Weight of skier
N	Normal force
μ	Coefficient of friction
μ_{total}	Total kinetic coefficient of friction
μ_{plow}	Coefficient of friction contribution from plowing effects
μ_{dry}	Coefficient of friction contribution from solid deformation effects
μ_{lub}	Coefficient of friction contribution from lubrication effects
μ_{cap}	Coefficient of friction contribution from capillary attraction effects
μ_{dirt}	Coefficient of friction contribution from contamination effects
σ_{sg}	Surface free energy of a solid
σ_{ls}	Interfacial tension between liquid and solid
σ_{lg}	Surface tension of liquid
θ	Contact angle
σ_s^D	Dispersive part of the surface free energy
σ_l^D	Dispersive part of the surface tension of the liquid
σ_s^P	Polar part of the surface free energy
σ_l^P	Polar part of the surface tension of the liquid
$\Delta\theta$	Contact angle hysteresis
θ_R	Receding contact angle
θ_A	Advancing contact angle
α	Tilting angle
m	Mass of droplet
g	Gravitational acceleration
w	Width of droplet parallel to inclined plane
Sa	Roughness; arithmetic mean of vertical deviations of height on a surface
A	Area of surface in which roughness is analyzed
z(x,y)	Height profile of surface
L	Profile length of surface along x-and y-axis
Ssk	Skewness of surface profile
Sku	Kurtosis of surface profile
Sq	Root mean square height of surface profile
Sv	Maximum pit height of surface profile
Sp	Maximum peak height of surface profile
Sz	Maximum height of surface profile

θ'	Apparent contact angle
r	Roughness ratio
f	Area fraction of a solid surface
a	Width of rough surface features in Cassie-Baxter wetting model
b	Size of surface grooves in Cassie-Baxter wetting model
P	Pressure applied in hot embossing process
Q	Heat applied in hot embossing process
$\bar{I}$	Current density
I	Current
A_{sample}	Surface area of sample to be anodized
H_{depth}	Pore depth of AAO surface
D_{pore}	Pore diameter of AAO surface
F_B	Brake force
F_L	Load cell force
F_F	Friction force
C	Point representing center of wheel in LARS
D	Point representing joint between aluminum arm and sled in LARS
r_H	Distance between point C and the lower surface of sample in LARS
r_B	Distance between point C and brakes in LARS
c	Distance between point D and load cell in LARS
d	Distance between point D and brakes in LARS
$m_{anterior}$	Mass on anterior part of ski
m_{total}	Total mass on ski
$f_{force\ on\ anterior}$	Fraction of total force on anterior part of ski
$f_{one\ of\ two\ skis}$	Fraction of one of two skis
m_{sample}	Mass of sample to test in LARS
$A_{anterior}$	Contact area between anterior part of ski and snow base
A_{sample}	Contact area between sample and snow base

Table of Contents

1 Introduction

Though skiing, as a way of transport during winter, dates back six thousand years [1], the substantial, international organized competitions did not develop until the 20th century [2]. The short history of competitions might explain why a solid, well-structured, and practically useful theory is not built around the subject [2]. A considerable amount of the practice among ski technicians today is to a large extent based on experience, and less on actual science. In Olympiatoppen's project, Forsprang 2018, the goal is to close the gap between empirical practice and proven scientific knowledge, with the focus on attaining a better understanding of ski friction.

Friction between snow- and ski base is a complicated process and depends on numerous factors. The main task is for the friction, which is dictated by an interfacial layer of partially melted water during gliding, to be minimized at the glide zones of the ski base. A key issue is to find which aspect to focus on, as factors are correlative, and cannot all be optimized simultaneously. While many efforts have been put into the research of the material for the ski base surface, approaches on nanostructured surface designs that, by geometry, can enhance hydrophobic properties of a given material, are yet to be explored. This work is based on the theory that by introducing a rough surface to the ski base, the contact area between ski-and snow base will be reduced, which in turn reduces friction.

In recent years, hydrophobic surfaces have attracted great interest due to its potential in several applications, such as self-cleaning and contamination inhibition in microfluidics and droplet-based technologies [3, 4]. This work will investigate a selection of methods within these fields, and how they can be transferred to the ski glide problem. The aim is to make the ski base consist of a permanent nanostructured surface promoting the advantages of hydrophobicity, potentially in a range of snow conditions. Additionally, this is thought to possibly limit the usage of hazardous fluoro-containing products. The work will be carried out to explore whether hydrophobicity may be a key factor to the ski glide problem. The focus will predominantly be on the structure of the ski base, and less on its material characteristics. The work will address the properties of the ski base at the glide zones of cross-country (XC) skis in the classical racing style, but can also be applicable for other ski- and race types.

1.1 Background and motivation

Olympiatoppen operates and develops the elite sports in Norway, and consequently has the overall responsibility for the results attained by the elite athletes. Olympiatoppen also has the responsibility of managing the Norwegian participation in the Olympics and the Paralympics [5]. Norwegians' pride is deeply entangled with the success of the XC skiing athletes, as being considered as the world's best nation within this sport [6]. Consequently, major resources are put into development and improvement of both the fitness of the athletes and the ski equipment to access the extra margins benefiting the Norwegian athletes in international competitions.

It is challenging to estimate to which extent improved performance in equipment can be attained, as dominant parameters between ski-and snow base are constantly shifting. An example will follow, to get a picture of the potential time savings that can be obtained by improving the equipment. Norwegian XC skier Marit Bjørgen did a 30 km race with the time 1:21:30 during the Norwegian Championship in Alta in 2018. If assuming her equipment was further improved by friction reduction at the glide zones resulting in 5 % reduced completion time, she would finish at approx. 1:17:25. Obviously, 4 minutes improvement is crucial, indicating the substantial motivation behind every small improvement.

Even though a full physical understanding of the ski friction processes is not yet achieved, skis have been developed to a very high level. However, if the unknown and uncertain correlations can be understood, an even greater level can be reached. To do this, several subjects related to tribology needs further investigation, including contact area between snow and skis, meltwater lubrication, capillary bonds, and dirt at the interface. The nation that can find the answers to the loose ends will have an enormous advantage in the international XC ski competitions.

Many researchers have been investigating the correlation between a rough ski base and ski friction. However, most of them test structures achieved from the conventional grinding and rilling tools. Not many have been rethinking the surface structure in terms of processing and patterns. Additionally, not many researchers have experimented with ski samples in an indoor facility where there is a higher number of controllable parameters. The availability of a snow lab at the Department of Civil and Environmental Engineering at NTNU makes these experiments possible, an opportunity that calls for a profoundly interesting study.

1.2 Problem description

This work is based on the theory that by reducing the contact area between the snow-and ski base, friction will also be reduced. While many efforts have been put into the material research of the ski base surface, approaches on nanostructured surface designs that, by geometry, can enhance hydrophobic properties of a given material surface, are yet to be explored. During the specialization project in fall 2017, which functioned as an introduction to this thesis, several methods for creating nanostructured hydrophobic surfaces were experimented with. The work conducted here will build on some of these findings, but also take the next step by bringing a nanostructured surface onto a constructed miniature ski prototype and apply a realistic load. The aim is to make the ski base consist of a permanent nanostructured surface promoting the advantages of hydrophobicity. The work will be carried out to explore whether hydrophobicity, in terms of geometric features, may be the key to the ski glide problem. Hence, the focus will predominantly be on the structure of the ski base, and less on its material characteristics.

1.3 Objectives

The following objectives were stated at the beginning of the project with the aim of bringing a hydrophobic surface on a ski prototype:

1. Define miniature ski prototype
2. Select applied weight to mimic the pressure distribution of a real ski
3. Design protocol for experiments in snow lab
4. Vary the hydrophobicity of prototypes and perform measurements

A bonus was given as the following:

- Video(s) on the performance difference between real ski and miniature ski prototype

1.4 Thesis structure

The thesis will firstly contain an extensive section presenting the relevant underlying theory, forming a baseline for the further research conducted. This will include fundamental physics of ski friction and relevant aspects of cross-country skis. Additionally, it will include an introduction to nanostructuring techniques - with emphasis on anodizing of aluminum. Finally, the basic working principle of the characterization instruments used will be presented.

The subsequent section contains all experimental methods, setups, and protocols designed throughout the work, both successful approaches and less successful approaches that were later discarded later. All results achieved will be presented in the subsequent section but without a further analysis of the outcomes. However, a discussion section structured in the same way as the result section will follow. Here evident and potential errors, inaccuracies, and uncertainties will be considered. The next section is making concluding remarks on the overall work conducted and the results achieved. Potential improvements will be addressed in the subsequent section, which will emphasize on suggested further work.

After all references cited throughout the work are summed up in a bibliography section, relevant appendices follow. The appendices contain larger portions of data that are referred to throughout the thesis, but that are not necessary for a reasonable understanding of the work performed.

In sum, the thesis can both be seen as a review of already published research as well as novel experimental research. Additionally, the thesis will introduce new questions and contribute to the ongoing discussion on the subject.

2 Theory

This section starts with an establishment of the cross-country (XC) skiing techniques, to get a practical introduction to the subject before entering the theory. The three subsequent sub-sections present the underlying theory to understand the physical mechanisms and parameters related to ski friction. It continues with a sub-section about the ski XC ski configuration, including pressure distribution, material selection, processing steps, and ways of testing its performance. The two subsequent sub-sections will further concern nanostructuring. The first in terms of fabrication methods, including both general and specific approaches. The second in terms of characterization instruments to investigate the geometry of the nanostructured surfaces.

2.1 Classical cross-country skiing

As the ski sport branches into several different styles, techniques, and distances, there are numerous ski types with variously associated preparation procedures. Even though ski friction and hydrophobicity are relevant for all types, this work for Olympiatoppen focuses on the classical style in XC skiing, in which technique can be classified in four; (1) *the diagonal stride*, in which opposite arms and legs are pushing off simultaneously in a diagonal manner (Figure 1A), (2) *the kick double poling*, where arms are used in parallel together with one leg to push off (Figure 1B), (3) *the double poling*, in which only arms are used, moving in parallel to push the body forward (Figure 1C), and (4) *the herringbone technique*, where arms and legs move in a diagonal fashion. In the latter, the skis are angulated in relation to the skiing direction and the push off is performed in a combination of sideways and backwards. This technique is only used in steep uphills [7]. Hence, in classical XC style the skis are mainly moving in one direction, which is certainly essential knowledge when designing the surface structure of the ski base. The following section contains four sub-sections related to the current way of design, manufacturing, preparation, and testing of cross-country skis, with focus on the factors related to friction, especially in correlation with the ski base structure.

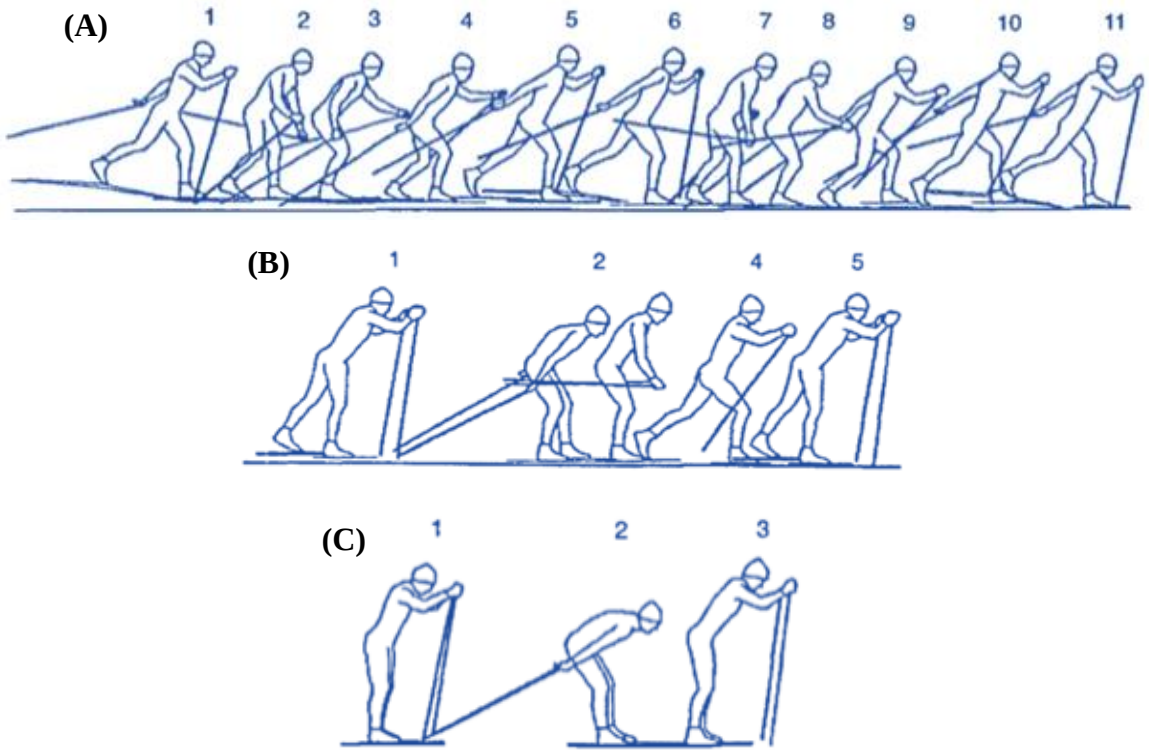

Figure 1: *Three of four techniques in classical XC skiing: (A) diagonal stride, (B) kick double poling, and (C) double poling [7]*

2.2 Ski friction

Friction experienced by a cross-country skier can best be understood by considering the free-body diagram in Figure 2, representing a skier of weight W gliding on snow. The skier encounters a resistant force by the air drag, F_{air}, and a friction force at the interface with the snow base, F_{snow}. The weight is counterbalanced by the normal force, N. According to Amontons' law, F_{snow} is proportional to N and independent of the size of the geometrical contact area between the snow-and ski base. The ratio between the vertical normal force and the horizontal friction force is assumed to be constant, and called the coefficient of friction (COF), with symbol μ (Equation 1) [8]. The COF is a measure of how readily a material surface slides over another. Hence, COF applies to a pair of material surfaces and not just one surface by itself. It is evident that a low COF is desirable to minimize the propulsion force required by the skier. Friction can further be divided into static and kinetic friction. Static friction force must be overcome to initialize movement of an object, while kinetic friction force must be overcome to keep the object sliding. As greater force is required to start the movement, the static friction is of larger magnitude than the kinetic friction.

$$\mu = \frac{F_{snow}}{N} \qquad (1)$$

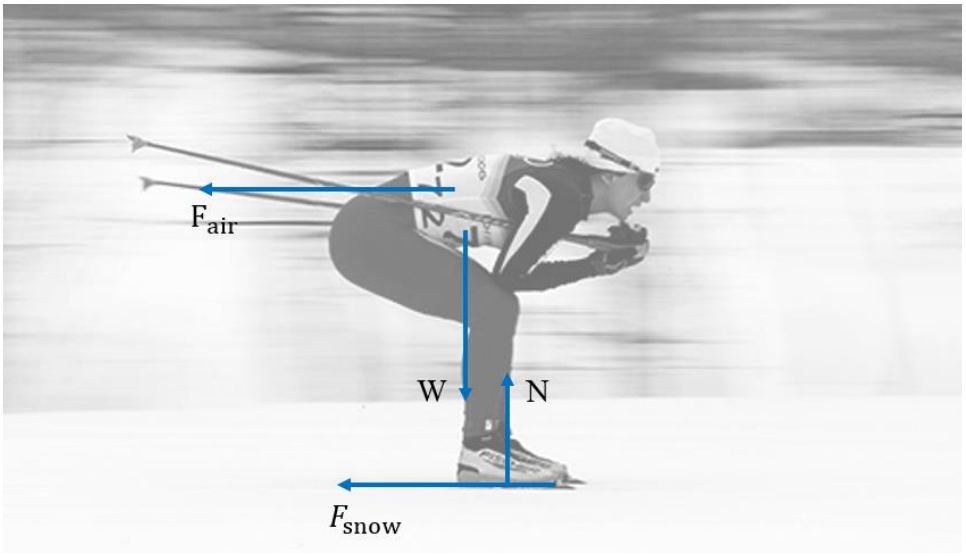

Figure 2: *Free-body diagram of XC skier. Made from a picture by [9] of Norwegian XC skier Marit Bjørgen*

Friction, both static and dynamic, between the ski -and snow base is a highly complicated process and consist of numerous contributions. There are several friction mechanisms operating based on different parameters, such as load distribution, temperature, humidity, snow type and properties of the ski material [10]. A suggested simplified representation of the total kinetic coefficient of friction, if assuming the different mechanisms are operating independently, is given by Equation 2 [10]:

$$\mu_{total} = \mu_{plow} + \mu_{dry} + \mu_{lub} + \mu_{cap} + \mu_{dirt} \qquad (2)$$

The total kinetic COF between ski-and snow base is represented by μ_{total}. μ_{plow} represents the COF contributions from plowing, which becomes relevant if the ski base is of a harder material than the snow base. This will cause asperities on the ski base to penetrate into the softer snow and plow out grooves – a resistance to the skier's motion [11]. μ_{dry} represents contributions from solid-to-solid deformation at the interface between ice grains and ski base asperities. μ_{lub} describes frictional effects due to water lubrication between the ski- and snow base. μ_{cap} represents the COF contribution from capillary attraction, and μ_{dirt} from surface contamination.

Despite being a suitable indication of friction contributions, Equation 2 is an oversimplification as the appearing mechanisms are not actually independent. The relative

importance of the friction components depends on the conditions at hand. A major factor has shown to be the thickness of a water film generated by frictional heating between the ski -and snow base when skiing. This water film is the baseline for investigating the impact of hydrophobic properties of the ski base in this work, and the mechanisms behind it will be discussed in the following section.

2.2.1 Water film formation

It is generally accepted that the water film between snow-and ski base, generated due to frictional heating, is the most important factor for low friction during skiing [12, 13]. By frictional motion, heat is generated and raise the temperature at the contacting points of the two surfaces to the melting temperature of ice. As a result, the ice surface melts locally at the contacting asperities resulting in the formation of a non-continuous meltwater film [13]. Solar radiation absorption also contributes to the heat generation [14, 15].

It has been found that the film thickness greatly correlates with the dominating friction mechanisms observed. Affecting parameters are correlated but can be divided into ski base parameters and snow parameters. *Ski base parameters* include roughness, wettability [13, 16, 17], thermal conductivity [13, 14, 17], ski color [14], hardness, and pressure distribution [17]. *Snow base parameters* include temperature [13, 14, 16, 17], humidity [13, 17], snow density, as well as grain size and shape [17]. Additionally, speed and normal load contribute to the system [13, 14, 16, 17]. Several researchers have measured the typical film thickness. Among them, [18] reported the film to be in the range between 5-13.5 μm within the temperature range of $-40\,℃ - 0\,℃$.

To understand the importance of the film thickness, a basic understanding of the physics at the interface between ski-and snow base is necessary. When the ski velocity is high, and meltwater volume is large enough, the ski surface and the snow base will be fully separated by the water film due to hydrodynamic effects (Hydrodynamic Lubrication (HL) regime, Figure 3A). Here the water pressure is high enough to separate the surfaces. If velocity or meltwater volume or both decreases, the water pressure will drop as well. This will initialize contact between some of the asperities of the two solid surfaces, which makes the asperities increasingly carry the load (Mixed Lubrication (ML) regime, Figure 3B). This will increase friction, which is now given by both shear between interacting asperities and shear of the lubricant. If velocity or water volume or both is decreased even further, the pressure of the meltwater in contact becomes equal to the ambient pressure. The result is an escalation in the number of asperities in contact, and the total normal load being carried by the interacting asperities (Boundary Lubrication (BL) regime, Figure 3C). Now the friction is controlled by

shear stress of boundary layers on the ski running surface and the snow base, meaning the ski base surface structure and the snow crystals respectively [2].

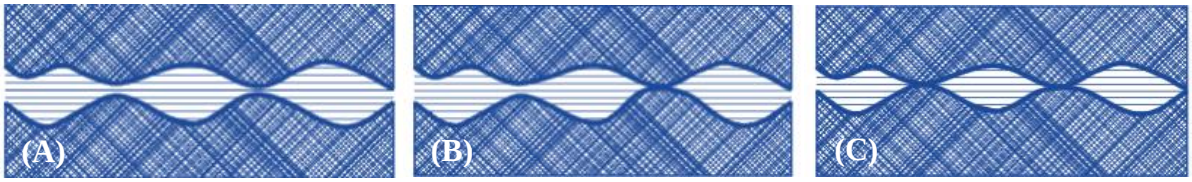

Figure 3: *Lubrication regimes between ski-and snow base: (A) Hydrodynamic Lubrication (HL), (B) Mixed Lubrication (ML), and (C) Boundary Lubrication (BL) [19]*

Temperature is for obvious reasons a major factor for the film thickness. [2] has modified the general Stribeck curve, an illustration of a lubricated glide issue, to the skiing problem (Figure 4). In this figure, velocity is kept constant and friction is plotted as a function of snow temperature. In zone I in the figure, low temperatures constraint the snow from melting, and friction is high due to the dominating friction mechanisms plowing, solid deformation, and partly lubrication. As the temperature increases, the film thickness increases correspondingly and progressively lubricates the surface and decreases friction. The optimal film thickness is reached at t_0, at the border between zone I and II. However, this turns around when entering zone II, as the water film gets thick enough to cover the entire contact area. Now friction contributions from lubrication, capillary forces and dirt are dominating. To understand the concept of capillary attraction between ice grains and ski base, a basic understanding of the interacting forces at the interface between solid, liquid and gas is needed, which will be explained in the next section.

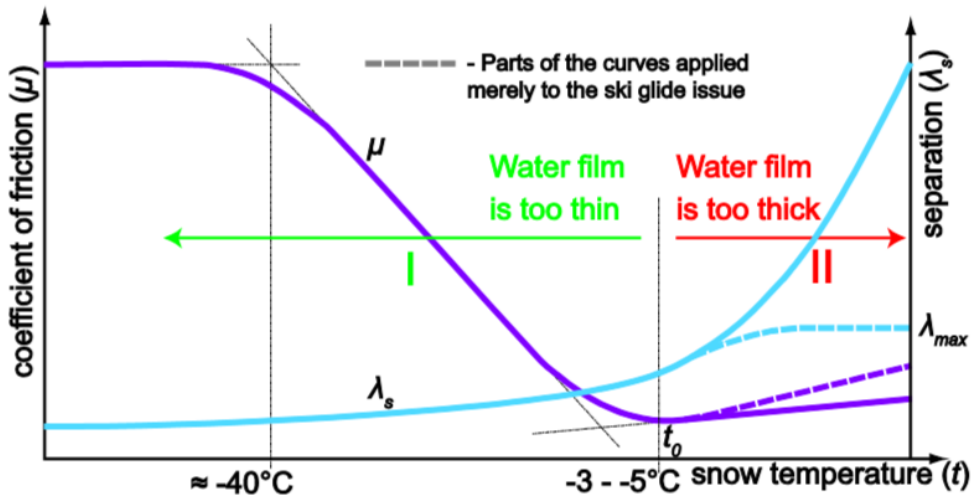

Figure 4*: Generalized Stribeck curve, an illustration of a lubricated glide, modified for the skiing issue, in which gliding velocity is kept constant [2]*

Even though snow temperature is used as the baseline in Figure 4, the actual temperature at the interface between the snow- and ski base also depends on the thermal conductivity of the ski base material. Not all the energy from frictional heating is available for water film creation, there is also energy loss by heat conduction into the snow base and the ski. Hence, the higher thermal conductivity, the faster heat is transferred away from the interface, giving rise to less production of meltwater. [20] showed that thermal conductivity of the ski is not a determining parameter at temperatures around 0º C, but at lower temperatures, a ski base with a high thermal conductivity results in higher friction due to lack of the lubricating water film. Furthermore, this effect was found to be increasingly pronounced by further decreasing the temperature. Additionally, [15] measured the basal temperature of XC skis with both black and white base material. It was observed that the black bases ran at higher temperatures than white bases, an effect they claimed should be measurable during all daylight hours. It is then evident that the solar radiation absorption at the ski base can contribute significantly to the meltwater production, and hence affect ski friction.

2.3 Hydrophobicity, adhesion, and wetting

Wettability describes the preference of a solid to be in contact with one fluid rather than another [21]. Hence, wetting is an attractive interaction between a liquid and a solid. The opposite is dewetting, or repellency. Adhesion is a slightly different but related term that describes the attachment between a liquid and a solid in contact.

A droplet deposited on a surface will spread until it reaches an equilibrium. From an energy point of view, a droplet is minimizing its surface area by taking the shape of a sphere. A molecule in the bulk of a liquid is uniformly in cohesion with surrounding molecules, but molecules on the surface have an imbalance of cohesion and are under tension (Figure 5A). This tension is called surface tension (SFT) and is defined as the energy required to increase the surface area by one unit, in units $\mathrm{J/m^2}$ [22]. If the material adjacent to the droplet is a solid or another liquid, the equivalent term is interfacial tension (IFT). For a material in solid phase, the equivalent term is surface free energy (SFE), which is a material property of the solid material. The degree a droplet will wet a surface, i.e. spread on it, depends on all these tension contributions. SFE can be expressed on a completely smooth surface with a static droplet by Young's Equation (Equation 3).

$$\sigma_{sg} = \sigma_{ls} + \sigma_{lg} \cdot cos\theta \qquad (3)$$

The equation is based on a force balance where the three phases meet, the three-phase point, as illustrated in Figure 5B. σ_{sg} is the surface free energy of the solid, σ_{ls} is the interfacial

tension between liquid and solid, σ_{lg} is the surface tension of the liquid and θ is the static contact angle (CA) [23]. As seen in Figure 5B, the CA defines the angle between the horizontal solid surface and the tangent of the droplet surface at the three-phase point.

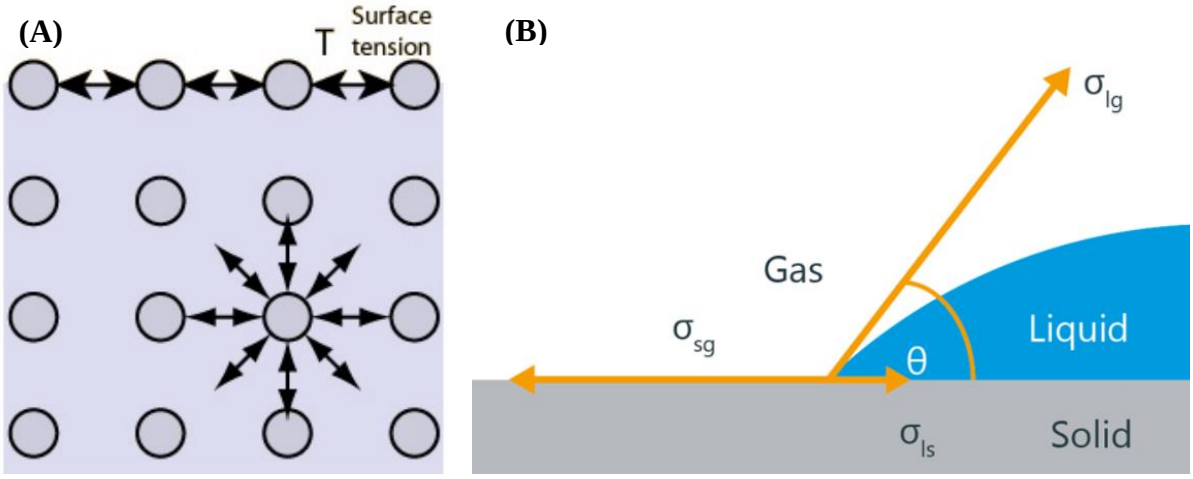

Figure 5: *(A) Molecules in the bulk and on the surface of a material [24]. (B) Illustration of competing forces for a liquid droplet on a surface [23]. The three-phase point is found at the interface of gas, liquid and solid*

2.3.1 Determination of surface free energy

The Owens, Wendt, Rabel, and Kaelble (OWRK) method is a common practice for calculating the SFE of a solid surface from the CA of several liquids. In this method, the interactions between the solid and the liquid are interpreted as the geometric mean of a disperse part, σ^D, and a polar part, σ^P, of both the surface tension and the surface free energy. Firstly, dispersion or London forces are a part of the van der Waals forces, and based on temporary variations in the electron density in the molecule. This produces temporary dipoles, which can further induce temporary dipoles in adjacent molecules [25]. Secondly, polar forces occur in molecules with a dipole moment; these are asymmetrical molecules with permanent inequality of electron density due to difference in electronegativity of the bonding partners [26]. The interfacial tension, which is so far unknown, is then given by Equation 4 according to the OWRK method [27].

$$\sigma_{ls} = \sigma_{lg} + \sigma_{sg} - 2\left(\sqrt{\sigma_s^D \cdot \sigma_l^D} + \sqrt{\sigma_s^P \cdot \sigma_l^P}\right) \qquad (4)$$

The total surface free energy of the solid surface and the surface tension of the liquid are included as the sum of their respective dispersive and polar parts as given in Equation 5-6 [28].

$$\sigma_{sg} = \sigma_s^D + \sigma_s^P \qquad (5)$$

$$\sigma_{lg} = \sigma_l^D + \sigma_l^P \qquad (6)$$

The dispersive parts of the solid's SFE only interact with the dispersive parts of the liquid's SFT, and the polar parts of the solid's SFE only interact with the liquid's SFT. An illustration of this is shown in Figure 6. The small hands represent the weaker dispersive parts and the large hands the stronger polar parts of the solid's SFE and the liquid's SFT. In both figures, a liquid with a total SFT of 50 mN/m is in contact with a solid in which SFE is also 50 mN/m. The difference in the two cases are the dispersive and polar components of the liquid.

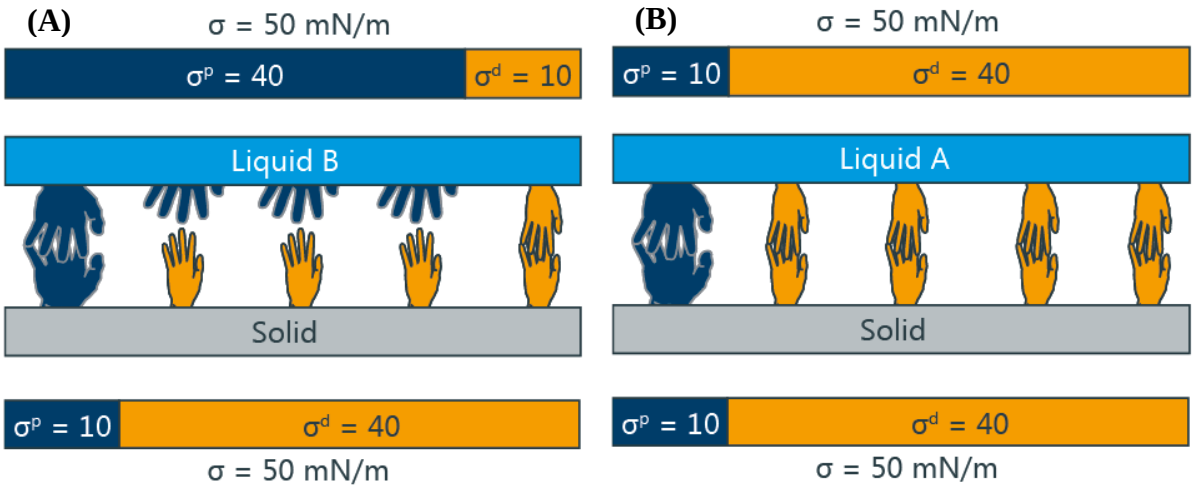

Figure 6: *(A) Difference in dispersive and polar parts of liquid and solid, giving rise to poor wetting. (B) A perfect match between dispersive and polar parts of solid and liquid, resulting in complete wetting [27]*

In Figure 6A only one pair of small dispersive hands and one pair of large polar hands are holding on to each other. Because there are limited attractive interactions between the solid and the liquid, the liquid will reduce its interface with the solid, meaning low wetting and high CA. On the other hand, in Figure 6B there is a perfect match between the dispersive and the polar parts; every polar hand of the solid grabs a polar hand of the liquid, and similarly for the dispersive hands. Here the liquid will perfectly wet the solid surface. Thus, in the absence of interactions, it is evident from Equation 4 that the IFT is maximized and yields the

highest CA. However, the IFT will decrease with increasing interactions between liquid and solid [27, 28].

The four equations (Equation 3-6) contains a total of eight unknowns, which is obviously insolvable. However, both σ_{lg} and the CA are susceptible to direct experimental determination [29]. Additionally, σ_l^D have been published for many liquids [30]. Hence, if utilizing at least two liquids with known disperse parts of the surface tension, together with their respective measured σ_{lg} and CAs, the solid's SFE can finally be found by Equation 3-6 [29]. The OWRK method is utilized in many instruments that determines the surface free energy of a material surface, a property which is necessary when wettability is an essential parameter for material selection. The main reason for including it here is that the method and associated figures indicate how the wettability of materials differ due to their chemical composition.

2.3.2 Contact angle measurements

To accurately determine SFE is essential for characterizing the wettability of a solid material surface and its adhesion to a liquid [31]. It was evident in the previous section that measuring SFE is not straightforward. However, an indication of the surface free energy can be found by simply measuring the CA for a droplet on a surface. If comparing the CAs attained by droplets of the same liquid deposited on several surfaces under the same conditions, an indication of relative SFE can be stated.

There are additional measurements than the static contact angle that are commonly used to study the wetting, dewetting, and adhesion characteristics of a material surface. Dynamic contact angle measurements describing these characteristics are the receding contact angle θ_R (RCA), and the advancing contact angle θ_A (ACA). These terms are related to how a droplet behaves if water is added or removed to it when already in equilibrium [31]. Figure 7A illustrates water added to a droplet; the solid-liquid interface area will stay constant, while the contact angle increase, until reaching the ACA, in which the interface area increases. On the contrary, Figure 7B illustrates water removed from a droplet; the solid-liquid interface area stays constant, while the contact angle decrease, until reaching the RCA, in which the interface area decreases [22]. [32] states that θ_A is a measure for surface wettability (or repellency), while θ_R is a measure for surface adhesion. The contact angle hysteresis (CAH) is another CA measurement commonly used, which is the difference in the advancing and the receding contact angles (Equation 7).

$$\Delta\theta = \theta_R - \theta_A \qquad (7)$$

One additional relevant term is introduced for a droplet on an inclined plane. The angle in which a droplet rolls off an inclined plane is termed tilting angle (TA) and symbolized by α. The contact angle hysteresis is a measure describing whether a droplet will roll off or stick to an inclined surface, as CAH and TA have shown to be proportional (Equation 8, Figure 7C) [33].

$$\Delta\theta \propto \alpha \qquad (8)$$

On an inclined plane, wettability affects the movement of a water droplet, and the state of equilibrium can now be found by Equation 9 [34]:

$$\frac{mg(sin\alpha)}{w} = \sigma_{lg}(cos\theta_R - cos\theta_A) \qquad (9)$$

Where σ_{lg}, θ_R and θ_A are related to the α in which droplet starts sliding, m is the mass of the droplet, g the gravitational acceleration, and w is the width of the droplet parallelly to the inclined plane. To summarize, CA, ACA, RCA, CAH, and TA are all indicative measures of hydrophobicity.

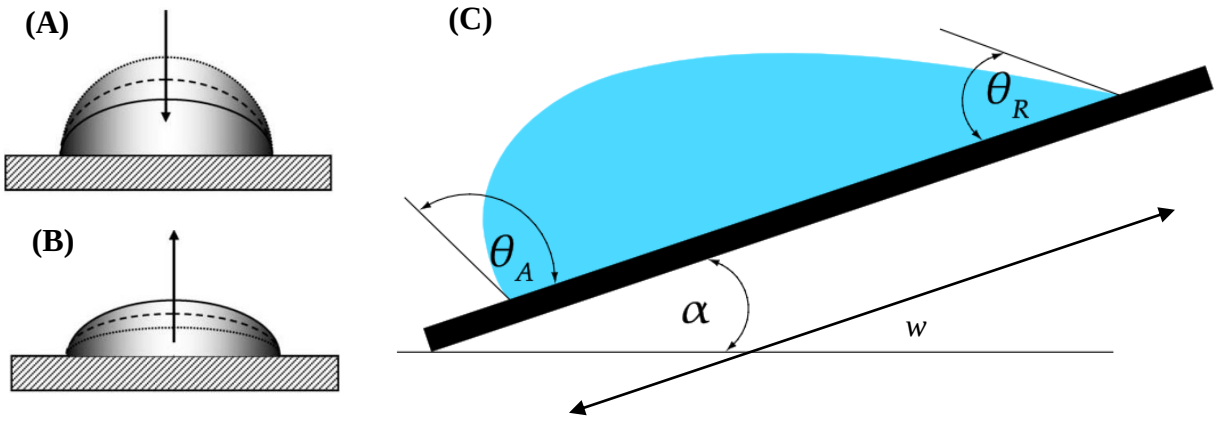

***Figure 7**: (A) Measuring advancing CA, θ_A, when adding liquid to a droplet, and (B) measuring receding CA, θ_R, when subtracting liquid to a droplet [35]. CAH is the difference between the two angles, and proportional to α in (C), which illustrates dynamic wetting of a water droplet on an inclined, solid surface [2]*

2.3.3 Hydrophobicity

From Young's equation (Equation 3) it is evident that a CA of 90° marks when the surface tension of the solid-gas and the liquid-gas interfaces are equal. A hydrophobic material is

defined as a material in which a water droplet deposited on its surface will attain a CA $> 90°$, marking that the surface tension from the solid-gas (SFE) interface is smaller than that of the liquid-gas interface (SFT). Equivalently, a hydrophilic material is defined as a material in which a water droplet deposited on its surface will attain a CA $< 90°$, marking that the surface tension from this solid-gas interface is greater than that of the liquid-gas interface [22].

Further, a superhydrophobic material is defined to have a CA exceeding 150 ° for a deposited water droplet, while a superhydrophilic material a CA below 10 °. As SFE is the tension component pulling the droplet outward, resulting in a smaller contact angle, it is evident that materials with low SFE are preferred to attain a high CA. This again corresponds to a hydrophobic material, which is the intention in this work.

However, these definitions are somewhat disputed. For example, [32] found that a more accurate definition of a hydrophobic material is when $\theta_R > 90°$, and similarly a hydrophilic when $\theta_R < 90°$. Nevertheless, the definition of hydrophobicity which includes the static CA will be used in this work.

2.3.4 Connection to meltwater

The reason for increased friction when the water film thickness exceeds t_0 (Figure 4) because of capillary attraction, as stated in section 2.2.1, can now be explained. The definition of capillary attraction by [36] can be rephrased to the ski problem; a demonstration of surface tension by which the portion of the water film surface coming in contact with the ski base is elevated. This can be seen as water bridges between the asperities on the snow base that are not carrying the load, and their adjacent asperities on the ski base (Figure 8). As the ski slides on the snow, the created water bridges require a certain energy to break. The force needed to break up these capillary bridges, increases friction, as was seen in zone II in Figure 4. [12, 37]. This fact completes the previously stated argument that the forming water film can both act as an efficient lubricant and as a medium increasing friction, depending on its thickness and the associated dominating friction mechanisms. However, no physical model or experiments exist to fully explain the contribution of capillary bridges to the friction force [16].

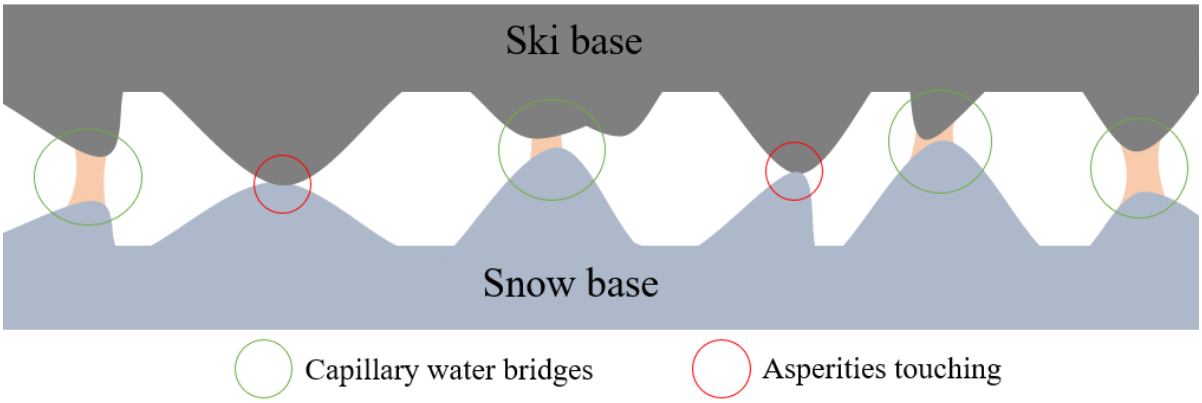

***Figure 8**: Interface between ski-and snow base illustrating where asperities are carrying the load, and capillary water bridges where asperities are not carrying the load. Remade from [38]*

After separately considering the friction mechanisms of ski glide, with focus on the impact of the water film thickness and the phenomena of hydrophobicity, correlations can be drawn between the two in the aim of reduced ski friction. Under cold conditions, resulting in lack of lubricating meltwater, the limited water available would slide more readily on a hydrophobic ski base. Correspondingly, in warmer conditions, resulting in excess of lubricating meltwater, breaking the capillary bridges would require less energy on a hydrophobic ski base as the area of attachment is smaller. Hence, a hydrophobic ski base is believed be advantageous in all snow conditions [39], as it would ease the transportation of meltwater opposite to the sliding direction and correspondingly enable the ski to slide forwards more efficiently.

2.4 Roughness and hydrophobicity

Until now, hydrophobicity has been defined on a smooth surface and described as a material property due to the chemical components of the solid surface and its interactions with a deposited liquid. However, this is not the only or the complete way to attain a hydrophobic surface. This section will address how a material surface can hold hydrophobic properties by the geometry of its surface structure.

2.4.1 Roughness

A solid surface has a complex structure, with characteristics depending on the properties of the material elements, potential processing, and interactions with the ambient environment.

Young's equation (Equation 3), expresses SFE for a completely smooth surface. However, surfaces contain irregularities and deviations, which can be of various order [40]. Most commonly, surface roughness refers to the height variations of the surface relative to a reference plane, as illustrated in Figure 9A. Roughness can be characterized as the *arithmetical mean height, Sa,* as described mathematically in Equation 10 [41].

$$Sa = \frac{1}{A}\int_0^L \int_0^L |z(x,y)| dxdy \qquad (10)$$

Even though roughness expressed as the vertical deviation from a mean line is a valuable measure of a surface, it does not give comprehensive information about the topography of the surface. This is illustrated in Figure 9B, where six obviously very different surface features patterns all have the same Sa. Hence, a few more terms will in the following be described, but without stating their mathematical definition.

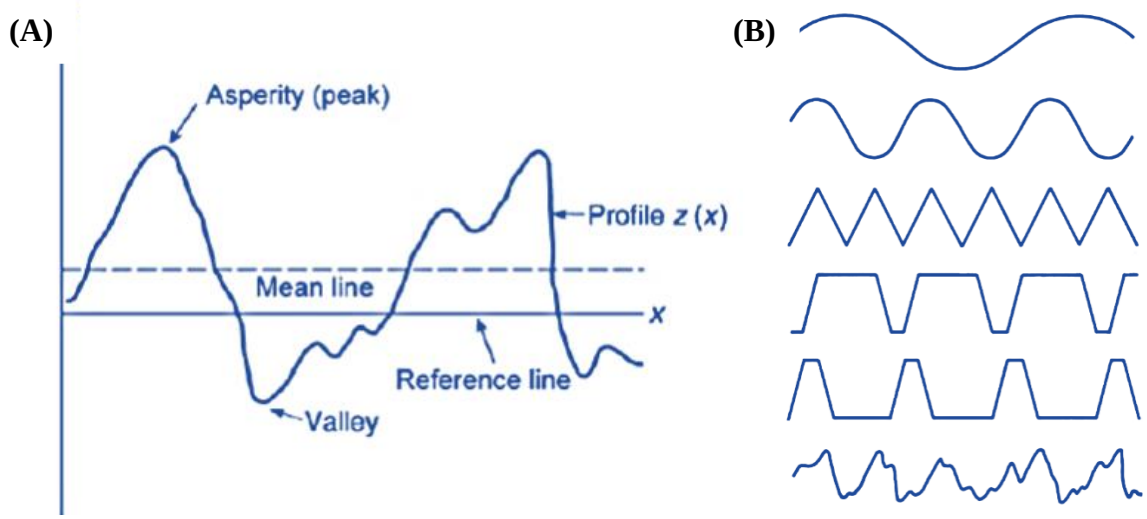

Figure 9: *(A) Schematic illustration of surface profile z(x). (B) Six different surface profiles with identical Sa values [40]*

Skewness, Ssk represents the degree of bias of the roughness shape. *Ssk* = 0 if the height distribution of the surface is symmetrical around the mean plane (Figure 10). However, if *Ssk* < 0, the height distribution of the surface is biased above the mean line. On the contrary, if *Ssk* > 0, the height distribution is biased below the mean plane. *Kurtosis, Sku,* is a measure of the sharpness of the roughness profile. *Sku* = 3 if the height distribution is normal distributed (Figure 11). If *Sku* < 3, the height distribution is biased above the mean line, meaning that the distribution produces fewer and less extreme outliers than the normal distribution does. Similarly, if *Sku* > 3, the height distribution is spiked, meaning that the distribution produces

more outliers than the normal distribution. Hence, both kurtosis and skewness are descriptors of the shape of the probability distribution of the surface height profile. *Root mean square height, Sq,* is equivalent to the standard deviation of heights.

Maximum pit height, Sv, is defined as the depth of the largest pit in the area measured. On the other hand, *maximum peak height, Sp,* is the height of the highest peak. *Maximum height, Sz,* is defined as the sum of the largest peak height value and the absolute value of the largest pit depth value within the area measured [41].

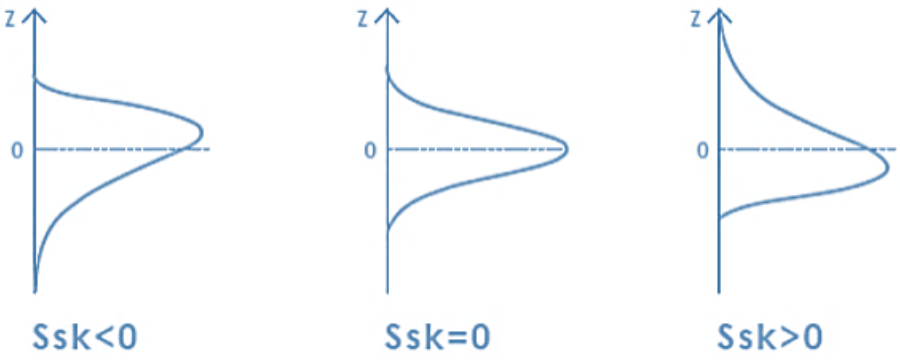

Figure 10: *Skewness of a surface [41]*

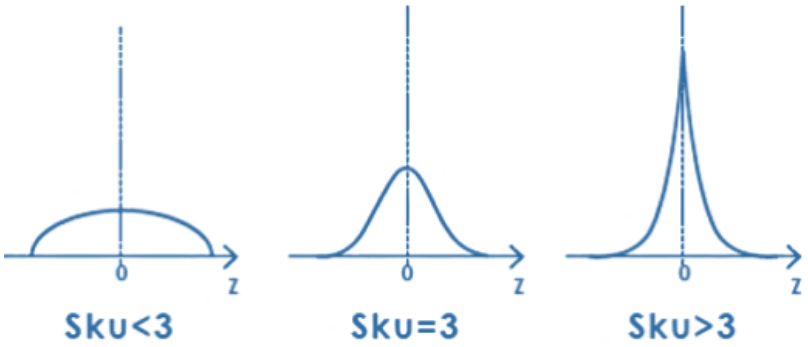

Figure 11*: Kurtosis of a surface [41]*

2.4.2 Contact angle on rough surfaces

As was seen in section 2.2.1, a very thin water film would result in increased contact between asperities of the ski-and snow base, making shear of the ski structure and the snow crystals the restraining factor for ski glide. Similarly, in section 2.3.4, an explanation was given to

how a thick water film would give rise to the formation of capillary bridges, another factor for increased friction. For all water film thicknesses somewhere in between these two extremes, a combination of the two, in addition to related effects, will occur (Figure 8). The challenge is to find the shape and dimensions of the surface features that enhance a high contact angle and results in low ski friction.

The first step in determining the contact angle on a rough surface is, according to [35], to define the actual contact angle (ACCA) and the apparent contact angle (APCA), which are illustrated in Figure 12. It turns out that in many cases it is appropriate to set APCA equal to the contact angle in Young's model (Equation 3), making the latter the only one needed to find the SFE of a solid, rough surface. However, this is a challenging parameter to measure on a rough surface, as there may exist a wide range of practically stable APCAs.

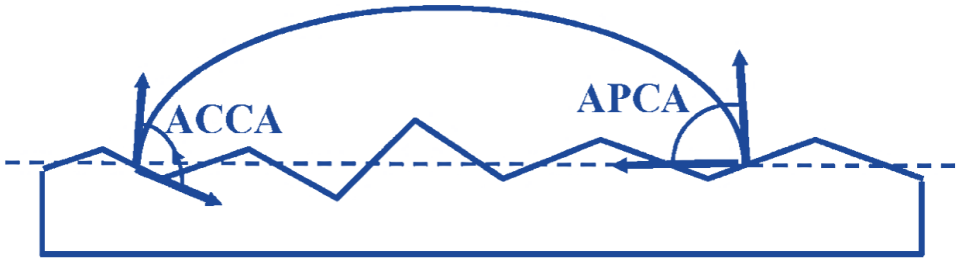

***Figure 12**: Actual and apparent contact angle, ACCA and APCA, on a rough surface [35]*

The two most accepted wetting models approximate APCA on a rough surface and were developed by Wenzel (1936), and Cassie and Baxter (1944) [42]. Firstly, the Wenzel wetting model, illustrated in Figure 13, assumes that a droplet completely penetrates the rough features, and is given by Equation 11 [2, 35]:

$$cos\theta' = \frac{r(\sigma_{sg} - \sigma_{ls})}{\sigma_{lg}} = rcos\theta \qquad (11)$$

Where θ' is APCA, θ is the CA from Young's model on a smooth surface, and r is the roughness ratio, defined by Equation 12:

$$r = \frac{Real\ surface\ area}{Apparent\ surface\ area} \qquad (12)$$

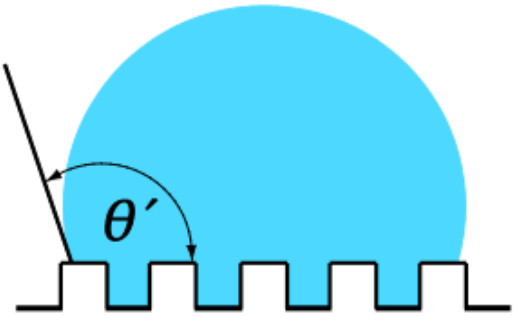

Figure 13: *Wenzel wetting model [2]*

Secondly, the Cassie-Baxter wetting model, illustrated in Figure 14, assumes that air pockets are trapped between the asperities under the droplet, and is given by Equation 13:

$$cos\theta' = fcos\theta + (1-f)cos180° = fcos\theta + f - 1 \qquad (13)$$

Where $\cos 180°$ is the water contact angle for air and f is the area fraction of a solid surface defined by Equation 14 [2]:

$$f = \frac{\sum a}{\sum(a+b)} \qquad (14)$$

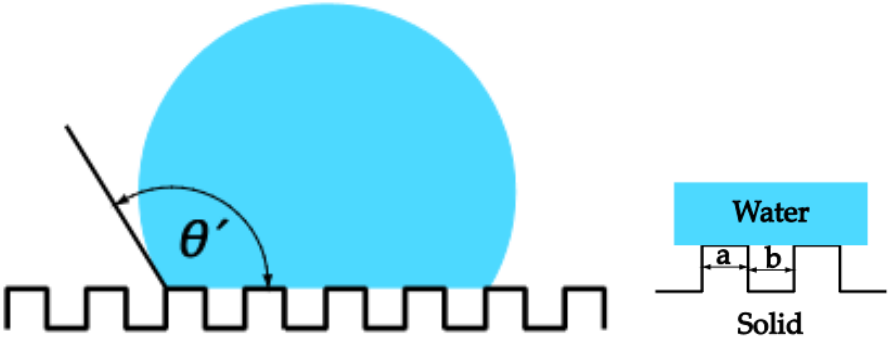

Figure 14: *Cassie-Baxter wetting model [2]*

Equilibrium wetting on a rough surface can be seen as a competition between complete liquid penetration into the grooves, as in the Wenzel model, and the entrapment of air pockets inside the grooves underneath the liquid, as in the Cassie-Baxter model [43]. For the application of skiing, roughness in the Wenzel regime is not very promising for reducing capillary drag [2]. According to [3], both Cassie-Baxter and Wenzel states can give high static CA, but only the Cassie-Baxter state can additionally give low TA. Hence, it is desirable in this work to achieve the Cassie-Baxter state at the interface between the ski and the snow, due to the mobility of water droplets on a surface in this regime. However, it is likely that the droplet

configuration on the surface can be partly explained by the Wenzel model and partly explained by the Cassie-Baxter model. According to [22], it is unlikely that a real droplet will appear completely as suggested by the preferred Cassie-Baxter model.

The Wenzel and Cassie Baxter models are only illustrating the interface between a droplet and a rough surface but do not state the optimal dimensions of the surface features to attain the highest CA and the lowest TA, which in combination would yield the greatest hydrophobicity. The reason for this is that the feature dimensions depends on the application and conditions at hand. In the ski glide problem, the optimal ski base structure roughness varies under different snow conditions according to the thickness of the generated water film. Many researchers have experimented with ski base structures with a roughness on the micro-, and some on the sub-micrometer scale. Their findings are not giving one specific correlative trend, as their experiments are affected by many factors. For example, according to [44], a coarse ski base structure (*Sa* between 7-10 μm) is optimal when the water film is thick, while a finer ski base structure (*Sa* between 1-4 μm) is optimal when the water film is thin. The parameters affecting the thickness of the water film are numerous and were discussed in section 2.2.1. Secondly, [37] detected the optimum surface roughness of the ski base to be in the range of $Sa = [0.2, 1]$ μm at snow temperatures between -2 and -4 ℃. [45] found that higher CAs gave lower COFs and subsequently increased speed in alpine skiing, in which surface features at the micro-scale were tested. It should be noted that the individual peak or valley is not the only determining factor of the surface structure, but also the overall configuration of the pattern matters in terms of directivity and parallelism compared to sliding direction [46, 47].

Every section up to now has discussed minimization of ski friction in terms of water film generation, hydrophobicity, and ski base roughness, both their individual and correlative effects. It has become evident that surface free energy is a material property describing how a solid surface will interact with a liquid due to its chemical composition. The contact area between a droplet and a solid surface will vary, describing the wettability of the solid material. Additionally, it was shown that by introducing a rough surface instead of a smooth, the contact between the asperities on ski-and the snow base would also be reduced. This, in turn, will reduce shear stress between contacting asperities and the number of capillary bridges between adjacent asperities, which is believed to further reduce friction. The main point from all above sections can be summarized; both the chemical composition of the solid surface and its physical surface structure are factors that determine wettability and are hence believed to be essential in the aim for reducing friction on the ski base. However, only the latter will be of focus in this work.

2.5 Ski configuration

This section will emphasize on different aspects of full-scale XC skis that will be relevant to the fabrication of miniature prototype skis. On one hand, it includes design related elements, such as the ski's construction, physiochemical processing steps, and material selection. Additionally, it covers the ways of testing its performance.

2.5.1 Pressure distribution

A XC ski is split into a *glide zone*, which is located at the front and rear of the ski, and a *grip zone*, which extends from the heel to about 30 cm in front of the toes (Figure 15). The grip zone needs to possess high friction to help the skier push forward. However, the flex in the ski limits the contact between this zone and the snow base when sliding forward. The two glide zones are ensuring the forward sliding and should hence have minimal friction. In double poling (Figure 1C), good glide is essential to reduce the work for a certain speed. In the diagonal stride (Figure 1A) and the kick double poling (Figure 1B) techniques, both good glide and a good grip are crucial. These two factors might contradict each other's functions [48]. As this work is concerning friction minimization, the two glide zones of the ski are of main interest, where low friction is necessary for high-speed skiing.

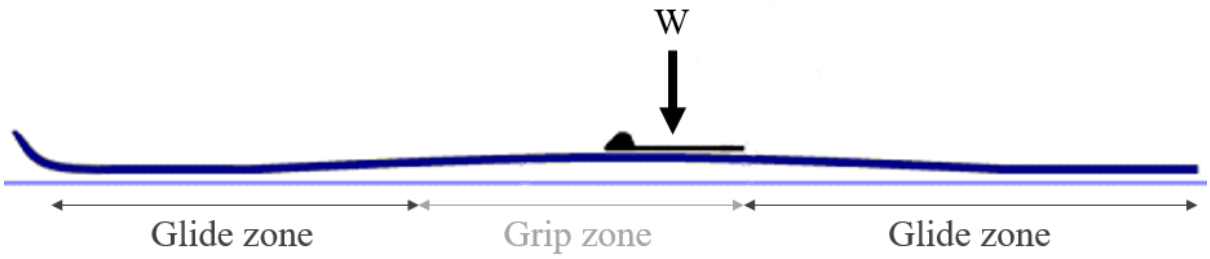

Figure 15: *Illustration of glide- and grip zone of XC ski where W represents the weight of the skier. Remade from [49]*

It is obvious from the ski configuration in Figure 15 that the weight of the skier will not distribute uniformly along the ski. The pressure distribution also depends on which technique the skier is practicing, and at which stage of movement within this technique. For example, the pressure distribution on the ski will be very different between stage 5 of the kick double poling technique (Figure 1B), and stage 1 with the double poling technique (Figure 1C). In the former, the skier has just kicked off with the posterior leg and the entire weight of the skier is on the anterior leg. When the weight is on one leg, and the pressure is distributed on

one ski only, it is termed a *full weight mode*. On the contrary, when the weight of the skier is equally distributed on each ski, as in stage 1 in Figure 1C, it is termed a *half weight mode*.

Figure 16 shows the force distribution from six pairs of Madshus Nano skating skis. The measurements were recorded for 10 seconds while a skier with a body mass of 85.7 kg, including skis, boots and ski clothing, was standing evenly on both skis in a steady normal position [48]. Even though skating skis are generally shorter, narrower, and lighter than the classical skis that are of focus in this work, the static pressure distribution is considered to be similar enough to use it as a reference here. As already mentioned, the desire to maximize hydrophobicity and minimize friction is the same for all kinds of skis, the difference is the direction of the surface pattern in relation to the direction of ski motion.

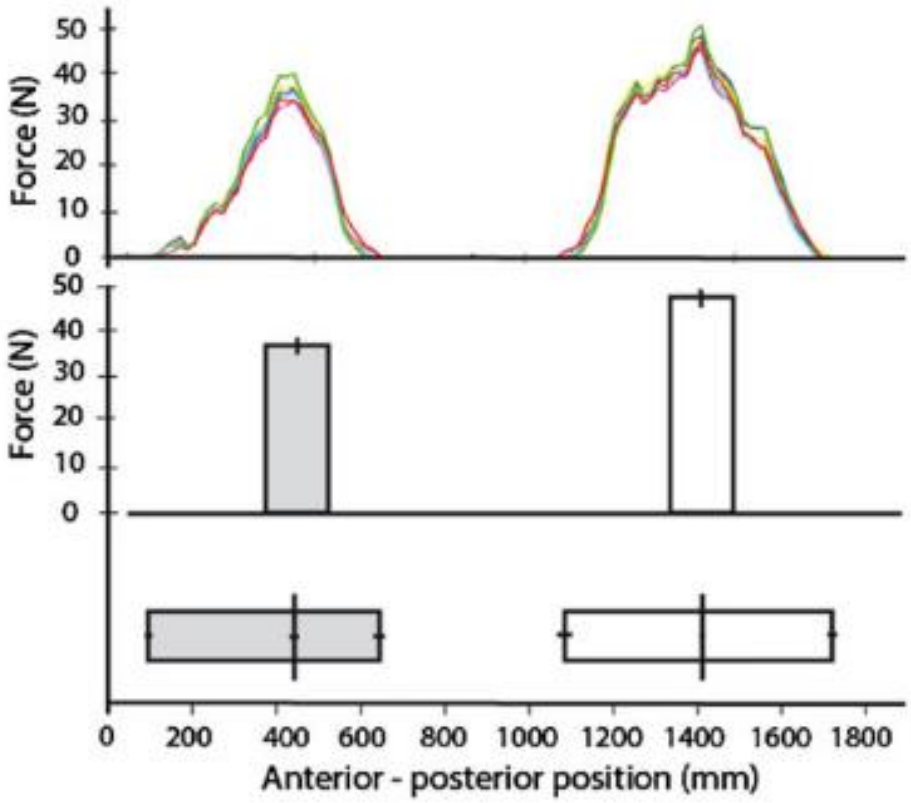

Figure 16: *Pressure distribution measured underneath six pairs of Madshus Nano skating skis. The upper part of the bottom panel displays bar plots of average peak force and location of max. forces of the graph in the top panel. The lower part of the bottom panel displays horizontal bars showing average anterior-posterior onset and offset of ski force distribution, as well as the location of average peak force, indicated by vertical lines [48]*

2.5.2 Ski base material

The ski base is only approximately the 1-2 mm bottom thickness of a ski (Figure 17). As this is directly in contact with the snow base and meltwater, it will be the part of the ski of major interest in this work. As was previously discussed, numerous properties of the ski base affect the thickness of the water film, such as roughness, wettability, thermal conductivity, color, and hardness, and hence all affect hydrophobicity and ski friction. Accordingly, these factors will have to be taken into account when determining the ski base material. [2] reports the four overall most important material properties of the ski base to be hardness, wear resistance, wettability and thermal conductivity. The importance of the two latter has already been discussed in previous sections. The hardness of the ski base is important to make sure that it is not softer than the ice base at the temperature in which skiing will be performed. Asperities on the hardest material will penetrate the softest. Hence, the comparative hardness properties of ice-and ski base at relevant temperatures are crucial for the performance in terms of ski friction. Additionally, wear resistance of a ski base material is important as cold and dry snow is an abrasive medium which can easily degrade the ski base [2]. Modified or unmodified UHMWPE and PTFE are the most used materials for the ski base, and will in the following be discussed in terms of the four properties above.

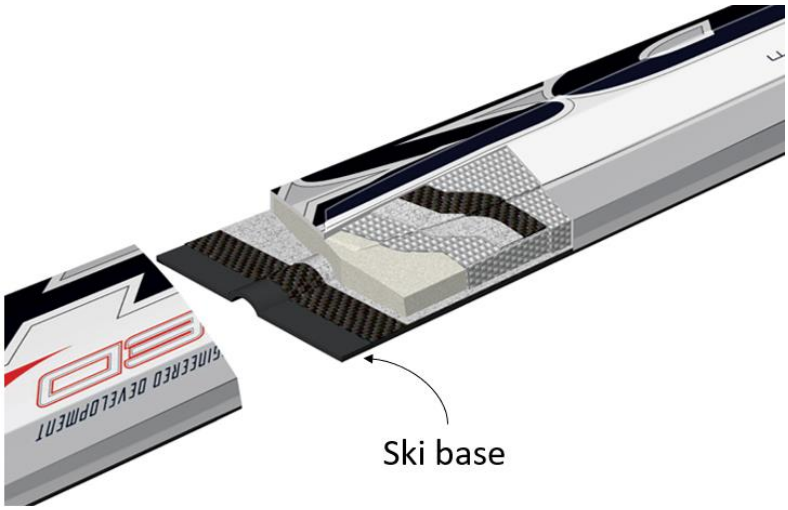

Figure 17: *3D cross-section view of XC ski [50]*

Polyethylene (PE) has been the most used ski base material since the 1950s. Today the use of ultra-high molecular weight polyethylene (UHMWPE), a semi-crystalline and thermoplastic polymer with the molecular formula $(C_2H_4)_n$, is especially widespread [51]. This is a type of PE with extremely long chains, and typical molecular weight between $3 \cdot 10^6$ and $12 \cdot 10^6$ g/mol [2, 47, 52]. There are two general varieties of the UHMWPE ski base; the pure transparent base and the “graphite” black base with carbon-black additive. Today almost all

cross-country skis are made of the latter [2]. UHMWPE is easy and cheap to produce. As all other plastics it, has a low thermal conductivity, with a value of approximately 0.52 W/mK [37], but which varies to some degree depending on potential additives.

UHMWPE is one of the most durable types of thermoplastic PE available; it is extremely wear resistant and has high both tensile and compressive strengths. Most plastics possess the important advantage of absorbing vibrations, but higher molecular weight polyethylenes are generally used at lower temperatures where high impact resistance and good wear resistance both are important. UHMWPE has outstanding abrasional resistance, which is clearly a necessity when sliding over numerous kilometers of snow, ice, and contaminations [14]. The hardness of ordinary PE is given in Table 1 for five different temperatures and compared to similar measurements of ice and PTFE. From this table, it is evident that the hardness of ice is surpassing PE between 0 ℃ and -5 ℃**,** which is clearly not very promising for a ski base. Even though the attempt to obtain similar data for UHMWPE at all these temperatures has not been successful, these hardness values are assumed to be higher. According to [2], UHMWPE is softer than ice at -15 ℃**.**

Most importantly for this work, UHMWPE has excellent self-lubricating and non-sticky character [53]. Additionally, the material has unique tribological characteristics and is reported with an SFE value of 36.8 mN/m [37], which can be further modified with additives and additional structuring to meet certain requirements [47].

Table 1: *Hardness of ice, PE and, PTFE at five different temperatures from a standard Vickers diamond test. Bold numbers in cursive marks when the hardness of the ice surpass the PE and PTFE. Remade from [54]*

Material	**Temperature**				
	0 ℃	**-5** ℃	**-10** ℃	**-15** ℃	**-20** ℃
Ice	1.8 kg/mm^2	3.8 kg/mm^2	5.0 kg/mm^2	6.0 kg/mm^2	6.8 kg/mm^2
PE	2.1 kg/mm^2	***2.4 kg/mm^2****	2.7 kg/mm^2	3.3 kg/mm^2*	3.8 kg/mm^2
PTFE	5.3 kg/mm^2	5.5 kg/mm^2	5.8 kg/mm^2	6.1 kg/mm^2	***6.5 kg/mm^2***

*According to [2] UHMWPE is actually softer than ice at -15 ℃

Polytetrafluoroethylene (PTFE) is another type of PE - best known as a type of Teflon®, developed by DuPont Co. - in which all hydrogen atoms are changed with flour [55], attaining the chemical formula $(C_2F_4)_n$ [51]. As UHMWPE it holds a low thermal conductivity, in which value is approximately 0.24 W/mK [51]. However, PTFE lacks the mechanical strength as UHMWPE and possess poor wear and abrasion resistance [56]. Nevertheless, PTFE is softer than ice at approximately the same temperature as UHMWPE

(Table 1 and comment marked with *). Additionally, the polymer has even better friction properties than UHMWPE. In fact, PTFE is the best candidate when it comes to hydrophobicity, possessing an extremely low SFE value of 18.5 mN/m [51]. Nevertheless, because of its low wear resistance, PTFE is less frequently used as ski base, and to a higher extent utilized as a coating wax or as an additive to UHMWPE. However, according to [57], ordinary PTFE can easily be replaced by a cross-linked version, increasing its wear resistance. A ski base of PTFE has another advantage; there is no need to use the hazardous fluor-compounds to improve hydrophobicity. The usage of of these substances, as a step in the preparation of XC skis, will be discussed in the next sub-section.

2.5.3 Physiochemical processing

From section 2.5.1, it is obvious that the glide- and grip zone will be prepared differently to attain their individual functions. Even though various physical and chemical interactions between snow and skis are well established, many correlative scientific factors are unknown or uncertain. Hence, preparations are greatly based on experience, and the ski technicians select the preparation steps that have shown to perform best under the snow and weather conditions at hand [58]. In the following, the different general processing steps of the glide zones, performed by the Norwegian waxing team for classical XC skiing, will be presented in a simplified version. The steps are recreated from demonstration and conversation at the Norwegian National opening FIS (Fédération Internationale de Ski) at Beitostølen in November 2017, with some additional external references where more information seemed useful.

I) *Stone grinding* is the first processing step, in which a special stone grinding machine developed for the application of skis are used (Figure 18A). Numerous grinding patterns are available, ranging from fine to course. This tool gives the ski base a permanent structure [59] and is therefore only conducted on a new pair of skis or if it is desired to reset the entire ski base. This step is either done by the ski manufacturer or by Olympiatoppen themselves.

II) *Gliding wax* is further deposited, in which type depends on the snow- and weather conditions. It is either applied as a fluid or as a hot wax, in which the latter is a solid block that is melted onto the ski base with an iron (Figure 18B). If using this type, the unsaturated material will be removed with a scraping tool when cooled down. Gliding may be performed 6-8 times.

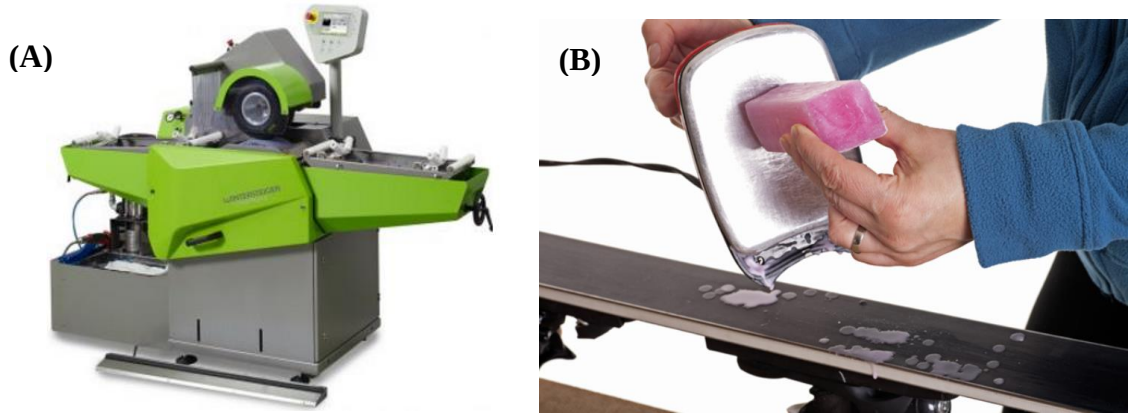

Figure 18: *(A) Stone grinding machine [60]. (B) Hot wax applied by iron melting [61]*

III) A *manual riller* is then rolled over the ski base (Figure 19A). A riller consists of a metal cylinder with a specific pattern that will be transferred along the ski base by hand force. There are numerous patterns, which are selected based on experience and weather conditions. The pattern penetrating the ski base is only around 100 μm, creating an elastic deformation [59]. Figure 19B illustrates the effect of a manual riller in a brown cheese. Obviously, the ski base will not have as deep features as the brown cheese depicted as it is a much harder material. This tool gives the ski base a temporary structure as the features created by the manual riller can be reset. This allows the skier to continue using the same pair of skis from race to race with the possibility of having a different ski base structure for varying conditions. Resetting can be done in several ways. In terms of both effectiveness and cost, melting glide wax on the ski base at 120 ℃ is considered one of the best reset methods [59], where the elevated temperature is the main reason for the reset of the structure.

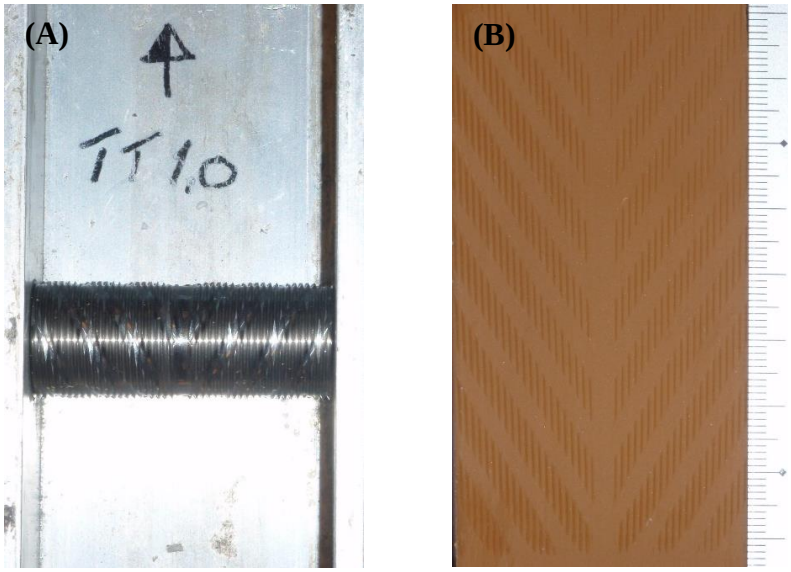

Figure 19: *The manual riller (A) is used on a brown cheese in (B) for illustrational purposes [62]*

IV) Another layer of a gliding substance is finally applied before the ski is ready to use. This is of a different type than in II) and can be in powder form. This substance is usually a fluorocarbon and possesses an extremely low SFE. It is therefore advantageous if this substance maintains on the ski base for as long as possible before worn away. Step III) and IV) can be performed several times interchangeably with varying parameters to attain a certain resulting surface.

During the process of wax application at elevated temperatures in step II), airborne particles and fumes containing a blend of gaseous fluor-compounds are released [63]. These compounds are disputed as recent studies have shown links to serious health issues, such as various types of cancer [64, 65] for the wax technicians applying it. It is also a threat for the nature in which the substance is worn off. The fluor-compounds from ski wax hardly breaks down and hence accumulates in both nature, including water, soil, and animals, as well as humans. Many of the possible health concerns with fluor-containing substances for humans are connected to inhalation of the fluor-compounds in gas phase, which ski technicians are exposed to despite ventilated areas [63]. It is desired to minimize or eliminate the usage of fluor containing substances in ski wax products in the future. PFOA (perfluorooctanoic) is one of the substances in question, in which the Norwegian and German governments are working together to prohibit the usage of in ski wax in EU within 2020 [65]. As the fluor-substances are currently believed to be some of the best products on the marked for optimal ski glide, there is a need for new solutions to substitute the fluors. This work can be seen as a step towards optimizing ski glide through hydrophobic surface structuring so that the usage of fluor-compounds would be unnecessary.

2.5.4 Ski performance testing methods

Testing of skis is essential both prior to major XC ski events, in addition to research on parameters relevant to performance in development and improvement of ski equipment. [66] categorizes the types of *in-field* testing methods into; *parallel testing, glide-out tests, feeling tests, timed gliding tests,* and *gliding tests with advanced technology*. Each test method has benefits, challenges, and drawbacks, and the test type is selected based on the circumstances and the time and equipment available.

Parallel testing is a much used XC ski testing method among the ski technicians in Olympiatoppen. The method is based on comparing the performance of two pairs of skis at the time, in a total set of eight pairs. The parallel test is carried out by two skiers starting with the same initial velocity, for example by holding hands down a slope until their speed is equalized (Figure 20A). Once equal speed is reached, the skiers can release the grip and slide down in a static squat position (Figure 20B). The pair of skis ahead at a marked point is further observed visually. After this run, the skiers will switch their pair of skis and note whether the winner is the same as in the previous run. This is done with all the eight pairs of skis, and in each run, the best pair continues to the next round. In the final round, one pair is found to be the best for the given conditions. This test method is relatively easy to carry out but is only of quantitative character as there are several potentially occurring errors. For example, velocity difference from run to run may differentiate and is not measured accurately. Additionally, the snow surface may differentiate throughout the tracks, but also from run to run. If the tests are conducted right before a ski event, the spot in which the tests are carried out may also not be representative for the actual race track.

Figure 20: *Parallel test by two Olympiatoppen technicians at the Norwegian National opening FIS competition at Beitostølen in November 2017. (A) The skiers are holding hands to equalize velocity. (B) The skiers run down the slope separately in a squat position*

A *glide-out test* is another common and straightforward test. In this test, one skier is operating all the ski pairs to be tested, one at the time. For each pair, the skier is starting at the same starting point with the same initial velocity. The pair reaching farthest before stopping is observed. As this test can be a lengthy process it is highly likely that the external conditions change throughout the duration. Variations are such as wind, temperature, weight distribution, and wear of the ski track are all factors potentially influencing the results [67].

A *feeling test* is a subjective test carried out uphill by a ski technician or the skier himself. The test is not based on concrete measurements but based on the skier's perception of the skis; the feeling of wearing them compared to the skier's personal preference and skiing style.

Timed gliding test is conducted by measuring the time a skier with a specific pair of skis spends traveling between two marked points on a downhill track. To improve the quality of such a test, each pair of skis should complete at least six runs with the same skier. The pair of skis tested in one set, usually consisting of eight pairs, are finally compared [66]. The potential errors in this test are the same as the ones mentioned in the glide-out test.

In recent years, evolving *technological developments* have given new ways to monitor important parameters during gliding tests. These can further be divided into *real-life experiments*, which are methods where a pair of ordinary skis is to be tested by a skier, or *slider model experiments*, which are methods in which ski prototypes have been custom made for the sake of testing [13]. All the test methods mentioned above are examples of the former but without the use of more complex technology. Slider models reduce unpredictable human factors and increase the control of parameters such as velocity and load. Numerous different methods of both real-life-and slider model experiments utilizing new technology have been reported in the literature.

An example of a real-life experiment was developed by [68]; a gliding test, in which time was measured between two photocells along the track at an outdoor facility. [66] also did a traditional gliding test, but together with a test in which the skis were equipped with an inertial measurement unit (IMU) to calculate the acceleration loss as a function of position down a test slope.

An example of a slider model method is reported by [69]; COF was determined by measuring the decay in velocity of a weighted test sled by passing over a series of sensors giving time and position information. [70] developed a system, consisting of load cells, accelerometers, data acquisition hardware and software, and wires, for measuring the COF. [71] made a slider where frictional forces were registered as a function of time, which was used to calculate COF.

Even though in-field experiments with technological development allow conducting tests in conditions close to the real ski situation, these tests are often expensive and require a lot of planning, equipment, and time to minimize errors. An easier way to test the glide performance is to measure friction of the ski base material through *laboratory experiments*.

Linear experimental devices consist of movement of a slider on an ice surface guided by a control mechanism. Accordingly, ice properties, load, and velocity can all be well-controlled. [72] measured the COF of different steel skis on a snow track in which a guided beam moved the skis utilizing an electromotor (Figure 21). In this study, the horizontal and vertical forces were measured with force transducers. COF was calculated by the relation $\mu = F_r/F_n$ when the ski had reached a constant velocity.

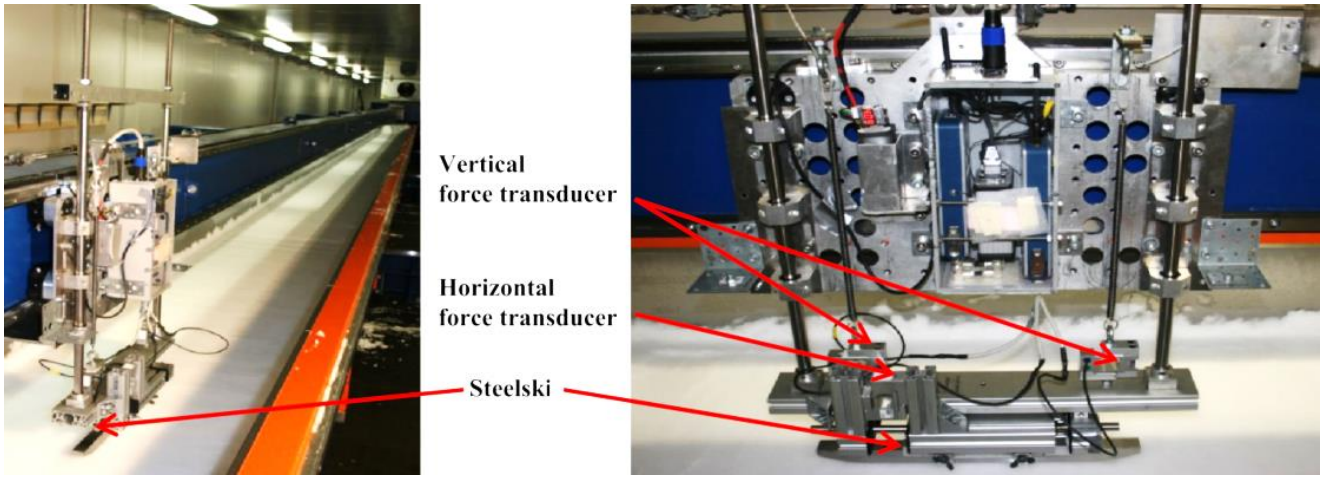

Figure 21: *Example of linear laboratory experiment: setup where [72] measured COF on steel skis*

Similarly, *rotational experimental devices* hold the ability to easily control load and velocity. Many of these experiments are making use of an ice ring or disk, which is rotating against a stationary sample to be tested. Different setups for rotational experimental devices have been reported for the cause of testing ski base materials with varying snow conditions. For example, [73] used a large-scale, pin-on-disc tribometer (Figure 22). IR sensors measured the temperature of the ice track in front of and behind the slider to be tested. Additionally, thermocouples were integrated into the slider to measure temperature close to the ice interface. The COF was found as a function of temperature, velocity, load and apparent contact area.

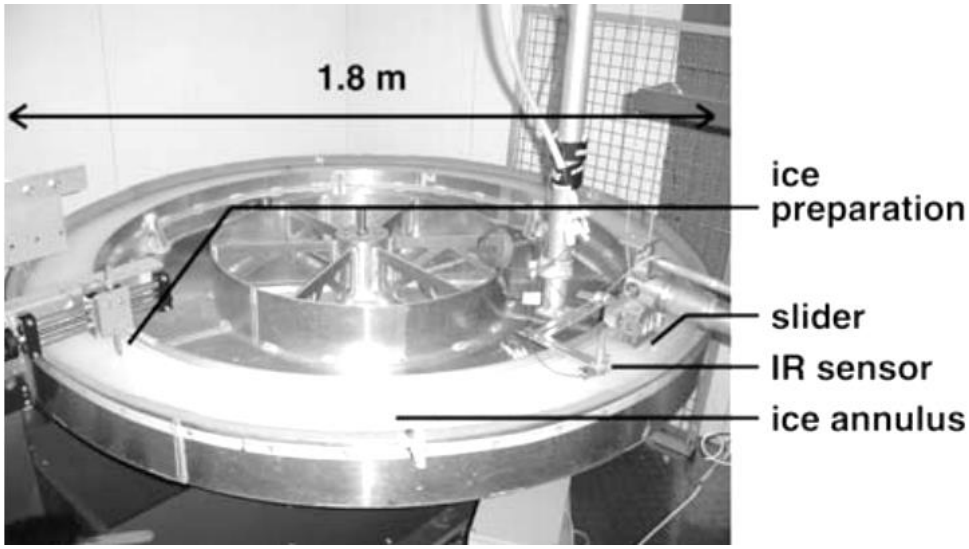

Figure 22: *Example of rotational laboratory experiment: pin-on-disc tribometer for measuring sliding friction of polyethylene on ice [73]*

Another advantage of the laboratory experiment is their small size, enabling the implementation of cold chambers to attain an ice surface. Despite the low cost, high control, and little space needed, there are also disadvantages to the use of laboratory devices in ski testing. Firstly, this type of testing only allows a small area of the testing track, which limits the ability of extensive individual tests. Secondly, the ice surface is recycled within each test set; when the sample is running over the same surface multiple time in a short time period this will affect the snow conditions throughout the test.

2.6 Fabrication of nanostructured surfaces

Nanotechnology focuses on structures and processes on length scales below 100 nm and is driven by the fact that materials often achieve unique properties when structured at this scale [74]. According to [75], fabrication processes to structure surfaces can be classified depending on the way the matter is manipulated to attain the surface in the following way:

I) *Adding material technologies*: structure is obtained utilizing chemical or physical deposition processes
II) *Removing material technologies*: holes are created by removing substrate material
III) *Material displacement technologies:* substrate material is plastically deformed and redistributed from one locating to another

IV) *Self-forming methods*: structure results from several processes. Wear-resistant regions are first formed, which are later not affected while the surrounding material is worn out, creating a pattern

In the following sub-sections, a brief review of some of the sub-groups within these techniques will be given, selected based on methods already used for the application of ski friction minimization or which are viewed as interesting for this application. Additionally, a more thorough sub-section will emphasize on anodizing of aluminum, as this is the main structuring method used in this work. This will include both theory and its application as a nanostructuring technique.

2.6.1 Lithography

Patterning is in the field of nanofabrication most commonly referred to as lithography. Lithography techniques consist of numerous subgroups, but they all have the following elements; (1) a designed set of patterns, either in the form of a mask or a master surface, and (2) utilities to perform a transfer or replication of the patterns [76].

Two of the main groups of lithography methods are projection lithography and nanoimprint [76]. The most conventional projection lithography method is *photolithography* (PL), in which the pattern is transferred from a mask to a photoresist which is coated on a wafer. A photoresist is a photosensitive substance that either cross-link upon exposure of UV light (negative photoresist) or become solvable upon exposure (positive photoresist). In this way, the choice of photoresist and a mask can enable the selection of patterns to stay on the wafer [77], and can hence be classified within II). However, designing the features of the mask in a PL process is difficult, time-consuming and expensive. Maskless optical lithography offers a path around these disadvantages [78]. For example, a relatively new Maskless Aligner (MLA) from Heidelberg [79] offers a simple process; creation of the pattern design with CAD (computer-aided design) software which is exposed directly on the wafer with photoresist, without the challenging process of mask fabrication.

Nanoimprint lithography (NIL) is an advanced patterning method for nanofabrication which has been explored the last 20 years. The general idea of NIL is to transfer a pattern by pressing a designed master mold onto a second material surface, creating an inverse shape of the master. Hence, NIL can be classified within III). While PL prevents physical contact between the mask and resist, NIL is carried out by close contact between the two. One of the first demonstrations of NIL was through *hot embossing*. This is a process where a rigid stamp is pressed into a polymer heated above glass temperature, letting the polymer material flow

around the patterns and adopt the inverse shape of the stamp. The stamp and substrate are further cooled, and after release, the polymer will hold the new structure (Figure 23) [74].

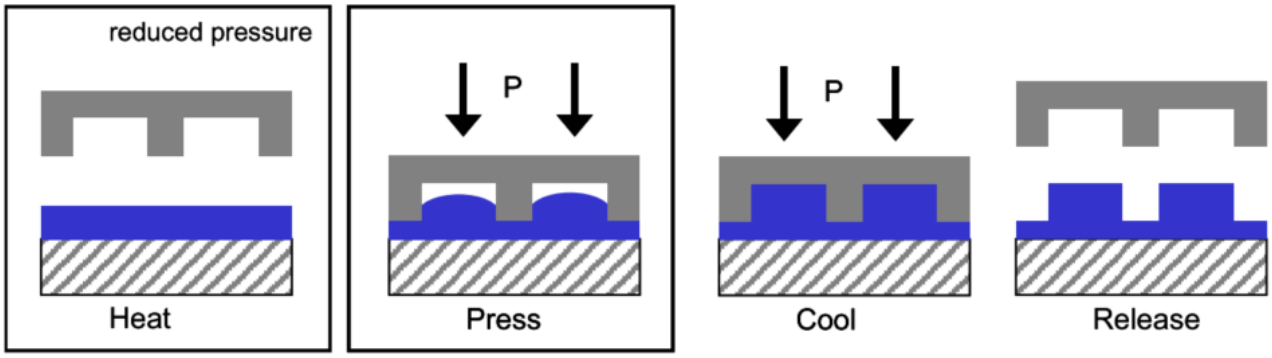

Figure 23: *Hot embossing of polymer utilizing a rigid stamp [74]*

[46] used embossing with different normal loads, without applying heat to the system, to transfer a linear pattern onto ski sliders which were further tested in a linear tribometer at different temperatures and loads. [45] performed hot embossing with stainless steel meshes of different grid size at the micro-scale as stamps to pattern a UHMWPE ski base material. The process was carried out by letting a 300 N block heated to 150 ℃ rest on the mesh placed on the UHMWPE for different periods of time. The CA was used as a measure of embossing efficiency. The steel mesh was inspired by natural leaves with superhydrophobic properties. In applications where hydrophobicity is required, scientists often investigate how nature has solved the challenge. For example, the rice leaf (Figure 24) is well-known to hold extremely water repellant properties, and hence an example of a bio-inspired product.

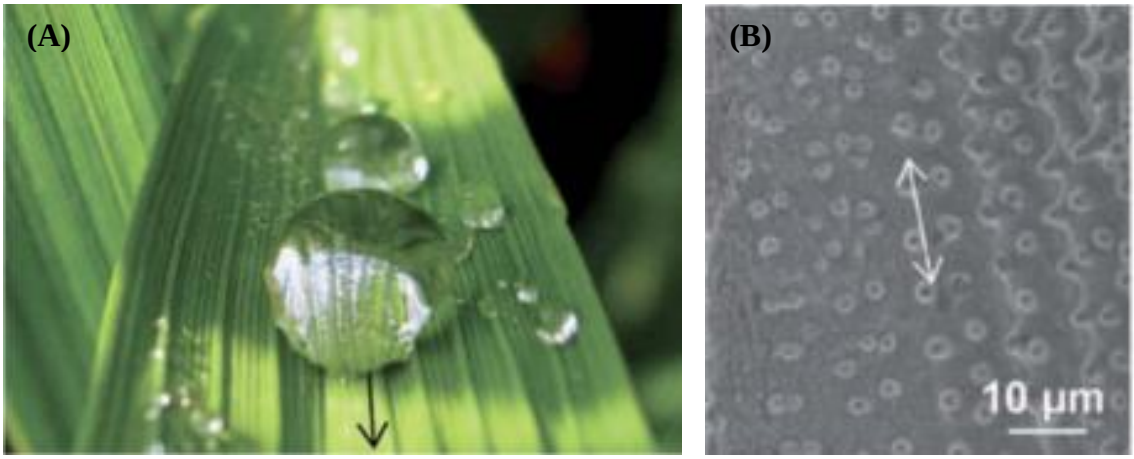

Figure 24: *Rice leaf is an inspiration for scientists in applications where superhydrophobic properties are desired. (A) Illustration of high CA and low TA on a rice leaf. (B) SEM image of rice leaf [80]*

However, there are several issues that can occur during a hot embossing process, especially for intricate features. For example, only partial contact between stamp and wafer due to misalignment or contaminating particles, incomplete filling of features, or damage of features during release. Consequently, a new type of NIL, called substrate conformal imprint lithography (SCIL) has newly been developed to solve these issues. In SCIL, the master is pressing into the material to be replicated by applying different amounts of pressure sequentially along the surface. This enables the replication of sub-10 nm resolution features [74], and solves some of the mentioned problems that are evident for the conventional hot embossing procedures.

2.6.2 Femtosecond laser irradiation

[16] studied the correlation between surface structure, hydrophobicity and ice friction. Their samples were fabricated by femtosecond laser irradiation, a method where ultrashort laser pulses are generated and amplified to ablate the sample surface (Figure 25), which classifies it within II). This study is another example in which the structure is made to mimic nature; the nano-scale structure was fabricated on steel sliders to resemble the lotus leaf. The sliders were later tested by mounting them on a disc rotating on an ice surface to analyze friction characteristics.

Even though femtosecond laser irradiation was not even considered to be used in this work, this study is included as a sub-section within nanostructuring as it is viewed as very important in advance of this work. Published in 2009, the authors claim to be the first to publish a study in which the influence of roughness at the nanoscale across all friction regimes is investigated. In the literature search conducted in the work, no publications were found investigating this exact correlation, which also is the essence of this work, after this paper.

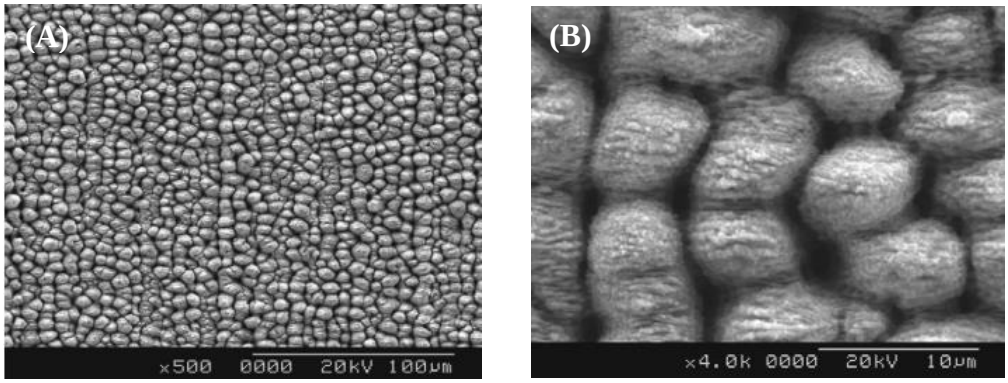

Figure 25: *SEM images of a hydrophobic surface structure created by femtosecond laser irradiation on steel sliders. (A) x500 magnification. (B) x4000 magnification [16]*

2.6.3 Anodic aluminum oxide (AAO)

This section will contain a more in-depth description of a nano-structuring method - fabrication of a porous aluminum oxide - which can be classified somewhere between I) and II). As this is the main nano-structuring technique used in this work, an entire section is dedicated to the subject.

The growth of porous oxide on aluminum, anodic aluminum oxide (AAO), under anodic bias has been studied in a variety of electrolytes for more than 40 years. The process has shown to enable a relatively ordered surface structure of hexagonal pores, in which dimensions can be controlled by varying electrolyte content and concentration, current density, time, and temperature [4, 81]. This is a rather simple and low-cost process with a variety of applications and possibilities in the field of nanofabrication. As was discussed in section 2.4.2, surface roughness has shown to greatly impact the wettability of a surface, which makes the baseline for why AAO is of interest in the ski glide problem. In the following sections, the process of creating an AAO surface, anodizing parameters affecting the surface structure, and its application in this work, will be discussed.

2.6.3.1 Formation of AAO

Aluminum is a metal best known for its low weight, high strength and machinability, heat conductivity, and recyclability [82]. Despite it being a reactive material, aluminum develops an oxide film that protects it from corrosion in many environments. This oxide film can form naturally, but can also be artificially produced by passing an electric current through the material [83]. This process is called anodizing, and the oxide film produced is known as anodic aluminum oxide (AAO), or more generally called alumina, with chemical formula Al_2O_3. Alumina is a ceramic, and possesses relatively high strength and hardness, in addition to corrosion resistance. Hence, alumina functions as a protective layer on the bulk aluminum, increasing its durability and strength. For some applications, the process is also used to attain a more aesthetically pleasing surface finish; by anodizing certain aluminum alloys can obtain a specific surface color.

In the formation process of AAO, pores grow perpendicular by two simultaneous processes; i) oxide growth at the metal/oxide interface, and ii) oxide dissolution at the oxide/electrolyte interface [84]. As illustrated in Figure 26, i) is due to migration of oxygen-containing ions (O^{2-}/OH^{-}) from the electrolyte through the oxide layer at the pore bottom. ii) is due to the simultaneous drifting of Al^{3+} through the oxide layer, ejected into the solution at the oxide/electrolyte interface. The Al^{3+} ions reaching the oxide/electrolyte interface contribute

to oxide formation, while the Al^{3+} ions that are lost to the electrolyte makes the oxide porous in the absence of as many ions as in the bulk aluminum [85].

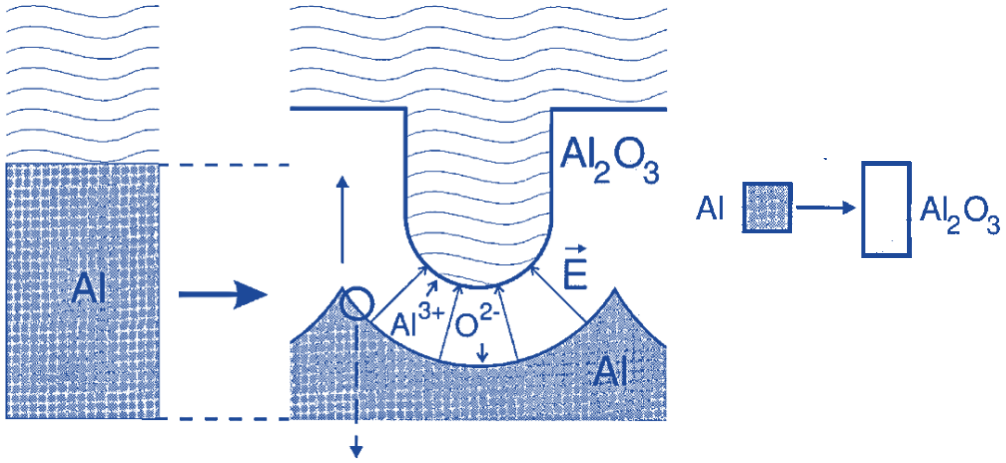

Figure 26: *Simultaneous growth and dissolution of aluminum oxide during aluminum anodization [81]*

2.6.3.2 Parameters affecting the AAO structure

As mentioned, AAO consists of regularly hexagonal pores, which is illustrated in Figure 27. The reason for this hexagonal formation is proposed by [81] to be due to repulsive forces between neighboring pores because of mechanical stress at the metal/oxide interface. A possible origin of this mechanical stress is reported to be associated with expansion during oxide formation. The material can only expand in the vertical direction, since the oxidation takes place at the entire pore bottom concurrently, pushing the existing pore walls upwards [81]. The regularity of cell arrangement is particularly high in association with naturally occurring ordered structures on the nanometer scale [86], and the honeycomb structure is the most stable structure in nature [87]. The dimensions of these hexagonal pores are modifiable. By varying anodizing parameters, such as *applied potential or current, anodizing time, concentration of electrolyte* and *temperature*, the dimensions shown in Figure 27 can all be controlled [4]. These parameters will briefly be discussed in the following.

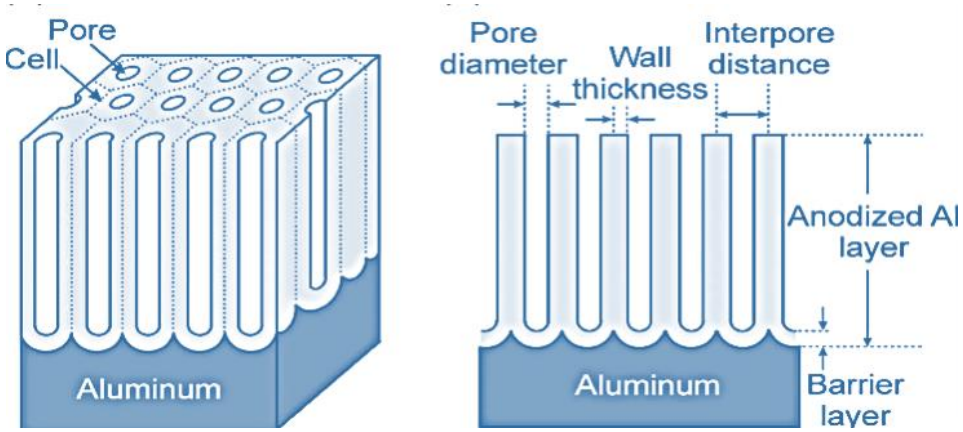

***Figure 27**: Illustration of dimension definitions of hexagonal pores of AAO [88]*

The anodization process can either be *voltage controlled* or *current controlled*, with either constant or varying values. As Al_2O_3 is dielectric, resistance will increase with the duration of exposure as the film grows. This means that if anodization is, for example, conducted with a constant current level, the voltage will vary correspondingly with the increased resistance. This relation has shown to be non-linear initially but will stabilize at a constant value when equilibrium between AAO formation and dissolution is reached [89]. The rate of oxide growth increases with higher values of applied voltage or current [4, 89].

Electrolyte mixture and concentration is also affecting the rate and dimensions of oxide formation. Even though it is difficult to state a general correlation between electrolyte concentration and pore dimensions from the literature, some clear dependencies can be presented. Individual electrolyte components will contribute to the pore structure differently, and combinations of these can give even new possibilities. In general, if current is applied when an aluminum sample is immersed in relatively neutral solutions, a flat, nonporous barrier oxide films forms. However, if immersed in an electrolyte of strong acids or alkalis, pores will grow [90]. This makes the baseline for mixing ratios to achieve desired porosity and pore dimensions. Other properties of the electrolyte than pH has also shown relevant. For example, [91] found that increased viscosity of the electrolyte is directly correlated to a larger interpore distance and a lower oxide growth rate.

Electrolyte bath temperature has shown to affect the anodization rate, in which low temperatures result in corresponding long anodization times [89]. As the electrolyte temperature may vary because of the chemical processes during anodization, it is a critical parameter to the resulting surface. [89] controlled the electrolyte temperature during anodization by immersing a thermostat and a chiller into the bath. However, anodization can also be carried out without temperature control and, for example, be reported with room temperature conditions.

2.6.3.3 The application of AAO for hydrophobicity

Several different methods have been used for fabricating hydrophobic surfaces, and most of them are based on either creating a rough structure on a hydrophobic surface, or on modifying a rough surface with materials with low SFE, or both [92].

Because of its relatively controllable surface structure- and chemistry, anodizing of aluminum has in recent years shown to be a simple and low-cost fabrication method in which roughness-induced wettability has been evident on resulting surfaces. However, the natural wettability of alumina is hydrophilic, with a CA measured to be about 80° on a smooth surface [4]. Hence, an aluminum surface must first be processed, in which anodizing will be performed in this work, to obtain a rough surface promoting the desired hydrophobicity. Further, it can become even superhydrophobic by coating a thin layer of a hydrophobic substance on the rough structure [3]. Because of alumina's natural hydrophilicity, this has been obtained by coating with low SFE materials, in which especially polymeric coatings have been investigated [3, 4]. For comparison, the most common ski materials in use today, PTFE and UHMWPE, have very low SFE values, 18.5 mN/m and 36.8 mN/m respectively (section 2.5.2). On the other hand, the SFE of alumina can be up to 50.5 mN/m [93].

[3] created a superhydrophobic surface by aluminum anodization, achieving a CA of 162° upon coating the sample with polypropylene (PP), in which fabrication protocol will be used as a template for anodizing in this work. The paper did not include an SEM image of this specific best result, but instead images of similar trials, in which one of them is depicted in Figure 28A.

Pore dimensions are not given by the paper to be replicated, and it seems like the nanopores were not measured at all. An image of a higher magnification, yet of a sample fabricated by [4] with a different protocol, is shown in Figure 28B. Other researchers performing aluminum anodization for the application of hydrophobic surface reported their optimal pore dimensions. [4] attained hydrophobic surfaces from pore openings in the range 140-190 nm and with a constant interpore distance of about 405 nm. [94] found that the surface attaining highest CA had pore diameters of 232.76 ± 6.37nm and interpore distances of 260.47 ± 9.83 nm. [95] showed that nanoporous AAO films with pore diameters in the range of 10-80 nm could be transformed from superhydrophilic to superhydrophobic by a thin layer of a polymeric coating.

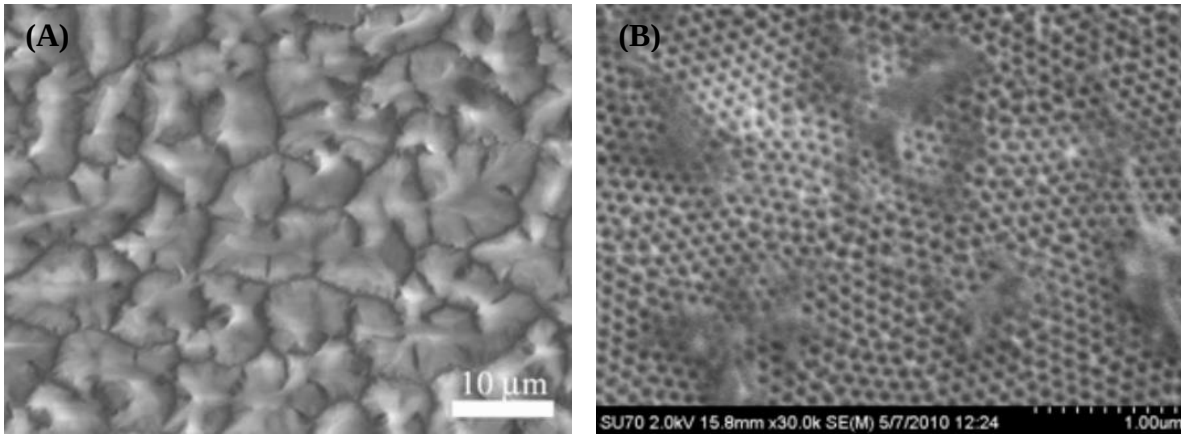

Figure 28: *(A) SEM image of AAO sample fabricated by [3], which protocol is replicated in this work. (B) SEM image of AAO sample with pore diameter 50 nm, fabricated by [95] with a different protocol. Included to illustrate the AAO surface at a higher magnification*

It is evident from the literature that anodizing of aluminum can result in surface structures at the nano-scale. This can further yield hydrophobic surfaces if covered by a layer, thin enough the replicated its surface structure, of a low SFE material. If it can also reduce ski friction is yet to be seen.

2.7 Characterization of nanostructured surfaces

This section contains a brief explanation of the basic working principles of the characterization instruments used in this work. This is given to know some of the limitations, advantages, and features of the instruments used when the results are later presented.

2.7.1 Optical profilometer (OP)

A profilometer is used to measure the surface profile of a sample to determine its height variations. There are two types of profilometers; stylus and optical. A stylus profilometer uses a probe to physically scan the sample by traversing the peaks and valleys of the surface with a small contacting force. As the optical profilometer (OP) available could give 3D images of surfaces, this type viewed as a better option in this work.

An OP uses light as a probe to scan the surface, which can be done in numerous ways. The key concept for them all is to utilize the wave properties of light, in order for the instrument to compare the optical path difference between the test surface and a reference surface [96].

A 3D OP from Bruker, model Contour GT-K, has been used in this work. This instrument has two measurement techniques available; Vertical Scanning Interferometry (VSI) and Phase Shifting Interferometry (PSI). Both VSI and PSI are based on interferometry - a family of techniques that utilize the division of a beam of light which is later recombined to determine the path difference the two beams traveled. Although VSI is less precise than PSI, it allows for measurements of rough surfaces with larger discontinuities [97]. Hence, VSI was chosen to use for the surfaces fabricated in this work. The basics behind the technique will be described in the following.

The VSI uses interferometric objectives consisting of an objective lens, a reference mirror and a beam-splitter (Figure 29). A beam of light from a light source is directed onto the sample surface through the interferometric objective, where the beam-splitter divides the light into two beams. One of the beams is reflected back by the reference mirror, while the other travels along the optical axis and interacts with the sample before it is reflected back.

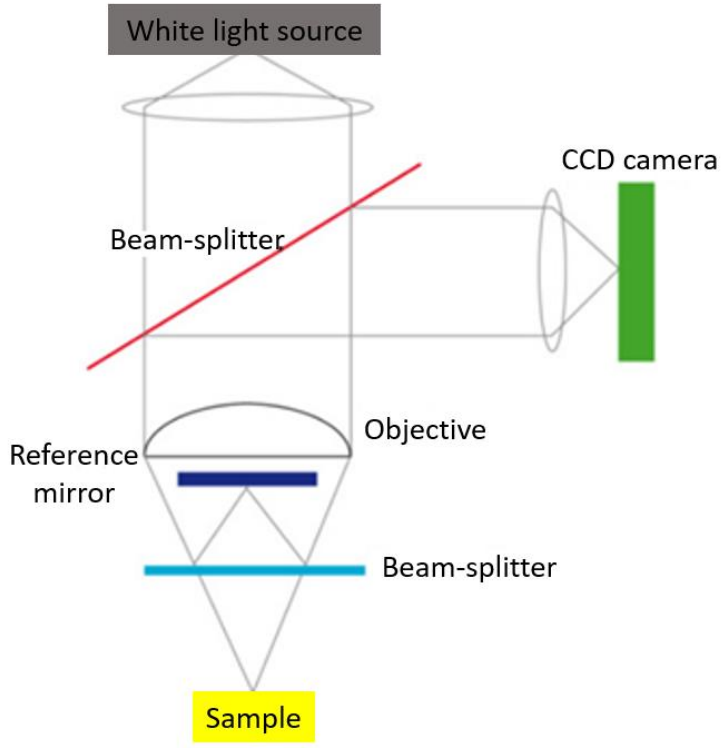

Figure 29: *Schematic illustration of VSI. Remade from [98]*

The two reflected light beams result in an optical path difference, which forms a pattern of interference fringes when the beams are recombined. A difference between the optical paths causes a difference in phase. The interference pattern is made up of light and dark bands. Light bands are formed when the two bands are in phase and their amplitudes are summed.

On the contrary, the dark bands are formed when the beams are out of phase and their amplitude is subtracted, giving a resulting zero amplitude. The interferometer will conduct a vertical scan of the surface by changing the distance to the sample (Figure 30). This is changing the focus position in a stepwise procedure, and the optical interference will occur at every point of the sample surface where the optical path length is the same for both light beams. A CCD (charge-coupled device) sensor records the interference fringes, and the signal is further digitized and processed to obtain a 3D topography map of the sample surface [98].

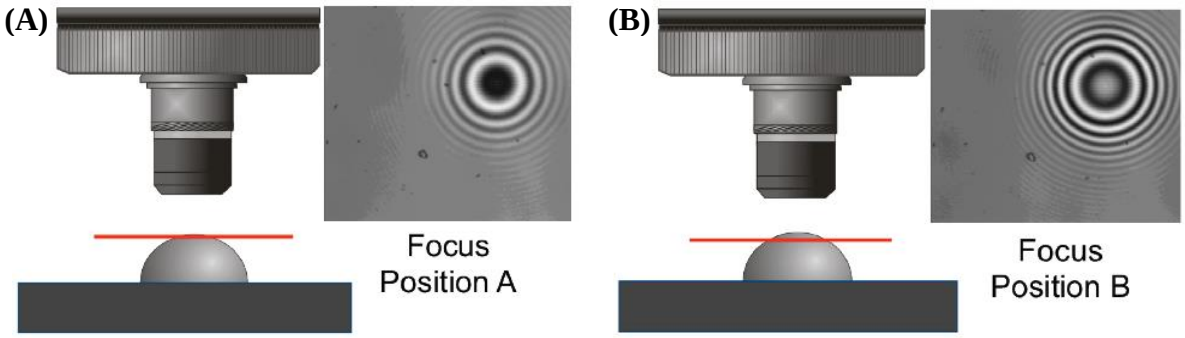

Figure 30: *Stepwise vertical scan of the sample changes the focus from position A in (A) to position B in (B) and hence the contrast of the fringes [99]*

The VSI technique offers several advantages over other techniques used for the same application. Firstly, it enables a non-destructive evaluation of a sample's surface, presented as a 3D map. Secondly, it has an extremely high resolution of approximately 1 Å in the vertical direction, in addition to the ability to scan a large area in short time [98]. However, as all other optical methods, the VSI is sensitive to numerous surface qualities besides the surface height. For example, these include optical constants and fine surface features causing diffraction, meaning bending of light around corners of an object [100].

The OP instrument from Bruker used in this work is equipped with 2.5x, 20x, and 50x objective lenses, and with 0.55x and 2x zoom lenses. The vertical resolution is sub-1 nm, while the lateral resolution depends on the objective used. The software Vision64 Map™ was used to analyze data from the profilometer after imaging.

2.7.2 Optical microscope (OM)

An optical microscope (OM) of the model Alicona Infinite Focus G4 was used to analyze a selection of the samples. Its 3D surface roughness measurement function was used to attain

2D and 3D images, as well as surface parameters of samples. The measurement principle of the Infinite Focus instrument is called Focus-Variation and is very similar to the principle of the OP (section 2.7.1). The optics is moved vertically to continuously capture data from the surface. This means that each region of the object is sequentially sharply focused [101].

This instrument had objectives with 5x, 10x, 20x 50x and 100x magnification. Higher magnification yields increased vertical resolution, but potentially also reduced image quality. The objective must be chosen in order to be able to analyze depth differences accurately enough, as the opposite can give an image that has completely incorrect measurements. In the images captured in this work, it was found that the x20 objective was the highest magnification that was possible to use for most samples before attaining poor image quality. This gives a vertical resolution of 100 nm, and the instrument can correctly measure surfaces with R_a below 0.5 µm.

2.7.3 Scanning electron microscope (SEM)

The limit of resolution can be defined as the minimum distance in which two structures can be differentiated and still appear as two separate objects. The scanning electron microscope (SEM) is an instrument used when the required resolution is beyond that of the OP and OM [102]. The OP and OM are limited by the wavelength of light. Therefore, the SEM was developed as electrons have much shorter wavelengths, enabling higher resolution. An SEM of model Quanta™ FEG 650 from FEI was used for analyzing the samples with an extremely high magnification. This instrument can achieve a xy resolution of 0.8-3 nm, depending on mode used [103].

An SEM utilizes electrons as a probe to scan a sample surface. The electrons interact with the surface, and different signals from the scan can be used to obtain information about the topography and composition. Electrons are directed, accelerated and focused into a beam pointing at a spot on the sample (Figure 31). The process is carried out in a vacuumed chamber, as otherwise the gas molecules in the air would scatter the electrons and decrease the resolution signal [22].

The instrument can create images from signals of both backscattered electrons (BSE) and secondary electrons (SE). The BSEs originate from the electron beam and interacts with the sample. The BSEs make up approx. 60-80% of the initial energy of the electrons sent from the beam. SE are electrons from the surface that has been emitted due to interaction with the electron beam. The signals from BSEs and SEs have different functions. The SEs can be used for investigating the topography of a surface. These electrons are loosely bound from the sample atoms after being emitted as a result of the electron beam’s ionization of the atoms.

The signals from these electrons will change depending on the topography of the sample. The signal is greater with feature-containing surfaces than flat ones. The BSEs can be used for investigating the composition of the surface. As the BSEs have interacted with the atoms of the sample, they will be affected by the atom numbers of the atoms on the sample surface. Heavier elements will scatter back more electrons than lighter ones, which will make them appear brighter in the resulting image [22]. As the SEM is used for surface topography determination in this work, the SEs will be utilized.

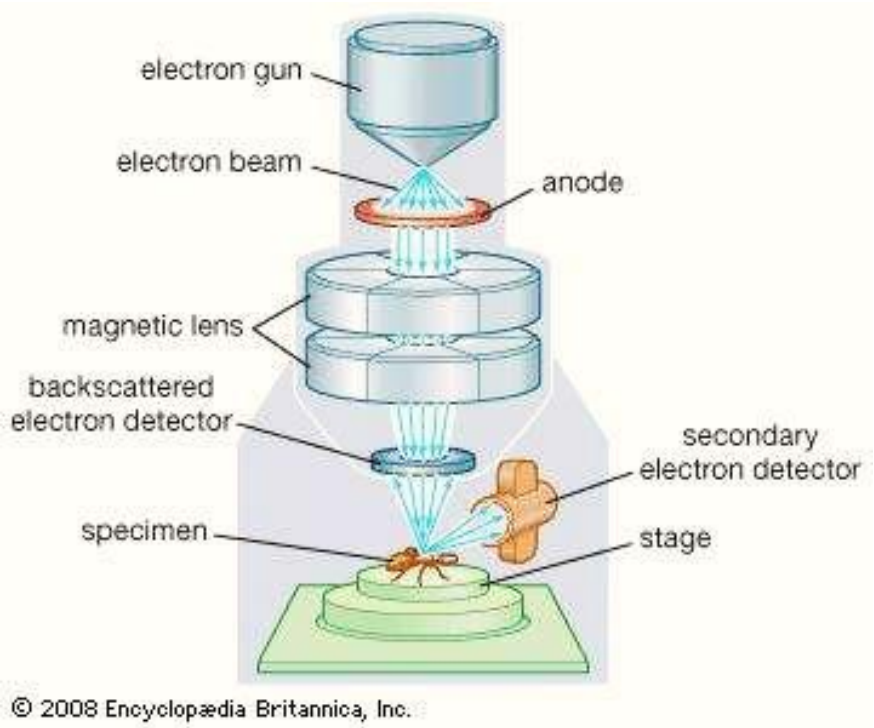

Figure 31: *Simplified illustration of components in SEM [104]*

Samples imaged with an SEM must be conductive to avoid electrons accumulating on the surface resulting in noise and potential damage of the sample. When handling non-conductive samples, an alternative is to image with the low-vacuum SEM function. Here the pressure is higher than for the traditional SEM. The electrons that would build upon the surface are instead transferred to positive ions generated from the electron beam interaction with gas molecules [22]. Both traditional and low-vacuum SEM will be utilized in this work.

3 Experimental methods

This section contains descriptions of the setups and procedures related to all experiments and tests conducted throughout this work. It starts with a section about a selection of methods within fabrication of nanostructured samples. Both the samples used for further testing and the ones discarded are presented. The most successful nanostructuring technique is applied to a sample which is designed as miniature ski prototypes. Next section is a presentation of a setup for CA measurement, developed during the specialization project. The last section concerns the development of a setup for friction tests, in which the miniature ski prototypes are tested. This section is further divided into three. The first sub-section focuses on the system for measuring COF in a snow lab, and the next describes the development of the associated snow track. The last sub-section concentrates on the load selection and subsequent pressure distribution of the miniature ski prototypes.

3.1 Nanostructured surfaces

Through previous sections, it has become clear that the wettability of a material greatly depends on its surface structure. The theory that a hydrophobic ski base surface might yield lower friction on a snow was also discussed. It was showed in section 2.6.3 that one can create a porous structure on aluminum through anodizing which will, with the right parameters, yield a hydrophobic surface. Additionally, section 2.6.1 was briefly presenting how methods such as maskless alignment, SCIL, and hot embossing can transfer a structure from one surface to another. On the other hand, it was also shown in section 2.3 how materials possessing low SFEs are naturally more hydrophobic. The overall idea in this work was to combine these properties into a final surface with even greater hydrophobic properties.

Initially, the plan was to fabricate a master template with the desired hydrophobic nanostructure through a method with easily controllable parameters (Step 1, Figure 32). The master template was meant to be used as a mold making a negative replica (Step 2), which would function as a transfer pattern (Step 3). The transfer pattern would further be molded (Step 4), making a positive replica of the master template, and becoming the resulting surface (Step 5). The resulting surface was imagined to be of a UHMWPE ski base material sample, while the master template was imagined to be of various types.

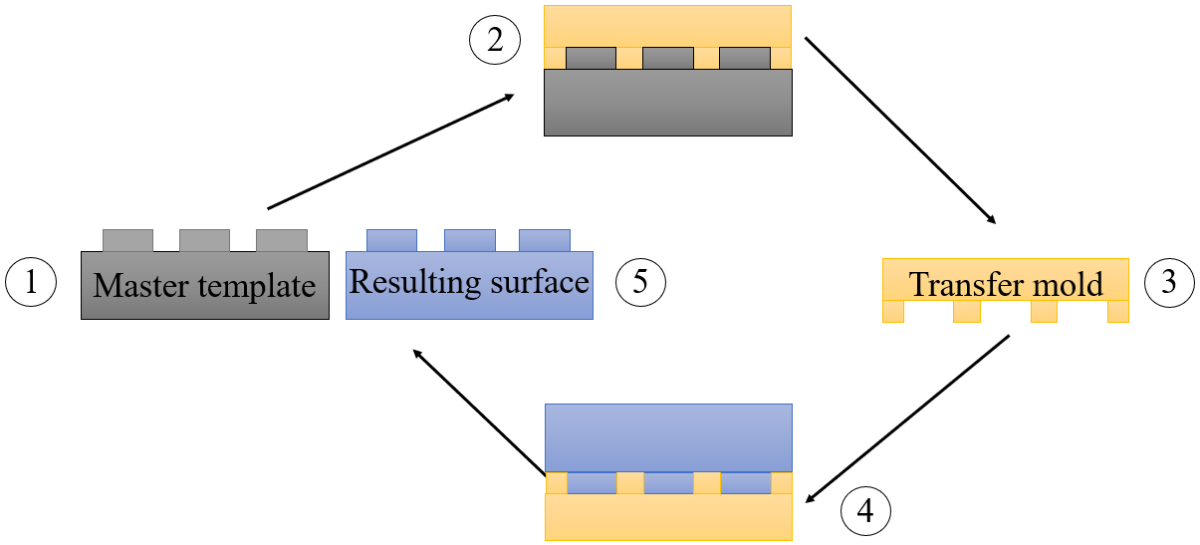

Figure 32: *The Initial idea of two-step molding process for transferring nanostructured surfaces*

Finding ways to perform the two-step transfer process in Figure 32 turned out to be more challenging than predicted. The main challenge was caused by the desire to structure UHMWPE, which is difficult to process as it decomposes before the melting point. However, the material does become softer at elevated temperatures [45]. Nevertheless, the real challenge was related to the fact that the features to transfer were at the nano-scale.

Despite thorough literature search, no previous studies were found on processes to transfer nanostructures from a master template to a UHMWPE surface with a direct contact technique. However, the final material did not necessarily have to be of UHMWPE. A possibility was to carry out the steps in Figure 32 by materials that would imitate the desired material; wear resistance and preferably a relatively low SFE.

Several studies have transferred nanostructures to other polymers than UHMWPE. [105] used AAO as a master template in two-step soft lithography process; an embossing process with an elastomeric stamp. In this study, a UV-curable polyurethane acrylate (PUA) mold was fabricated as a negative replica and further used to make a positive replica of a UV-curable resin. [106] did a hot embossing procedure to transfer the structure from an AAO template to a poly(methyl methacrylate) (PMMA) surface. Other techniques that were contemplated to use to structure the UHMWPE was the SCIL method, briefly described in section 2.6.1, which equipment was available at facilities at NTNU. However, it was advised to avoid this method as there was no personnel knowledgeable enough to offer training, and time was also insufficient. It was considered to use a maskless aligner, also briefly described in section 2.6.1, in which instrument also was available at NTNU. However, the features could not be smaller than 1 µm, which would steer the project away from the nano-scale structures.

Additionally, the MLA available is extremely expensive which would eliminate one of the initial ambitions of a cheap structuring method.

Even though hot embossing was attempted, which will be described in the next sub-section, these structures did not give sufficient results to continue testing with. Hence, the fabrication of AAO surfaces, as was already experimented with in the specialization project, was used as the main structuring method. The area of the samples was now, however, greatly increased from the previous fabrications, giving rise to a more challenging procedure in terms of equipment and level of hazard. The fabrication of the AAO samples will be described in the second sub-section.

3.1.1 Hot embossing

A total of 9 hot embossing experiments were conducted by varying pressure and temperature in a laboratory press. For all experiments, UHMWPE ski base was as the material to be patterned. The master was varied between an AAO surface from the specialization project and P1000 emery paper. The latter was used to make negative replicas of polydimethylsiloxane (PDMS) during the specialization project as it was found by [22] that this gave a highly hydrophobic structure. For both cases, the pair of surfaces were sandwiched between two aluminum plates for uniform heat and pressure application, and to avoid a collision of the adjacent plates in the pressing machine (Figure 33). A laboratory press by Fontijne Presses of model LPB 300 was used in the experiments. The temperature on the plates in the machine - either on one or both - as well as force and time, could all be selected. However, the force of the machine was limited to the range 60-400 kN.

Three published studies on hot embossing of UHMWPE, though neither with features at the nano-scale, were used as guides to decide for temperature and pressure. [107] performed the hot embossing with a pressure of 2.8 MPa and a hold temperature of 100 °C for 60 minutes. [108] did their process with 6 MPa for 10 minutes at 130 °C, while [45] applied 0.5 MPa for 15 minutes at 150 °C. As it was challenging to apply as low pressure as in these papers with the laboratory press available due to its minimum force specification and limited ski base material available, a higher pressure was exerted on the samples in this work. However, it was experimented with different temperatures, and with heating up both force plates or one only. Additionally, it was experimented with the process of pre-heating and cooling afterward.

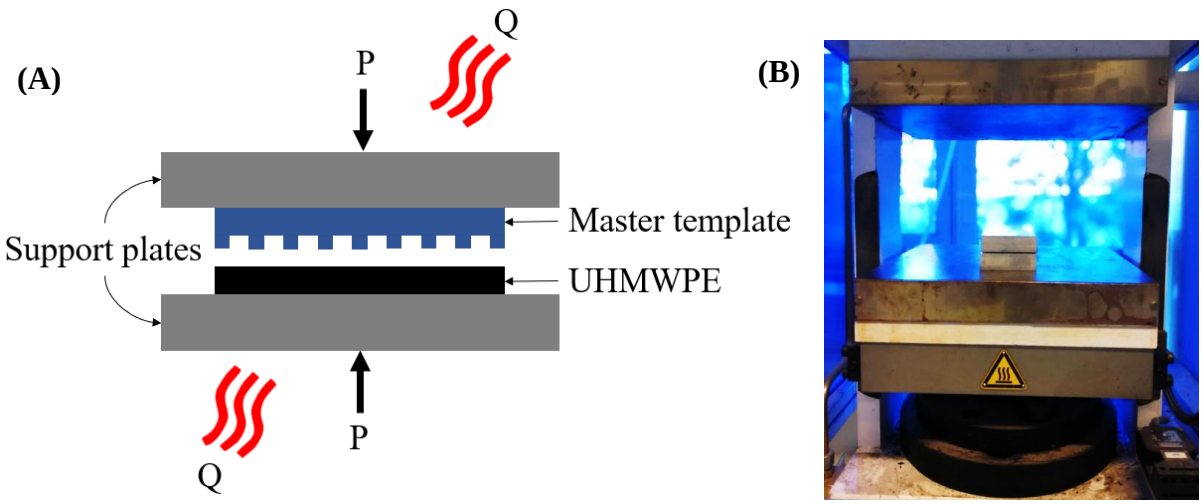

Figure 33: *(A) Schematic illustration of hot embossing of UHMWPE. (B) Hot embossing in a laboratory press*

3.1.2 Anodizing of aluminum

To attain a hydrophobic nanostructure through anodizing of aluminum, the parameters found optimal by [3] was replicated as best as possible with the equipment available. To perform the anodization, a computer-aided pulse plating instrument from AXA with an output current limit of $\pm$ 60 mV/100 A, was utilized in DC current control mode. The circuit consisted of a cathode of lead and the anode was the aluminum sample to be anodized. This is shown in Figure 34, where the cathode is the cylindrically shaped metal sheet partly immersed in the electrolyte and connected to the blue wire. The anode is the smaller piece, connected to a black rod, which in turn is connected to the red wire, in the middle of the beaker. The beaker with the electrolyte is placed in a water bath of 20º C.

Figure 34: *Setup for anodizing of aluminum*

The anodizing parameters are shown in Table 2. As neither pure sulfuric acid nor oxalic acid was available in the corrosion lab, actual amounts had to be calculated based on the concentration of the bottles available. These calculations are enclosed in Appendix E. An electrolyte of 1.3 L was made for the experiment. As it was desirable to make the exact amount of electrolyte necessary to minimize resources and time, required volume was calculated in advance for a 2 L beaker. These calculations can be found in Appendix F.

Table 2: *Anodization parameters, as replicated from the best result of [3]*

Anodization parameters	Current density, $\bar{I}$	0.0339 A/mm^2
	Anodization time	40 min
Electrolyte concentrations	Sulfuric acid (H_2SO_4)	170 g/L
	Oxalic acid ($C_2H_2O_4$)	10 g/L
	Sodium chloride (NaCl)	1.25 g/L

The aluminum alloy EN AW 5754, purchased from E.A. Smith Stål, was used, in which datasheet is enclosed in Appendix C. The dimensions of the sample to be anodized was constrained by the chamber limits in the SEM. As the sample was to be used as a ski prototype in the snow lab, it was designed to mimic a real ski as much as possible with the given restrictions. A XC classical race ski is typically 50 mm wide, and hence this width was chosen for the sample as well. The length was chosen to be 110 mm on the upper surface.

With a radius of 10 mm on both front- and rear edge, the lower surface was 90 mm. The latter is the surface in contact with the snow base. As the sample was in total 15 mm thick, 5 mm of the upper short edges were flat, in which function will be described shortly. The sample is depicted before anodizing in Figure 35A, with corresponding machine drawing in Appendix D. [46] made similar slider models, in which a radius of 22.5 mm was used. The radius used in this work could not replicate the mentioned study as the aluminum plate in which the sample was machined from was 20 mm thick. However, a radius of 10 mm is assumed to be sufficient to avoid considerable edge effects. The sample was milled longitudinally in the direction of sliding motion later on in the snow lab. This was inspired by [46] as they report that a linear structure will exclude effects from shear forces produced by skewness of the slider structure.

In anodization experiments conducted during the specialization project, it was found that the connection of the anode was critical to attaining a uniform anodizing process. Utilizing a threaded rod of stainless steel, isolated with a heat shrink tube to prevent it from affecting the process, was found to be successful. Hence, the same connection was used for the larger sample in this work. An M3 threaded hole was centered at the upper flat 5 mm of the short edge of the sample (Figure 35B). In this way, the anode contact did not depend on the growing oxide layer on the sample surface, but rather the bulk material. The connection rod was approximately 130 mm. The cathode is advised to be at least 3 times larger than the anode in anodization experiments. In this experiment a lead sheet with dimensions 1×210×250 mm was used, in which the upper 60 mm was not immersed in the electrolyte. Hence, the cathode area was almost five times larger than the anode area, which was more than sufficient. The cathode was placed at the beaker bottom and extended above the electrolyte surface to prevent the need to dip the connection cables into the electrolyte. The lead sheet was formed cylindrically around the anode to enable uniform anodization (Figure 35C).

Two identical samples were machined with the dimensions of the anode given above; one for anodizing and to function as a reference sample. Both will further be referred to as miniature ski prototypes. General sample preparations were performed in the following steps for both samples:

I. Machine samples with dimensions discussed above shown in Appendix D. The surfaces were milled longitudinally with the sliding direction for the subsequent snow lab experiments
II. Ultrasonically clean samples in acetone for 5 minutes to remove grease and other contamination
III. Rinse with distilled water
IV. Dry by ethanol spray

Further steps do only involve the sample to be anodized. The area of the sample exposed to the electrolyte when subtracting the hole for connection, in addition to the current density from Table 2, was used to find the constant current to apply (Equation 15). As the instrument only had a one decimal accuracy, a constant current of 5.2 A was applied for 40 minutes.

$$I = \bar{I} \cdot A_{sample} = 0.000339 \frac{A}{mm^2} \cdot 15277.887\ mm^2 = \mathbf{5.18\ A} \qquad (15)$$

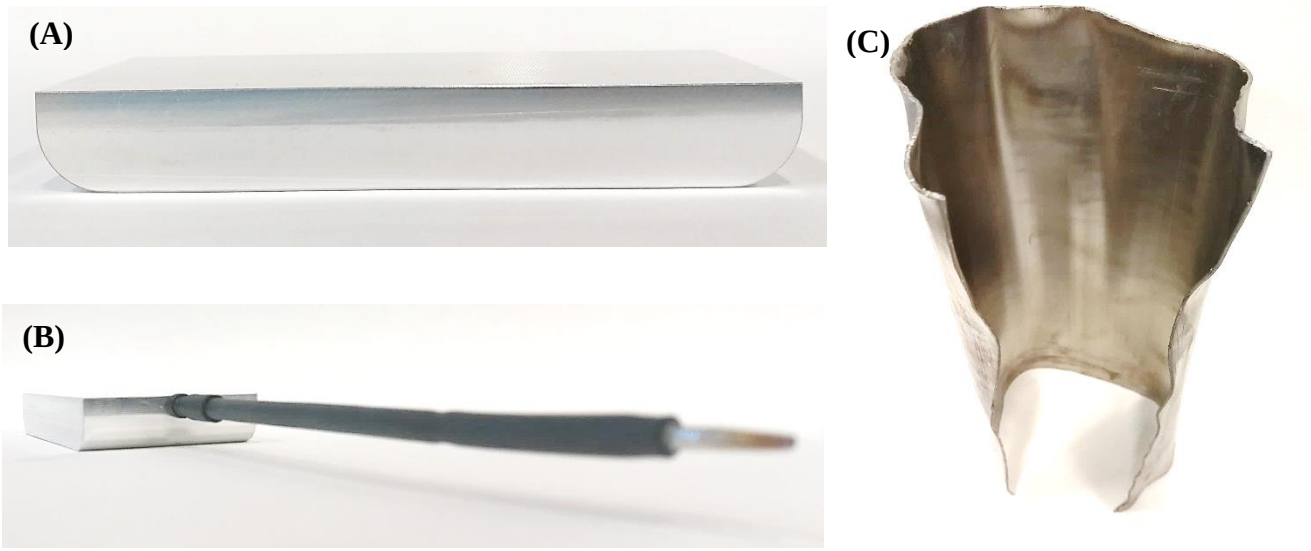

Figure 35: *Components before anodizing: (A) aluminum anode, (B) anode with a rod for connection, and (C) lead cathode*

[3] added oxalic acid in their experiment as this allowed the anodizing at higher temperatures. As it was not specified in this study whether the temperature was controlled at all after the addition of oxalic acid, it is believed that the process was carried out in room temperature conditions. Hence, the same was done in this work; the temperature of the electrolyte was not controlled during the anodizing process, but the beaker was placed in a water bath that was initially at 20º C.

3.1.3 PTFE coating

PTFE is one of the polymers with lowest SFE, making it optimal in applications for friction reduction, such as skiing [37]. MOTIP ® PTFE DRY was purchased from BEMA; a spray that dries immediately and does not leave the coated surface sticky. A thin layer of the product was carefully sprayed over the ski prototypes. It was initially preferred to spray the

PTFE in the air and let the mist fall on the sample surfaces. However, this turned out rather unsuccessfully as the mist would not cover the surfaces completely. Hence, the coating was sprayed with an angle to, and not directly on, the samples. The ray of PTFE was moved at a constant pace to cover the entire surfaces to be in contact with the snow base as uniformly as possible.

All samples were stored in marked, clean plastic bags, and handled with gloves to prevent contamination.

3.2 Characterization

As the OM, OP, and SEM are well-established characterization tools, their working principles associated with the specific model used in this work were described in section 2.7. Hence, only the characterization methods that were developed in this work will be described in this section.

3.2.1 Aspect ratio estimation

Pore diameter and interpore distance, as defined in Figure 27, can be found by analyzing the SEM images of the nanopores from the anodizing process in ImageJ. Figure 36 illustrates the measurement of a pore diameter in ImageJ from a fragment of an SEM image of an AAO surface. Information about the height profile of the surface can be found from the OP. As defined in section 2.4.1, *Sa* is the vertical deviation from a mean line. By utilizing these two parameters, the aspect ratio of the pores on the anodized surfaces can be estimated.

Aspect ratio can be found by the ratio between pore depth, H_{depth}, and pore diameter, D_{pore} (Equation 16a). *Sa* multiplied by 2 is viewed as the parameter to best resemble H_{depth} (Equation 16b); this would correspond to the average distance between peaks and valleys.

$$AR = H_{depth} : D_{pore} \qquad (16a)$$

$$AR = (2 \cdot Sa) : D_{pore} \qquad (16b)$$

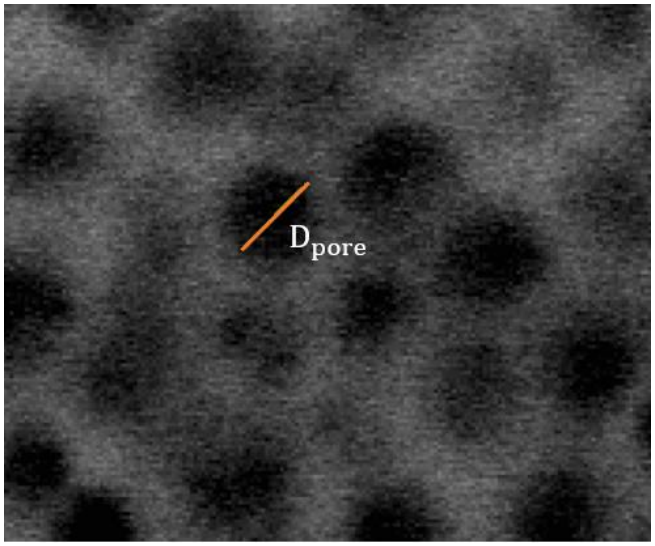

Figure 36: *Illustration of pore diameter determination from a fragment of SEM image*

3.2.2 Contact angle measurement

To quantify whether the samples had attained the desired hydrophobic surface, a simple contact angle measurement setup was designed to analyze a static droplet on a horizontal surface. The setup was developed during the specialization project but was also used here, in which a briefer presentation will be given. The complexity of a CA analysis can range from simple visual estimations to comprehensive mathematical techniques and equipment. In this work, droplet images captured under controlled conditions were analyzed utilizing ImageJ.

A schematic view of the final setup is shown in Figure 37, followed by an image of the actual setup in Figure 38. A single-lens reflex camera of model Nikon D5300 mounted with a Sigma macro lens with 105 mm focal length was used for image capturing. A Hensel diffuser with a flash was placed adjacent to the camera to make the droplet appear dark with a homogeneous background. This was necessary for measurement precision and image processing. According to [109], it was of importance to use a flash with stronger light intensity than the surrounding light in the room. A microscope table was mounted to a bench with a Stanley vise and a camera bracket, in which the latter was fabricated to position the camera statically relative to the droplet on the sample. All components were leveled to keep sample and camera as horizontal as possible.

A droplet on a sample was placed approximately 145 mm in front of the camera lens, which was found to be a good choice in terms of object size and focus. Minor manual focusing adjustments were done to each individual droplet image. The position of the camera was fixed in the horizontal plane but could move in the vertical plane with a threaded rod, depending on the thickness of each sample.

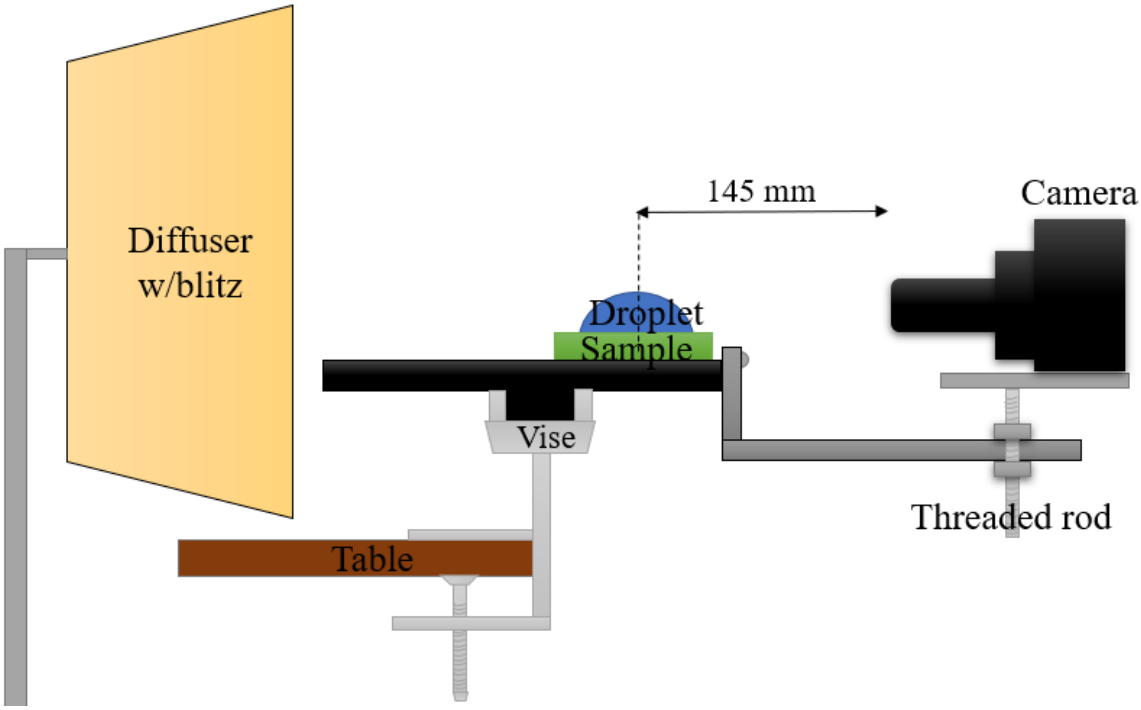

Figure 37: *Schematic illustration of static contact angle measurement setup*

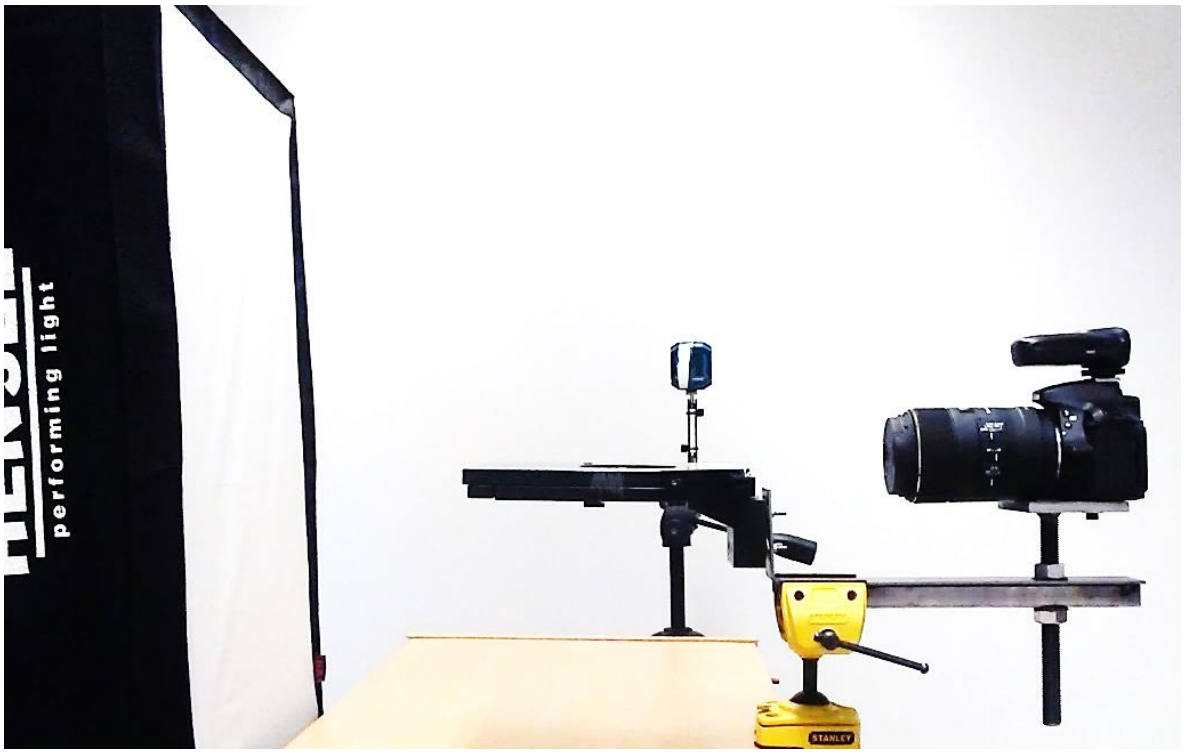

Figure 38: *Static contact angle measurement setup*

To attain the CA of a sample surface, a sessile droplet was used; the standard arrangement for optical contact angle measurement using drop shape analysis [110]. For the analysis, the public domain Java image processing and analysis program ImageJ, version 1.45, was used with a plugin specifically made for the application of sessile droplets [111]. The plugin used, DropSnake, is a method to determine the droplet shape with a piecewise polynomial fit [112].

According to [112], the visibility of both the actual droplet and its reflection on the substrate were recommended in order to easily define the three-phase line, which would help obtain accurate CA values and to detect potential tilt in the image.

The steps for defining the drop shape with DropSnake starts with a shape initialization by the user (blue knots in Figure 39), in which the software is optimizing by a polynomial fit (red knots in Figure 39). When no reflection is visual, the software will have more difficulty in optimizing the user-defined shape. However, from the images in [113], it is evident the CA measurements of samples were only based on the user-defined shape, i.e. the blue knots. Hence, it was evaluated that this would also be sufficient in this work as well for the rough samples where the reflection was not as visible.

A requirement for the DropSnake analysis is for the images to be in greyscale, which was performed with the software GNU Image Manipulation Program (GIMP), version 2.8.22 [114]. Additionally, the camera was set with a slow shutter speed of 2.5 s and a small aperture of f/16.

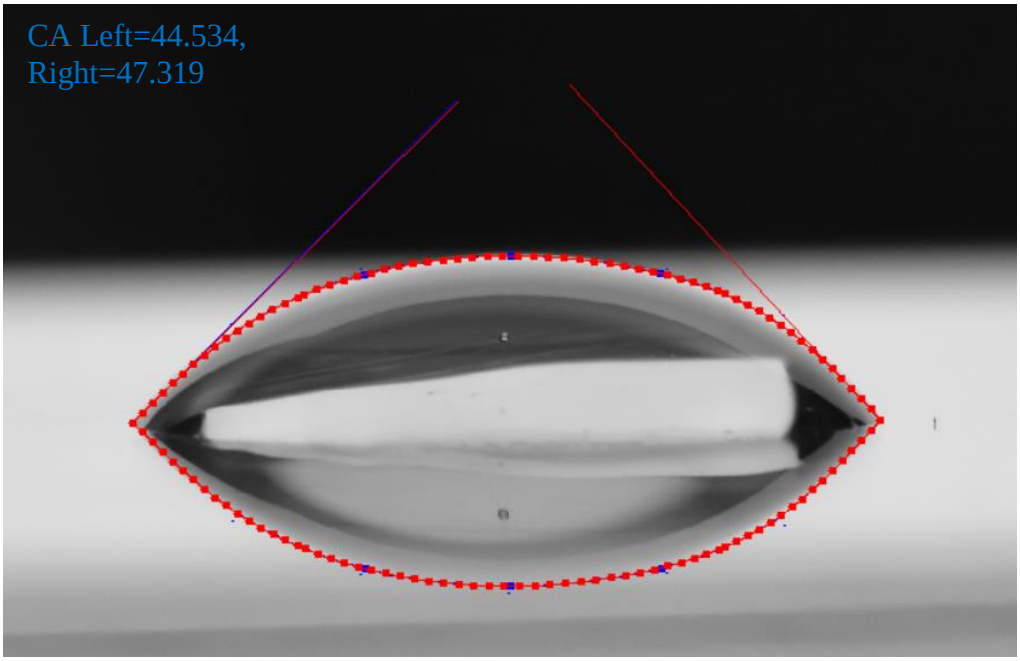

Figure 39: *Droplet shape analyzed in ImageJ. Droplet reflection is visible on the substrate*

The DropSnake method is ideal for the physical setup constructed as it allows droplets to be deposited on slightly tilted surfaces [112], which was difficult to avoid in such a simplified setup. A pencil tip was placed next to the middle of the droplet. This was done to establish a focus plane as the pencil tip was used as the reference when manually focusing. This was considered of importance when later comparing CAs from different samples.

Each droplet was deposited on the surface to be tested with an adjustable pipette from ACTGene with a droplet volume of 10 µL of distilled water. The reason for using a set droplet volume was to minimize errors, as it has shown that surface heterogeneity, roughness, and stability all are major factors potentially affecting a variation of CA with drop size [115]. This study states that on a smooth and homogeneous solid surface, the effect of drop size on contact angle was not observed for either ACA nor RCA. On the contrary, and most important for this work, the study reports observed variations in CA with drop size on samples with rough characteristics. On the other hand, [35], states that the rough surface should not impact the CA measurement with varying droplet volume, as the surface structure is of much smaller scale than the droplet. As the impact of droplet volume seems to be disputed, it was kept constant for all samples.

Drop deposition has found to be a critical step in previous work, and hence the droplets were dispersed gently with the pipette perpendicular to the sample [116]. To avoid changes in the shape of the droplets due to gravitational force, the time between droplet deposition and image capture was never exceeding 7 seconds [113].

For each sample, droplets were deposited on a few different spots with successive individual analysis. The average of left and right CA was found from each of the measurements and further, the mean and standard deviation was found for each set.

During the specialization project, the CA and SFE were analyzed with Olympiatoppen's Mobile Surface Analyzer (MSA) on one occasion. The MSA is based on the OWRK method described in section 2.3.1. It was then discovered that the samples analyzed with the designed setup seemed to consistently measure lower CAs than the MSA. It was therefore desired to compare a larger set of CAs measured by the two instruments to calibrate the designed setup in accordance with the MSA, which is seen as more reliable. However, the MSA was out of order throughout the semester and the calibration could not be carried out. Nevertheless, there is reason to believe that the designed setup is slightly underestimating the measured CAs.

3.4 Friction tests

To measure the COF of the ski prototypes on snow, a newly developed snow lab at the Department of Civil and Environmental Engineering at NTNU was utilized. This facility has so far only been used for testing a tire moving linearly at high speed on an underlying pavement surface partly covered by snow and salted snow. The lab consists of two unique apparatus; a Linear Analyzer of Road Surface (LARS) and a snow-producing machine called Lumi. A thorough technical description is given of both in [117], but a summary of the key characteristics relevant to this work will be described in the following.

LARS is an 8.8 m long test track allowing linear movement with a maximum speed of 10 m/s, which can be reached in two meters starting from zero. The ramp-up and desired velocity along the track can be programmed extremely accurate. Test temperatures can be controlled between -25 ºC to +25 ºC. The system consists of a beam along the entire track in which an electrical motor is mounted at one end. A sprocket wheel is installed at each end of the beam, which allows movement of a tensioned belt. Underneath the beam is a sled with an aluminum arm for attachment of a wheel resting on the track (Figure 40). The motor transfers energy to one of the sprocket wheels, inducing motion of the sled through the belt. A pressurized air bellow controls the applied normal force on the wheel. An encoder on the motor counts the revolutions of the sprocket wheel. The system can measure position and time, and braking torque when the brakes are activated. The system is able to accelerate up to 10 m/s the first 3 meters of the track, then roll at a constant speed for two meters, before it starts braking [117].

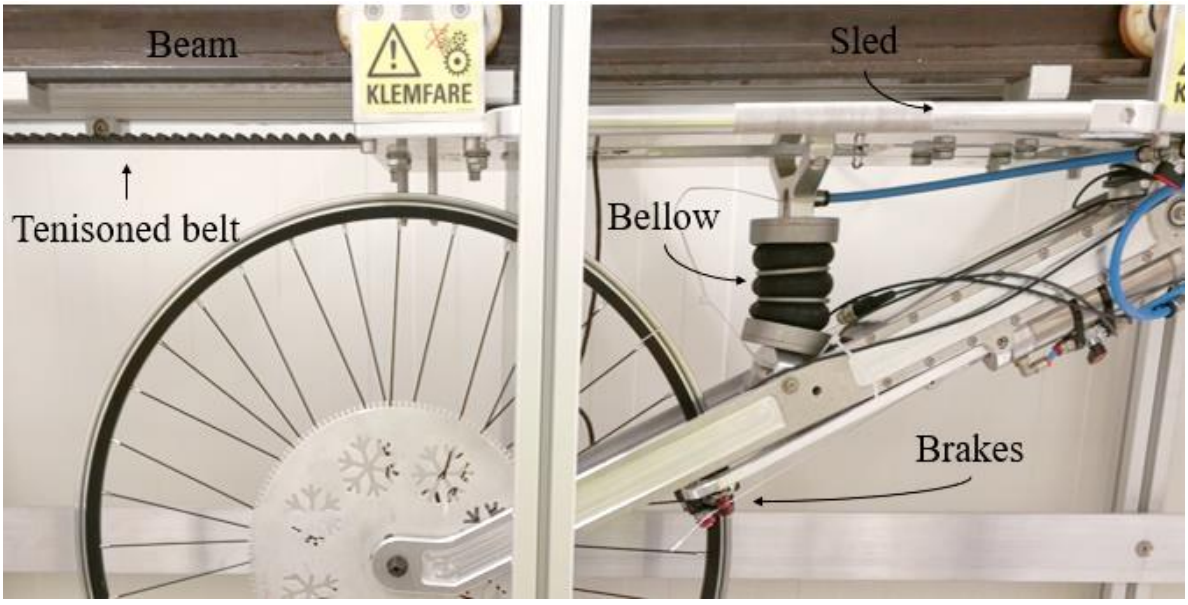

Figure 40: *Fixation of aluminum arm from beam to center of wheel with air bellow controlling the applied normal force*

The snow machine Lumi is made to enable snow production at known humidity and temperature resulting in a rather homogenous portion of snow. This artificial snow reduces the variety in snow characteristics such as shape, size, and density, which are significant factors when investigating friction on snow. The basic working principle of the machine is to blow air over moderately hot water baths. This transfers the cold and humid air into a chamber where snow crystals are growing on polymer coated steel grids. At a set interval, a motor induces vibration to the grids, allowing the snow to fall into a harvesting box. The machine produces dendritic snow [117].

As the facility was completed recently, the track has not yet been tested while completely covered with snow, making it a snow track. Because of this, the work of developing a procedure for COF measurements of skis with the LARS, and associated snow track preparation, can be viewed as a pilot project. The resulting setup was desired to be categorized as a linear experimental device within ski performance testing methods (section 2.5.4). The two next sections will cover how the LARS has been modified for the purpose of testing the miniature ski prototypes. The first sub-section will focus on the mechanical and electrical components that enable the measurements. Followingly, the second sub-section will discuss the snow track preparations. The last sub-section will focus on load selection and pressure distribution on the miniature ski prototypes on the snow track.

3.4.1 Measuring COF

Several ways to measure the COF in the snow lab were discussed early in the start of the project. For example, one idea for determining an indication of COF was to compare the time spent between the point in which the sample was accelerated, and a point in which a high-speed camera was installed, detecting when the sample entered its viewing window. However, this would raise a problem when the sample would have to slow down; as it had to run freely to not be constrained by the system between the two points of measurement, it would potentially have to be collected by something to stop it. This was viewed as a feasible, but probably not the easiest way to go. Also, it was not a direct measurement of COF. Another idea was to do a test similar to the parallel test (section 2.5.4). The sample could be given a push, attaining a known initial velocity. Then the COF could be calculated by energy conservation between this point and the point in which the sample came to a complete stop by measuring the travel length. However, this would only give an average COF and not a varying graph along the track.

It was finally decided to use a method giving actual force measurements from the system along the entire track. As the LARS is built for wheels, it was found that this could also apply

when testing small flat samples. If positioning the sample right under the wheel when the brakes were not activated, it was believed that the wheel would somewhat self-align at the center of the sample when activating the brakes and locking the wheel for spinning. A free-body diagram of the setup is illustrated in Figure 41.

The brakes are connected to a metal plate, which also the lower part of a load cell is mounted to (Figure 42A). Hence, when sliding with the brakes activated, the friction force between the sample- and snow base, F_F, would induce a downward movement of the brakes, and hence the metal plate. This would translate into a force in the load cell, F_L, which is logged throughout the track with a frequency of approximately 176 Hz.

The normal force, *N*, is determined with another load cell. The desired normal force, in which calculations will be given in section 3.4.3, was found by iteratively switching between letting the system rest on the sample and hanging slightly above the sample surface with a tension adjuster. Simultaneously, the output of the load cell was monitored to achieve the correct normal force (Figure 42B). Both load cells are of type U9C from HBM.

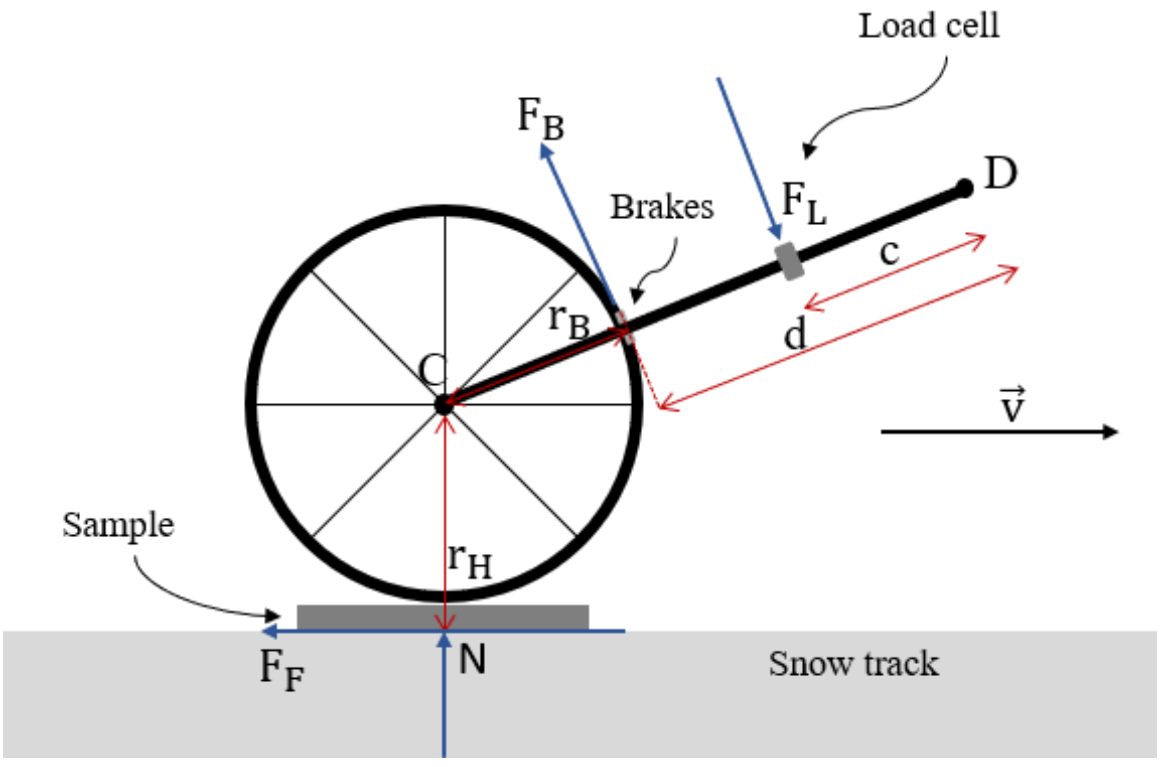

Figure 41: *Free body diagram of COF setup, including sample, wheel, brakes and load cell*

From the free-body diagram in Figure 41, and by utilizing the definition of COF (Equation 17) and moment equilibrium around point *C* and *D* (Equation 18-19), the final COF can be given as a function of the varying force from the load cell, F_L (Equation 20). The resulting

equation also contains the constant values from four different dimensions and the normal force. The constant dimensions were found to be: c=176 mm, d=260 mm, r_H=340 mm and r_B=313 mm. The constant value of the normal force will be presented in section 3.4.3. Air drag is assumed to be negligible.

$$\mu = \frac{F_F}{N} \qquad (17)$$

$$\sum M_C \rightarrow F_F \cdot r_H = F_B \cdot r_B \qquad (18)$$

$$\sum M_D \rightarrow F_B \cdot d = F_L \cdot c \qquad (19)$$

$$\mu = \frac{r_B \cdot c}{r_H \cdot d} \cdot \frac{F_L}{N} \qquad (20)$$

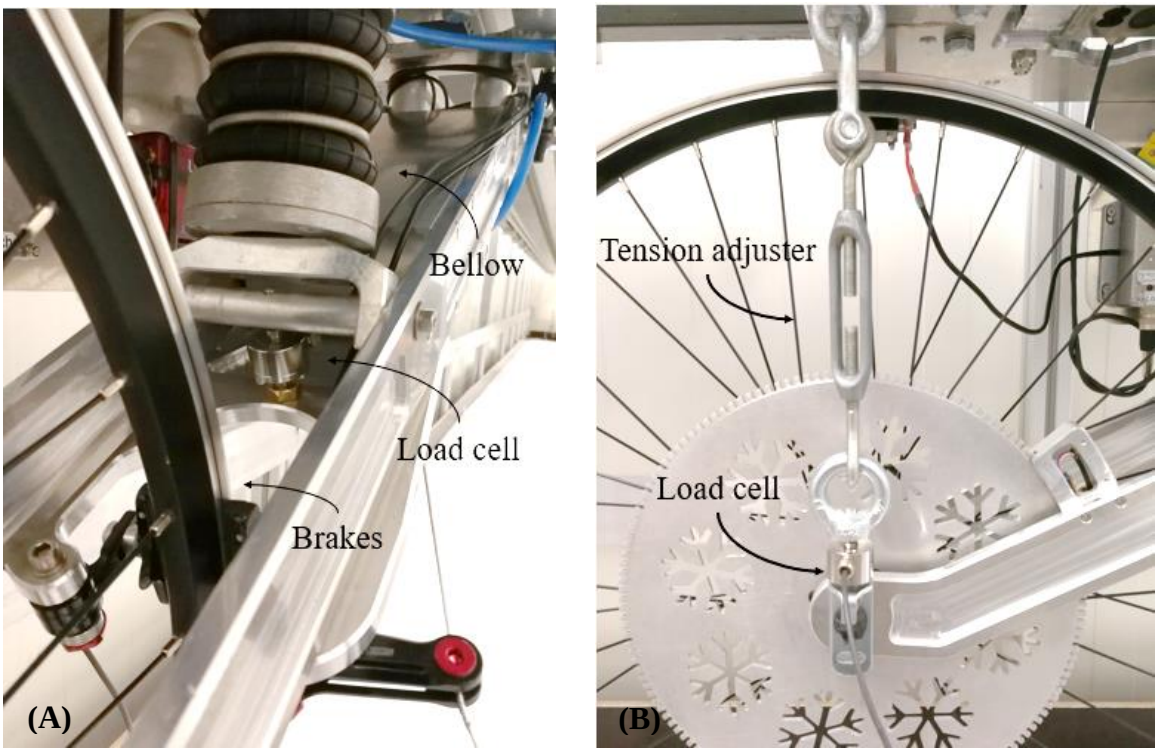

Figure 42: *(A) Brakes and lower part of load cell mounted to a common metal sheet. (B) Tension adjuster raising and lowering the wheel on the sample*

An air bellow was already mounted on the aluminum arm, extending from the sled to the center of the wheel (Figure 40 and 42A). This enabled height differences, and hence variations in normal force, on the wheel. As the desired normal force on the sample was

much smaller than what the system was designed for, the bellow had to be evacuated rather than pressurized.

The point of loading on the samples was viewed as critical for two reasons. Firstly, to avoid so-called cross-talk, meaning that a part of the normal force interferes with the measured signal from the load cell. This can occur if the normal force is applied slightly off center so that it consists of horizontal contributions, which may interfere with the friction force and further the force measured by the load cell. Secondly, if the point of loading is slightly in front of the center, it can make the sample plow into the snow, which is resistant to motion. In any case, the most important is that the load distribution is the same in each run to eliminate the factors differences from run to tun.

Several ways to attach the sample to the wheel was attempted. Due to limited space, the rubber tire was demounted, and the rims were hence the only contact with the sample. It was found that the bare friction at the interface between rims and sample was not sufficient for contact as the wheel would slide off the sample. It was also attempted to attach a cushioned tape on the sample to increase friction at the interface. However, this rose problems regarding alignment as it would be challenging to ensure the rims were positioned identically for every set of runs. The final solution was to make a threaded hole at the center of the samples, in which an M5 bolt with truncated bolt head was placed (Figure 43). M5 was chosen as this would fit into the already existing hole at the rims, meant for the air hose, with a bit of space for the self-alignment. Additionally, a bracket was found in which width fitted almost perfectly inside the outer edge of the rims. The bracket was attached to the upper surface of the sample with double-sided tape and assured that the sample would not twist along the track. The sample, pin, bracket, and tape were measured to weigh 300 g in total.

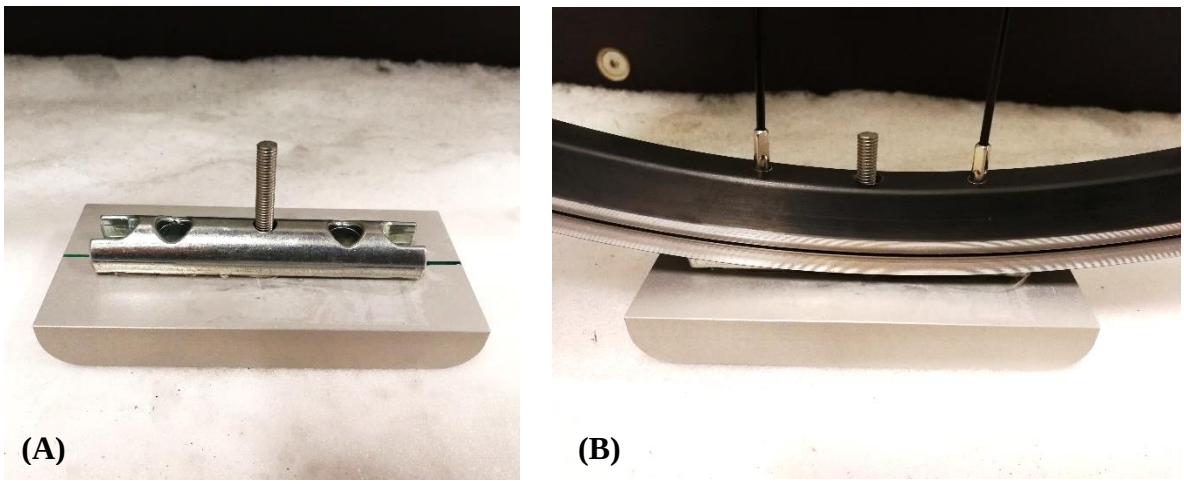

Figure 43: *Sample with pin and bracket to fit into the rims of the wheel*

Four sets of COF measurements were conducted; anodized- and reference sample at -10 ℃ and anodized- and reference sample at -2.7 ℃. Both temperatures given were the air temperatures in the snow lab at respective test sets. The corresponding snow temperatures will be discussed in section 5.7, but as there is a slight uncertainty to this the test temperatures they will temporary be referred to as -10 ℃ and -2.7 ℃. The LARS was programmed to reach a constant speed of 2 m/s with a ramp of 1 m. The sliders were only run at the track between 3-6.7 m, as this was observed to be the most uniform part of the snow surface. The speed profile is given as a function of time in Figure 44. Relative humidity (RH) is estimated to 70-80% for all experiments.

MATLAB was used for data processing and visualization of the resulting COF values, in which code is given in Appendix O. Approximately 35 heats were conducted in each of the four sets. Tests where, for some reason, the data was not logged for more than 2 seconds were discarded from the set. Additionally, the five first tests within each set were discarded, just as [72] did. This was done as a so-called run-in; to enable the two surfaces to become compatible and break the tops of the snow base that could give unreliable high friction at the beginning of a set. After discarding the tests mentioned above, 25 tests remained in each set. As the load cell measuring the brake force did not read zero before each test started, a zero point was made during data processing by finding the mean brake force of the first five measurements of each test and subtract this value from all braking force data points. Other than the two different temperatures, conditions were held constant throughout the sets. Each set was run without disassembling the sample from the LARS setup. Only a few seconds between each test was allowed due to time limitations.

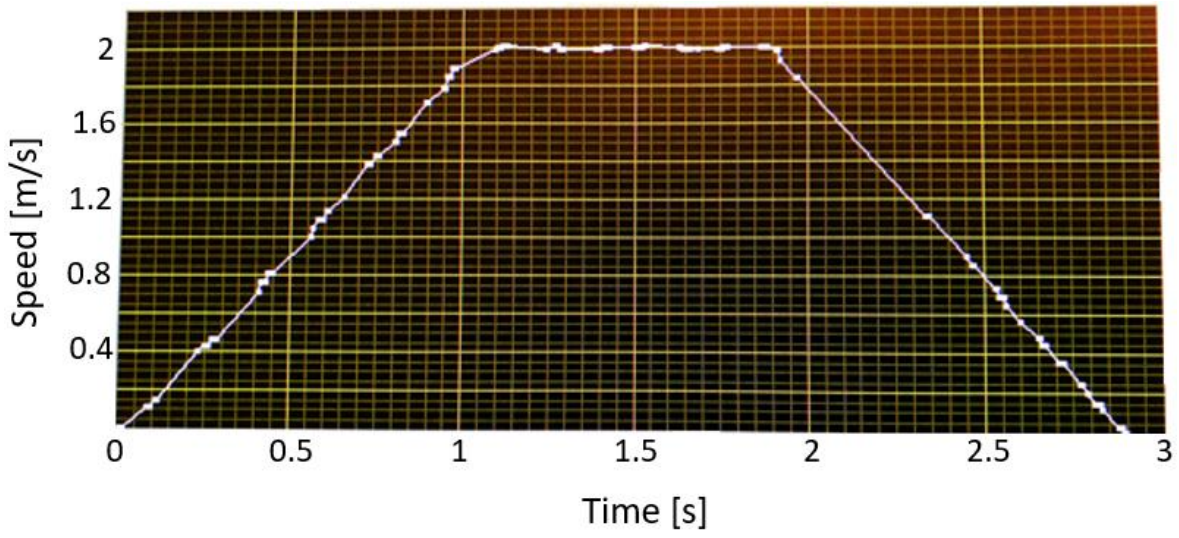

Figure 44: *Speed profile of miniature ski prototypes in LARS*

3.4.2 Snow track

The development of the snow track was a highly dynamic process, and the next step was to a large extent determined based on the outcome of the previous. However, a rough plan of the procedure was to first make a snow base of snow harvested outside and then apply a thin layer of artificial snow from Lumi on top. The reason for the latter was due to the importance of known and constant characteristics of the snow in contact with the samples. It was also desired for the snow track to be completely horizontal. In the following, a summary of the different steps, the reasoning behind them, and their outcomes will be given.

Corse-grinded produced snow was harvested from outside the ski facilities at Granåsen in Trondheim and transported back to the snow lab. The temperature in the lab was initially set to -10 ℃ and the snow was applied as evenly as possible along the track. Unfortunately, this snow was quite clumpy and icy, which seemed to further increase with time after arrival in the lab. A snow compactor (SC) was made by the machine shop employees at the Department of Civil and Environmental Engineering (Figure 45). The function of the SC was to compact the snow to make the track as uniform as possible. It was mounted with rollers on aluminum bars, enabling it to slide along the track when pulled by the sled. Hinges, hooks, and a tension adjuster enabled adjustment of the vertical positioning of the SC. It ran while varying between applying an additional load of up to 40 kg and speeds between 0.1-0.2 m/s. Unfortunately, the SC was only partly successful; as the snow had already started to sinter it was difficult to smooth out the track. Therefore, it was decided to let the snow harden overnight and then apply a layer of artificial snow to smooth it out.

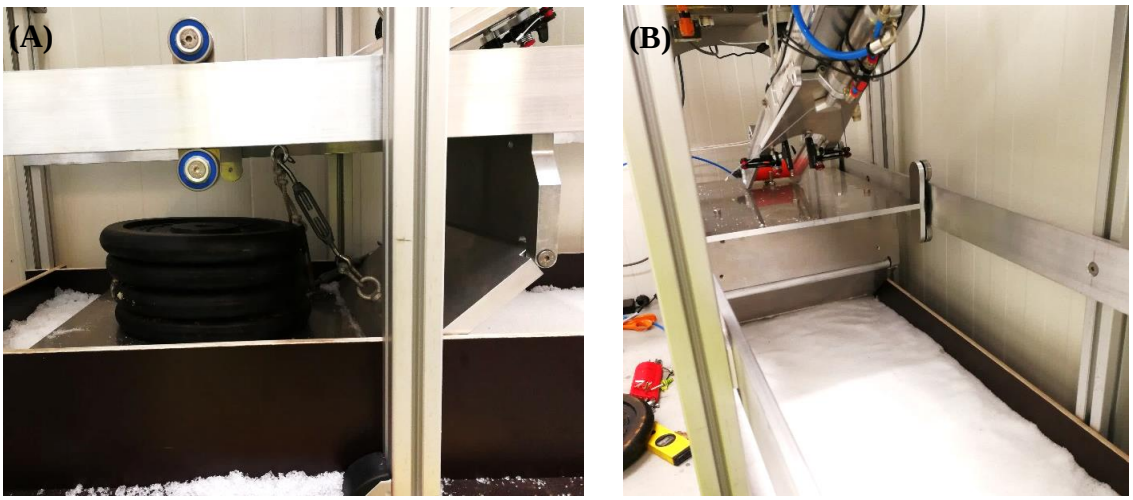

Figure 45: *Snow compactor (SC) to make snow track horizontal. Extra weights were applied to increase pressure*

The next day the snow had, as expected, increasingly hardened. A thin layer of the artificial snow was applied. As in accordance with [72], the snow was sieved, in which a 2 mm grid was used. However, it was clear that this layer would not adhere to the hard snow base, as the SC was just pushing the new snow in front of itself. Hence, the layer of artificial snow was removed, and the hard snow base was structured with a trowel (Figure 46A). The artificial snow was again applied. This time a painted steel cylinder was first cooled down and then manually rolled over the snow (Figure 46B) before the SC was again slid over the track. It was evident that the artificial snow would adhere much better this time. However, it was observed that snow would also stick to the SC, made of aluminum, making a rather bulky surface. This was solved by gluing a thin layer of plastic foil to the surface of the SC in contact with the track.

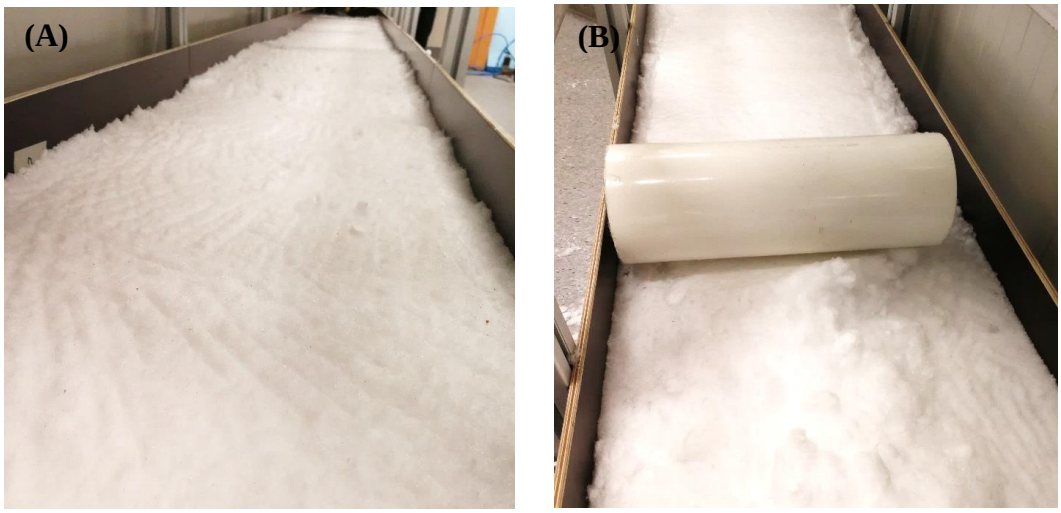

Figure 46: *(A) Structured snow base. (B) Cylinder was rolled over the track manually*

Another challenge was to attain a completely horizontal track. As working with snow is extremely hard to master, it was decided to allow a height difference of approximately 10 mm along the track. After a relatively flat surface was attained, it was attempted to run the system with a cross country- and a downhill ski to further compact the snow at the narrow stripe that the samples would run over. This seemed to work with great success; a nice, smooth path was made along the track. However, it was clear that the topography of the track was partly changing for each run, which witnessed the snow track not being hard enough. It was therefore sprayed water on the surface. The wet snow was left for some minutes before riding over it with a ski again. This was believed to break up some of the formed snow bindings and flatten the surface before it would sinter completely, which seemed to work. Contamination visible to the naked eye was removed either manually or by a vacuum cleaner. The

importance of cooling any tool or sample that would be in contact with the track was detected; any object not sufficiently cold would undesirably melt the snow.

3.4.3 Load selection and pressure distribution

To determine to load to be applied on the ski prototype, a scale down of the load on a pair of full-scale skis was conducted. Figure 16 illustrates the force distribution underneath six pairs of Madshus Nano skating skis, measured by [48], which will be used as the base for load calculations in this work. Even though these skis are meant for the skating style rather than the classical, they have been evaluated as suitable for an estimation because of reasons already mentioned in section 2.5.1. It was decided to conduct tests with one miniature ski prototype only, and not two, which is a more realistic arrangement. Some researchers have used two skis when testing skis on a snow track [69, 70, 118], however, these setups did not have a guided movement. On the other hand, others [72] (Figure 21) used one ski only in a setup in which the skiing movement was guided in a similar way as in this work. Hence, it was viewed as unnecessary to use more than one ski prototype for each test as the beam would accelerate the samples on a path and the center of mass would be close to the ground. Additionally, it would require more work to make double the amounts of samples, in which as close as identical pairs of samples would be highly beneficial.

Before presenting the calculations resulting in the load selection, essential facts from the study in which the scale down is based on ([48]), in addition to assumptions made, is stated in the following:

- Due to the flex in the ski, the weight of the skier is divided into two parts. The anterior part of the ski in Figure 16 is the most Gaussian distributed, and will, therefore, be the part studied here
- The length of the area of the force distribution on the anterior part is estimated to reach from approximately 120 mm to 680 mm on the scale bar, hence 560 mm in total
- As it is not feasible to sum the force on the anterior part, it is estimated to be 40 % of the total force on the ski, based on the areas under the graph
- It is given that the weight of the skier is 85.7 kg, which is equally distributed on each leg, making it a half weight mode (section 2.5.1)
- The force distribution are the sum of both skis, and each of the skis in this study are 50 mm wide
- As given in section 3.1.2, the surface area in contact with the snow base is 90×50 mm for the miniature ski prototypes

Hence, the mass on the anterior part of one Madshus Nano skating ski is 17.14 kg by Equation 21:

$$m_{anterior} = m_{total} \cdot f_{force\ on\ anterior} \cdot f_{one\ of\ two\ skis} \qquad (21a)$$

$$m_{anterior} = 85.7\ kg \cdot 0.4 \cdot 0.5 \qquad (21b)$$

$$m_{anterior} = \mathbf{17.14\ kg} \qquad (21c)$$

Where $f_{force\ on\ anterior}$ is the ratio between the force on the anterior of the skis and the total force on the skis. $f_{one\ of\ two\ skis}$ represents the scale down from two skis, in the model for the skating skis, to one ski, for the miniature ski prototypes.

The mass on the ski prototype can be found by claiming equal pressure as on the full-scale ski by Equation 22:

$$m_{sample} = \left(\frac{m_{anterior}}{A_{anterior}}\right) \cdot A_{sample} \qquad (22a)$$

$$m_{sample} = \frac{17.14\ kg}{560\ mm \cdot 50\ mm} \cdot (90\ mm \cdot 50\ mm) = \mathbf{2.75\ kg} \qquad (22b)$$

This corresponds to a normal load of approximately 27 N. The mass calculated here is only guiding as it is based on 85.7 kg as the weight of a skier. Deviations in the range between approx. 2-3.5 kg is considered acceptable, as long as the exact weight is reported. It was found in section 3.4.1 that the sample, pin, and bracket weighed 300 g, which was decided to be added to the mass found in Equation 22b. Hence, the total weight on the sample surface is 3.05 kg, equaling a total normal force of 29.9 N.

As was seen in Figure 43, the rims are resting on the bracket exactly at the center of the sample. A simulation of this loading scenario in static mode is shown in Figure 47A. In this simulation, the surface in contact with the snow base is only allowed to slide on the horizontal plane. However, as this makes the load twist the sample, the upper short edge on the left side in the figure is fixed for movement in all directions. The load of 27 N is applied uniformly on an area approximating the contact area between the sample and the bracket. However, this is not a completely realistic distribution. It is expected that the pressure will be higher at the center of the sample, right below the contact points between rims and bracket. The simulation is carried out with the aluminum alloy 7079, which have a yield strength somewhat higher than the alloy EN AW 5450 actually used for the miniature ski prototypes. However, as the load applied and the resulting von Mises stresses are of limited size, this is not viewed as an issue. Figure 47B shows the pressure distribution of the sample surface in contact with the snow base. Even though this simulation is not completely realistic, especially

not for the pressure distribution when the sample is accelerating, it gives a useful indication. Furthermore, it is desired to only use data in which the velocity is constant when calculating the COF.

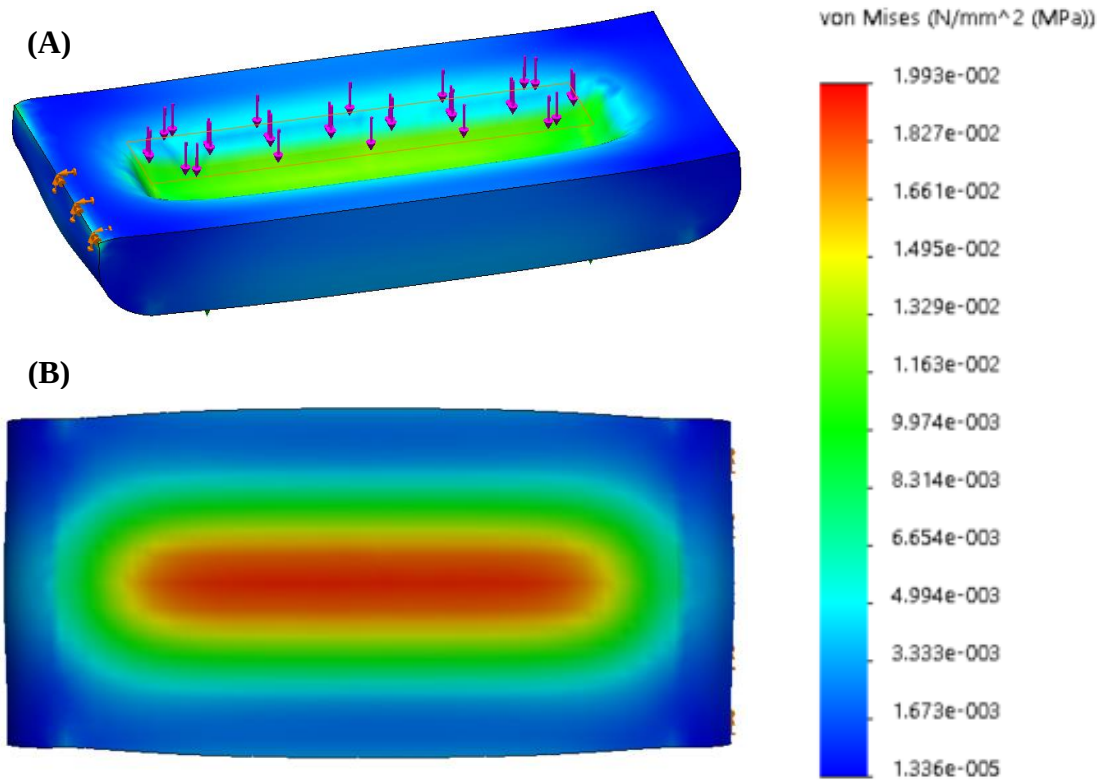

Figure 47: *Simulation of pressure distribution on miniature ski prototypes on snow track. (A) Illustration of constraints and applied pressure. (B) Sample surface in contact with the snow*

4 Results

This section will first present the results of the hot embossing of UHMWPE, which was not further used for the miniature ski prototypes. The remaining sections, 4.2-4.7, will contain sub-sections of processes relevant for the final sliders. For both the anodized and the reference miniature ski prototype, the surfaces were investigated with characterization instruments both before and after friction tests. Before the friction tests, they were imaged with OP, SEM, and the CA was measured. The CA was also measured in between some of the friction tests. After all friction tests, the surfaces were again analyzed with the OP and the CAs were measured.

4.1 Hot embossing of UHMWPE

Several attempts of hot embossing of a UHMWPE ski base material were conducted, with a few different master surfaces, loads, and temperatures. Table 3 sums up the processing parameters for all experiments. The hot embossed samples are coded with “UH-” in front of an abbreviation of their master (AAO or P1000) and ending with a number, representing the individual experiment. Figure 48 shows OM images of a UHMWPE surface that have not been embossed, the master surfaces before embossing, and all UHMWPE surfaces after embossing. Note that different brightness and contrast levels in the images may give a somewhat misleading visual impression. The images in this figure, in addition to images in which the topography is visualized by color differences, as well as surface roughness parameters, is given in Appendix B.

All experiments were conducted at 60 kN and for 15 minutes, but the contact area between the UHMWPE sheet and the master was varying, resulting in different pressure values. For test number UH-P1000-1, UH-P1000-2 and UH-P1000-4 (cursive in Table 3) the UHMWPE and master surface adhered during the embossing and were not possible to detach. Hence, no OM images are given of these. The AAO sample used was fabricated during the specialization project. In the table, column number six comments on whether both or just one of the pressure plates were heated. However, it was observed that for the experiments where only one plate was heated, the temperature of the other would naturally also increase upon embossing.

Table 3: *Processing parameters for hot embossing of UHMWPE experiments*

Sample	Master	Contact area	Pressure	Temp.	Plates heated	Comments
UH-P1000-1	P1000 emery paper	50×50 mm	24 MPa	150 ºC	Both	No pre-heating
UH-P1000-2				150 ºC	Both	Emery paper coated with PTFE. UHMWPE pre-heated 89 ºC, 8 min.
UH-P1000-3				120 ºC	Plate close to UHMWPE	UHMWPE pre-heated 85 ºC, 5 min.
UH-P1000-4				150 ºC	Plate close to emery paper	No pre-heating
UH-P1000-5				150 ºC	Plate close to UHMWPE	No pre-heating
UH-AAO-1	AA3	26×19 mm	121.5 MPa	150 ºC	Both	No pre-heating
UH-AAO-2				150 ºC	Plate close to UHMWPE	No pre-heating
UH-AAO-3				100 ºC	Plate close to master	No pre-heating
UH-AAO-4				150 ºC	Plate close to master	No pre-heating

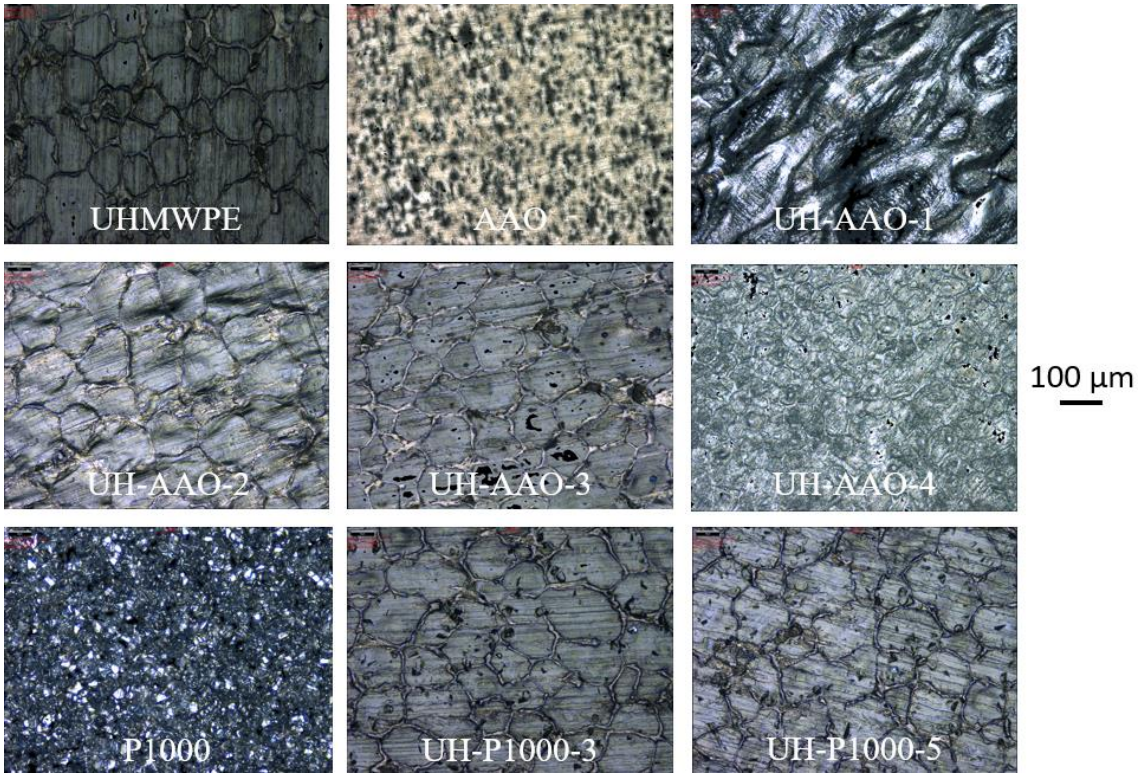

Figure 48: *OM-images of hot-embossed surfaces, and their master before embossing*

4.2 Anodizing process

This sub-section will contain results from the anodizing process of one of the miniature ski prototypes. As the instrument used for anodizing could not log the potential, and the next sub-sections are dedicated to OP, SEM, CA, and friction tests, this section will rather provide comments on the process.

As mentioned in section 3.1.2, the beaker with electrolyte was placed in a water bath at 20 ºC before anodizing. However, right after the anodizing process was completed, it was observed a temperature increase in the electrolyte. The upper part of the electrolyte was measured to around 35 ºC, while it is believed that the temperature was somewhat lower further down in the beaker. However, in the stressful situation of getting the sample up on time, the latter was not measured accurately.

The sample after anodizing is shown in Figure 49A, while the cathode after anodizing is shown in Figure 49B. It is evident from the former that the circular area around the hole for the connecting rod has not undergone the anodizing process as this was covered by the shrink tube.

It could be seen with the naked eye that there was a transverse line at about the middle of the anodized sample dividing the look of the surface slightly. The half furthest down in the electrolyte seemed to have a more uniform surface and will from now on be referred to as Side 1. The half furthest up, from now on referred to as Side 2, had a less uniform surface. It was evident that if rubbing Side 2 with a cotton pad some of the oxide would detach, which will be discussed in section 5.2. The contour of this line can be detected in Figure 49A, and the two sides' characteristics will be investigated further in subsequent sections.

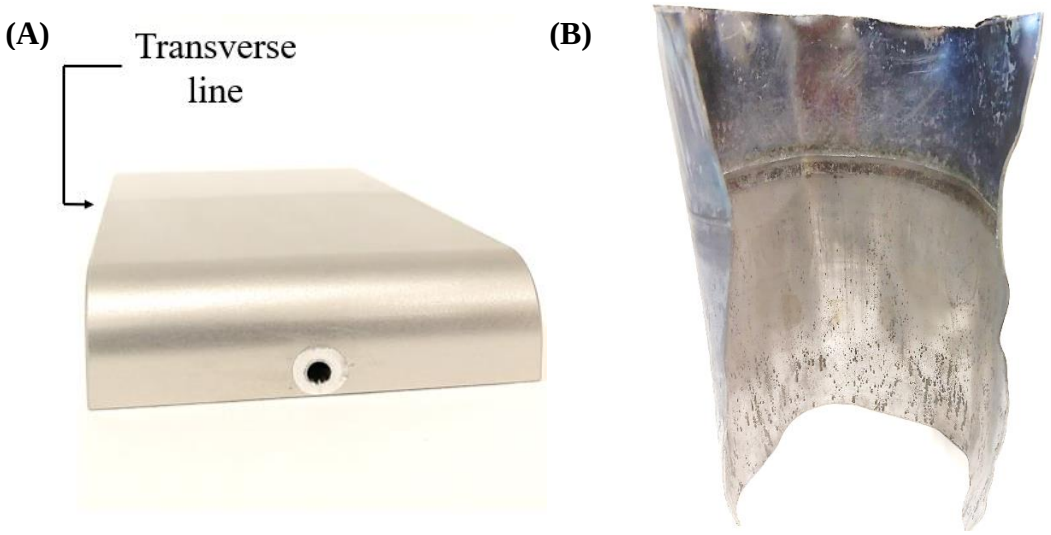

Figure 49: *(A) Miniature ski prototype after anodizing. (B) Cathode after anodizing*

4.3 OP data from ski prototypes

The miniature ski prototypes were analyzed with the OP both before and after friction tests. The anodized miniature ski prototype was analyzed on Side 1 and Side 2 individually. The surface roughness parameters were logged at a varying number of spots for each surface. Table 4 shows the roughness parameters presented in section 2.4.1 at two spots for Side 1 and three spots for Side 2 before friction tests, and at three spots for Side 1 and six spots for Side 2 after friction tests. The reference sample is similarly analyzed at four spots before the friction tests and at three spots after the friction tests. Note that the location of each numbered spot before friction tests does not correspond to the location of the spot with the same number after friction tests, this is only for keeping track of the number of spots analyzed. As section 5.3 will include a discussion about the evident large difference of roughness parameters for some of the surfaces, all spots are tabulated, in addition to averages and standard deviation values within each surface set. The anodized sample is labeled AAO and reference sample REF.

Table 4: *Roughness parameters for AAO sample, Side 1 and 2, before and after friction tests*

Case	Surface	Spot	Sa [µm]	Sku	Sp [µm]	Sq [µm]	Ssk	Sv [µm]
Before friction tests	AAO, Side 1	1	0.452	87.374	56.092	0.624	0.307	-11.194
		2	0.431	27.963	23.094	0.584	-0.448	-10.409
		Average	0.441	57.669	39.593	0.604	-0.071	-10.801
		Std.	0.010	29.706	16.499	0.020	0.378	0.392
	AAO, Side 2	1	10.667	4.538	70.330	14.082	-1.694	43.192
		2	9.273	6.905	67.422	13.539	-2.246	-50.854
		3	10.015	6.094	85.821	14.147	-2.072	-56.785
		Average	9.985	5.846	74.524	13.923	-2.004	-21.482
		Std.	0.569	0.982	8.076	0.273	0.230	45.796
	REF	1	0.270	3.010	5.040	0.335	0.278	-2.340
		2	0.261	3.143	7.016	0.323	0.227	-1.902
		3	0.445	3.498	18.604	0.533	0.219	-2.033
		4	0.390	2.735	4.117	0.484	0.105	-2.283
		Average	0.342	3.097	8.694	0.419	0.207	-2.139
		Std.	0.079	0.275	5.816	0.092	0.063	0.179
After friction tests	AAO, Side 1	1	0.445	7.661	20.272	0.569	-0.669	-8.060
		2	0.626	3.412	19.126	0.763	-0.324	-9.479
		3	0.314	15.513	15.598	0.423	-0.837	-7.826
		Average	0.462	8.862	18.332	0.585	-0.610	-8.455
		Std.	0.128	5.013	1.989	0.139	0.214	0.730
	AAO, Side 2	1	0.437	14.941	29.946	0.545	0.267	-9.673
		2	6.052	11.275	25.211	10.241	-3.029	-48.502
		3	4.072	18.922	21.000	7.979	-4.017	-42.971
		4	0.339	43.489	20.877	0.461	-0.308	-10.823
		5	0.414	34.064	33.277	0.540	-0.697	-10.351
		6	6.225	9.109	16.937	9.843	-2.675	-62.605
		Average	2.923	21.967	24.541	4.935	-1.743	-30.821
		Std.	2.619	12.569	5.624	4.474	1.575	21.357
	REF	1	0.253	3.031	2.467	0.318	0.154	-2.110
		2	0.457	2.325	2.734	0.548	0.158	-2.335
		3	0.283	17.896	20.403	0.366	-0.175	-3.547
		Average	0.331	7.751	8.535	0.411	0.046	-2.664
		Std.	0.090	7.180	8.393	0.099	0.156	0.631

Figure 50 shows a 2D view of the analyzed surface at spot 1 of Side 1 before friction tests. Figure 51 shows a 3D view of the same surface spot. For comparison, spot 2 on Side 2 is shown in Figure 52-53 before friction tests. Similarly, Figure 54-55 shows the surface of the reference sample at spot 2 before the friction tests. 3D OP images are given for all surface spots in Appendix M.

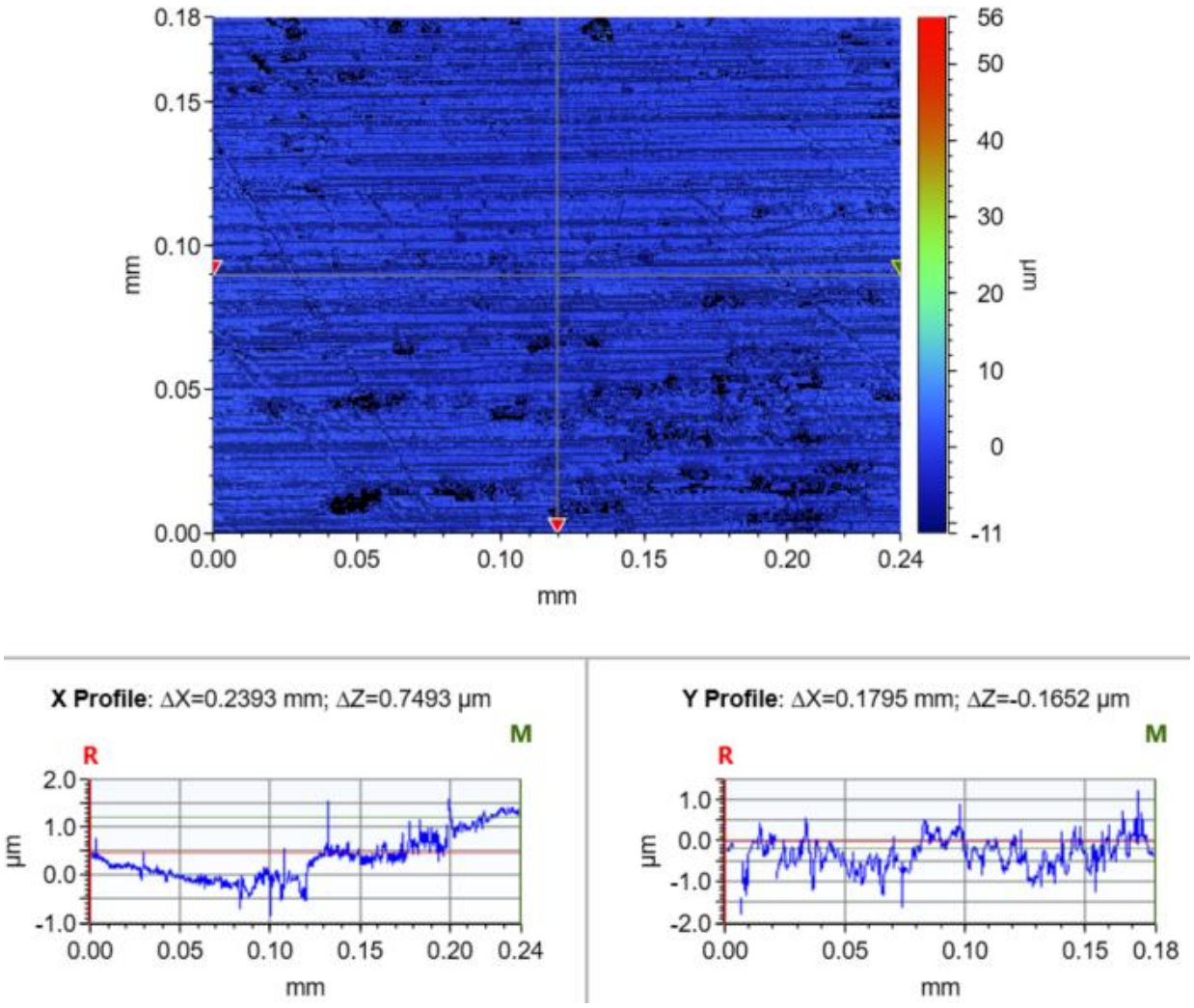

Figure 50: *2D view of Side 1, spot 1 for anodized miniature ski prototype before friction tests*

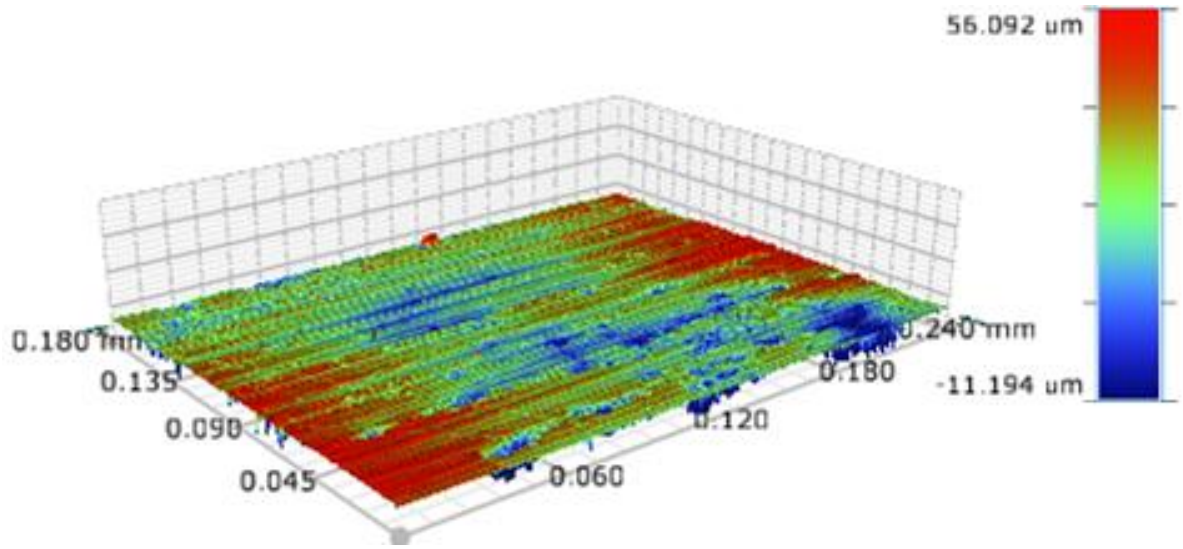

Figure 51: *3D view of Side 1, spot 1 at anodized miniature ski prototype before friction tests*

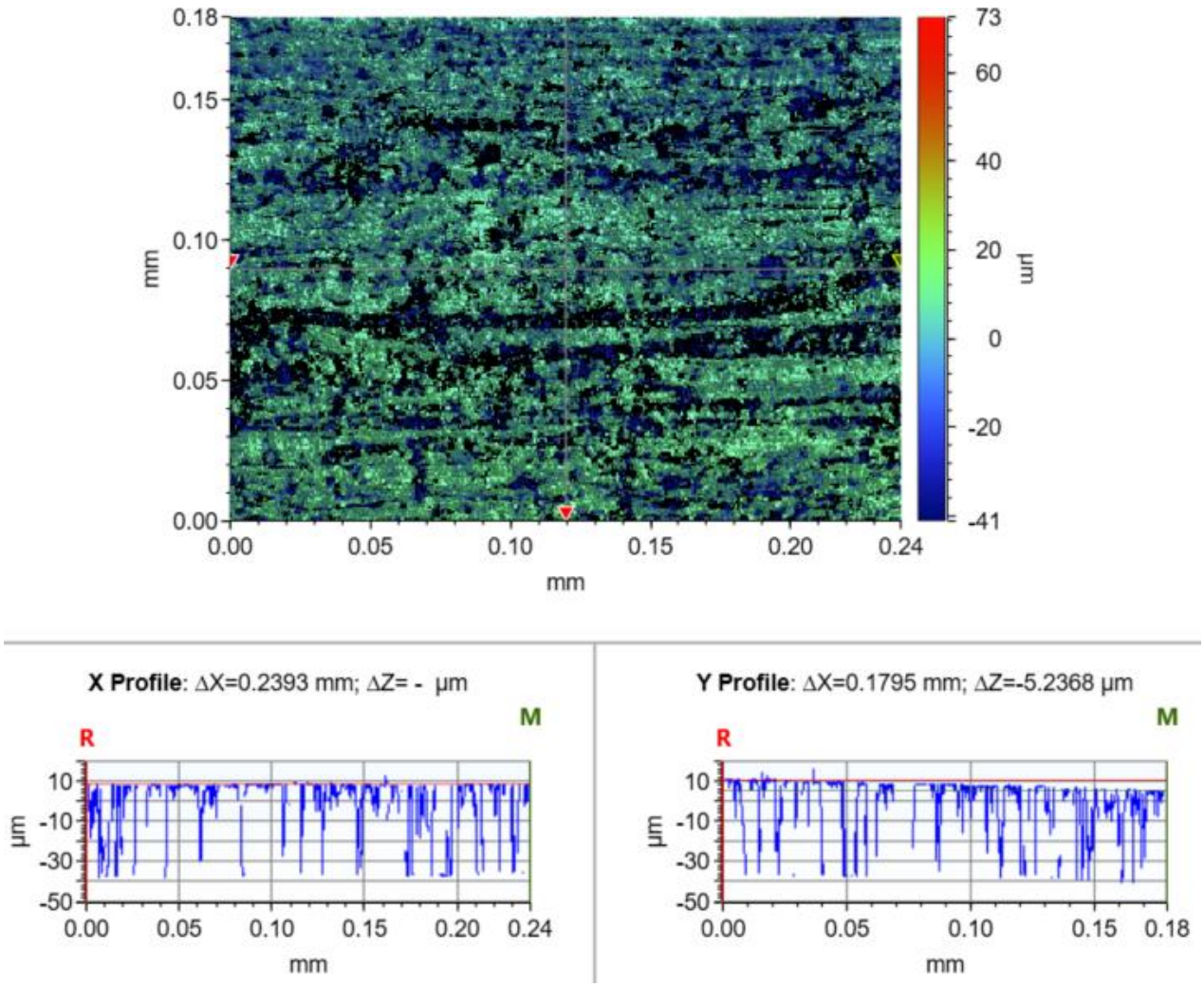

Figure 52: *2D view of Side 2, spot 1 at anodized miniature ski prototype before friction tests*

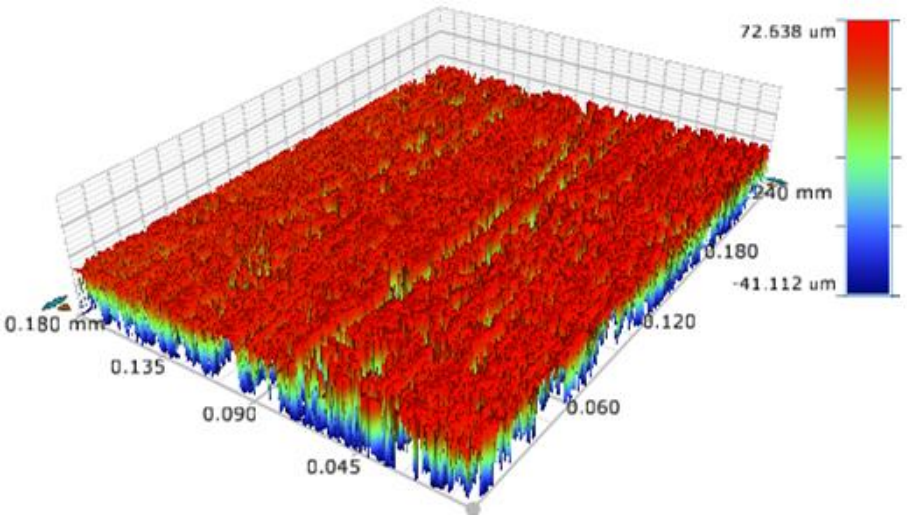

Figure 53: *3D view of Side 2, spot 1 at anodized miniature ski prototype before friction tests*

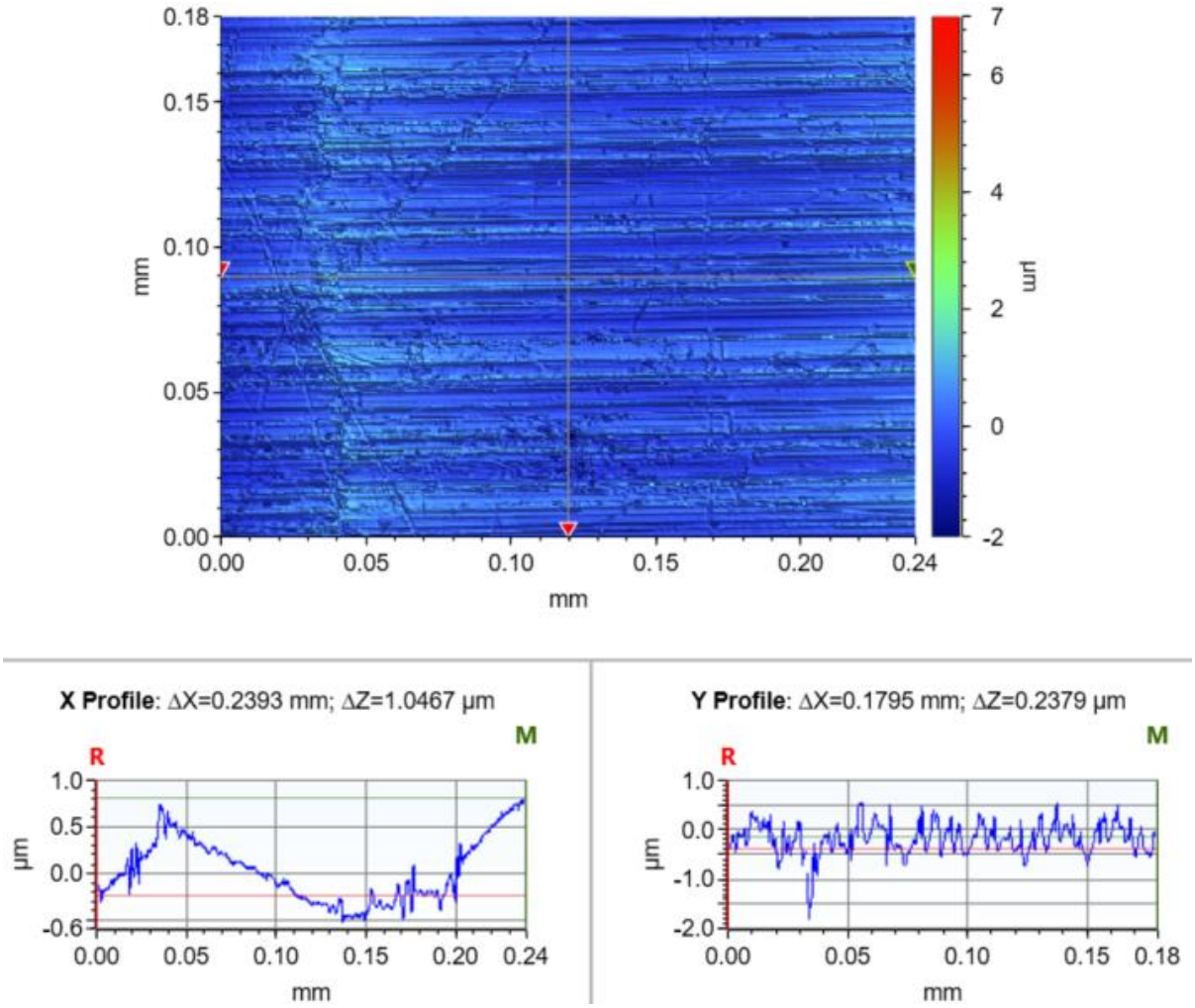

Figure 54: *2D view of spot 2 at reference miniature ski prototype before friction tests*

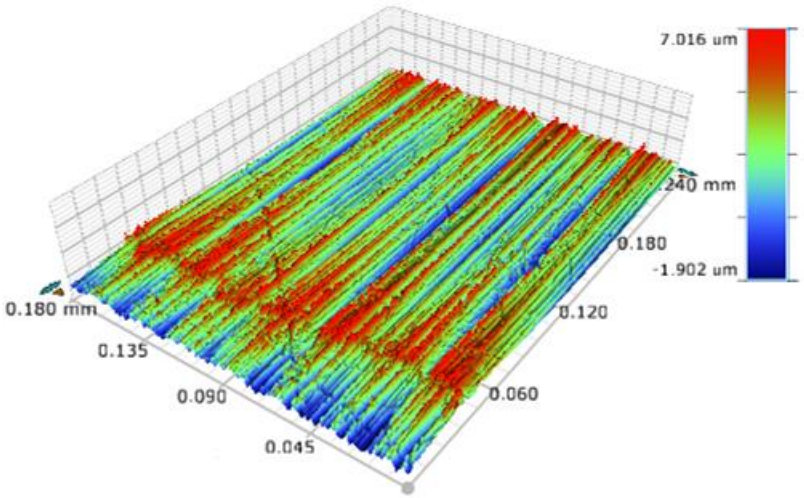

Figure 55: *3D view of spot 2 at reference miniature ski prototype before friction tests*

4.4 SEM images of ski prototypes

Due to limited availability of SEM, images could only be captured before friction tests. Figure 56 shows an SEM image of Side 1 of anodized miniature ski prototype, and Figure 57 of Side 2. Both images are captured with the low-vacuum function. Similarly, Figure 58-59 shows SEM images of the reference ski prototype, captured with the high vacuum function. Additional images are given in Appendix L.

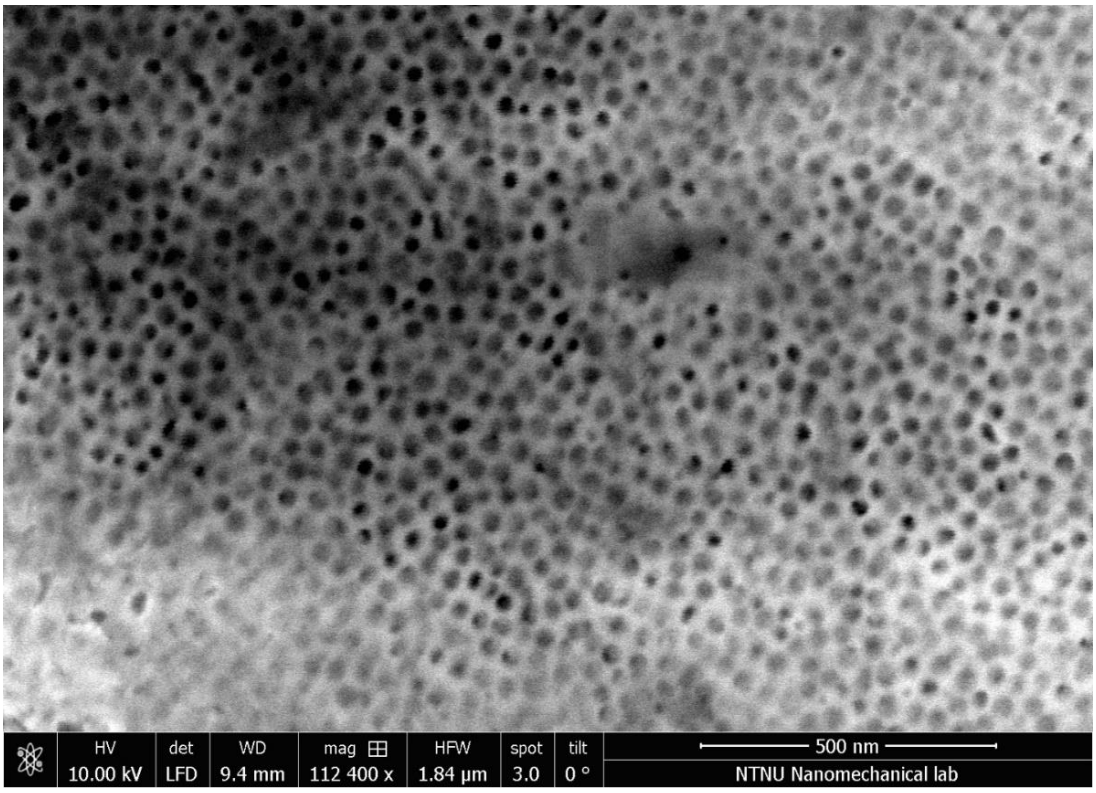

Figure 56: *SEM image of Side 1 of AAO sample before friction tests*

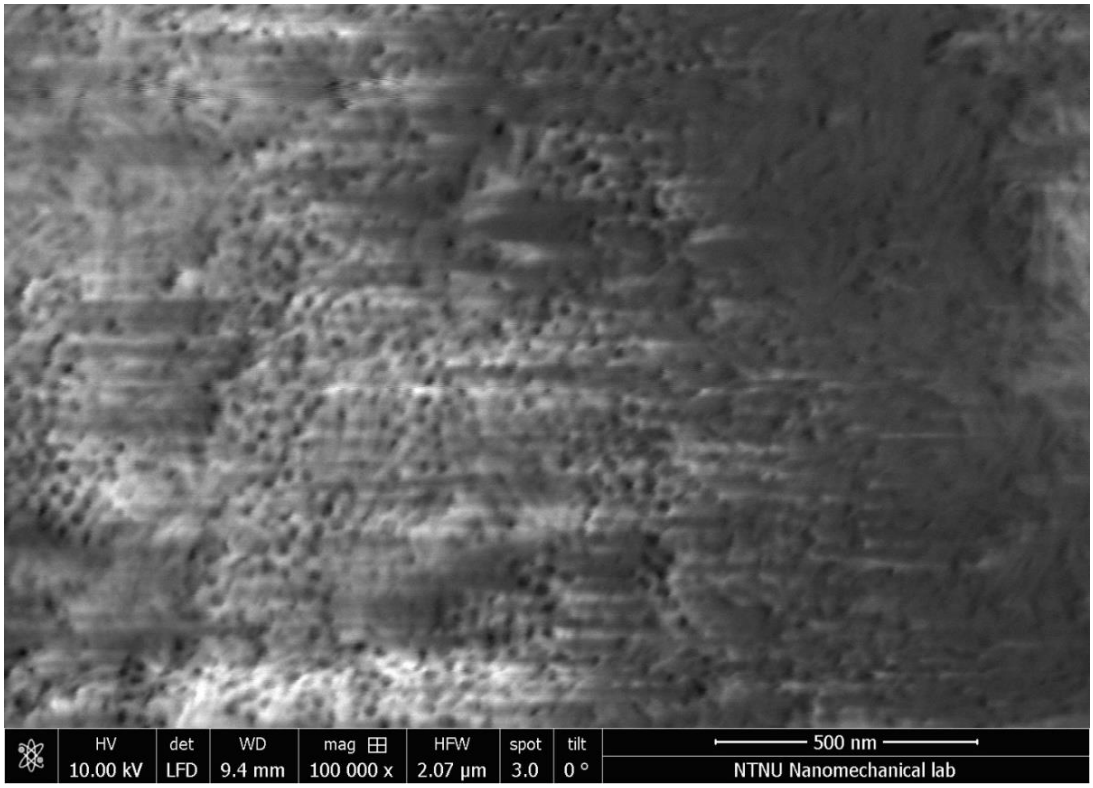

Figure 57: *SEM image of Side 2 of AAO sample before friction tests*

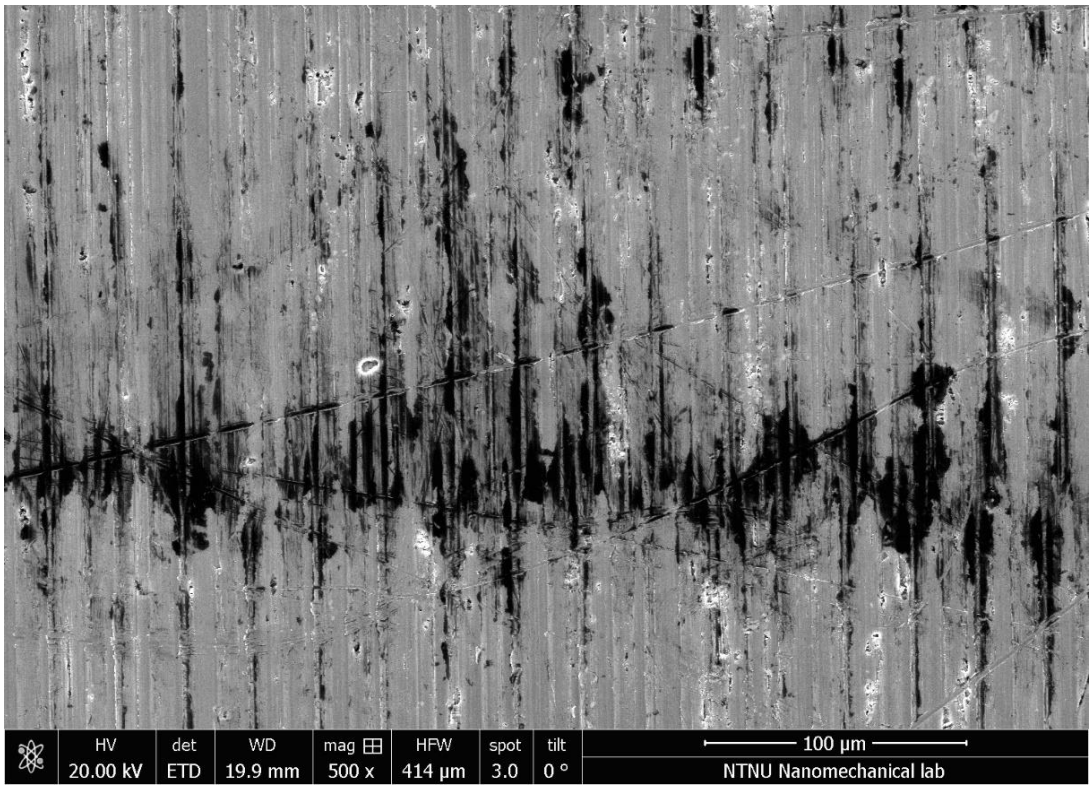

Figure 58: *SEM image of the reference sample with low magnification*

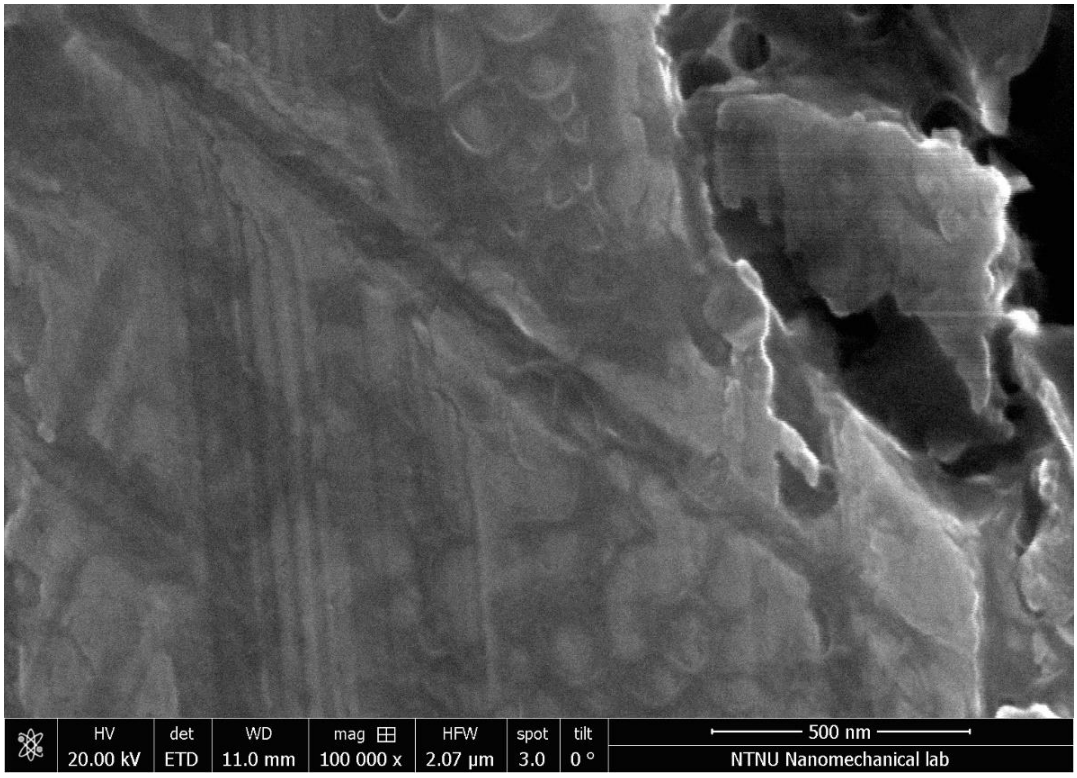

Figure 59: *SEM image of the reference sample with high magnification*

4.5 Aspect ratio estimation for ski prototypes

For Side 1 the pore diameter was found to be between 20-33 nm and the interpore distance between 35-62 nm from the SEM images and ImageJ. However, it was not possible to accurately determine these dimensions for Side 2 as the electron beam was charging the surface too much, making the image appear blurry. Based on the average *Sa* value for Side 1 before friction tests, this would estimate the AR to be in the range between [2·0.441 µm:35 nm, 2·0.441 µm:20 nm] = [882:35, 882:20] = [25.2, 44.1]. As no SEM images were captured after friction tests, the AR cannot be determined accurately for this case.

4.6 CA measurements for ski prototypes

CA measurements were conducted for three cases; (i) clean samples before friction tests, (ii) clean samples after some friction tests, and (iii) unclean samples after all friction tests. For iii), remainings of PTFE could be present at the surfaces. Droplets were deposited and analyzed for 2-4 spots on both Side 1 and Side 2 of the anodized sample, as well as the reference sample, with and without PTFE coating (Table 5). The anodized sample is labeled

as AAO and reference sample as REF. For comparison, a smooth glass slide is included, also with and without PTFE coating.

Table 5: *CA measurements of AAO- and REF miniature ski prototype, and smooth glass slide. The average of left and right CA is first found for the individual measurements, and further, the average of these values for an entire set is given here*

Case	Surface	PTFE coating	Avg. CA of set [º]	Std. of set [º]
Clean, before friction tests	AAO, Side 1	No	59.79	7.96
	AAO, Side 2	No	67.54	2.05
	AAO, Side 1	Yes	128.17	11.97
	AAO, Side 2	Yes	132.10	3.16
	REF	No	78.43	5.18
	REF	Yes	92.47	4.36
Clean, after some friction tests	AAO, Side 1	No	84.03	0.10
	AAO, Side 2	No	90.86	2.08
	AAO, Side 1	Yes	131.50	10.14
	AAO, Side 2	Yes	136.55	8.60
Uncleaned, after all friction tests	AAO, Side 1	Partly	80.86	6.36
	AAO, Side 2		90.23	12.33
	REF		71.93	6.14
Glass slide		No	62.17	10.42
		Yes	92.10	4.33

4.7 Friction tests for ski prototypes

The four sets of friction tests; anodized sample at air temperature of -10 ºC, reference sample at -10 ºC, anodized sample at -2.7 ºC and reference sample at -2.7 ºC, all included 25 tests each. Three plots were made for each set in MATLAB: (i) COF as a function of time for all 25 individual tests along the entire track, (ii) the average COF of all 25 tests as a function of the average time along the entire track, and (iii) the average COF of all 25 tests as a function of the average time between 1.7 s and 2 s. Figure 44 shows that the velocity is constant at 2 m/s approximately between 1-2 s. However, it was evident from all plots of type (ii) that there was a large drop right after 1.2 s. Hence, (iii) was chosen as the portion of (ii) ranging between 1.7-2 s, as this part of the graph that was more uniform, in addition to being at a constant velocity. The content of type (iii) will be emphasized throughout the work and are

shown for all four sets in Figure 60-63 with blue lines. Corresponding curve fits of an 8th-degree polynomial is included with yellow lines. Type (i) and (ii) are given in Appendix R.

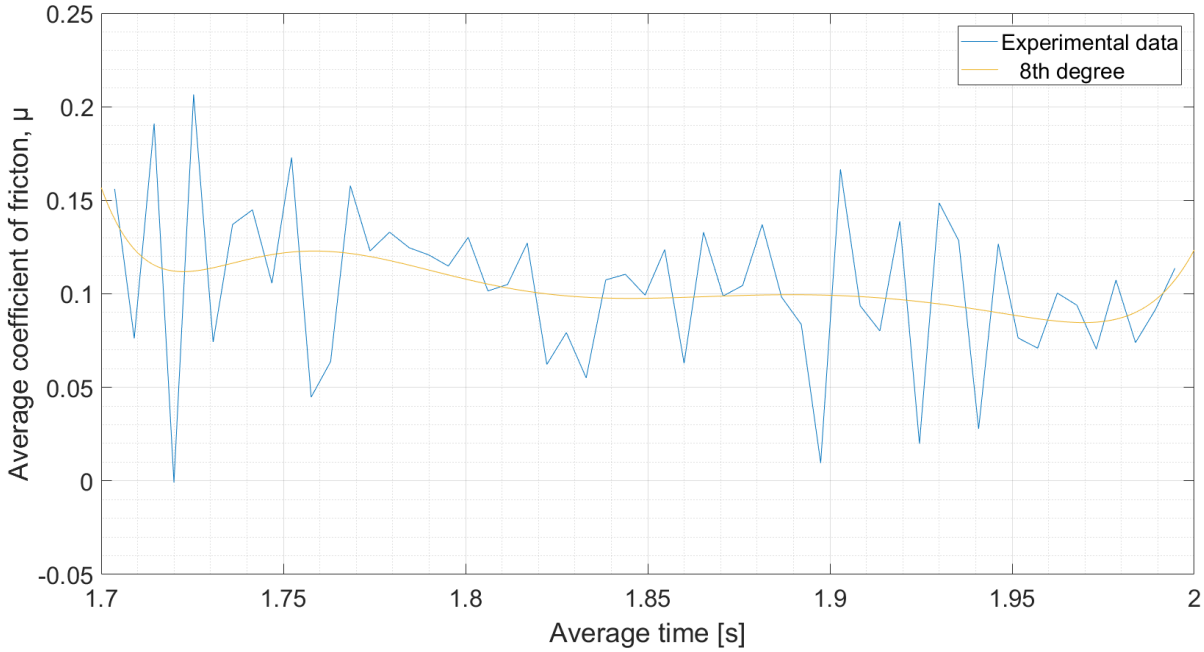

Figure 60: *Average COF for the anodized sample at -10 ºC and constant velocity 2 m/s*

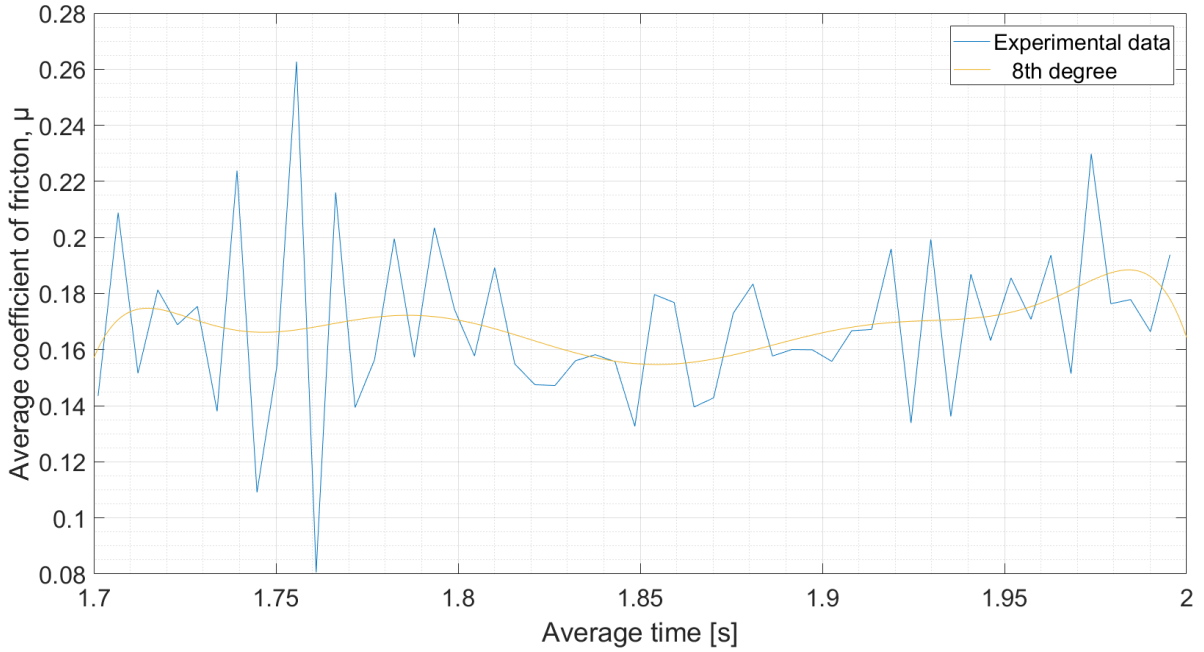

Figure 61: *Average COF for reference sample at -10 ºC and constant velocity 2 m/s*

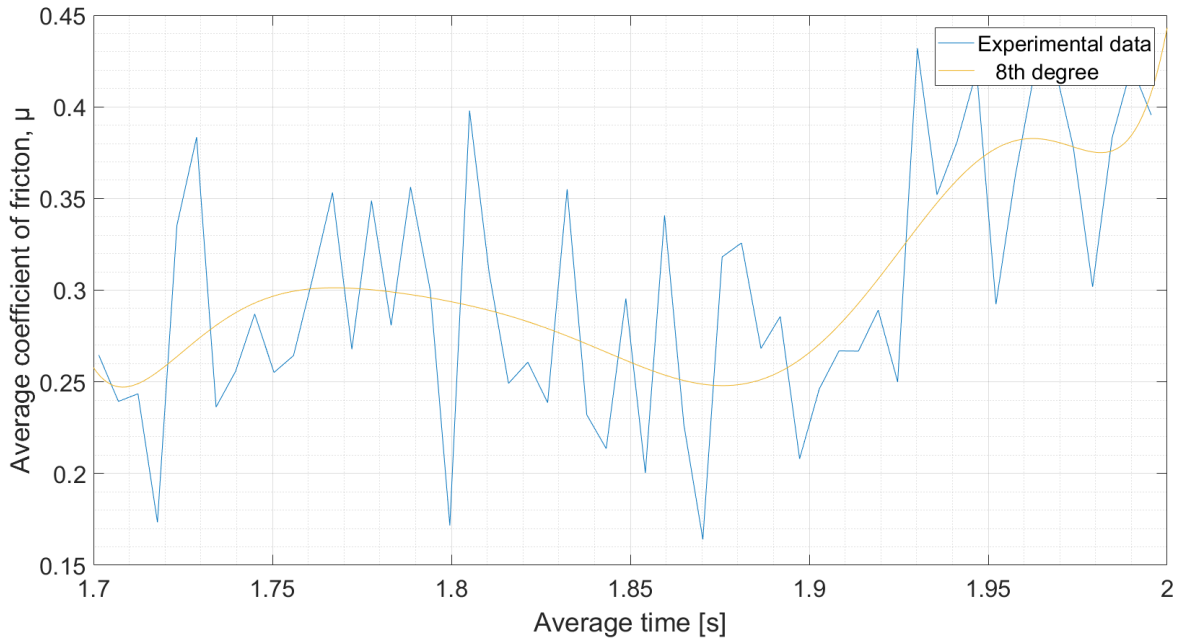

Figure 62: *Average COF for the anodized sample at -2.7 ºC and constant velocity 2 m/s*

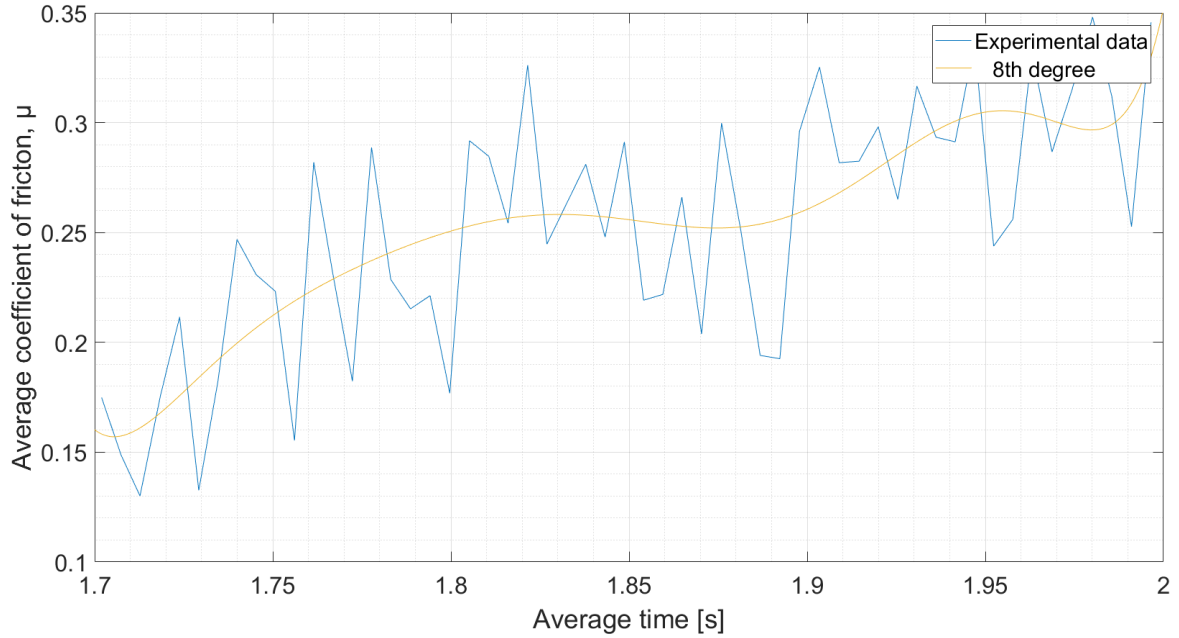

Figure 63: *Average COF for reference sample at -2.7 ºC and constant velocity 2 m/s*

Boxplots utilizing the data from Figure 60-63 is shown in Figure 64. In each box, the central marks indicate the median and the edges at the bottom and top indicate the 25th and 75th percentile respectively. The most extreme data points, not considering the outliers, are represented by the whiskers. The outliers are plotted individually by the '+' symbol [119].

Average and standard deviation values of the average COF of the 25 tests in each set in the interval between 1.7 and 2 s are given for all four sets in Table 6.

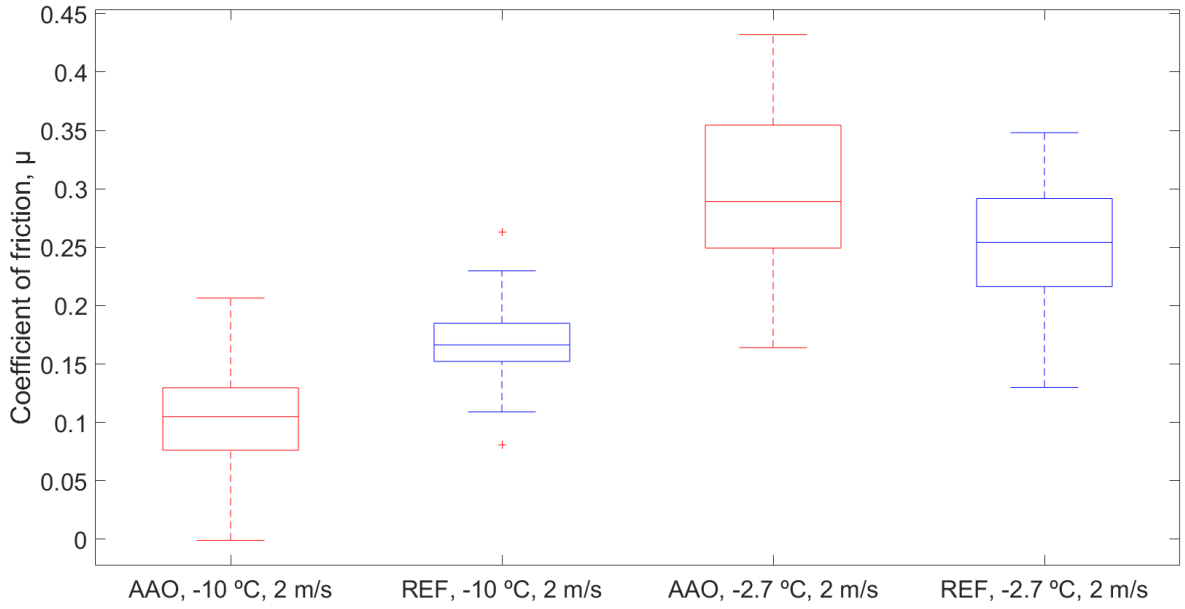

Figure 64: *Boxplot of average COF for all sample sets at 2 m/s between 1.7-2 s*

Table 6: *Average COF and standard deviation of the average of each set between 1.7 and 2 s*

Dataset	Average COF, μ	Standard deviation
AAO, -10 ºC	0.1037	0.0423
REF, -10 ºC	0.1685	0.0300
AAO, -2.7 ºC	0.2999	0.0702
REF, -2.7 ºC	0.2518	0.0558

A two-sample t-test was performed in MATLAB as a statistical analysis of the data from Figure 60-63. The ttest2(x,y,'Vartype','unequal') function returns a test decision for the null hypothesis that the two data vectors x and y are from populations with equal means, but without assuming that the populations also have equal variances [120]. The t-test was testing the similarity of the data set in four different ways: (1) AAO and REF at -10 ºC, (2) AAO and REF at -2.7 ºC, (3) AAO at -10 ºC and at -2.7 ºC, and (4) REF at -10 ºC and at -2.7 ºC. For all t-tests, the null hypothesis was rejected at a 95% confidence interval. Hence, there is a 95% probability that there is a difference between the data sets that were compared pairwise. The code for the statistical analysis, as well as the average values and corresponding standard deviations, is given in Appendix P.

5 Discussion

This section will contain a discussion on each part included in section 4, grouped into the same sub-section arrangement, with the intent of a structured discussion of the different aspects of the work. However, most results are intertwined and some sections will naturally employ results from other sections in their reasoning.

5.1 Hot embossing of UHMWPE

Section 4.1 presents a table with the processing parameters of all hot embossing experiments conducted on UHMWPE, as well as OM images from the surfaces that did not adhere upon embossing. The pressure and temperatures are chosen with inspiration from [45, 107, 108], but as already stated in section 3.1.1, the laboratory press used could not exert a force below 60 kN. As a result, the pressure values used in this work greatly exceeds the ones used in the mentioned papers. A solution to decreasing the pressure could, for example, be to exert the force on a larger area by placing additional specimens, of the same thickness as the total thickness of the surfaces to emboss, in the press. However, as these experiments were only initial tests, it was attempted with high pressure values to start out with.

It is evident from Table 3 that a temperature of 150 ºC on the pressure plate in contact with the emery paper is too high, as it fails to detach from the UHMWPE for the samples UH-P1000-1, UH-P1000-2, and UH-P1000-4. For the remaining surfaces where emery paper was used as master (UH-P1000-3 and UH-P1000-5), it looks like the UHMWPE surfaces do not have considerable changes from the original surface (UHMWPE) at this scale.

Changes are more evident for the surfaces in which the AAO sample was used as the master. In general, it seems like the ridges on the UHMWPE surface have partly been smoothed out. For UH-AAO-1 it looks like the deformation is the greatest; the polymer has melted and then cured with a different surface structure. The reason for more visible deformation for the experiments with the AAO sample compared to the emery paper is probably because of the much higher pressure for these samples as a result of the smaller contact area.

Unfortunately, characterization tools available to investigate the hot embossed surfaces were limited to the OM at this point, which would not detect whether the nanostructure was transferred between the two surfaces. It was attempted to image the surfaces with low-vacuum SEM, which failed as the polymer was not conductive at all. An alternative would be to first sputter coat the samples before imaging them with the SEM. Then the samples would be coated with an extremely thin layer of a conductive material, replicating the surface

features, and enabling the SEM imaging. However, the training for using a sputter coater was not completed at this time. Hence, it was decided to research other aspects of the project until access to the sputter coater was attained. However, later the whole idea of transferring the nanostructures from an AAO sample by a one- or two-step molding process was discarded for reasons discussed in section 3.1. Even though these experiments were not further used in this work, it gave experience with and knowledge about the process and its parameters.

5.2 Anodizing process

It is clear from the SEM images in Figure 56-57 that nanopores have been obtained in the anodization process. However, the pore architecture is somewhat disordered. Nevertheless, this is not unnormal; for example, [4] reports the same result. As mentioned in section 2.6.3.3, the study conducted by [3], which was replicated to perform the anodizing in this work, did not include images of sufficiently high magnification to detect the nanopores (Figure 28A). For this reason, Figure 28B was included for a comparison of the obtained nanostructures from another study. Even though the scale deviates, the SEM images in Figure 56 and Figure 28B have apparent similarities, and it can be concluded that Side 1 has obtained the desired nanostructure by anodization successfully.

The bulky structure that is evident from [3] at lower magnification in Figure 28A was not seen at the same scale for the AAO sample fabricated in this work. However, during the specialization project, it was experimented with the same anodization protocol but with different preparation steps. Then it was observed that preparing the sample with a fine grind would not result in the bulky structure, but a coarser circular milling process would. Figure 65 shows an SEM image of an AAO sample made during the specialization project with a slightly coarser circular milling pattern than the longitudinal milling performed on the anodized sample in this work. This is at the same scale as the study replicated and the similar bulky structure is evident. Hence, it is believed that the bulky structure observed at the low magnification view depends on the surface preparations before anodization. The very fine milling performed in advance of the anodization on the miniature ski prototype was not favorable to the bulky structure. However, the nanopores are obtained.

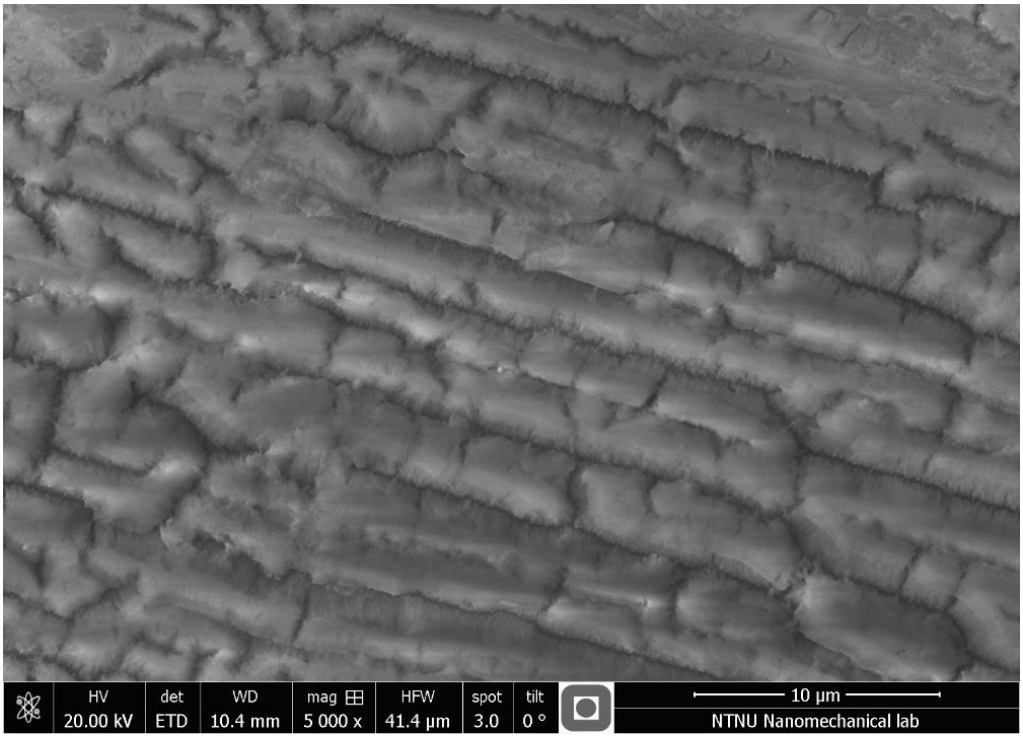

Figure 65: *Anodization sample from the specialization project*

Even though Side 1 is considered as successful, Side 2 needs further analysis. As can be seen from Figure 57, Side 2 also contains nanopores, but the surface looks less uniform which was the same observation made by visual inspection as mentioned in section 4.2. Defects associated with anodic finishes can be differentiated either as specific types as in terms of their appearance or by the processes they originate from. Some defects can originate in the substrate material even before the anodization takes place; from the thermic or mechanical fabrication processes used to produce the metal sheet, during handling, or storage. The most common defects resulting from the anodization process itself may be categorized into pitting, streaking, and non-uniform appearance. Defects can also result from contamination or lack of control of the solutions used in the various anodization stages [121]. A defect called "white etch bloom" (Figure 66A), categorized as a non-uniform appearance defect, seems to fit the appearance of Side 2 relatively well. An attempt to image the Side 2 of anodized miniature ski prototype is shown in Figure 66B. The defects were most visible right after the anodization process as some of the irregularities seemed to partly wear off by rubbing it with a cotton pad and in the friction tests. Unfortunately, this was not documented, and the image below was captured after all tests. [121] claims that the "white etch bloom" is due to incomplete degreasing before anodization. However, it is believed that the cleaning steps – ultrasonic acetone bath, rinsing with distilled water, and spraying with ethanol – should have been sufficient.

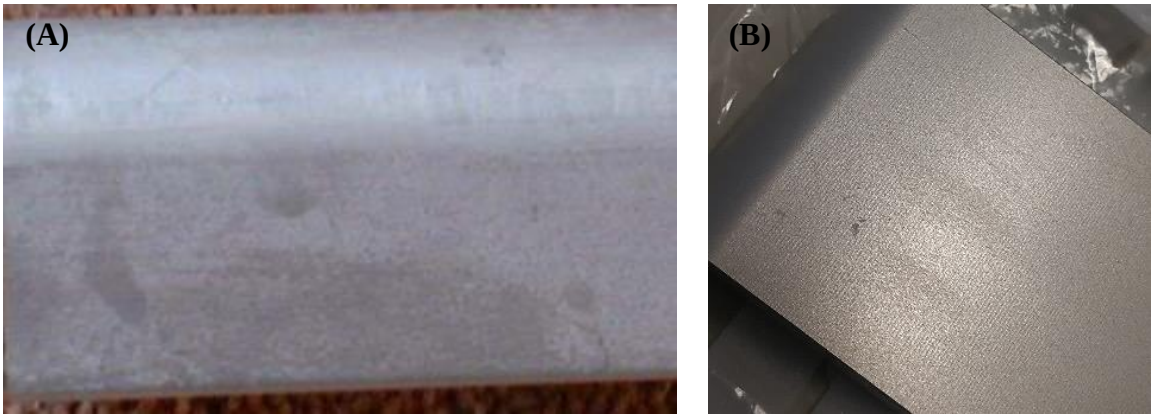

Figure 66: *(A) Example of "white etch bloom" [121]. (B) Defects on Side 2 of anodized sample*

The observed temperature differences in the electrolyte at the completion of anodizing, as mentioned in section 4.2, is another interesting aspect that may be relevant for the defects found on Side 2. Significant heat is produced during anodizing, in which the three main sources are exothermic heat (chemical reaction releasing heat) from the oxide growth, Joule heating (passage of electrical current through a conductor producing heat) of electrolyte, and Joule heating of the aluminum covered with oxide due to high oxide resistance [122]. As this experiment was conducted with a relatively large sample compared to electrolyte volume, there is reason to believe that there was quite a considerable heat generation.

The uniformity of the film thickness of an AAO surface is related to the local electrode temperature distribution, which in turn depends on the heat transfer convection. [122] reports the correlation between a high local temperature and a thick local oxide thickness. This confirms the observation of Side 2 compared to Side 1; as mentioned Side 2 was the upper half of the sample and in which a higher temperature than Side 1 was measured after anodization. The reason for higher electrolyte temperature at the top is believed to simply be because a hot liquid has a lower density than cold and will naturally "float" on top of the cold. According to [122], an increased local temperature will enhance local field assisted oxide dissolution at the pores, which will consequently increase the local current density. Further, high current densities and/or high electrolyte temperatures can result in poor uniformity of the anodic film, meaning a varying oxide thickness over the aluminum surface. Reasons for this behavior can be due to the hydrodynamic flow pattern of the electrolyte during anodization [122]. The referenced study also reveals that for DC-anodizing in sulfuric acid, which is one of the constituents of the electrolyte in this work as well, the AAO thickness is not uniform for certain anodizing conditions, such as high current densities.

The description above seems to fit relatively well with observations made in the experiment. [123] considered effects of stirring the electrolyte during anodizing with oxalic acid, which is

another of the constituents of the electrolyte in this work. It was further found that for higher stirring speeds, a larger amount of heat from the barrier layer can be dissipated to the bulk electrolyte. This will further decrease the extent of the likely temperature rise at the pore bases, which again will give less serious field-assisted dissolution of the barrier layer. Something to consider is that the border between Side 1 and Side 2 initially appeared to be quite distinct; it seems peculiar that the threshold temperature giving a less uniform surface would be so clearly defined for such, presumably, small temperature differences.

It is now evident that there are a few different potential reasons for a different surface appearance of the anodized sample. However, it cannot be given a certain statement of which reason is the correct. There might be a combination of reasons, and additional arguments that have not been considered here may be of importance. As the CAs of the two different sides was very similar (Table 5) it was decided to continue with the anodized sample despite some defects, as time and availability of equipment were limited.

The appearance of the cathode also changed during anodizing. It is evident from Figure 49B that a line shows how far the electrolyte reached. The color change below the line is probably due to a layer of dissolved aluminum from the sample.

5.3 OP data from ski prototypes

When analyzing a surface with the OP, as many other instruments, information is gathered from a very small portion of the surface. Hence, the specific spot analyzed may not be representative for the entire surface. To know all about the sample, the entire surface would have to be analyzed, spot by spot. However, this would be extremely time consuming, and consequently, a compromise is carried out by analyzing a certain number of spots. As mentioned in section 4.3, 2-6 spots were used for each surface in this work, in which Side 1 and Side 2 of the anodized sample are regarded as different surfaces. The reason for a varying number of spots was a result of considering the degree of uniformity and the size of the area for the different surfaces. The following six paragraphs will each discuss the OP results before and after the friction tests for each of the three different surfaces.

It is evident from Table 4 that the two measurements of Side 1 before friction tests holds comparable values for *Sa*, *Sq*, *Ssk*, and *Sv*. This means that the average vertical deviations from the mean line and the depth of the largest valley are almost the same. However, the height distribution at spot 1 is slightly biased below the mean plane, while it is slightly biased above the mean plane for spot 2. Additionally, the highest peak and the slightly deepest valley is found at spot 1, which supports the even more spiked distribution at this spot than at

spot 2. From Figure 50-51, it is evident that the peaks and valleys at spot 1 are not completely uniformly distributed as areas with peaks only and valleys only can be seen.

Further looking at Side 2 before friction tests, it can be observed that also here the *Sa* values are relatively constant within the three spots, however much larger than for Side 1. In fact, for all surface parameters of Side 2 before friction tests, the values do not deviate much between the three spots. Hence, it is more likely that these results are representative for Side 2 than the two measurements are for Side 1, as they were differing slightly more from each other. This is also evident in Figure 52-53; Side 2 does not have the same division of areas with peaks only and valleys only. Nevertheless, Side 1 and Side 2 have a completely different height profiles, which supports the observations discussed in section 5.2. Side 2 has both deeper valleys and higher peaks than Side 1.

The reference sample also seems to have a relatively uniform surface height profile before friction tests. The longitudinal marks, which can be seen clearly in Figure 55, are probably from the milling process, counting 7 lines within the 0.18 mm wide image. However, the height of the ridges of the milling marks is varying along the length. According to Table 4, the *Sa* values are varying somewhat more than for the anodized sample, but remaining surface parameters are relatively constant for the four measured spots. Compared to the anodized sample, the reference sample has a surface with a height distribution biased slightly above the mean line in terms of skewness. Additionally, in terms of kurtosis, the distribution produces few outliers from the normal distribution than the AAO samples does. In general, the peaks are smaller than for the anodized sample and the valleys shallower.

Further investigating the samples after friction tests, the surface parameters for Side 1 are relatively unchanged. One difference is still evident; *Sku* is still positive but holds much lower values. This means that the sharpness of the profile is decreased. This can either mean that the measurements after friction tests happen to be at different spots with slightly different characteristics. Or it can mean that the height distribution holds fewer outliers after the friction tests due to changes on the surface. It is believed to be more likely that a potential change of the surface is due to insufficient cleaning of the sample resulting in PTFE remainings, than that the AAO surface has been abraded during friction tests.

Interesting measurements are evident in Table 4 for Side 2 after the friction tests. The six spots measured seems to group into two; spot 1, 4 and 5 have relatively similar values for *Sa*, *Sq*, and *Sv*, which deviates from spot 2, 3 and 6. The three formers seem to resemble Side 1, both before and after friction tests, while the three latter seem to resemble Side 2 before friction tests. Hence, it is evident that Side 2 has partly changed upon friction tests. This was also seen with a visual inspection; the non-uniform areas were less visual after the friction tests, which explains why these features are not very distinct in Figure 66B. Hence, there is reason to believe that some of the areas with the highest peaks of the AAO on Side 2 was

worn away during the friction tests, resulting in a more uniform surface roughness across the entire AAO sample. It is less likely that the observations are due to remainings of PTFE, which was stated for Side 1, as one can easily see that the two sides are less different after the friction tests than they were before. Unfortunately, it was not possible to confirm this observation by SEM images after friction tests due to limited availability of the instrument.

Lastly, the reference sample does not seem to have changed significantly from the friction tests. It is therefore believed that no considerable amount of PTFE remained on the surface or that the aluminum was abraded from the friction tests.

5.4 SEM images of ski prototypes

As have already been stated, Figure 56-57 reveal that the desired nanopores are attained through the anodization process. As stated in section 4.5, the pore diameter of Side 1 is measured to be between 20-33 nm and the interpore distance between 35-62 nm. Hence, the pore dimensions are quite varying. However, it should be considered that the measurement tool in ImageJ is based on human definition of the pore features, which is not eminently accurate. Nevertheless, [124] reports that differences in pore dimensions can be explained by the uneven distribution of current density and temperature surrounding the sample during anodizing, in which phenomena were discussed in section 5.2.

As can be seen in Figure 57, the features of the nanopores on Side 2 are less distinct. Additionally, the pores seem to both be smaller in diameter and more numerous than at Side 1. As already stated in section 4.5, the reason for poor image quality of Side 2 from the SEM was because the electron beam was charging on the surface. This occurs if a surface is not conductive enough to lead the electrons away, which may result in noise (section 2.7.3). The reason for charge-up, in this case, was probably that the oxide layer, which is a non-conductive material, was thicker or more covering at the exact spot of imaging on Side 2 than on Side 1. To investigate the latter, Side 2 was imaged at several spots, but the image quality remained poor. These findings confirm the observations made by the naked eye right after the anodization, which was discussed in section 5.2.

For comparison, two SEM images of the reference sample were included. Figure 58 shows the reference surface at low magnification. The lines from milling can be seen vertically, counting approximately 4 lines above the 100 µm scale bar. Hence, the milling cutter removed 25 µm of material for each cut longitudinally. This confirms the findings from the OP in section 5.3; 7 lines were counted on the width of 180 µm, which gives an individual width of 25.7 µm. The oblique lines are scratches that might originate from uncareful handling while machining or storing. The black area across the middle of the sample may be

a result of either of the same reasons or from processes during the manufacturing of the aluminum plate.

Figure 59 shows the reference surface at the same scale as the anodized in Figure 56-57 to enable direct comparison. It is evident that both Side 1 and Side 2 have changed drastically in the anodization process, as the reference surface does not contain the regular nanopores. However, the reference surface also contains dents and lines at the nano-scale. There is no clear pattern to these features, and their origins are probably a combination of material properties, processing, and storage.

5.5 Aspect ratio estimation for ski prototypes

As already briefly discussed in section 5.4, the pore diameters at the anodized sample were quite varying. Additionally, a simplification of pore depth was set to $2\times Sa$, which is the double of the average absolute distance between peaks and valleys, and the mean line of the surface. Hence, the AR found for Side 1 of the anodized sample is a rough estimation but considered sufficiently accurate for the scope of this work.

The paper in which anodization process was replicated reports neither a measured AR nor a surface height profile, and hence no conclusion can be stated on whether similar pore depths were attained in this work. However, other studies have reporter their AR where AAO was fabricated with the aim of creating hydrophobic surfaces. [4] fabricated AAO surfaces with pore diameters between 140-190 nm and with an AR around 50. Hence, this is somewhat larger than the [25.2, 44.1] that was calculated in 4.5. [125] reports a remarkable AR of nanopillars attained from anodizing to be 1000, where the pillar diameter is 40 nm. This is obviously much higher than what was obtained in this work.

5.6 CA measurements for ski prototypes

The CA measurements conducted for the three cases; (i) clean samples before friction tests, (ii) clean samples after some friction tests, and (iii) unclean samples after all friction tests, will be discussed one by one in the next three paragraphs.

It is evident from Table 5 that the CA of both anodized and reference sample increased when PTFE coating was applied to the clean samples before the friction tests. It was initially contemplated if the PTFE coating would fill the nanopores and the high CA would be a result of the PTFE only and not the nanostructure. However, this is not considered a problem as the

AAO sample, both Side 1 and 2, holds lower CA values without PTFE coating than the reference sample, but much higher CA than the reference sample after PTFE coated. The study in which replication of anodization process was used attained their highest CA of 162º after coating the surface with PP. In this work, the average CAs of the anodized, clean sample before friction tests were measured to be 128.17 º and 132.10 º for Side 1 and 2 respectively. This is not only much higher than for the coated reference sample, but also much higher than the coated smooth glass slide. Hence, the anodized sample is considered to successfully attain a hydrophobic surface both chemically and structurally. As the CA does not deviate particularly much between Side 1 and Side 2, the non-uniform surface at Side 2 is acceptable for further testing in the snow lab.

It is evident that the CA of the anodized sample, both Side 1 and 2, after some friction tests, subsequent cleaning, and new PTFE coating, is almost unchanged. From this, it can be concluded that the friction tests probably did not change the AAO structure. It was discussed in section 5.3 that some of the oxide layer was believed to have worn off Side 2 during friction testing. However, this does not seem to have affected the CA. Due to high aspect ratios, it is believed that the nanopores remained even though a part of the oxide disappeared. Similar measurements were not conducted on the reference sample, but there is no reason to believe the result would have been changed for this sample either.

The last set of tests were conducted on both anodized-and reference sample after all friction tests were completed. Notice that the samples were not cleaned upon CA measurements this time. Two examples of how the surface of a sample could look like after a set of friction tests are shown in Figure 67; here the white areas are PTFE that has been partially worn off. From Table 5, neither Side 1 nor 2 have high CAs for this case, and also the reference sample have slightly lower CA than without coating before any friction tests. It should also be noted that Side 2 on the AAO sample for this set of CA measurement has the highest standard deviation of all measurements. In general, the low CAs are probably because of the uneven remainings of PTFE remainings at surfaces, and the fact that the CA measurements were partly conducted on spots in which PTFE was still present and partly at spots where it was worn off.

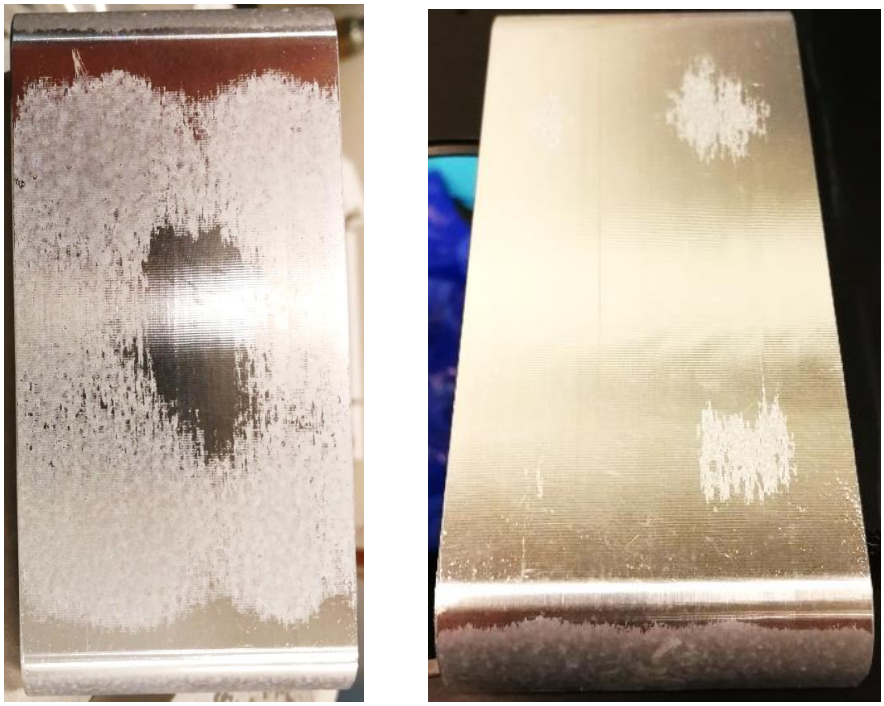

Figure 67: *Two examples of a sample after one set of friction tests. White areas are PTFE*

5.7 Friction tests for ski prototypes

It is evident from the boxplot in Figure 64 that the AAO sample was found to have a lower COF than the reference sample at -10 ºC. However, the COF increased for both samples at -2.7 ºC, in which the anodized sample was found to hold the highest COF. From Table 6 it can also be seen that the standard deviation of measured COFs is highest for the AAO sample at -2.7 ºC. It was further conducted a statistical analysis in which the null hypothesis was rejected in all four t-tests. This is desirable in science as it shows with a certain probability, here 95%, that there is a difference between that data sets compared. Even though the null hypothesis is rejected as desired, this is no proof of correct results. The differences between the two samples make the baseline for several discussion points concerning accuracy, repeatability, potential errors, and uncertainty of test apparatus and relevant parameters, which will be discussed in the following.

To start out, the results of a previous study, which is the only found that is also investigating the correlation between surface roughness at the nano-scale, hydrophobicity, and ice friction can be compared to the results of this work. This study was presented in section 2.6.2 and Figure 25, where [16] nanostructured steel sliders by femtosecond laser irradiation. Experiments were performed over a wide range of temperatures and sliding velocities. However, this study did not specify the application for skiing, and the experimental apparatus consisted of a rotating disc instead of a linear track, which may induce errors as presented for

rotational experimental devices in section 2.5.4. They report the CA of a polished reference sample to be 84º and the irradiated sample to 128º, which are both relatively similar to the values measured in this work (Table 5). Both sliders from this study show a decreasing COF with increasing velocity. However, since the tests in this work have only been conducted at 2 m/s, a similar velocity dependence cannot be stated. Nevertheless, COFs can partly be compared, but different velocities, materials and test apparatus must be taken into account. A few examples of results from the study are as follows; at a snow temperature of -7 ºC and 1.1 m/s the polished sample measured a COF of 0.055, while the irradiated 0.060. For -1.5 ºC and 1.1 m/s the polished sample measured a COF of 0.130, while the irradiated 0.055. Hence, they demonstrated that a hydrophobic slider significantly decreases ice friction at ice temperatures close to the melting point. This is the opposite results of what was found in this work, where the nanostructured surface held a higher COF than the reference sample in warmer conditions. The study argues that the decrease in friction is mainly due to suppression of capillary bridges despite the presence of surface asperities that facilitate their formation.

Another study already mentioned is [72], which was briefly presented in section 2.5.4 and friction test rig shown in Figure 21, which is similar to the one used in this work. This study does not have entirely comparable results as their samples are not reported in terms of hydrophobically structured sliders. However, it can be summarized that their friction tests also show that the rough surfaces had especially lower COF than smooth surfaces close to the melting point.

In section 2.2.1 and 2.3.4, it was discussed how there is an optimal water film thickness between the ski-and snow base. This is at the perfect balance point where, the film is thick enough to reduce considerable solid deformation of adjacent asperities, and plowing, but thin enough to limit the capillary water bridges. The main idea behind introducing roughness on the sliders at the nano-scale was further presented in section 2.4.2; roughness reduces the contact area between the snow-and ski base, which further decreases the number of asperities. This, in turn, is believed to reduce friction as there would be less shear between adjacent asperities and limited capillary water bridges. Several studies have shown that the optimal water film appears close to the melting point of ice [2, 16, 72], but that the film thickness is also greatly affected by parameters such as thermal conductivity, ski color, hardness, pressure distribution, and humidity (section 2.2.1). The idea in this work was to keep all these parameters constant, except for temperature and slider surfaces, to detect a difference in how surfaces with different roughness at the nano-scale interact with the water film. As already stated, the results in this work show that the hydrophobic surface structure held a higher COF than the only slightly hydrophobic reference sample in the test sets in which the temperature was closest to the melting point. The following paragraphs will discuss different potential errors that can be the baseline for the unexpected results.

Firstly, it can be seen from Figure 60-63 that the logged COF values are greatly varying along this portion of the track, even though the velocity is constant. One reason for this is probably that the track was not completely uniform but contained bumps and valleys. The number of bumps seemed to increase as more sliders ran over the track. This is reflected in the increasing trend for the standard deviations in Table 6, as the test sets at -10 ºC were conducted first. Additionally, it seems like the standard deviations are higher for the tests with the anodized sample than their corresponding reference tests. Nevertheless, the measurements were chosen to both be at an area in which constant velocity was attained, and in which the track was as bump-free as possible to minimize the noise from the non-uniform track bed. One measure that could have been done to potentially keep the track more uniform would have been to apply freshly produced snow for each test set. [72] did this to ensure that snow grains always had the same size and shape. However, due to limited time allocated to the project in the snow lab, this could not be conducted, as it would require several compression processes between each set, which would also introduce new changes to the snow condition. Additionally, the varying values may be a result of noise elements in other parts of the system. Examples are vibrations in the tensioned belt or slender connection between sled and aluminum arm. Inaccuracies can also occur in the load cell measuring the brake force. In general, there is a somewhat poor control over the brake force.

In addition to varying quite a lot in the interval 1.7-2 s, it is evident from the logged data that the initial measurements are quite variable from test to test. For some tests, the brake force is relatively steady in the first few data points. However, for others, it may jump greatly between values from one point to another. These two scenarios are exemplified in Table 7, taken from actual measurements of two sets. The initial brake force measurements to the left are greatly varying, while the ones to the right are relatively steady. As these first five logged brake force values were used to define a zero point - the average was subtracted from all brake force values - this may be an important potential error.

Table 7: *Two examples brake force variations for initial five measurements*

Position [mm]	**Time [s]**	**Brake force [N]**	**Position [mm]**	**Time [s]**	**Brake force [N]**
3000	0	32.8088	3000	0	57.1108
3000	0.005414	86.6043	3000	0.005578	56.403
3000	0.010598	45.0683	3000	0.010798	57.2643
3000	0.015782	41.9533	3000	0.016167	57.5982
3000	0.020986	90.0631	3000	0.021582	57.1408

It can also be argued that the testing distance is not sufficient. Even though the entire track is 8.8 m, the tests were only conducted at a length of 3.7 m, and the average COF was only measured at an interval of 0.3 seconds. With a velocity of 2 m/s, this corresponds to a testing distance of 0.6 m.

Temperature is another important parameter to discuss. It has already been stated that the experiments were conducted at air temperatures of -10 ºC and -2.7 ºC. For the experiments conducted at -10 ºC the snow lab had been at this temperature for around two weeks before the actual tests were conducted. However, for the experiments at -2.7 ºC, the snow lab was set to this temperature only half a day in advance. Therefore, the snow temperature was additionally measured and shown to be -4.6 ºC at the snow surface for these tests. The snow temperature was unfortunately not measured for the experiments conducted at -10 ºC, but since this air temperature had been constant for such a long time, it is assumed that the snow temperature was approximately -10 ºC as well. Another temperature aspect is the impact of the heat generation of one test on the next. Each of the around 35 tests in all four sets was run with only a few seconds in between. Hence, there may be a temperature rise at the snow track from one test that was changing the results of the next test. A literature search was conducted on models for snow temperature increase caused by sliders but without success. Hence, no clear conclusion can be stated on whether the snow cooled down sufficiently in between each test or steadily rose throughout the set.

It is evident from both Figure 67 and the difference in CA values in Table 5 between a newly coated surface and a surface not cleaned after friction tests, that the PTFE was partially worn off at some point during the friction tests. However, it is unknown when this happened; it could have been during the very first test or it could have been happening throughout the test set. Additionally, how much of the PTFE wore off. There is a chance the wear occurred at the first five tests, which are discarded from all sets, as described in section 3.4.1. To investigate this, MATLAB was used to plot the average COF of the first five tests (after the first five that were discarded) and the last five tests within each set. The two plots were included in the same figure for comparison. The average COFs were both plotted both along the entire track and for the interval 1.7-2 s, in which the latter is seen in Figure 68-71. The former plots are given in Appendix R, and the associated MATLAB code is found in Appendix Q. From now on, the first five tests will refer to the first five tests in a set after the first discarded. If referring to the five the discarded, this will be specified.

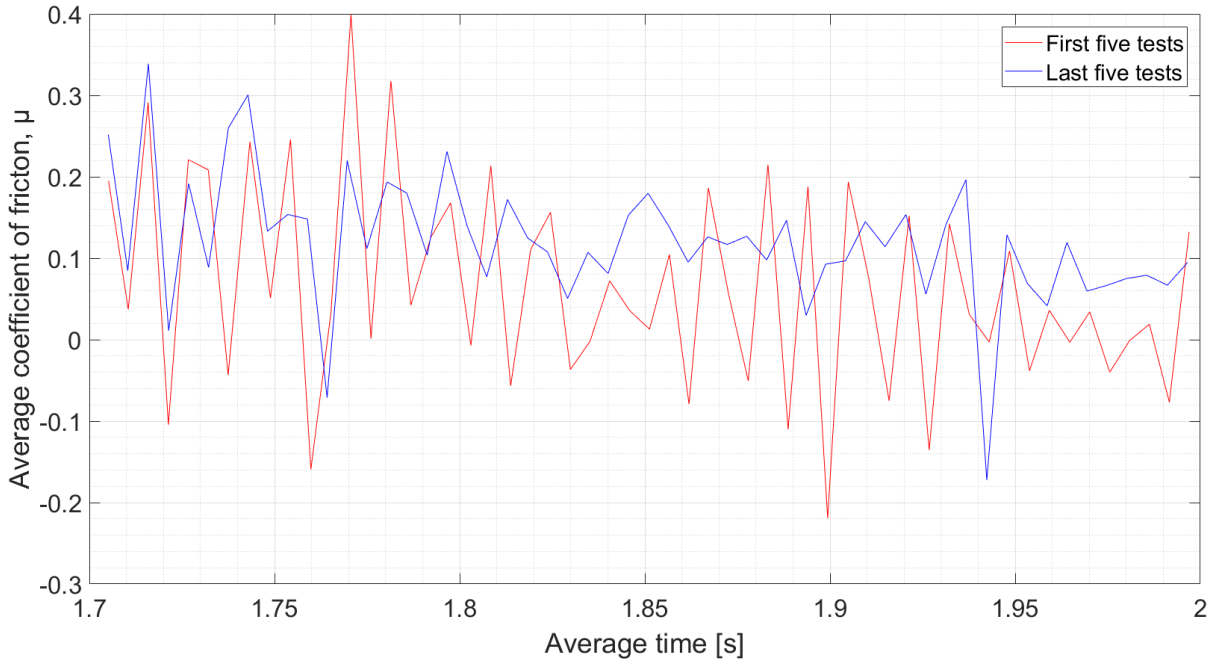

Figure 68: *Average of the COFs of first-and-last five tests for AAO at -10 ºC between 1.7-2 s*

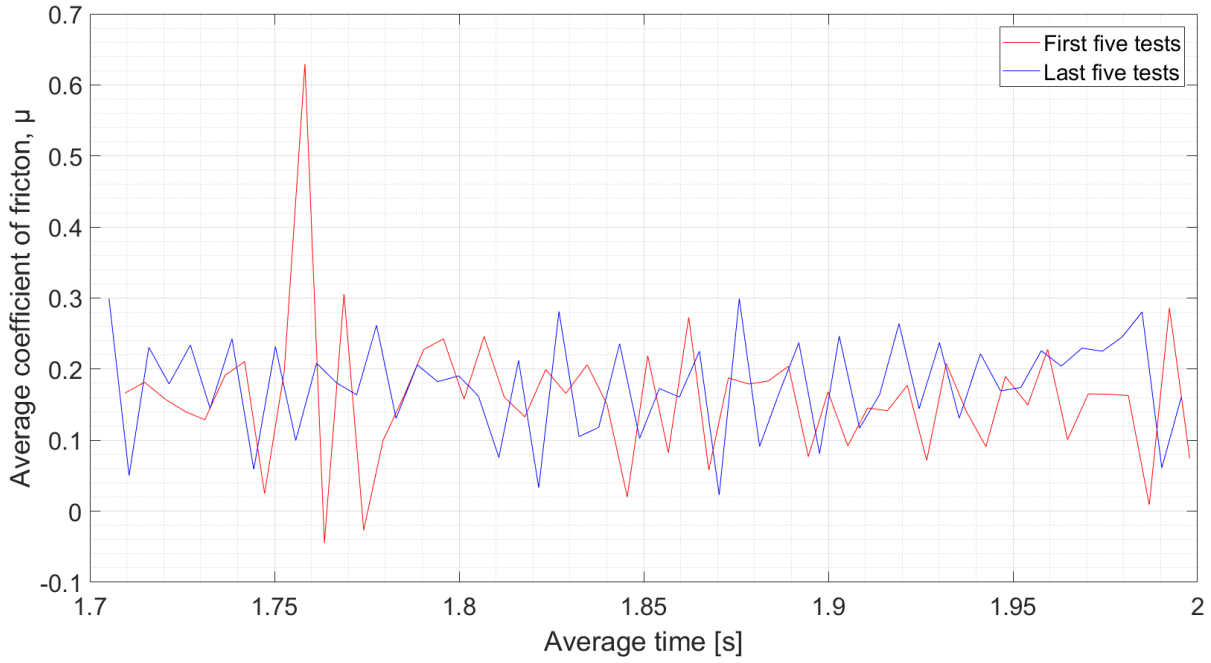

Figure 69: *Average COFs of first-and-last five tests for REF at -10 ºC between 1.7-2 s*

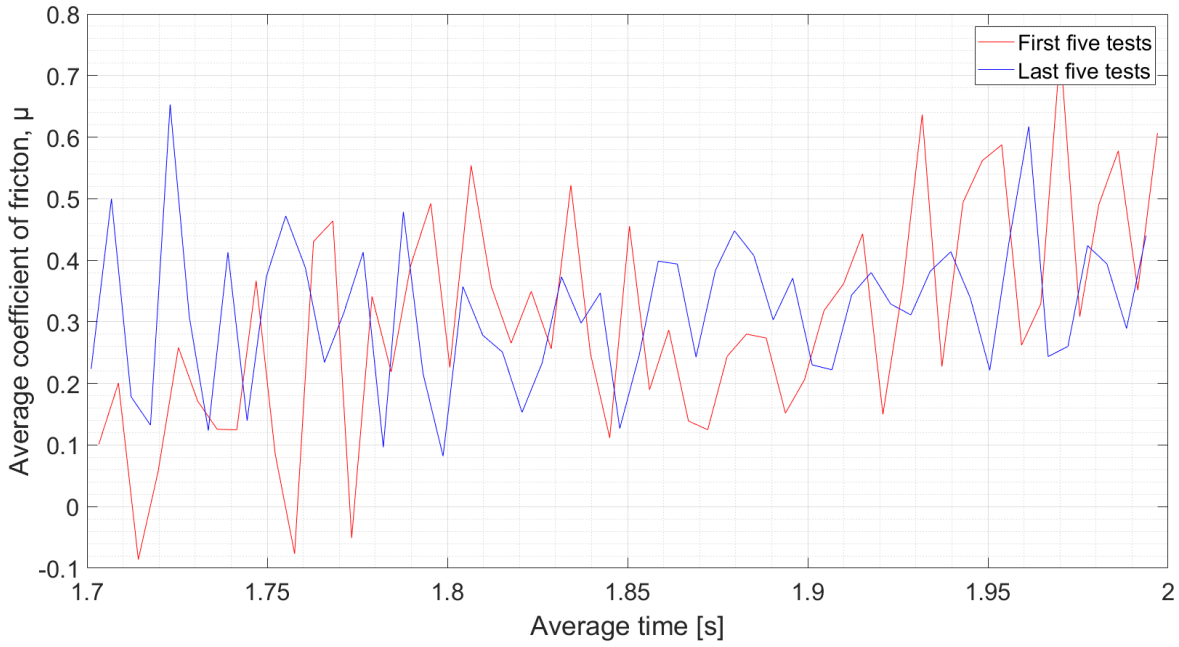

Figure 70: *Average COFs of first-and-last five tests for AAO at -2.7 ºC between 1.7-2 s*

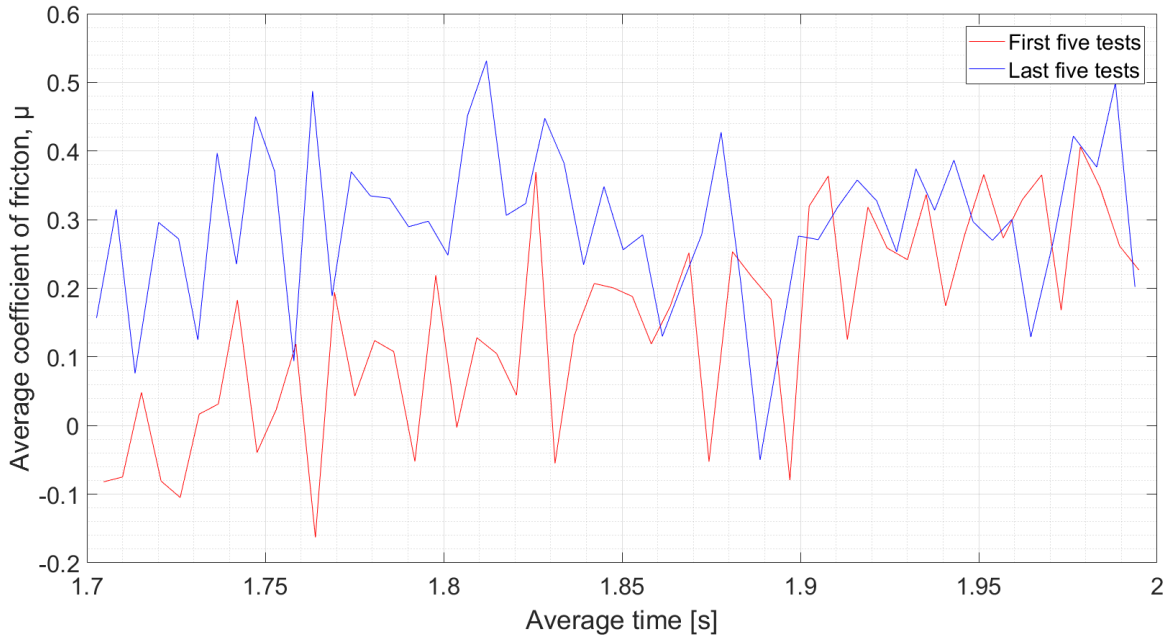

Figure 71: *Average COFs of first-and-last five tests for REF at -2.7 ºC between 1.7-2 s*

It can be observed from Figure 68-71 that the red lines, representing the last five tests, generally hold greater values than the blue lines, representing the first five tests. Table 8 shows the single average COF value and corresponding standard deviation of the data in these figures. In each set, the first five tests have a lower average COF than the corresponding

last five tests. Wear of PTFE is assumed to be the main explanation for this observation. In that case, the PTFE must have worn off throughout the sets and not only during the first five discarded tests. It should also be noted from Figure 67 that the PTFE is worn off differently on the surfaces in different test sets. The simulation of the pressure distribution in Figure 47 does not seem to have been realized for all sample sets, if assuming the wear of PTFE indicates the areas with the highest pressure. The asymmetric wear of PTFE is believed to either be due to an uneven coating layer or due to a point of loading slightly off center. However, these factors are assumed relatively small as measures were done to avoid these issues in advance.

It should also be noted that the standard deviation is extremely high for all sets. A two-sample t-test was conducted between the average of the first five and the last five COF values between 1.7-2 s for each set. This concluded with a rejection of the null hypothesis for the AAO sample at -10 ºC and for the REF sample at -2.7 ºC. As was discussed in section 5.6, the anodized sample was only outperforming the reference sample in terms of hydrophobicity when coated with PTFE. From these findings it can be stated that the PTFE coating should have been of a much more wear resistant type as the validity of the study is now highly depending on when the coating wore off rather than on concluding on the effect of the nanostructure itself.

Table 8: *Average COF and corresponding standard deviation of the average of first-and-last five tests within each set between 1.7-2 s*

Dataset	Start or end	Average COF, μ	Standard deviation
AAO, -10 ºC	First five tests	0.0657	0.1285
	Last five sets	0.1205	0.0811
REF, -10 ºC	First five tests	0.1604	0.0980
	Last five sets	0.1774	0.0703
AAO, -2.7 ºC	First five tests	0.3030	0.1830
	Last five sets	0.3205	0.1219
REF, -2.7 ºC	First five tests	0.1491	0.1487
	Last five sets	0.2935	0.1148

It was shown in Table 5 that the CA for an uncoated anodized sample was lower than for an uncoated reference sample. Hence, it is evident that the wear of PTFE on the anodized sample would be more detrimental for its hydrophobic properties than the wear of PTFE on the reference sample would. However, this is for a static CA measurement. Different mechanisms occur when the surface is sliding on ice. One hypothesis is that the water film penetrated the nanostructures of the anodized sample increasingly when the PTFE wore off;

instead of entrapping air in the nanopores, water entered them which contributed to the increased friction. Another hypothesis is that the edges of the nanopores acted as obstacles for the meltwater. However, this theory alone does not explain why the COF is increasing for both samples, but most for the anodized, at increased temperature in the friction lab. One possible explanation is that the PTFE wore off more easily at the slightly increased temperature of the tests conducted at -2.7 ºC compared to the ones at -10 ºC. Further, this wear was more critical for the anodized sample than the reference sample.

Additionally, it has already been stated that thermal conductivity of the slider is a major parameter. The thermal conductivity is 210 W/m-K for aluminum, while 25 W/m-K for aluminum oxide [126], which is a considerable difference. However, it was also stated that it is preferable with a low thermal conductivity, favoring aluminum oxide. Nevertheless, this depends on the thickness of the meltwater; if there is too much meltwater between snow-and ski base it would rather be preferable with a ski base leading away the heat to decrease the water film thickness. Hence, one possibility is that at -2.7 ºC there is too much meltwater, in which thickness is reduced to a more optimal condition for the reference sample made of a thermally conductive material. However, this is not a highly likely theory, as the snow temperature is not more than -4.6 ºC, which should not produce an excessive amount of meltwater.

Other factors are the scratches and grooves from processing and handling of the samples, which [46, 47] is emphasizing the impact of on friction. These seemingly randomly oriented and located marks are evident on both the anodized-and the reference sample, in which for the latter was described in section 5.4. It would be challenging to quantify the effect of these scratches, and hence their potential effect is only highlighted without further discussion.

The theories above attempting to explain the results are all assuming the results attained are correct. There could be other factors that are giving incorrect or inaccurate results. For example, uneven coating or changes on the snow track, which are continuously evolving, may be relevant factors.

6 Conclusions

This report has investigated, both theoretically and experimentally, the effect of a nanostructured hydrophobic ski base surface in the aim of friction minimization. It can be stated that all objectives given in section 1.3 have been accomplished. Firstly, a miniature ski prototype has been defined; an anodized sample with hydrophobic properties was fabricated. The prototype mimicked the shape of a full-scale ski in terms of width and curvature on front edge, but with a smaller contact area and without the flex nor the grip zone. Secondly, the weight of a skier on a full-scale pair of skis was scaled down to the contact area of the miniature ski prototype. Furthermore, experiments were designed in terms of setup and snow track preparations to carry out tests in a snow lab where the coefficient of friction was measured. Additionally, characterization instruments were utilized ahead and following the friction tests. Lastly, in addition to the anodized miniature ski prototype, a reference sample with identical dimensions, but with a different contact surface, was fabricated. As the reference sample did not show the highly hydrophobic properties as the anodized sample did, measurements of varying hydrophobic samples were performed and compared. The bonus of providing videos showing performance difference between a real ski and a miniature ski prototype was not carried out. As the friction measurements were all conducted with the same constant velocity, little difference would be evident in such a video. However, individual videos of a XC ski and of a miniature ski prototype sliding on the snow track in LARS are enclosed with the thesis on DAIM.

A few different methods were tested to attain nanostructured hydrophobic surfaces. Hot embossing, in which nanostructures were transferred from a master template to a UHMWPE ski base, was attempted but not proceeded with due to limited time and equipment available to enable sufficiently successful results. However, it is believed that this method has great potential for nanostructured, hydrophobic ski surfaces if investigated more thoroughly. Anodizing of aluminum consequently became the main nanostructuring method in this work, and a miniature ski prototype was successfully anodized. However, the upper and lower part of the sample, referring to the sample's positioning while immersed in the electrolyte, attained a slightly different appearance. This is most likely due to an uneven heat distribution in the electrolyte as a slightly warmer regime was observed in the upper part of the electrolyte after completing the process. It is described in the literature that a high local temperature can result in a less uniform AAO surface, which can explain that this part had attained a less uniform nanoporous structure. A larger electrolyte volume, in addition to constant stirring, could be a way to work around the problem, but due to limited availability of equipment, this could not be performed in this work.

By comparing OP images from before and after friction tests, it was evident that the nonuniform side of the anodized sample became more uniform in some areas during the

friction tests. It is believed that this is due to wear of areas with extra oxide when sliding on the snow track. The results from the friction tests state that the anodized sample holds lowest COF for the air temperature of -10 °C, but the reference sample has lowest values for -2.7 °C. These temperatures are believed to correspond to snow temperatures of -10 °C and -4.6 °C. These results are deviating from the predicted results, which stated that a high contact angle would yield a low coefficient of friction. However, there are numerous potential errors that may contribute to incorrect or inaccurate results. For example, nonuniformity of ski track and a somewhat poor control of brake force measurement is believed to be important factors.

The major contribution to the unexpected results is believed to be due to the PTFE coating before friction tests for all test sets. It was evident that the coating wore off to some degree throughout the friction tests. It was also shown that the CA of the anodized sample was lower than the reference sample without coating but much higher with the coating. Consequently, the wear of PTFE is considered more critical for the anodized sample than the reference sample for the resulting COF, if assuming a hydrophobic surface is an advantage for minimization of ski friction. It is believed that water may penetrate the uncoated nanopores, or that the edges of the uncoated nanostructures act as obstacles for the meltwater. Consequently, the findings show that the validity of the study is highly depending on the wear of the PTFE coating, and conclusions cannot be stated on the effect of the nanostructures itself. It is desirable to conduct similar tests in which the PTFE is of a more durable type, and to perform tests across a larger set of velocities, temperatures, and snow characteristics. It is also beneficial with increased control of snow base temperature and brake force. Due to limited time and availability of equipment, this was not feasible within the scope of this work.

7 Further work

This section is devoted to suggested future improvements of setups and methods used in this work, as well as ideas for next steps. As a Master's thesis is a limited portion of work, not all questions can be answered. However, potential errors, correlations, and additional questions may be identified. Hopefully, this section can be a supplementary help to get started for students potentially continuing this project.

Hot embossing was presented as a method that was attempted but discarded. However, it is believed that the method has great potential in transferring a master surface to the final surface. As mentioned, due to limited availability of equipment, the hot embossed UHMWPE samples were never sputter coated and subsequently imaged with the SEM. Hence, it is still unknown whether the nanostructures were transferred or not. If equipment is available, this could be a step to start out with; either analyzing the samples fabricated in this work, which will be stored at the department, or creating new ones. Even though the nanostructure of these samples can be investigated, it is believed that the hot embossing process used was not able to transfer the nano-scale features. In terms of hot embossing, the SCIL method is another process, which is very promising, but needs time and trained personnel to carry out at NTNU NanoLab.

The anodizing process proved to be a simple and low-cost method and is absolutely recommended to proceed with. However, some measures, in which knowledge was gained from the fabrication in this work, can easily be carried out to increase the uniformity of the sample. Firstly, a larger electrolyte volume in relation to sample is preferable. If sample will be designed similarly to the one in this work, it should be placed horizontally instead of vertically, to reduce effects of temperature difference at the different water depths. Stirring can potentially by conducted during anodizing, to further limit the accumulation of hot regions. Additionally, more samples should, in general, be fabricated to cross-check results. The result of one test may be a coincidence, but the more samples fabricated the same way, yielding the same result, supports a potentially apparent trend.

The coating of PTFE should be performed in a manner such that it will not wear off as easily as was observed in this work. This is believed crucial in determining whether the friction response is a consequence of the ski base structure. PTFE coating with increased wear resistance should be available to purchase online.

Even though anodizing is a well-proven method to achieve hydrophobic surfaces, there are alternatives, in which some of them were discussed in this thesis. For example, the MLA gives accurate and custom-designed features at the micro-scale, and equipment is available at NTNU NanoLab. The main drawback is the cost of the fabrication instrument, a factor which is further complicated if it becomes desired to eventually scale up to a full-scale ski.

However, it would be interesting to investigate over time. Other nano-or microstructuring techniques should also be investigated.

A thorough understanding of ice friction requires investigation of sliding over a wide range of temperatures and sliding speeds [16]. In this work, the experiments were only carried out at one sliding velocity and at two temperatures for two samples, resulting in a total of four data sets. In the future, an increased number of test sets should be carried out to enable more comprehensive correlative observations. A completely smooth surface should also be tested and compared to the nanostructured sample. This could yield results indicating certain velocities and/or temperatures where the nanostructured sample would have a higher COF than the smooth sample, which would prove as an interesting finding.

If proceeding experiments with the snow track used in this work, even more time and resources should be provided for the track preparations in the aim of attaining a more uniform track. This will enable both a longer track length in which measurements can be conducted, as well as less noise from the uneven snow surface. It should also be attempted to increase the control of the brake force through other measures. For example, potential vibrations and slender connection in the LARS should be investigated. An even more accurate way of applying pressure on the samples could also be addressed. One idea could be to define the outer edges of the samples with a laser after positioning it on the snow track to accurately apply pressure at the sample center. Figure 72 gives an example of how this could be done. In (1) a laser is directed at the upper sample surface, vertically from above, and defining the center. In (2) a beam is lowered until it is positioned at the exact spot in which the center is defined. In (3) the desired load is applied.

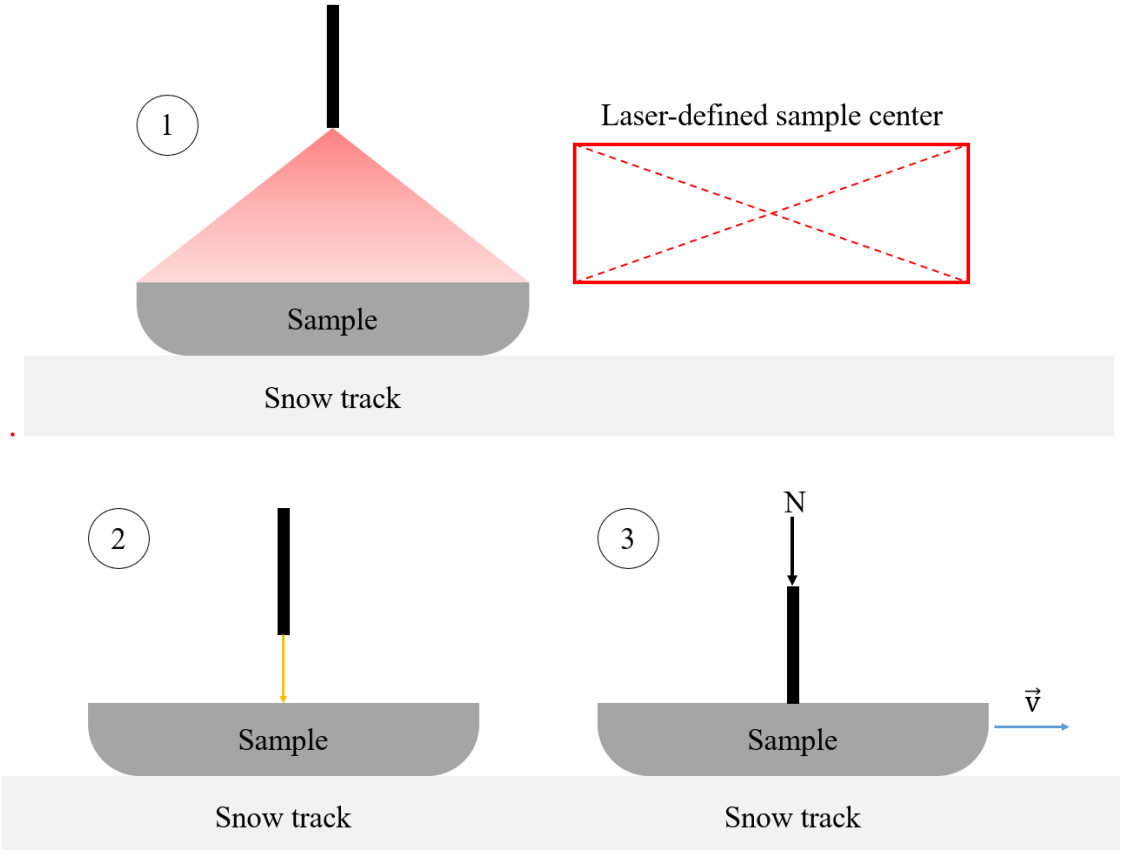

Figure 72: *Example of how the sample center could be defined more accurately for pressure application in the future*

Bibliography

1. Allen, E.J.B., *The culture and sport of skiing : from antiquity to World War II*. 2007, University of Massachusetts Press.
2. Kuzmin, L., et al., *Interfacial kinetic ski friction*. 2010, Östersund: Mittuniversitetet: Östersund.
3. Liu, W., et al., *Fabrication of the superhydrophobic surface on aluminum alloy by anodizing and polymeric coating.* Applied Surface Science, 2012. **264**: p. 872-878.
4. Buijnsters, J.G., et al., *Surface Wettabiliy of Macroporous Anodized Aluminum.* 2013.
5. *NORGE - Olympiatoppen*. [cited 2018 30.05]; Available from: http://www.olympiatoppen.no/page943.html.
6. *Sjokkert over nivået: Hyller Norge som verdens beste idrettfolk*. 2018, Dagbladet.
7. Nilsson, J., P. Tveit, and O. Eikrehagen, *Cross-Country Skiing: Effects of speed on temporal patterns in classical style and freestyle cross-country skiing.* Sports Biomechanics, 2004. **3**(1): p. 85-108.
8. de Koning, J.J., G. de Groot, and G.J. van Ingen Schenau, *Ice friction during speed skating.* Journal of Biomechanics, 1992. **25**(6): p. 565-571.
9. Commitee, T.I.O. *Cross country queen Bjørgen still reigning supreme*. 2016 [cited 2018 21.02]; Available from: https://www.olympic.org/news/cross-country-queen-bjorgen-still-reigning-supreme.
10. Colbeck, S.C., *A review of the Processes That Control Snow Friction.* U.S Army Corps of Engineers, Cold Regions Research & Engineering Laboratory, 1992.
11. *Chapter 3 Tribology of Coatings*. 1994. p. 33-124.
12. Colbeck, S.C., *Kinetic Friction of Snow.* Journal of Glaciology, 1988.
13. Kietzig, A., S.G. Hatzikiriakos, and P. Englezos, *Physics of ice friction*, in *J. Appl. Phys.* 2010.
14. Colbeck, S.C., *The friction of snow skis.* J. Sports Sci., 1993. **12**(285).
15. Colbeck, S.C. and D.K. Perovich, *Temperature effects of black versus white polyethylene bases for snow skis.* Cold Regions Science and Technology, 2004. **39**(1): p. 33-38.
16. Kietzig, A.-M., S.G. Hatzikiriakos, and P. Englezos, *Ice friction: The effects of surface roughness, structure, and hydrophobicity.* Journal of Applied Physics, 2009. **106**(2).
17. Buhl, D., et al., *The kinetic friction of polyethylen on snow: the influence of the snow temperature and the load.* Cold Regions Science and Technology, 2001. **33**(2-3): p. 133-140.
18. Ambach, W. and B. Mayr, *Ski gliding and water film.* Cold Regions Science and Technology, 1981. **5**(1): p. 59-65.
19. Faraon, I.C., *Mixed Lubricated Line Contacts*. 2005, University of Twente.
20. Bowden, F.P. and T.P. Hughes, *The mechanism of sliding on ice and snow.* The Royal Society, 1939.
21. Abdallah, W.e.a., *Fundamentals of Wettability.* Oilfield Review, Schlumberger, 2007.
22. Melberg, B., et al., *Nanostructured surfaces with patterned wettability*. 2012, Institutt for fysikk.
23. KRÜSS. *Surface free energy*. Available from: https://www.kruss.de/services/education-theory/glossary/surface-free-energy/.
24. HyperPhysics. [cited 2017 11.12]; Available from: http://hyperphysics.phy-astr.gsu.edu/hbase/surten.html.

25. KRÜSS. *Dispersive part*. [cited 2018 30.03]; Available from: https://www.kruss-scientific.com/services/education-theory/glossary/dispersive-part/.
26. KRÜSS. *Polar part*. [cited 2018 30.03]; Available from: https://www.kruss-scientific.com/services/education-theory/glossary/polar-part/.
27. GmbH, K. *Owens, Wendt, Rabel and Kaelble (OWRK) method*. [cited 2018 28.03]; Available from: https://www.kruss-scientific.com/services/education-theory/glossary/owens-wendt-rabel-and-kaelble-owrk-method/.
28. Materials, A. *Test Inks and Contact Angle Measurements: A Comparative Study*. [cited 2018 29.03]; Available from: https://www.azom.com/article.aspx?ArticleID=14299.
29. Owens, D.K. and R.C. Wendt, *Estimation of the surface free energy of polymers.* Journal of Applied Polymer Science, 1969. **13**(8): p. 1741-1747.
30. Fowkes, F.M., *ATTRACTIVE FORCES AT INTERFACES.* Industrial & Engineering Chemistry, 1964. **56**(12): p. 40-52.
31. Williams, D.L., et al., *Computerised measurement of contact angles.* Galvanotechnik, 2010. **101**(11): p. 2502-2512.
32. Law, K.-Y., *Definitions for Hydrophilicity, Hydrophobicity, and Superhydrophobicity: Getting the Basics Right.* The journal of physical chemistry letters, 2014. **5**(4): p. 686.
33. Bhushan, B., M. Nosonovsky, and Y.C. Jung, *Towards optimization of patterned superhydrophobic surfaces.* Journal of the Royal Society, Interface, 2007. **4**(15): p. 643.
34. Frenkel, Y.I., *On the behavior of liquid drops on a solid surface. 1. The sliding of drops on an inclined surface.* Journal of Experimental and Theoretical Physics, 1948. **18**(659).
35. Marmur, A., *Soft contact: measurement and interpretation of contact angles.* Soft Matter, 2006. **2**(1): p. 12-17.
36. Dictionary.com. *Capillarity*. [cited 2017 31.10]; Available from: http://www.dictionary.com/browse/capillary--attraction.
37. Giesbrecht, J.L., et al., *Polymers on snow: Toward skiing faster.* Journal of Polymer Science Part B: Polymer Physics, 2010. **48**(13): p. 1543-1551.
38. Riedo, E., F. Lévy, and H. Brune, *Kinetics of capillary condensation in nanoscopic sliding friction.* Physical Review Letters, 2002. **88**(18): p. 1855051-1855054.
39. Kuzmin, L. and M. Tinnsten, *The contamination, wettability and gliding ability of ski running surface.* Science and Nordic Skiing, 2007.
40. Bhushan, B., *Introduction to Tribology*. 2nd ed. ed. Tribology in Practice Ser. 2013, Hoboken: Wiley.
41. KEYENCE. *Introduction to roughness*. [cited 2018 10.05]; Available from: https://www.keyence.eu/ss/products/microscope/roughness/index.jsp.
42. Nosonovsky, M. and B. Bhushan, *Roughness optimization for biomimetic superhydrophobic surfaces.* MEMS, Systems for Information Processing and Storage, 2005. **11**(7): p. 535-549.
43. Marmur, A., *Wetting on hydrophobic rough surfaces: To be heterogeneous or not to be?* Langmuir, 2003. **19**(20): p. 8343-8348.
44. Moldestad, D.A. and k. Norges teknisk-naturvitenskapelige universitet Institutt for, *Some aspects of ski base sliding friction and ski base structure*. 1999, Department of Structural Engineering, Norwegian University of Science and Technology: Trondheim.
45. Nordin, N.A. and P. Styring, *Superhydrophobic Ski Bases for Reduced Water Adhesion.* Procedia Engineering, 2014. **72**: p. 605-610.

46. Böttcher, R., M. Seidelmann, and M. Scherge, *Sliding of UHMWPE on ice: Experiment vs. modeling.* Cold Regions Science and Technology, 2017. **141**: p. 171-180.
47. Puukilainen, E., et al., *Changes in the cross-country ski base properties resulting from the ski use.* Sports Engineering, 2013. **16**(4): p. 1-10.
48. Nilsson, J., L. Karlöf, and V. Jakobsen, *A new device for measuring ski running surface force and pressure profiles.* Sports Engineering, 2013. **16**(1): p. 55-59.
49. *Cross-country skiing in the Gatineau Park & Ottawa area*. [cited 2018 09.02]; Available from: http://xcskiing.ca/index.html#first-time.
50. MADSHUS, *Madshus REDLINE setter standard*. www.langrenn.no.
51. *Polymers : a property database*. Chapman & Hall/CRC Press: Boca Raton, Fla.
52. Fischer, J., G. Wallner, and A. Pieber, *Spectroscopical investigation of ski base material.* Macromol. Symp., 2008: p. 28-36.
53. Materials, A. *Ultra High Molecular Weight Polyethylene UHMWPE – Grades and Properties of Polystone UHMWPE from Dotmar*. 2008 [cited 2017 08.12]; Available from: https://www.azom.com/article.aspx?ArticleID=4237.
54. Bowden, F., *Friction on snow and ice.* Proceedings of the Royal Society of London. Series A, Mathematical and Physical Sciences, 1953. **217**(1131): p. 462-478.
55. Strobl, G., *Chapter 2: Single Chain Conformations*, in *The Physics of Polymers: Concepts for Understanding Their Structures and Behavior*. 1996, Springer.
56. Khedkar, J., I. Negulescu, and E.I. Meletis, *Sliding wear behavior of PTFE composites.* Wear, 2002. **252**(5): p. 361-369.
57. Oshima, A., et al., *Radiation induced crosslinking of polytetrafluoroethylene.* Radiation Physics and Chemistry, 1995. **45**(2): p. 269-273.
58. Breitschädel, F., *A New Approach for the Grinding of Nordic Skis.* Procedia Engineering, 2015. **112**: p. 385-390.
59. Breitschädel, F., Ø. Lund, and S. Løset, *Cross country ski base tuning with structure imprint tools.* Procedia Engineering, 2010. **2**(2): p. 2907-2911.
60. Wintersteiger. *Omega RS 150 - The racing stone grinding machine for skis and cross country skis*. [cited 2017 10.12]; Available from: https://www.wintersteiger.com/en/Ski-Service-Rental-and-Lockers.
61. Dickson, C., *Ski maintenance 101: The basics of waxing*. Active Junky.
62. Breiteschadel, F., M.r.a.b.c.w.m.r. pattern, Editor.
63. Hämeri, K., et al., *Formation of respirable particles during ski waxing.* Journal of aerosol science, 1996. **27**(2): p. 339-344.
64. Krafft, M.P. and J.G. Riess, *Per-and polyfluorinated substances (PFASs): Environmental challenges.* Current Opinion in Colloid & Interface Science, 2015. **20**(3): p. 192-212.
65. Moen, T.O., *Skiløpere sprer miljøgift [in Norwegian]*, in *NRK*. 2018.
66. Breitschädel, F., et al., *A comparison between timed and IMU captured nordic ski glide tests*. 2012. p. 397-402.
67. Brown, N., *The Complete Guide to Cross-Country Ski Preparations*. 1999, Seattle, WA: The Mountaineers.
68. Breitschädel, F., N. Haaland, and N. Espallargas, *A tribological study of UHMWPE ski base treated with nano ski wax and its effects and benefits on performance*. 2014. p. 267-272.
69. Budde, R. and A. Himes, *High-resolution friction measurements of cross-country ski bases on snow.* Sports Engineering, 2017. **20**(4): p. 299-311.

70. Miller, P., et al., *Development of a prototype that measures the coefficient of friction between skis and snow.* Sports Engineering, 2006. **9**(2): p. 107-107.
71. Slotfeldt-Ellinsen, D. and L. Torgersen, *Water in ice: influence on friction.* J. Phys. D: Appl. Phys, 1983. **16**.
72. Rohm, S., et al., *Friction Between Steel and Snow in Dependence of the Steel Roughness.* Tribology Letters, 2015. **59**(1): p. 1-8.
73. Baurle, L., D. Szabo, and M. Fauve, *Sliding friction of polyethylene on ice: tribometer measurements.* Tribology Letters, 2006. **24**.
74. Verschuuren, M.A., *Substrate Conformal Imprint Lithography for Nanophotonics* 2010, Utrecht University.
75. Coblas, D.G., et al., *Manufacturing textured surfaces: State of art and recent developments.* Proceedings of the Institution of Mechanical Engineers, Part J: Journal of Engineering Tribology, 2015. **229**(1): p. 3-29.
76. Makhlouf Abdel Salam, H. and I. Tiginyanu, *Nanoimprint Lithography (NIL) and Related Techniques for Electronics Applications*. 2011: Woodhead Publishing. 1-1.
77. Xiao, H., *Photolithography*. 2nd Edition ed. 2012: SPIE. 1-1.
78. Menon, R., et al., *Maskless lithography.* Materials Today, 2005. **8**(2): p. 26-33.
79. Diez, S. and H.I.M. GmbH, *The next generation of Maskless Lithography* Emerging Digital Micromirror Device Based Systems and Applications, 2016.
80. Bixler, G.D. and B. Bhushan, *Rice- and butterfly-wing effect inspired self-cleaning and low drag micro/nanopatterned surfaces in water, oil, and air flow.* Nanoscale, 2013. **6**(1): p. 76-96.
81. Jessensky, O., F. Müller, and U. Gösele, *Self-organized formation of hexagonal pore arrays in anodic alumina.* Applied Physics Letters, 1998. **72**(10): p. 1173-1175.
82. Materials, A. *Hydro - Aluminum Alloys and Products*. [cited 2017 09.12]; Available from: https://www.azom.com/suppliers.aspx?SupplierID=1156.
83. Kent, R., *Corrosion Engineering, ME406 UW course pack*. 1986, Univeristy of Washington. p. 236-238.
84. Wood, G.C., et al., *The anodizing of aluminium in sulphate solutions.* Electrochimica Acta, 1970. **15**(12): p. 1865-1876.
85. Xu, Y., G.E. Thompson, and G.C. Wood, *MECHANISM OF ANODIC FILM GROWTH ON ALUMINIUM.* Transactions of the Institute of Metal Finishing, 1985. **63**(3-4): p. 98-103.
86. Masuda, H. and K. Fukuda, *ORDERED METAL NANOHOLE ARRAYS MADE BY A 2-STEP REPLICATION OF HONEYCOMB STRUCTURES OF ANODIC ALUMINA.* Science, 1995. **268**(5216): p. 1466-1468.
87. Siu-Fung, L., et al., *Roll-to-roll fabrication of large scale and regular arrays of three-dimensional nanospikes for high efficiency and flexible photovoltaics.* Scientific Reports, 2014. **4**.
88. Skoglund, A., M. Steinert, and C. Kriesi, *Rethinking Surface Design and Materials of Skis*. 2017, NTNU.
89. Abd-Elnaiem, A. and A. Gaber, *Parametric Study on the Anodization of Pure Aluminum Thin Film Used in Fabricating Nano-pores Template.* Int. J. Electrochem. Sci., 2013. **8**(7): p. 9741-9751.
90. Thompson, G.E., et al., *Anodizing of aluminium alloys.* Aircraft Engineering and Aerospace Technology, 1999. **71**(3): p. 228-238.

91. Stępniowski, W.J., et al., *The impact of viscosity of the electrolyte on the formation of nanoporous anodic aluminum oxide.* Electrochimica Acta, 2014. **133**: p. 57-64.
92. Feng, L., S. Li, and e. al., *Super-Hydrophobic Surfaces: From Natural to Artificial.* Advanced Materials, 2002.
93. KRUSS. *Solids: Values for the surface free energy of solids*. Available from: https://www.kruss-scientific.com/services/education-theory/substance-data/solids/.
94. Norek, M. and A. Krasiński, *Controlling of water wettability by structural and chemical modification of porous anodic alumina (PAA): Towards super-hydrophobic surfaces.* Surface & Coatings Technology, 2015. **276**: p. 464-470.
95. Mateo, J.N., et al., *Wetting behavior of polymer coated nanoporous anodic alumina films: transition from super-hydrophilicity to super-hydrophobicity.* Nanotechnology, 2011. **22**(3): p. 035703.
96. Zygo. *Optical Profiler Basics*. [cited 2018 11.03]; Available from: https://www.zygo.com/?/met/profilers/opticalprofilersabout.htm.
97. Schmit, J., D. Chen, and V.I. Inc., *Greater Measurement Detail with High-Definition Vertical Scanning Interferometry*. 2010, Bruker.
98. Pignatelli, I., et al., *Vertical scanning interferometry: A new method to quantify re-/de-mineralization dynamics of dental enamel.* Dental Materials, 2016. **32**(10): p. e251-e261.
99. The University of Arizona, C.o.O.S., *Vertical Scanning (Coherence Probe) Techniques*. p. Teaching material.
100. Vorburger, T., et al., *Comparison of optical and stylus methods for measurement of surface texture.* The International Journal of Advanced Manufacturing Technology, 2007. **33**(1): p. 110-118.
101. Alicona. *Focus-Variation: The technical principle*. Available from: https://www.alicona.com/focus-variation/.
102. Zhou, W. and Z.L. Wang, *Scanning microscopy for nanotechnology: techniques and applications*. 2007: Springer science & business media.
103. FEI, *QUANTA 650 FEG*. 2014.
104. Britannica, E., *Scanning electron microscope*, in *Britannica*, B.J. Ford, S. Bradbury, and D.C. Joy, Editors. 2008.
105. Zhang, J., et al., *Low-cost fabrication of large area subwavelength anti-reflective structures on polymer film using a soft PUA mold*. 2014. p. 1842-1851.
106. Li, Y., et al., *Material versatility using replica molding for large-scale fabrication of high aspect-ratio, high density arrays of nano-pillars.* Nanotechnology, 2014. **25**(28): p. 285303.
107. Ippolito, C., et al., *Process Parameter Optimization for Hot Embossing Uniformly Textured UHMWPE Surfaces for Orthopedic Bearings.* Procedia CIRP, 2017. **65**: p. 163-167.
108. Kustandi, T.S., et al., *Texturing of uhmwpe surface via nil for low friction and wear properties.* Journal of Physics D: Applied Physics, 2010. **43**(1): p. 015301.
109. Lamour, G., et al., *Contact Angle Measurements Using a Simplified Experimental Setup.* Journal of Chemical Education, 2010. **87**(12): p. 1403-1407.
110. KRÜSS. *Sessile Drop*. Available from: https://www.kruss.de/services/education-theory/glossary/sessile-drop/.
111. Stalder, A. *Drop Shape Analysis*. 2013 20.10.2013 [cited 2017 01.10]; Available from: http://bigwww.epfl.ch/demo/dropanalysis/#soft.

112. Stalder, A. *DropSnake and LB-ADSA user manual*. [cited 2017 01.10]; Available from: http://mmrc.caltech.edu/Gniometeer/drop_analysis/drop_analysis.pdf.
113. Parreidt, T.S.e.a., *Validation of a novel Technique and Evaluation of the Surface Free Energy of Food.* 2017.
114. GIMP. *Download of GIMP 2.8.22*. 2017 [cited 2017 30.09]; Available from: https://www.gimp.org/downloads/.
115. Drelich, J., *The Effect of Drop (Bubble) Size on Contact Angle at Solid Surfaces.* The Journal of Adhesion, 1997. **63**(1-3): p. 31-51.
116. Skurtys, O., et al., *Wetting behavior of chitosan solutions on blueberry epicarp with or without epicuticular waxes.* LWT - Food Science and Technology, 2011. **44**(6): p. 1449-1457.
117. Giudici, H., et al., *A Technical Description of LARS and Lumi: Two Apparatus for Studying Tire-Pavement Interactions.* Routes/Roads, 2017.
118. Itagaki, K., G. Lemieux, and N. Huber, *Preliminary study of friction between ic and sled runners.* Journal de Physique Colloques, 1987.
119. Documentation, M. *boxplot*. [cited 2018 22.05]; Description of the MATLAB function boxplot()]. Available from: https://se.mathworks.com/help/stats/boxplot.html.
120. Documentation, M. *ttest2*. [cited 2018 22.05]; Description of the fuction ttest2()]. Available from: https://se.mathworks.com/help/stats/ttest2.html.
121. Short, T., *The Identification and Prevention of Defects on Anodized Aluminum Parts*. 2003, Metal Finishing Information Services Ltd.
122. De Graeve, I., H. Terryn, and G. Thompson, *Influence of heat transfer on anodic oxidation of aluminium.* Journal of applied electrochemistry, 2002. **32**(1): p. 73-83.
123. Tu, G., *The growth of porous anodic films on aluminium under DC and AC conditions*. 1981, University of Manchester Institute of Science and Technology (UMIST).
124. Kant, K., et al., *Nanopore gradients on porous aluminum oxide generated by nonuniform anodization of aluminum.* ACS applied materials & interfaces, 2010. **2**(12): p. 3447-3454.
125. Kim, D., et al., *Superhydrophobic nanostructures based on porous alumina.* Current Applied Physics, 2008. **8**(6): p. 770-773.
126. *MatWeb*. [cited 2018 28.05]; Material property data]. Available from: http://www.matweb.com/.
127. Orduña-Malea, E., et al., *About the size of Google Scholar: playing the numbers.* arXiv preprint arXiv:1407.6239, 2014.

Appendices

Appendix A: Images from hot embossing process

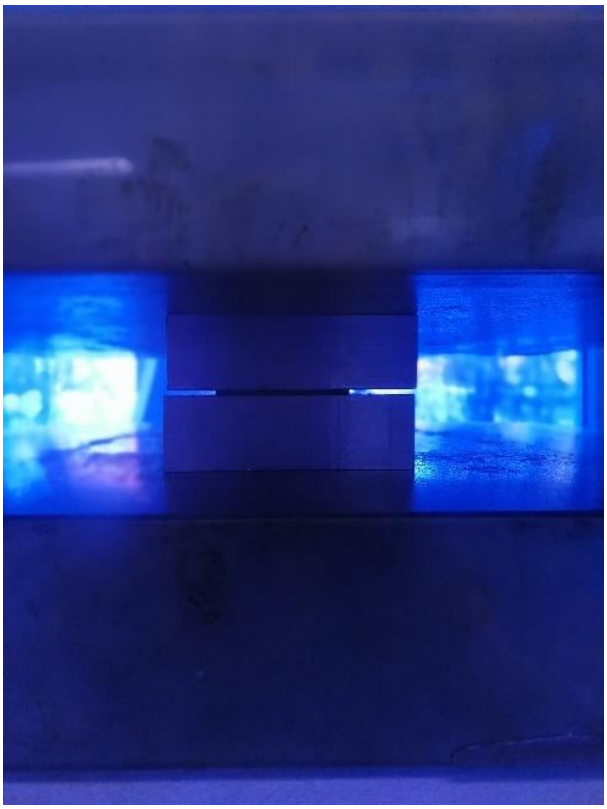

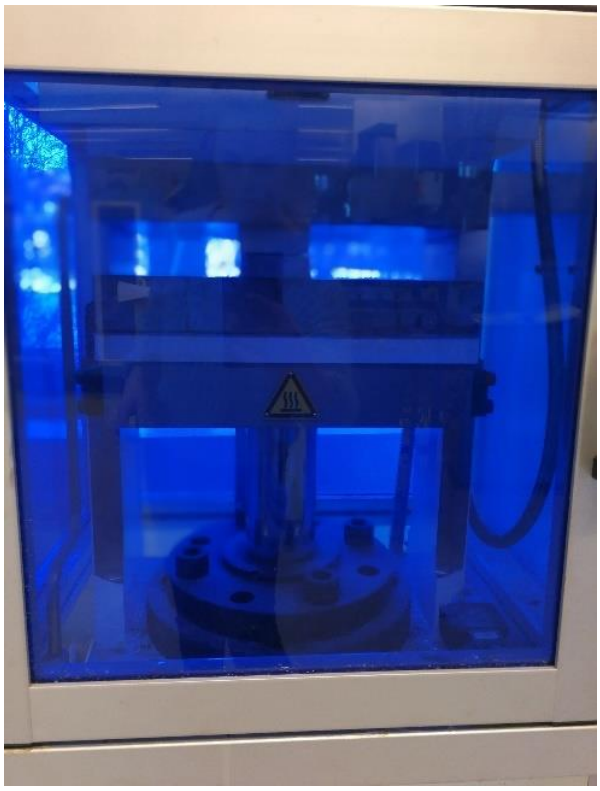

Appendix B: OM data

SMOOTH UHMWPE:

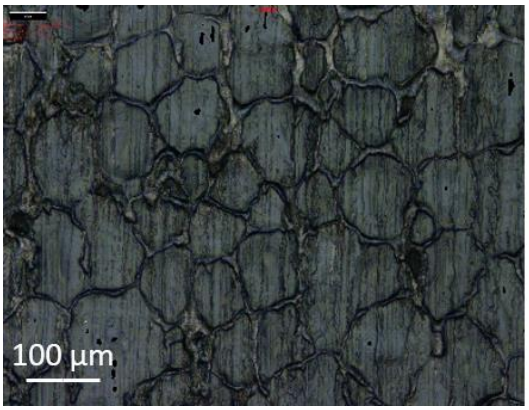

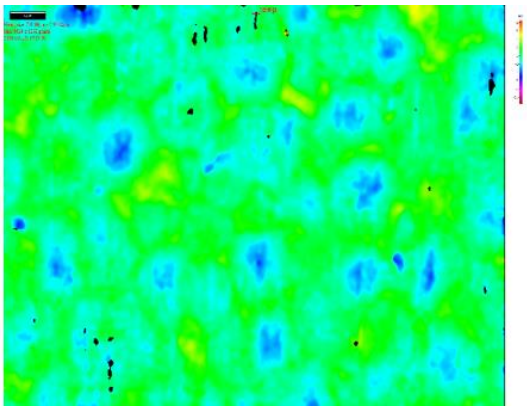

Parameter	Value	Unit
Sa	0.39286	µm
Sq	0.50344	µm
Sz	1.7644	µm
Sp	1.6373	µm
Sv	869.97	nm
Ssk	0.83166	
Sku	3.7029	

P1000:

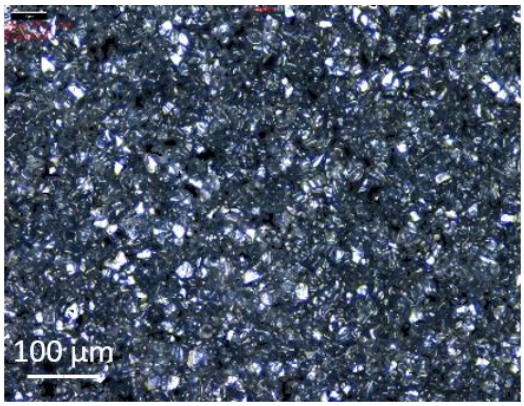

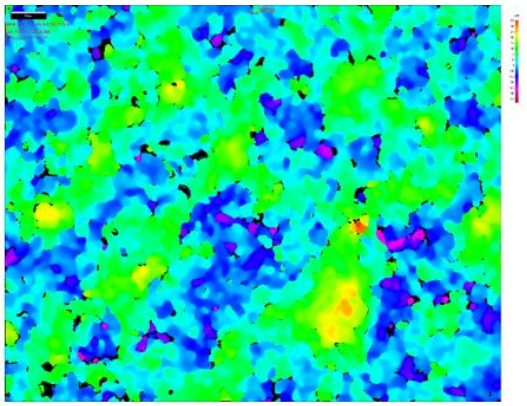

Parameter	Value	Unit
Sa	2.1006	µm
Sq	2.8177	µm
Sz	10.24	µm
Sp	5.6645	µm
Sv	10.711	µm
Ssk	-0.84658	
Sku	4.5132	

UH-P1000-3:

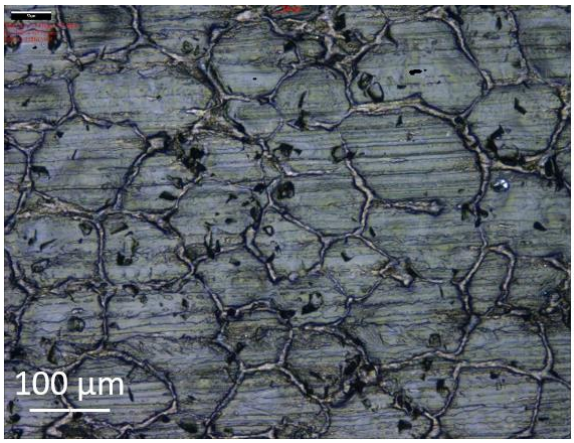

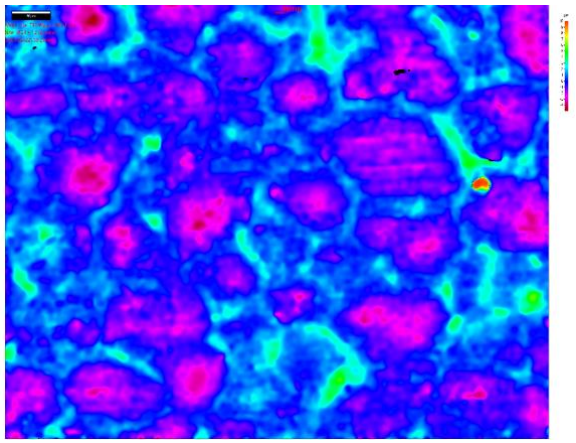

Parameter	Value	Unit
Sa	0.27006	µm
Sq	0.35382	µm
Sz	1.645	µm
Sp	1.1206	µm
Sv	917.6	nm
Ssk	0.44237	
Sku	3.7467	

UH-P1000-5:

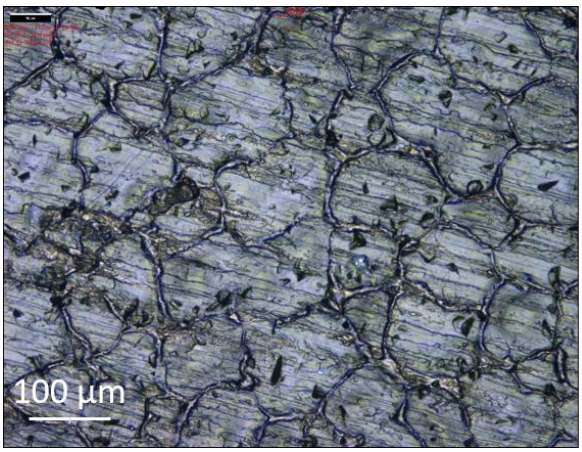

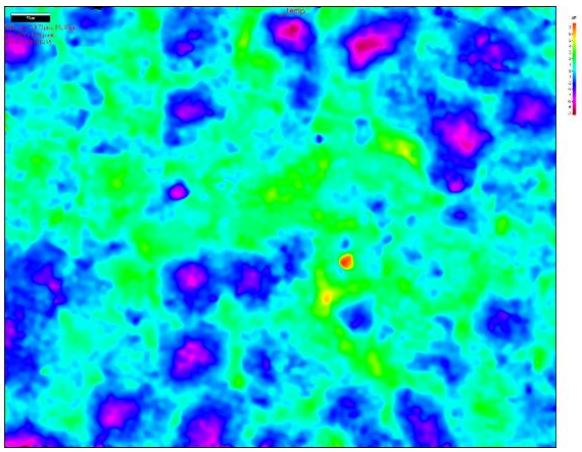

Parameter	Value	Unit
Sa	0.3354	µm
Sq	0.41464	µm
Sz	1.4309	µm
Sp	1.0267	µm
Sv	925.15	nm
Ssk	0.39456	
Sku	2.5892	

AA-3:

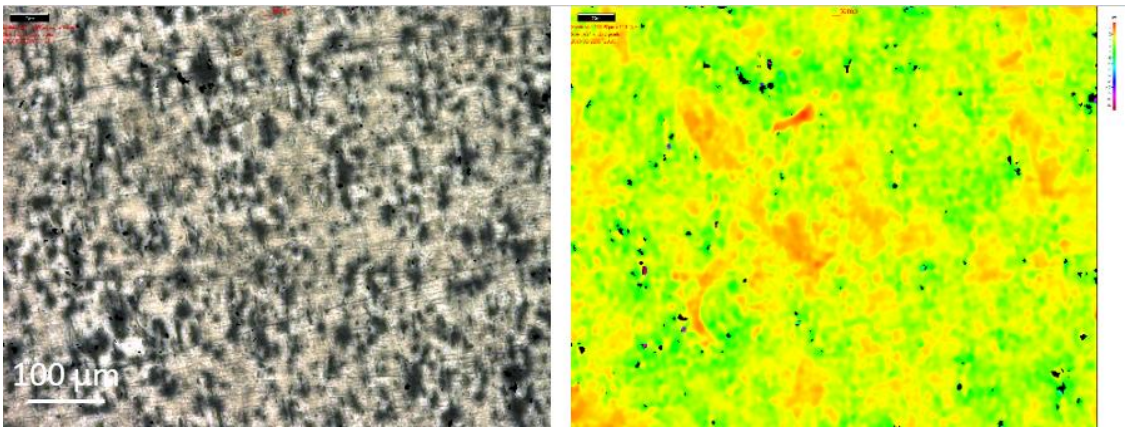

Parameter	Value	Unit
Sa	0.41442	µm
Sq	0.52457	µm
Sz	1.8105	µm
Sp	875.98	nm
Sv	1.557	µm
Ssk	-0.84188	
Sku	3.3475	

UH-AA3-1:

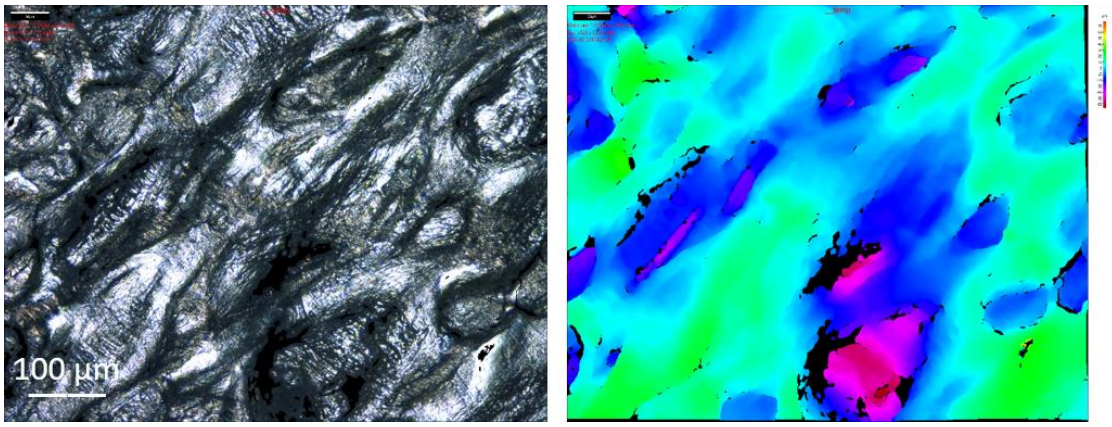

Parameter	Value	Unit
Sa	1.7607	µm
Sq	2.5485	µm
Sz	8.8772	µm
Rp	11.608	µm
Rv	12.541	µm
Ssk	-0.80661	
Sku	7.1072	

UH-AA3-2:

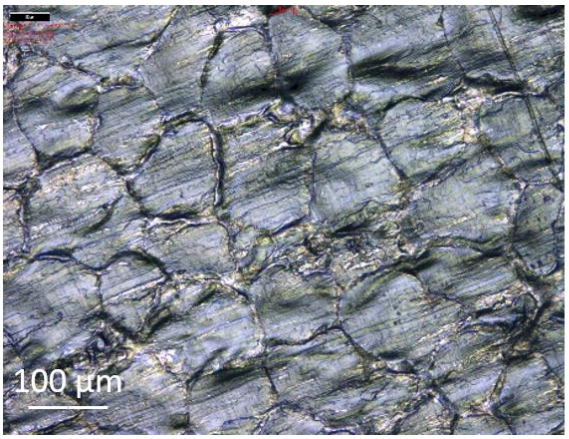

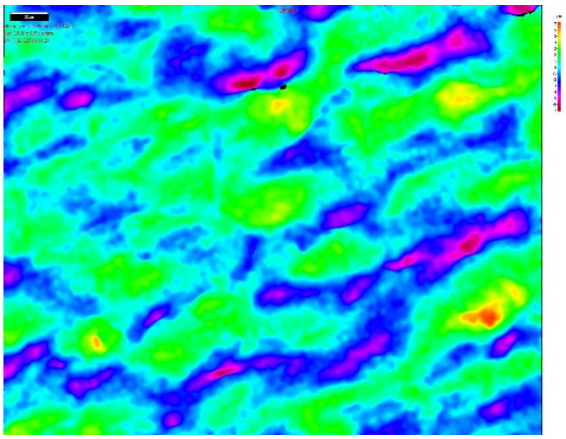

Parameter	Value	Unit
Sa	0.53513	µm
Sq	0.77879	µm
Sz	2.4205	µm
Sp	1.8674	µm
Sv	2.7269	µm
Ssk	-1.629	
Sku	6.3456	

UH-AA3-3:

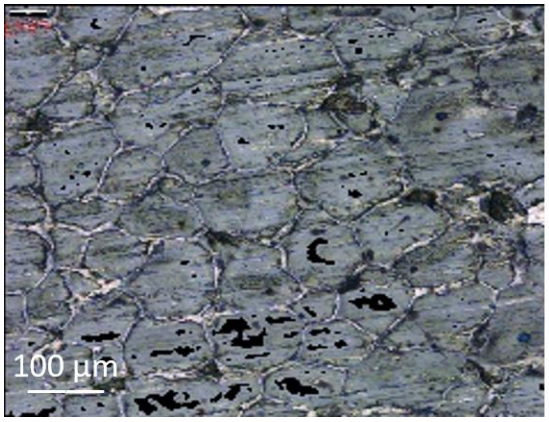

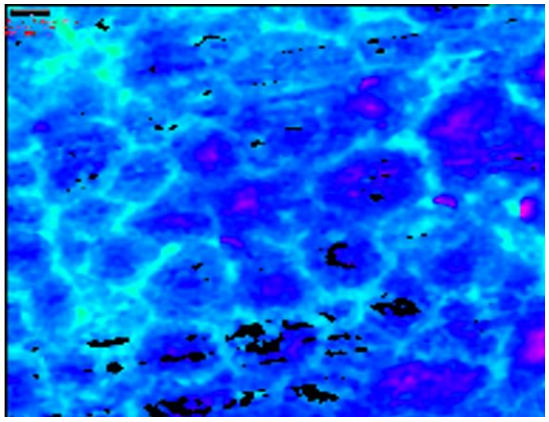

Parameter	Value	Unit
Sa	0.68346	µm
Sq	0.8752	µm
Sz	3.6001	µm
Sp	3.0469	µm
Sv	2.0938	µm
Ssk	0.61366	
Sku	3.7893	

UH-AA3-4:

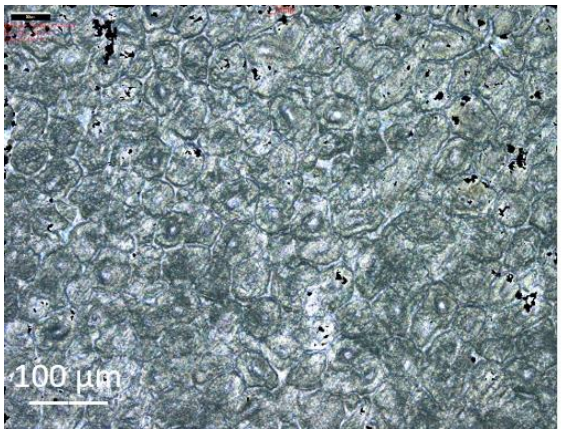

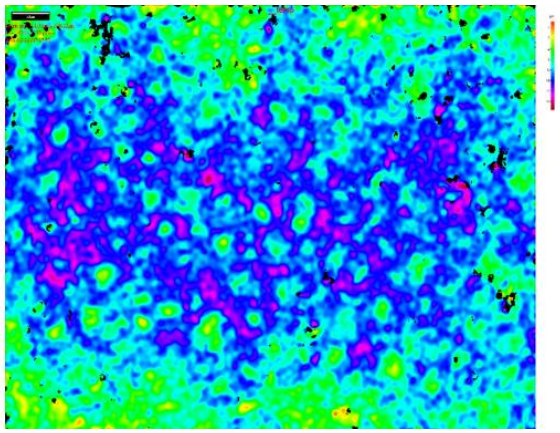

Parameter	Value	Unit
Sa	0.36942	µm
Sq	0.47688	µm
Sz	1.6259	µm
Sp	1.3711	µm
Sv	1.4386	µm
Ssk	-0.15253	
Sku	3.5513	

Appendix C: Aluminum data sheet

AMAG ROLLING

Abnahmeprüfzeugnis 3.1 (EN 10204)
Inspection certificate - mill certificate

Nr.: 89058512 **01 / 1**
Rev.: 0
Seite / page: 1 von / of 2
Datum / date: 2017 07 26

Zertifiziert nach / certified to ISO 9001, ISO/TS 16949, EN/AS 9100, ISO 14001, NADCAP

Auftraggeber / customer: E.A. Smith AS Dep. Smith Stal Nord Trondheim N-7493 TRONDHEIM **Warenempfänger / consignee:** E.A. SMITH AS Avd. Smith Stal Nord Trondheim Nedre Ila 66 N-7018 TRONDHEIM	Bestell Nr. / order no.: 2080627 Datum / date: 2017 04 27 Auftragsbest. Nr. / order confirm no.: 130770 Datum / date: 2017 04 26 Lieferschein Nr. / delivery note: 89058512 Datum / date: 2017 07 27

Produkt / product	**Bedingungen / terms**
Form / form: Platten Werkstoff / material: EN AW 5754 Zustand / temper: H111 Dim. / dim.: [mm]: 20,00x1020,00x2020,00	Technische Lieferbedingungen / techn. spec.: EN 485-2 : 2013 EN 485-3 : 2003 EN 573-3 : 2013 EN 602 : 2004 Sondervorschrift / special terms:

AB-Pos. ord.-Item.	BNr/Los Lot/No.	Teilios Part	Guss Nr. cast no.	Werkstoff material	Kollo packno.	Gewicht netto weight net	Stk. pcs.
01	35465/01	00	01/0084447/7	EN AW 5754	1307700017	1004 kg	9

Chemische Zusammensetzung ([%] Gewichtsanteile) / Chemical composition ([%] weight proportion (OES))

Guss Nr. / cast no.	material										
01/0084447/7	EN AW 5754	Si	Fe	Cu	Mn	Mg	Cr	Zn	Ti	Mn+ Cr	Sonst Einzel
	spec. min.	-	-	-	-	2,6	-	-	-	0,10	-
	spec. max.	0,40	0,40	0,10	0,50	3,6	0,30	0,20	0,15	0,6	0,05
	actual	0,33	0,34	0,06	0,33	3,2	0,05	0,06	0,03	0,38	0,02
		Sonst Summe									
	spec. min.	-									
	spec. max.	0,15									
	actual	0,04									

Zugprüfung LT / tensile test LT

BNr/Los Lot/No.	Zustand temper	Richtung direction			Rm [MPa]	Rp0.2 [MPa]	A5 [%]			
				spec.min.	190	80	17			
				spec.max.	240	-	-			
35465/01	H111	LT			222	112	24			

Sonstige Prüfungen / other tests

Maßkontrolle: OK. / Dimensional Check: OK.
Oberfläche: OK. / Surface inspection: OK.

AMAG ROLLING

Abnahmeprüfzeugnis 3.1 (EN 10204)
Inspection certificate - mill certificate

Nr.: 89058512 **01 / 1**
Rev.: 0
Seite / page: 2 von / of 2
Datum / date: 2017 07 26

Zertifiziert nach / certified to ISO 9001, ISO/TS 16949, EN/AS 9100, ISO 14001, NADCAP

Bemerkungen / notes
CE 0036 11 EN AW 5754 H111 CPR Nr.: 0036-CPR-M-46-2011 DIN EN 15088: 2005 Verwendung für DIN EN 15088 Tabelle ZA.1 – Produkte, Verwendungszweck und System der Bescheinigung / 0036 11 EN AW 5754 H111 CPR Nr.: 0036-CPR-M-46-2011 DIN EN 15088: 2005 use for DIN EN 15088 table ZA.1 – products, structural application and system of certification

Es wird bestätigt, dass die Lieferung geprüft wurde und den Vereinbarungen bei der Bestellung entspricht.
We hereby certify that the material described above has been tested and complies with the terms of the order contract.

Werksachverständiger / factory specialist	E-Mail / e-mail
Josef Klampfer	josef.klampfer@amag.at

Herstellerland: Österreich / goods origin: The goods are of Austrian origin.
Maschinell erstellt - Gültig ohne Unterschrift / Automated - valid without being signed.

Appendix D: Machine drawing of AAO sample

The reference sample is identical except for the threaded hole at the short edge

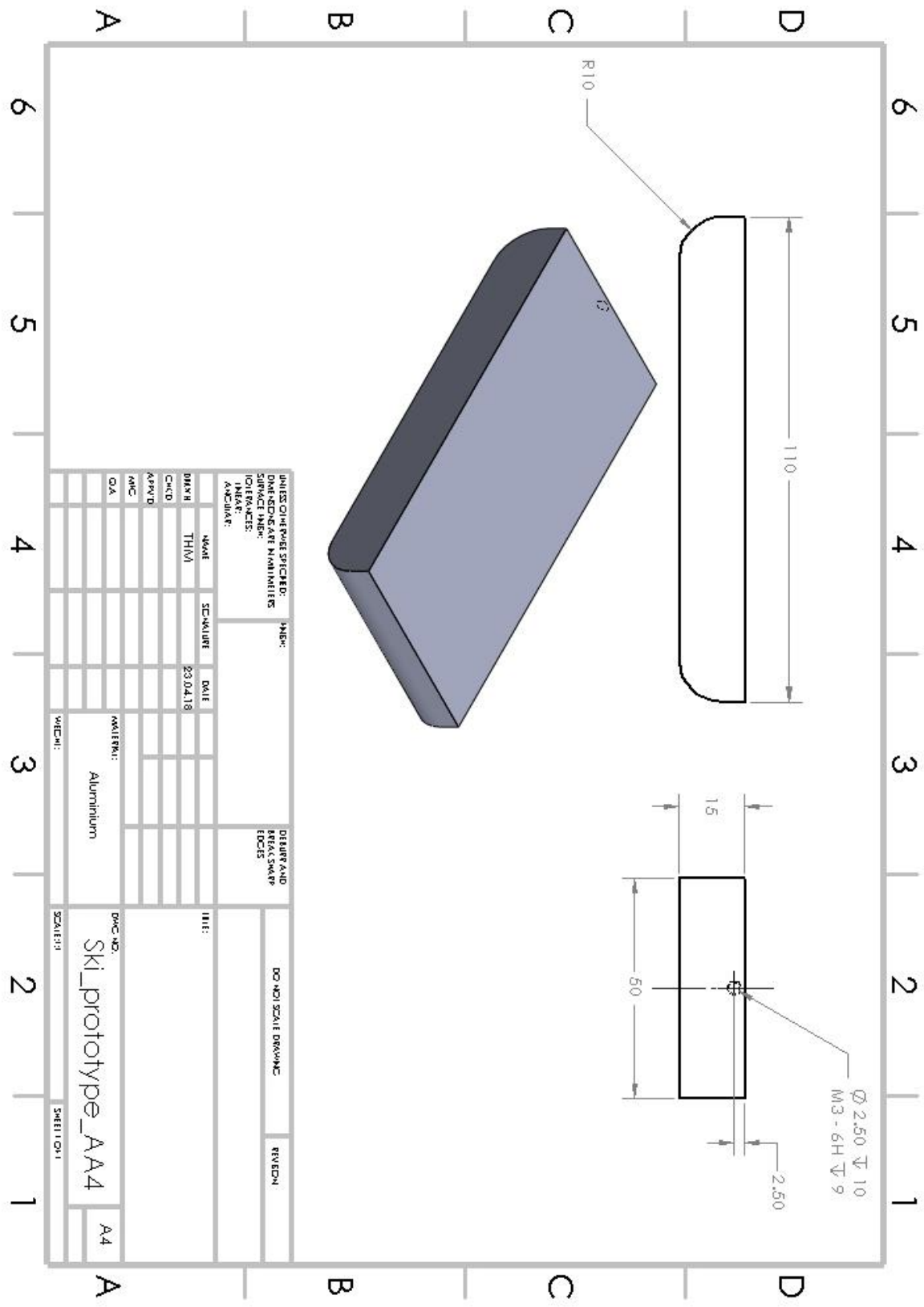

Appendix E: Electrolyte concentration calculations

As neither the sulfuric acid nor the oxalic acid available at the lab were of pure substances, amounts needed based on the concentrations of the bottles at hand had to be found.

The concentration of the bottle of sulfuric acid was of 95 % purity, and hence the molarity of the bottle was be found by Equation 23:

$$C_{bottle} = \frac{C_p \cdot \rho_{H_2SO_4}}{100\ \% \cdot M_{H_2SO_4}} = 17.8\ mol/L \qquad (23)$$

Where C_{bottle} is the molarity of bottle, C_p is the percentage of sulfuric acid in the bottle (95 %), $\rho_{H_2SO_4}$ is the density of pure sulfuric acid (1.84 g/mL), and $M_{H_2SO_4}$ is molecular weight of pure sulfuric acid (98.08 g/mol). The desired molar concentration of sulfuric acid was further found by Equation 24:

$$C_{H_2SO_4} = \frac{c_{su}}{M_{H_2SO_4}} = 1.73\ mol/L \qquad (24)$$

Where c_{su} is defined as the concentration of sulfuric acid in g/L based on Table 2. For a total electrolyte mixture of 1 L, the volume of sulfuric acid was further found by Equation 25:

$$V_{H_2SO_4} = V_{total} \cdot \frac{C_{bottle}}{C_{H_2SO_4}} = \mathbf{97\ mL} \qquad (25)$$

The oxalic acid available was in powder form, in which it was given on the etiquette that total molar mass of the substance is 126.07 $\frac{g}{mol}$ (M_{total}) and molar mass of pure acid is 90.03 g/mol ($M_{C_2H_2O_4}$). The correct amount of the mixture for 1 L of total electrolyte was found by Equation 26:

$$C_{C_2H_2O_4} = \frac{M_{total}}{M_{C_2H_2O_4}} \cdot c_{ox} \cdot 1L = \mathbf{14\ g} \qquad (26)$$

Where c_{ox} is defined as the concentration of oxalic acid based on Table 2.

Hence, in 1 L of electrolyte the following is needed; 97 mL of sulfuric acid, 14 g of oxalic acid, and 1.25 g of sodium chloride of the products available, and remaining volume distilled water.

Appendix F: Electrolyte volume calculation

Information:

- Most suitable beaker holds 2 L, had an internal diameter of ~115 mm, and a total height of ~220 mm
- The cathode has dimensions: 210×250×0.3 mm
- The anode has dimensions: ~110×50×15 mm

Assumptions:

- 10 mm distance between beaker bottom and anode
- 15 mm distance between electrolyte surface and anode
- Hence, the total height of electrolyte needed to immerse anode is: 110+10+15=135 mm
- Consequently, only 135 mm of the height of cathode will be immersed

Volume needed of electrolyte:

The total volume needed of the electrolyte is the volume of the beaker when it is filled 135 mm, subtracting the volume of the anode and the cathode, shown mathematically in Equation 27:

$$V_{electrolyte} = V_{beaker,\ 135\,mm} - V_{anode} - V_{cathode} \qquad (27a)$$

$$V_{electrolyte} = \pi \cdot {r_{beaker}}^2 \cdot h_{electrolyte} - [l \cdot w \cdot h]_{anode} - [l \cdot w \cdot h]_{cathode} \qquad (27b)$$

$$V_{electrolyte} = \pi \cdot \left(\frac{115}{2}\right)^2 \cdot 135 - [110 \cdot 40 \cdot 15] - [135 \cdot 210 \cdot 1] \qquad (27c)$$

$$V_{electrolyte} = 1{,}307{,}880.246\ mm^3 \qquad (27d)$$

$$V_{electrolyte} \approx \mathbf{1.31\ L} \qquad (27e)$$

1.31 L of the electrolyte is needed to fully immerse anode. As the area of the cathode is many times larger than the area of the anode, immersion of this is not necessary for the cathode. Note that the radius on the lower surface of the anode is neglected and its volume will, therefore, be slightly less than assumed here. The volume of the connecting rod to the anode is also neglected. Hence, the calculation is only guiding but considered accurate enough.

Appendix G: Images of ski prototype before anodizing

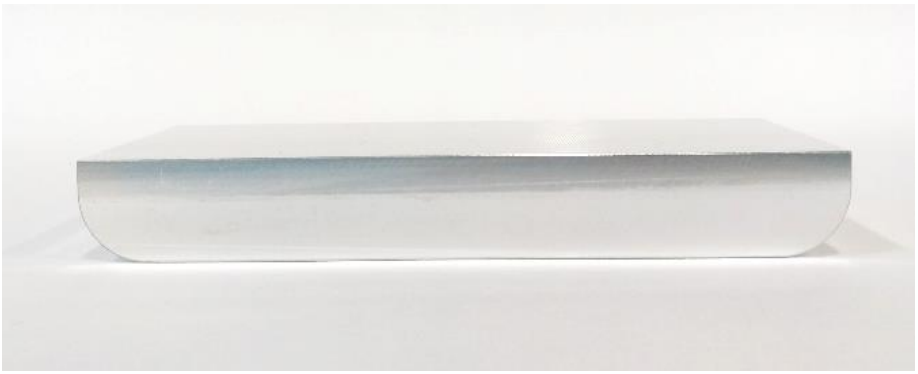

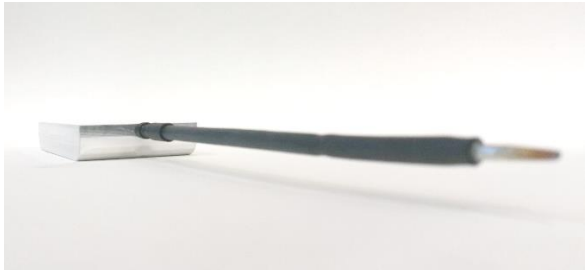

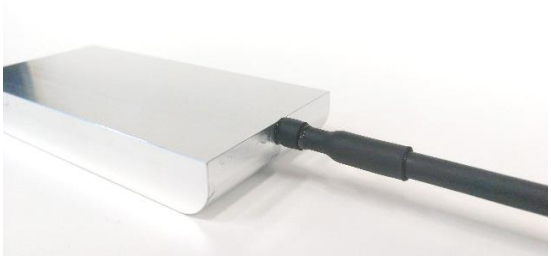

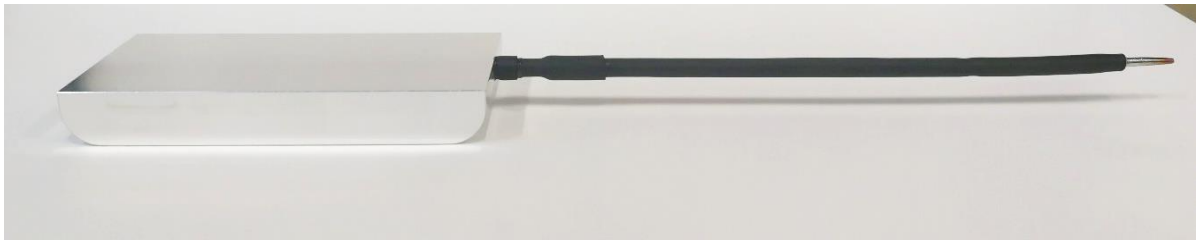

Appendix H: Images of ski prototype after anodizing

Appendix I: Images of cathode before anodizing

Appendix J: Images of cathode after anodizing

Appendix K: Images of anodizing process

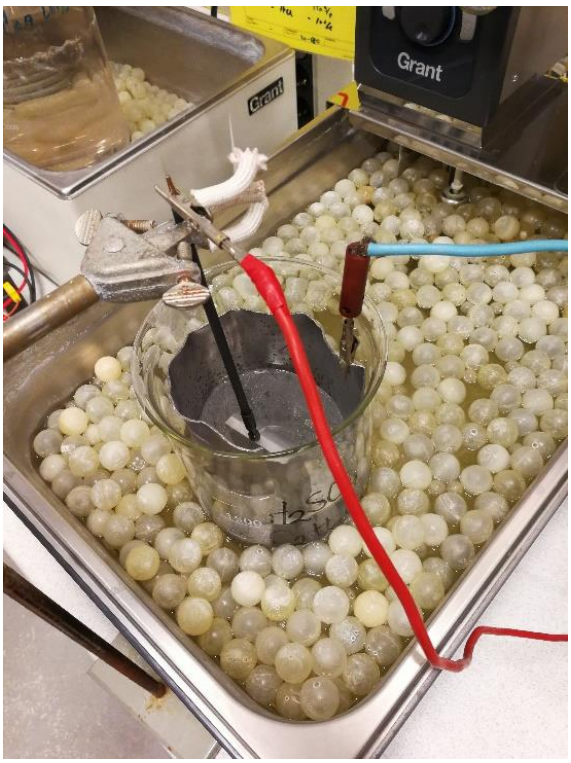

Appendix L: SEM images

Reference sample

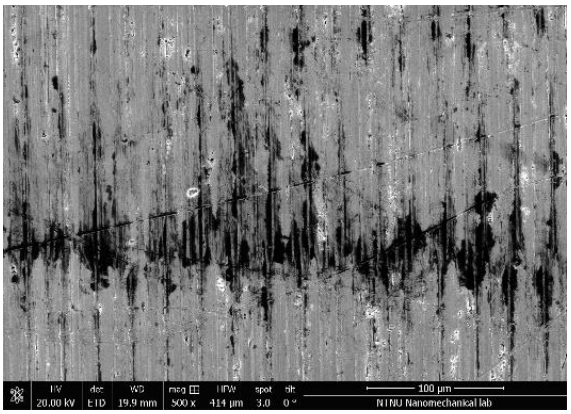

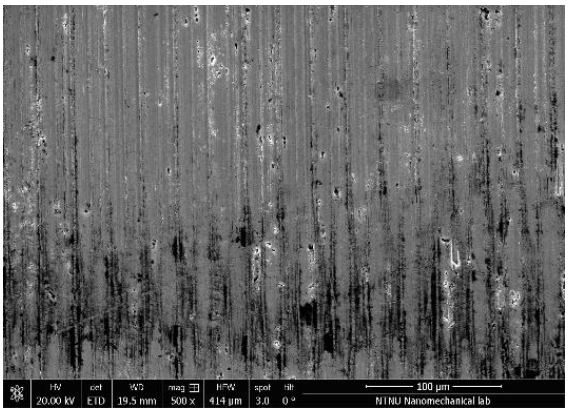

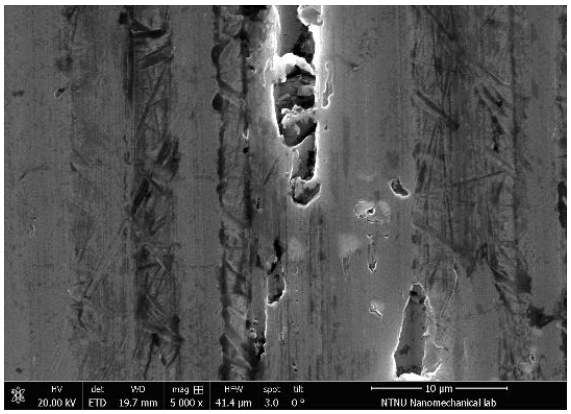

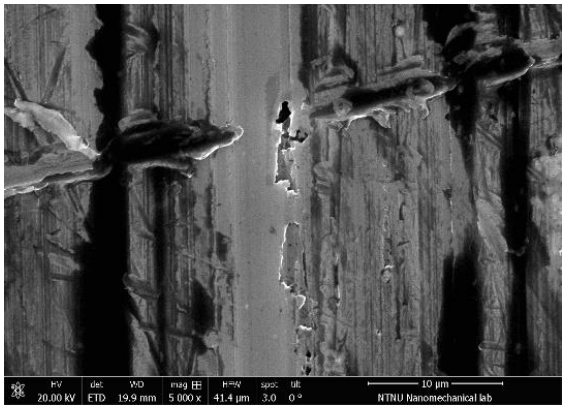

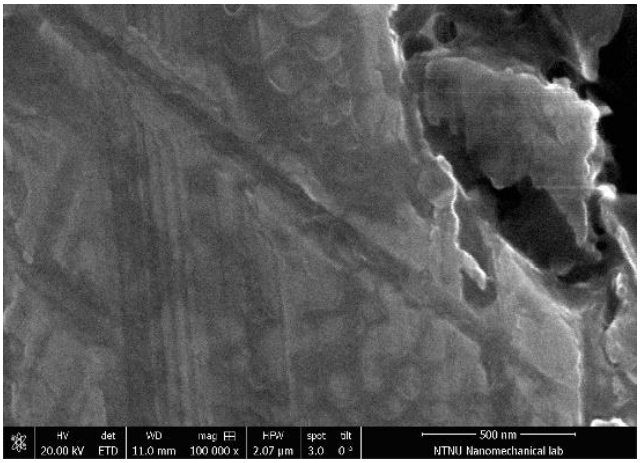

Reference sample (low-vacuum)

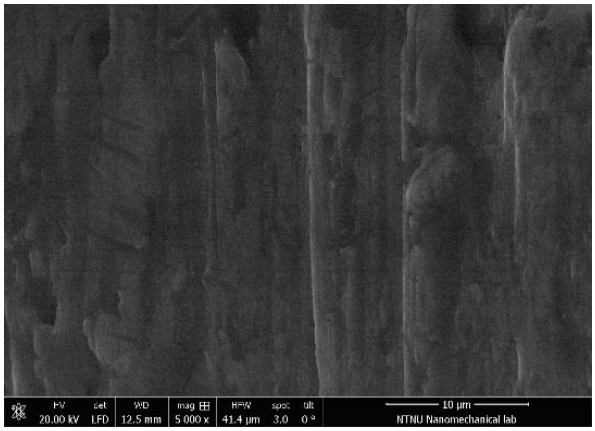

Anodized sample, Side 1 (low-vacuum)

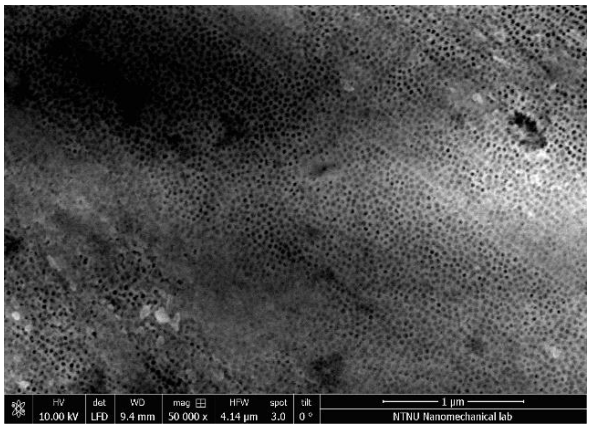

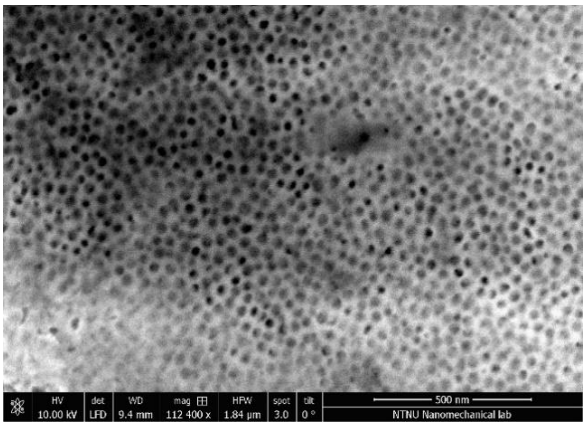

Anodized sample, Side 2 (low-vacuum)

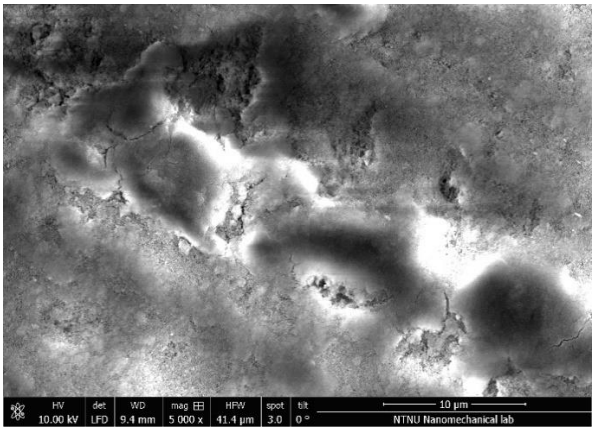

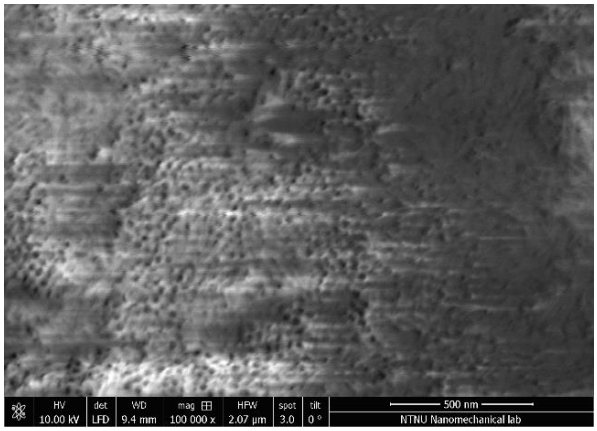

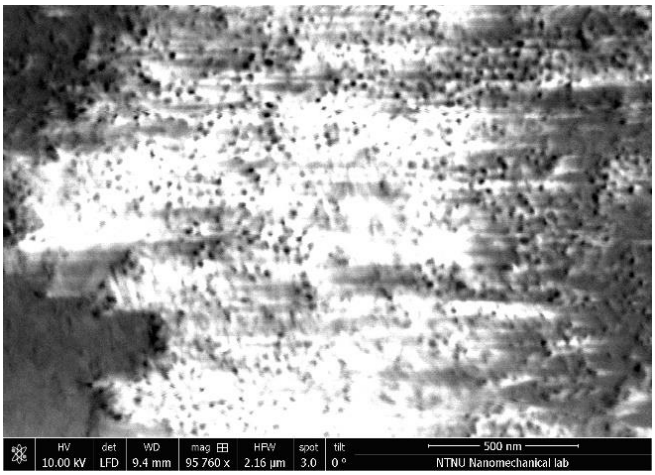

Appendix M: OP images

AAO, Side 1, spot 1, before friction tests:

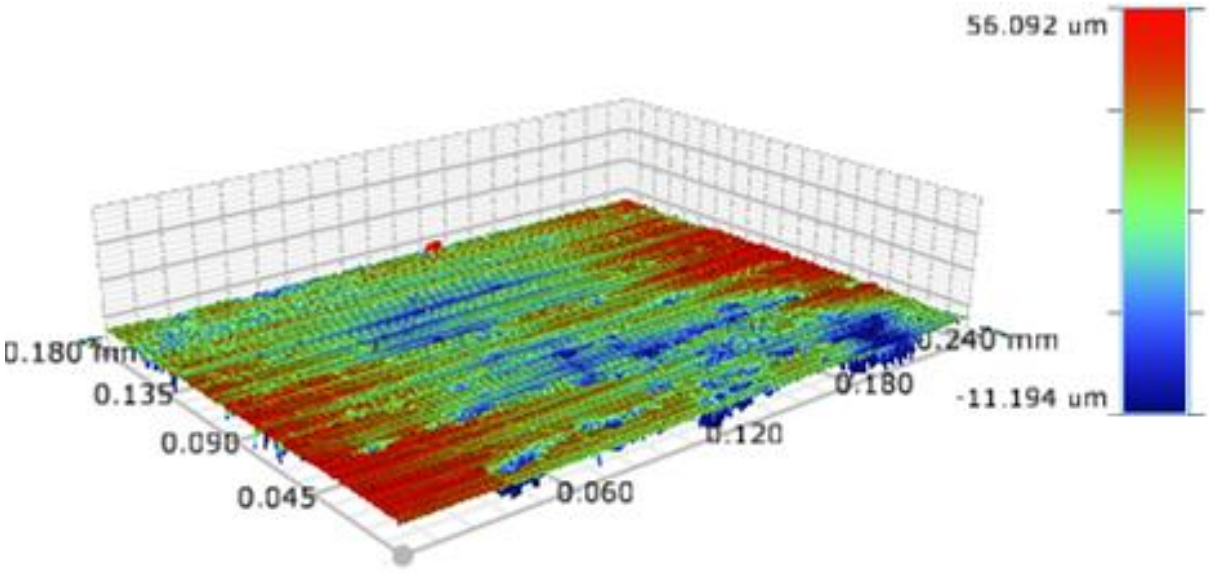

AAO, Side 1, spot 2, before friction tests:

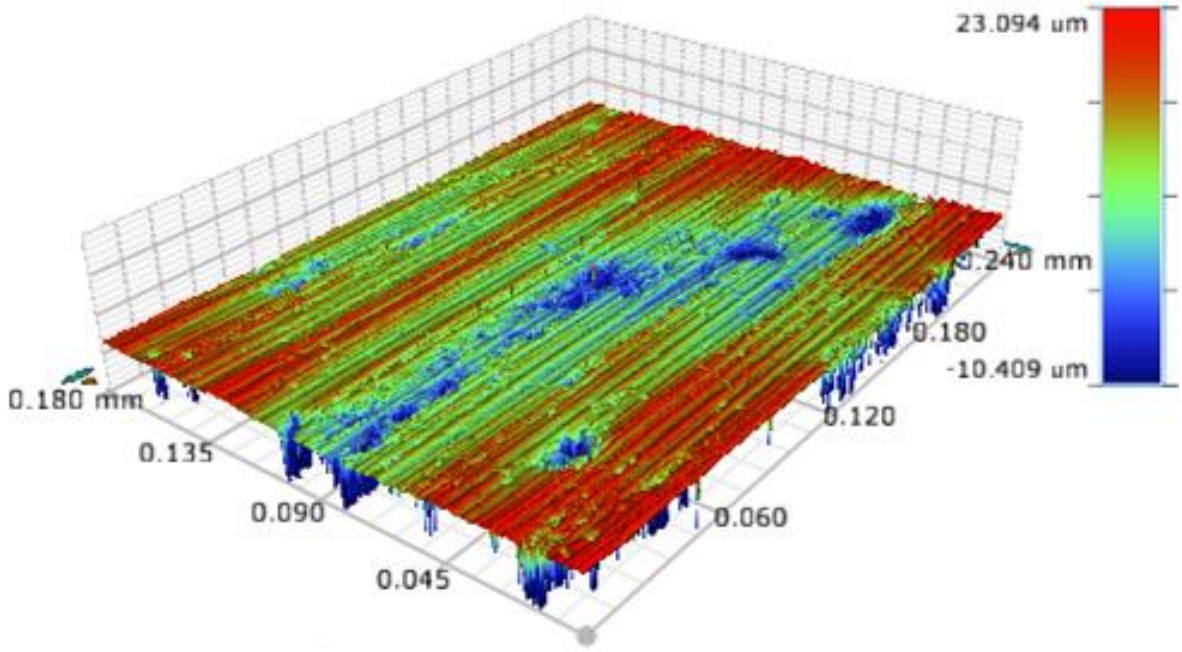

AAO, Side 2, spot 1, before friction tests:

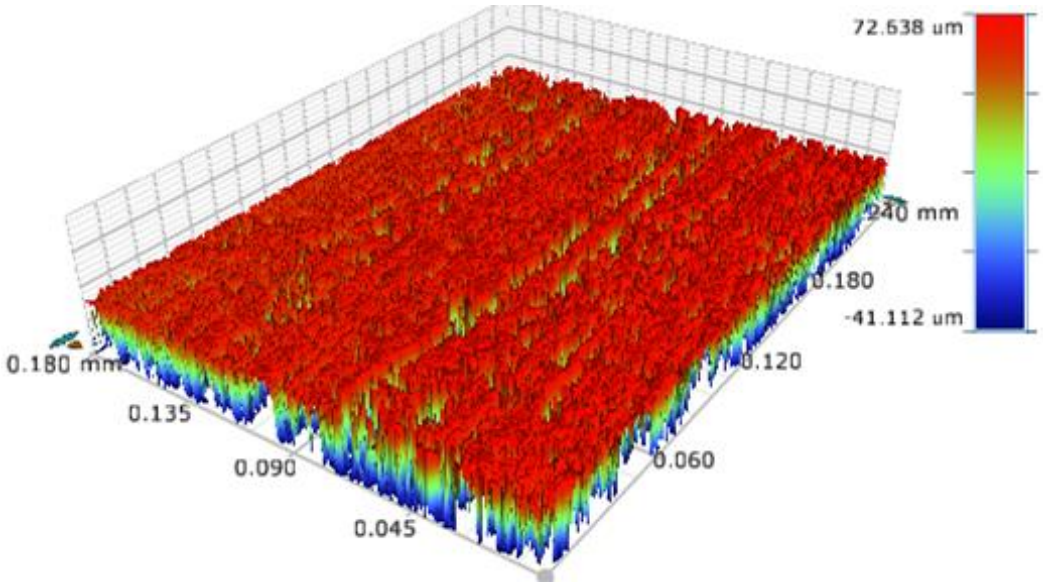

AAO, Side 2, spot 2, before friction tests:

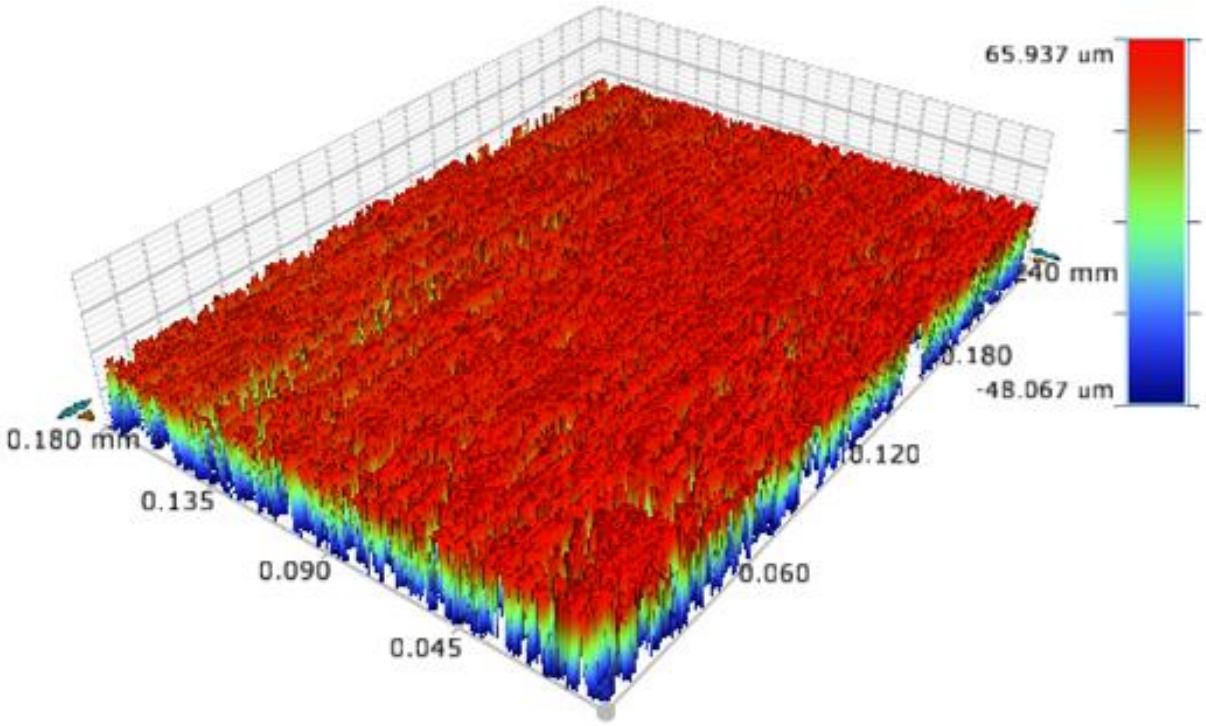

AAO, Side 2, spot 3, before friction tests:

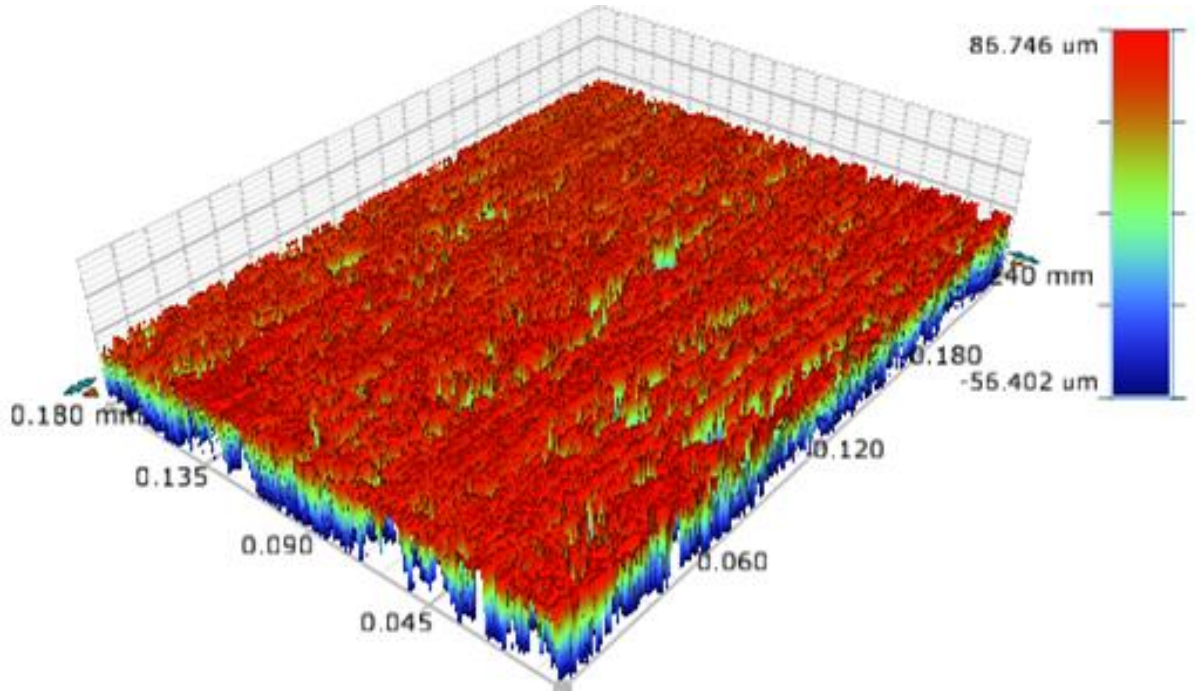

REF, spot 1, before friction tests:

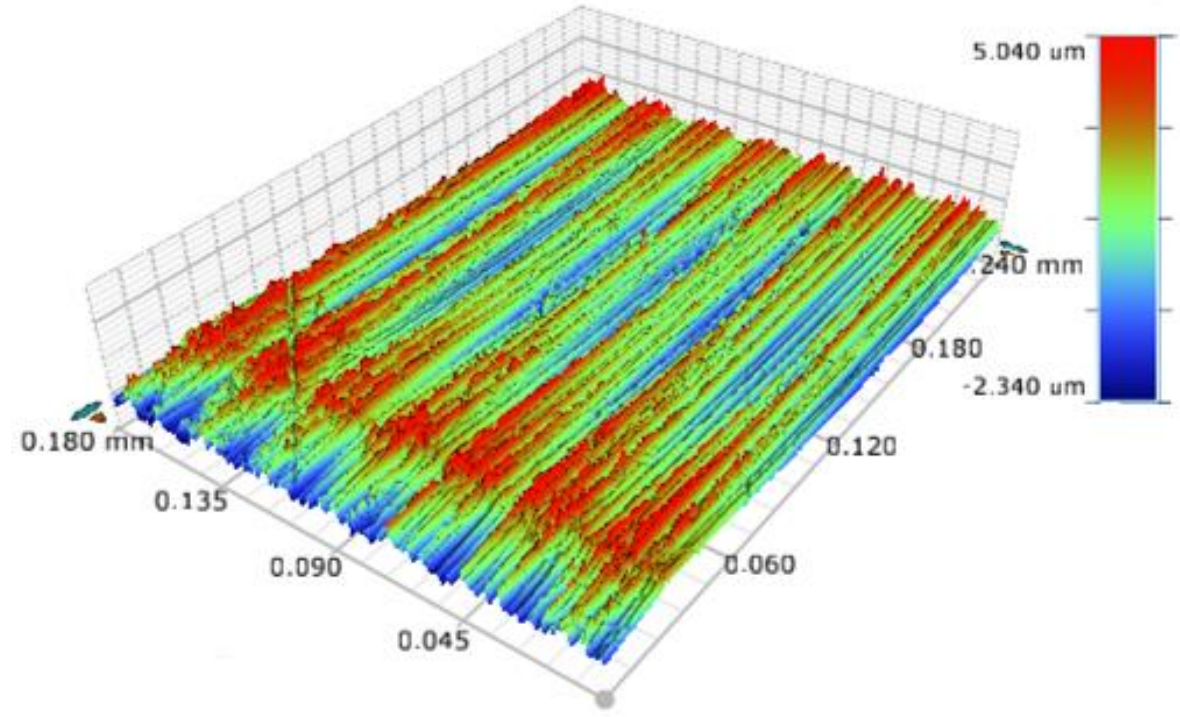

REF, spot 2, before friction tests:

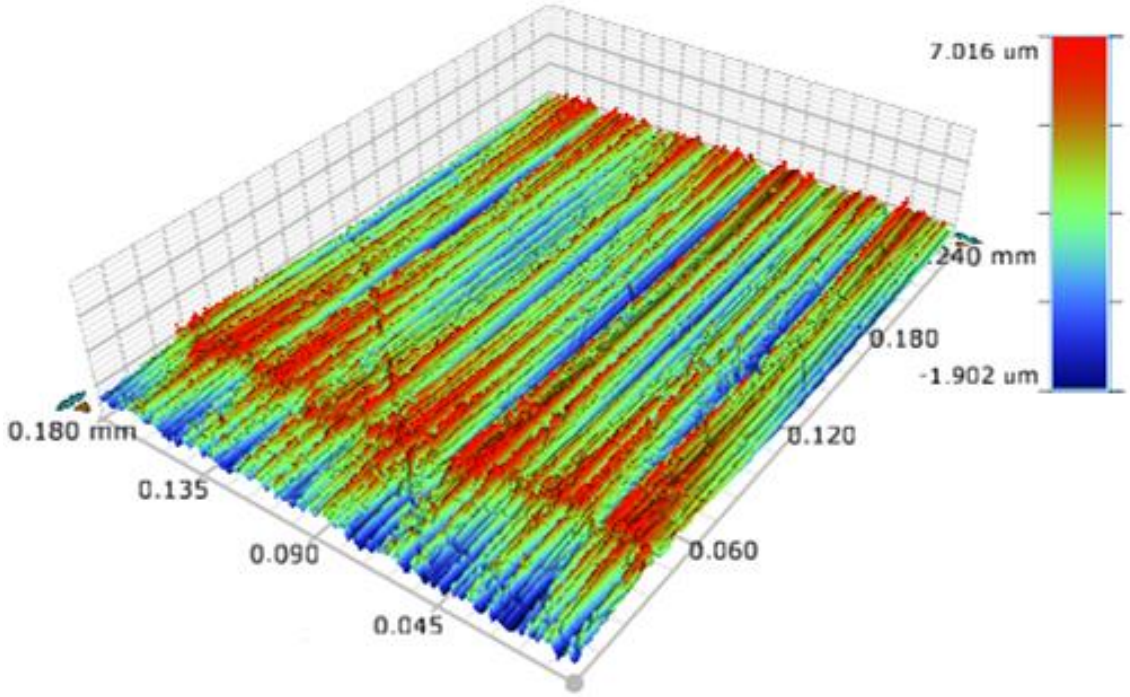

REF, spot 3, before friction tests:

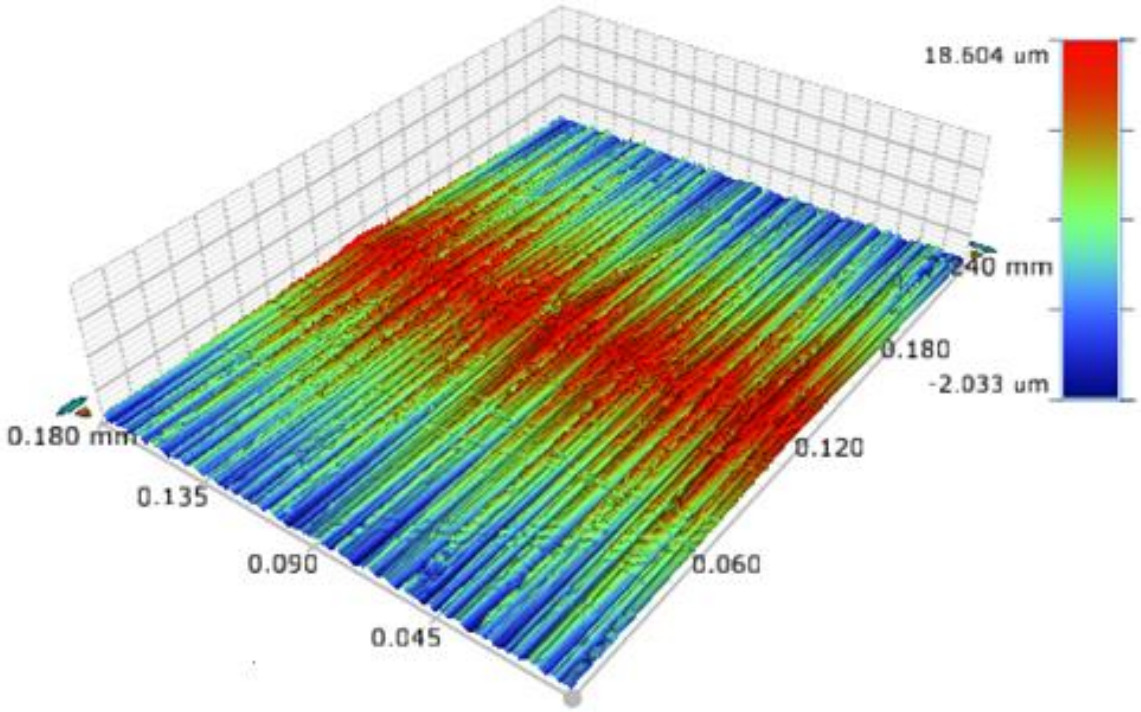

REF, spot 4, before friction tests:

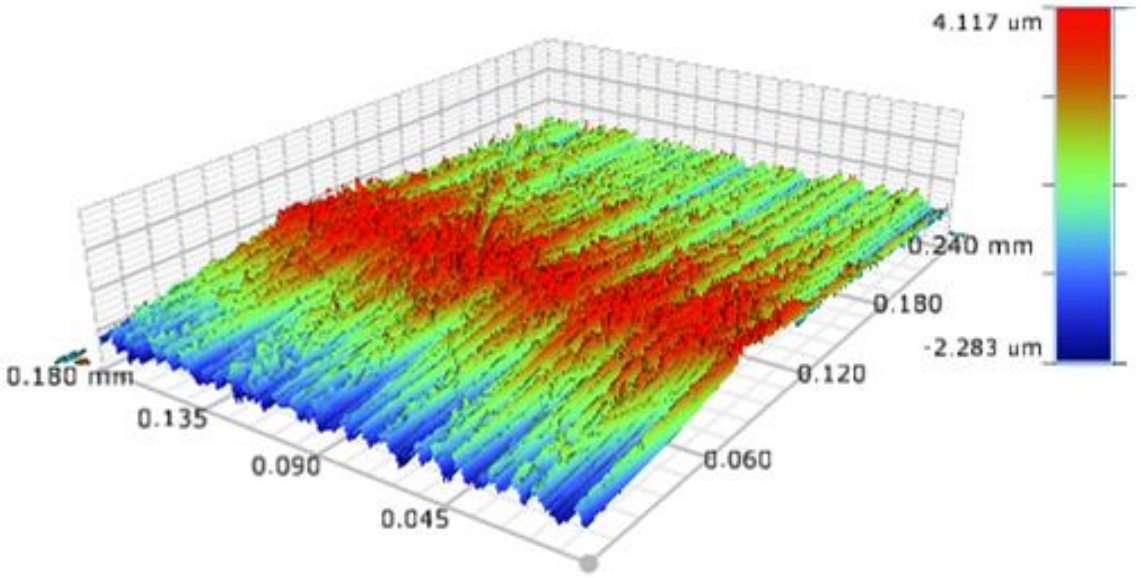

AAO, Side 1, spot 1, after friction tests:

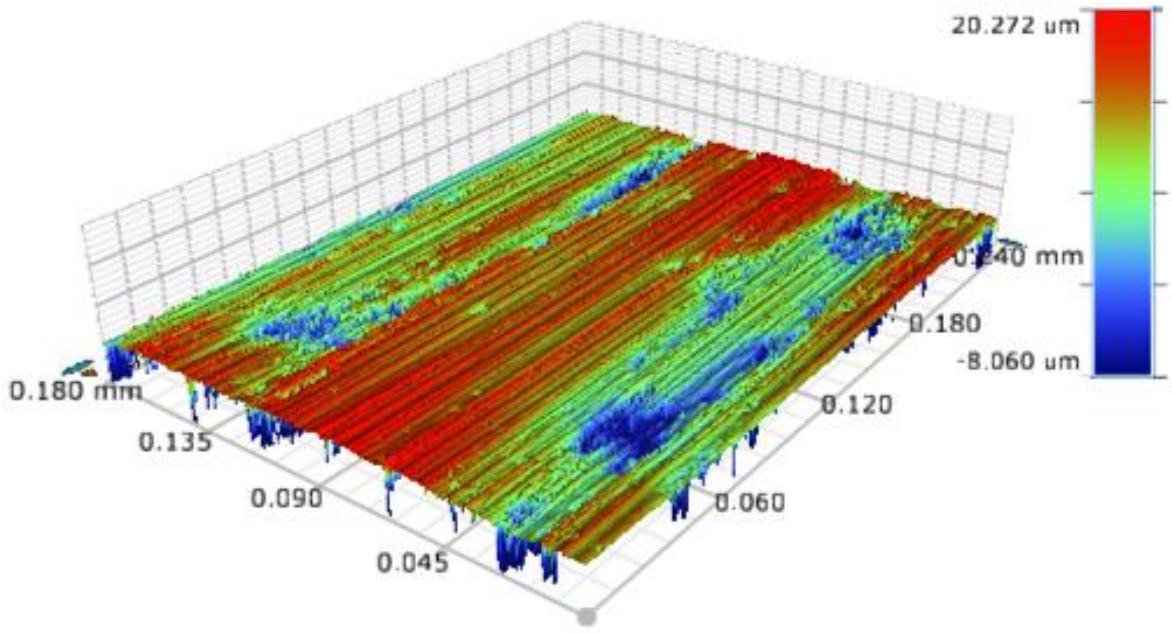

AAO, Side 1, spot 2, after friction tests:

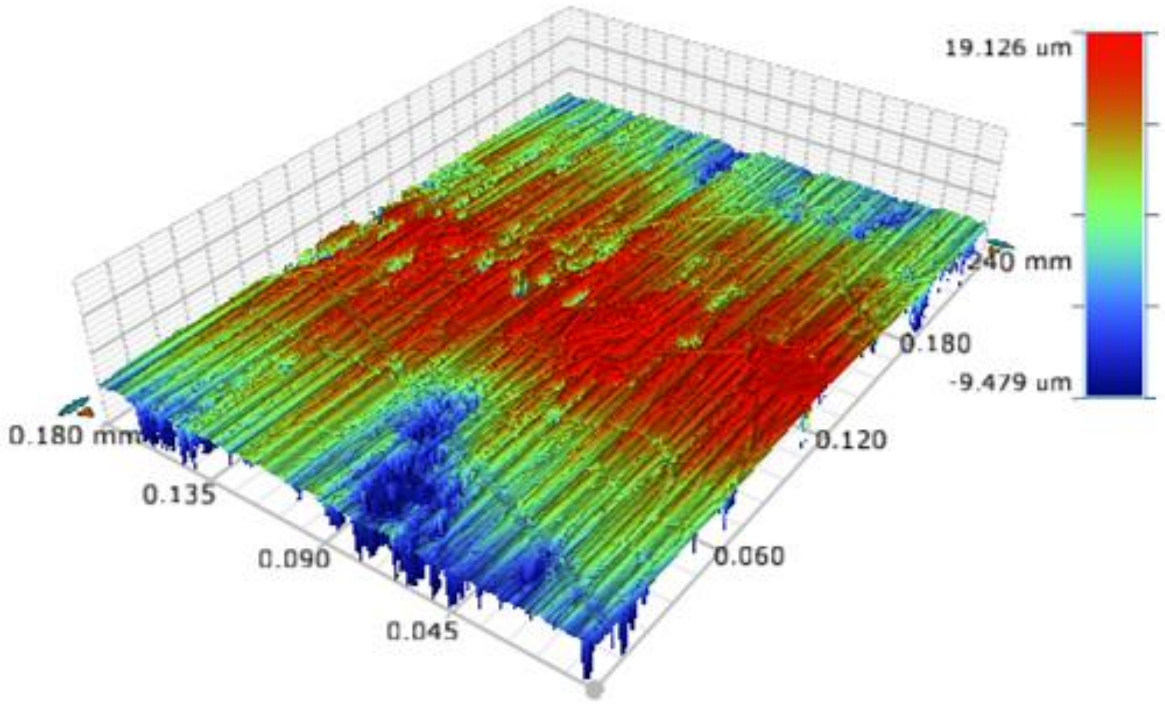

AAO, Side 1, spot 3, after friction tests:

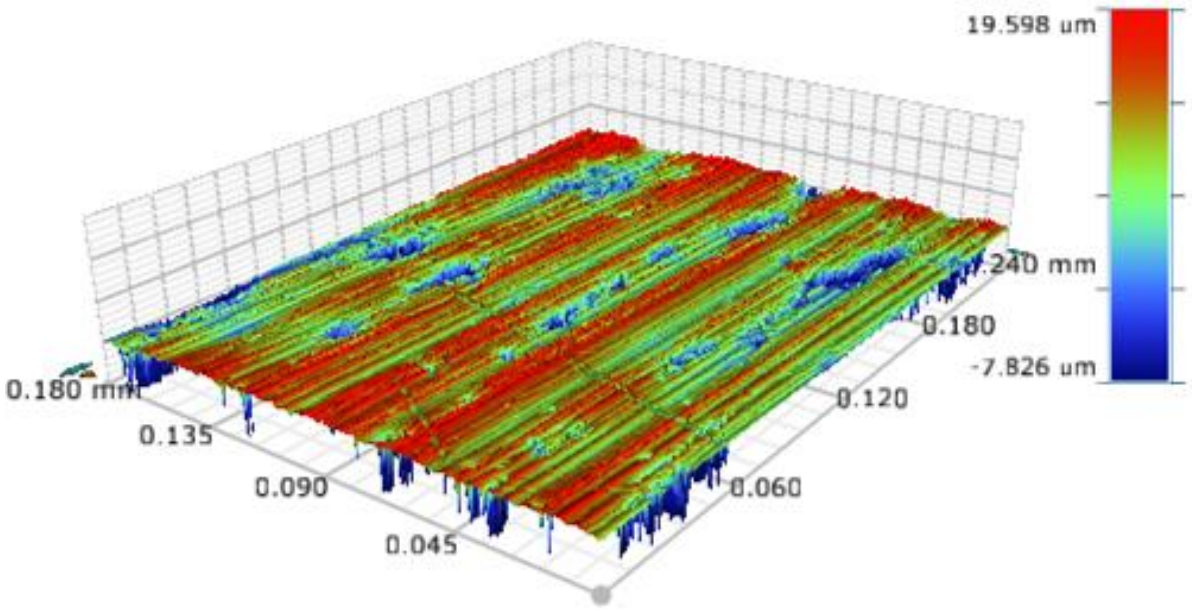

AAO, Side 2, spot 1, after friction tests:

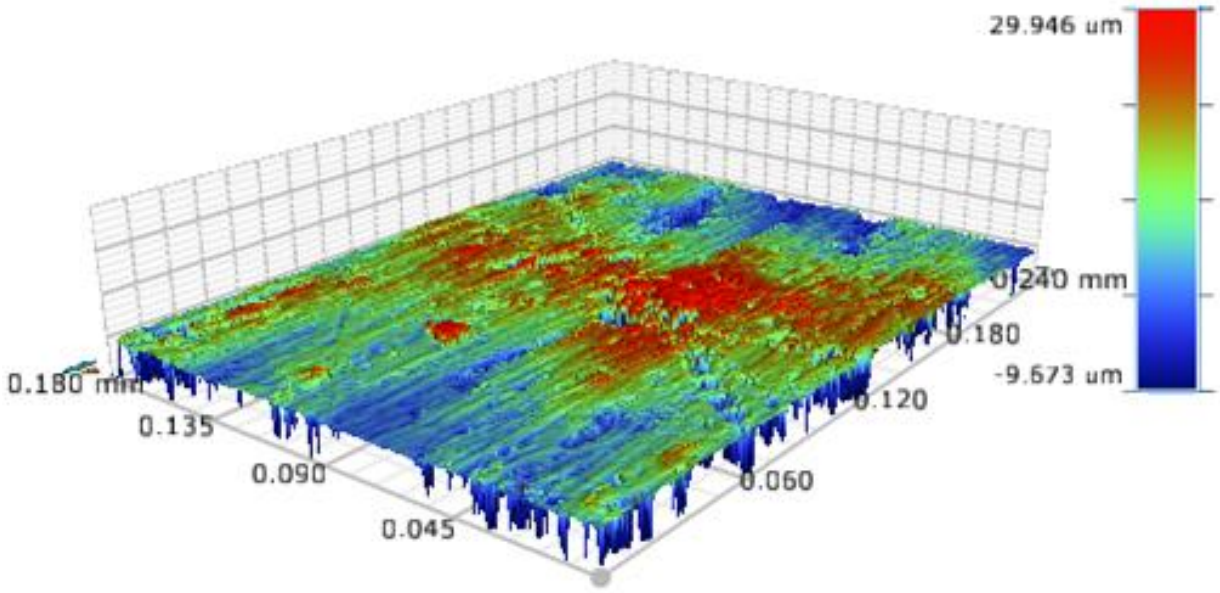

AAO, Side 2, spot 2, after friction tests:

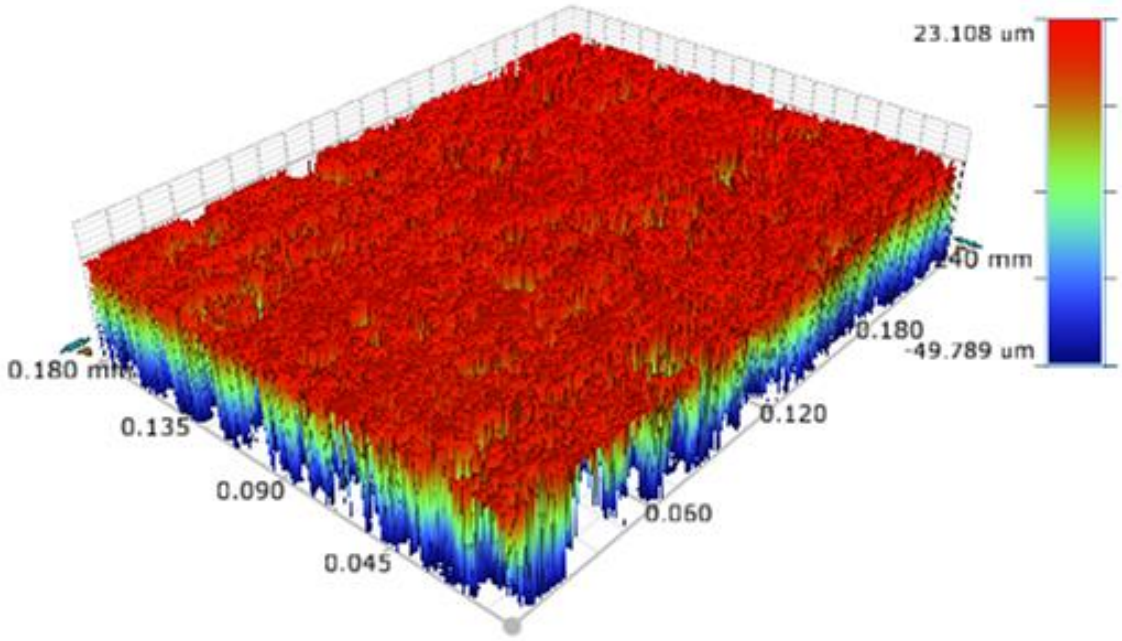

AAO, Side 2, spot 3, after friction tests:

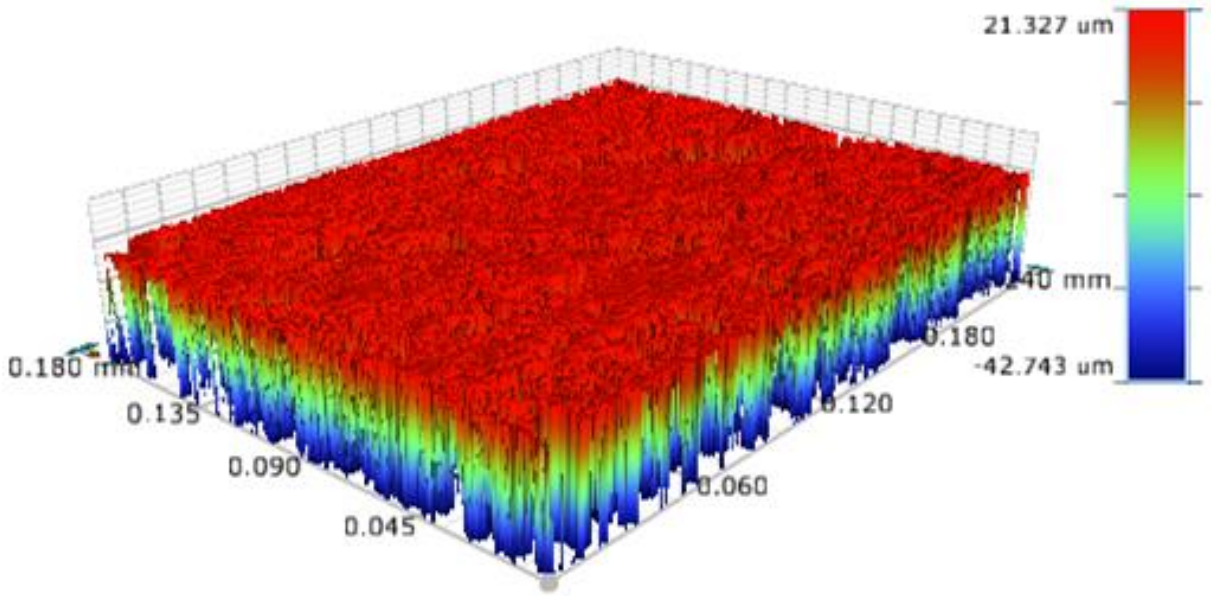

AAO, Side 2, spot 4, after friction tests:

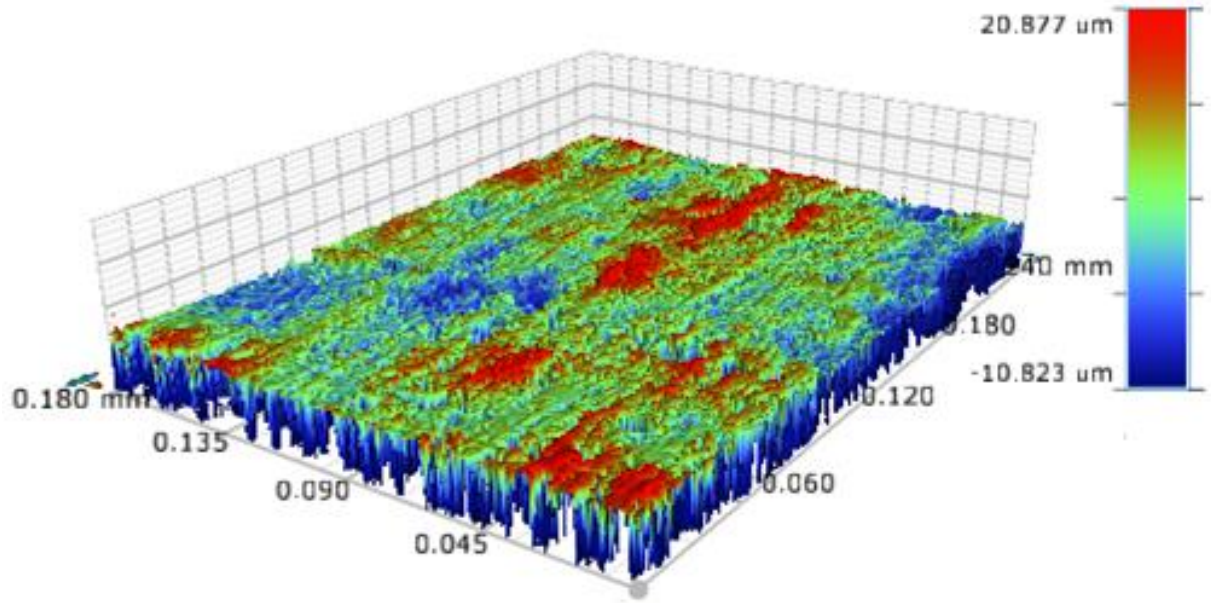

AAO, Side 2, spot 5, after friction tests:

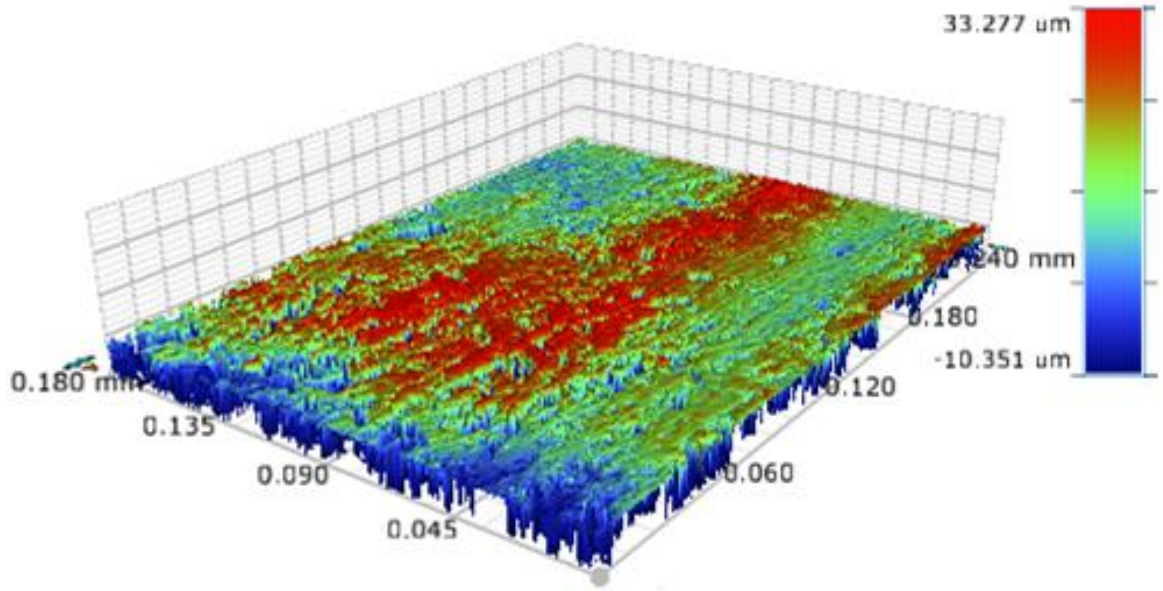

AAO, Side 2, spot 6, after friction tests:

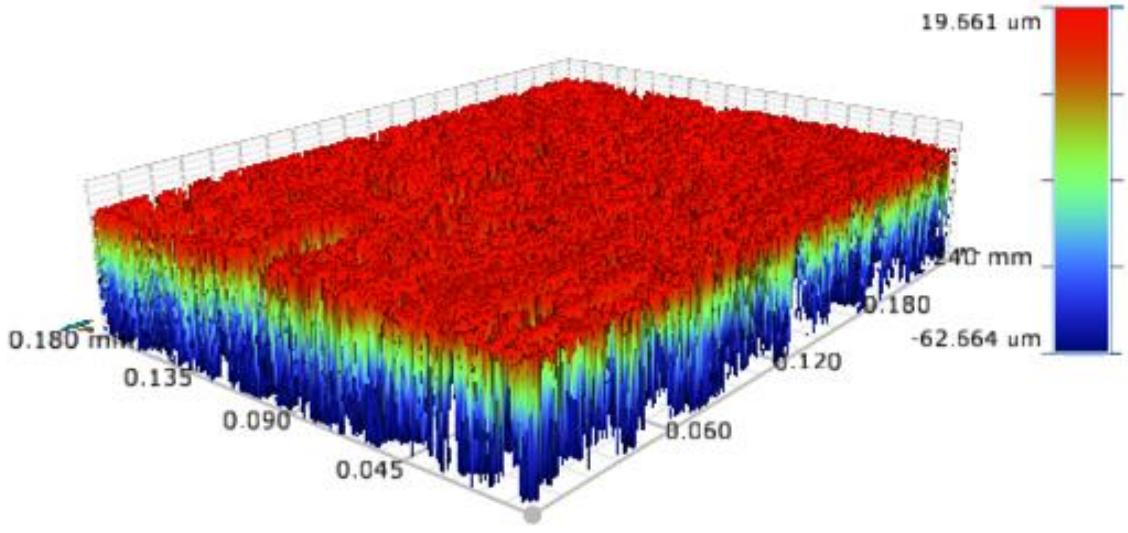

REF, spot 1, after friction tests:

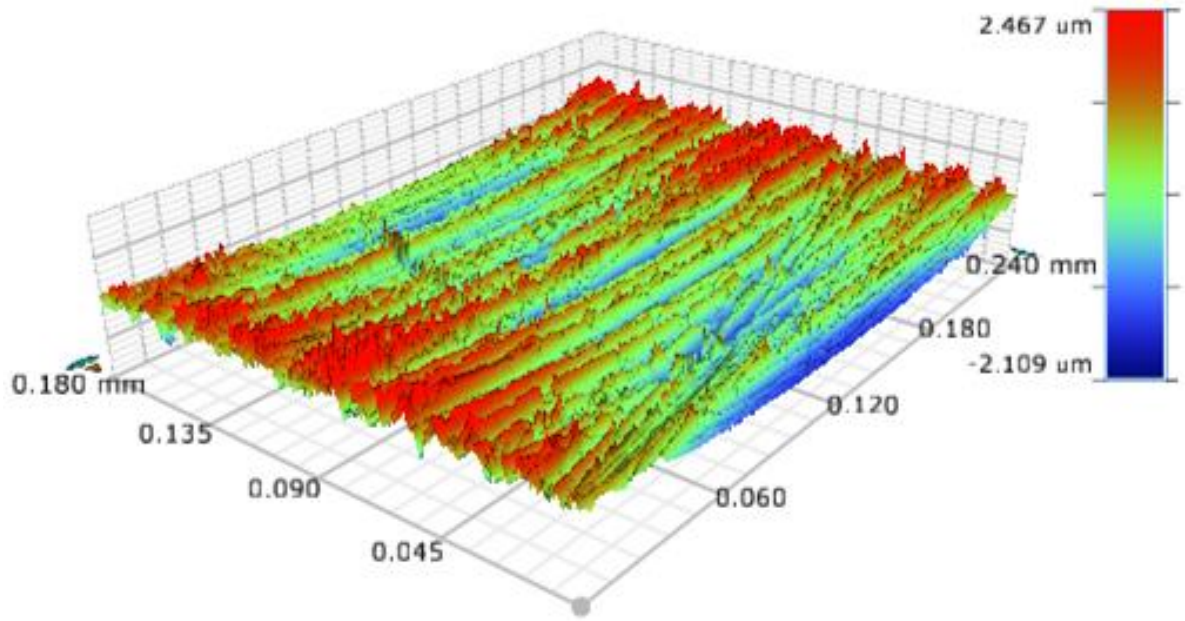

REF, spot 2, after friction tests:

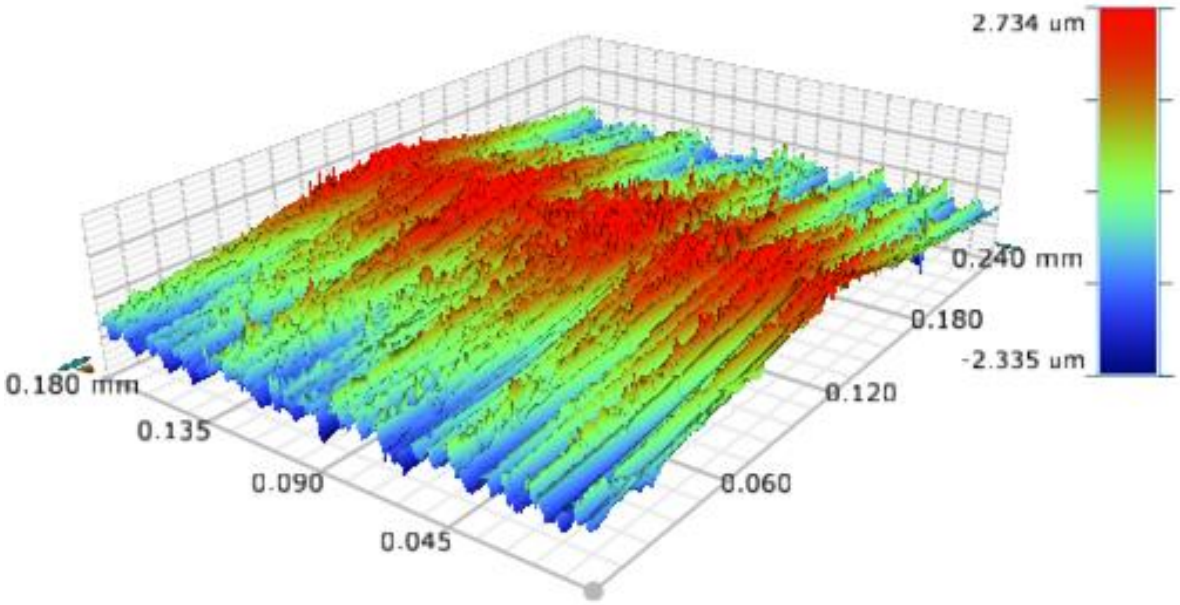

REF, spot 3, after friction tests:

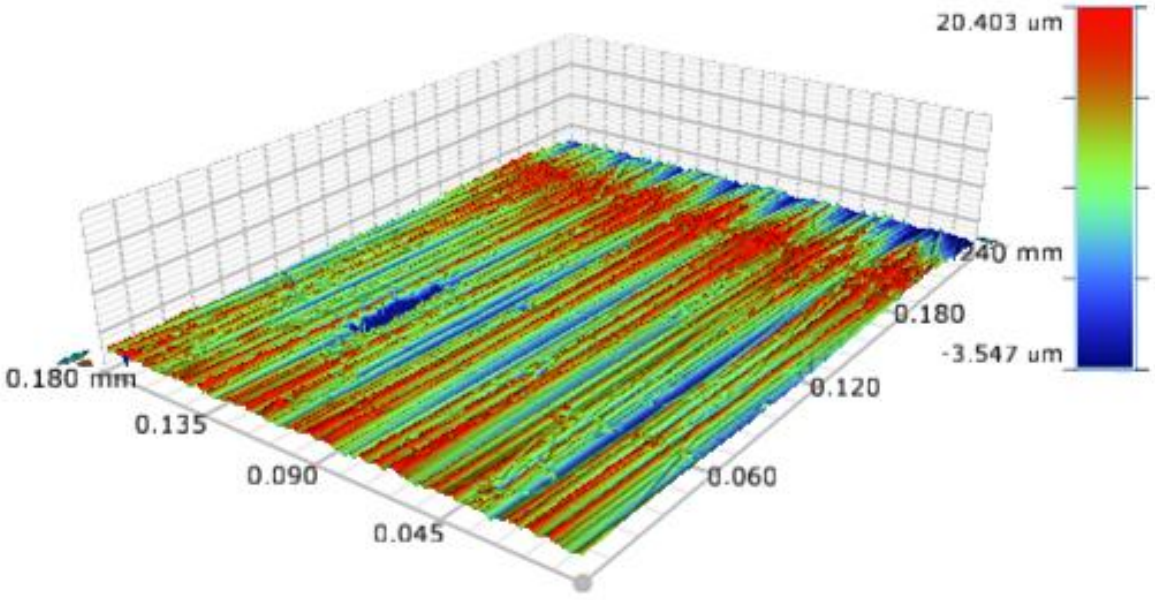

Appendix N: Snow lab images

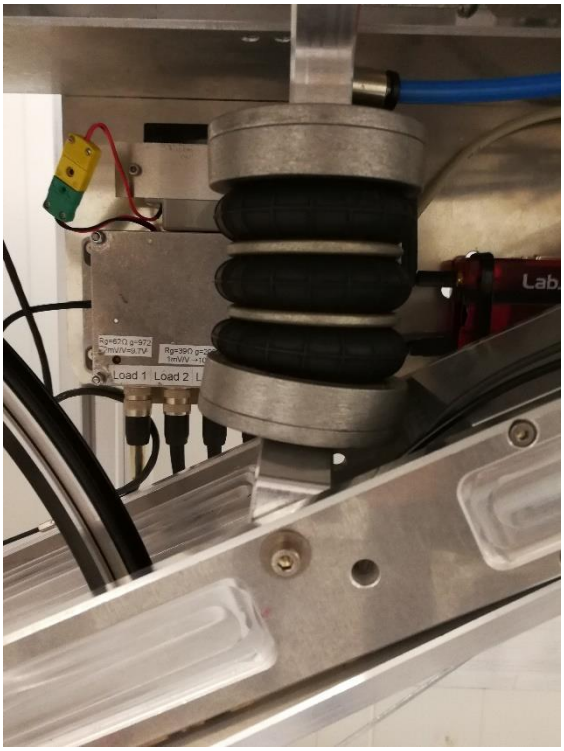

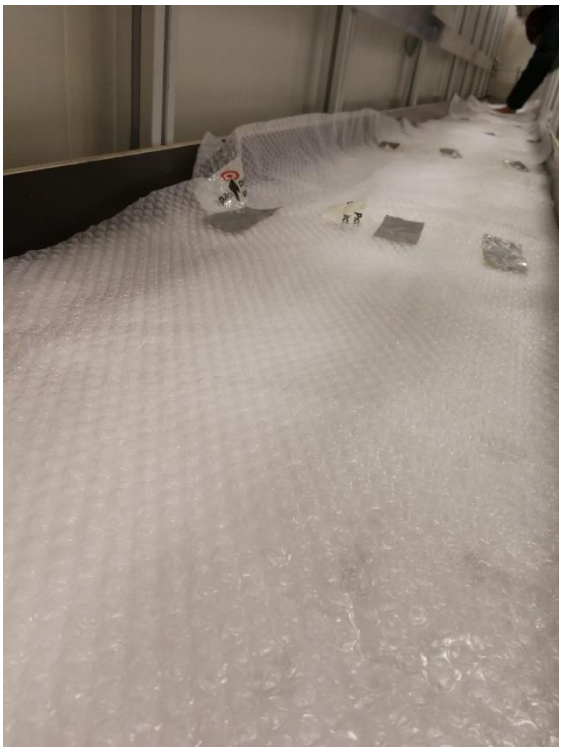

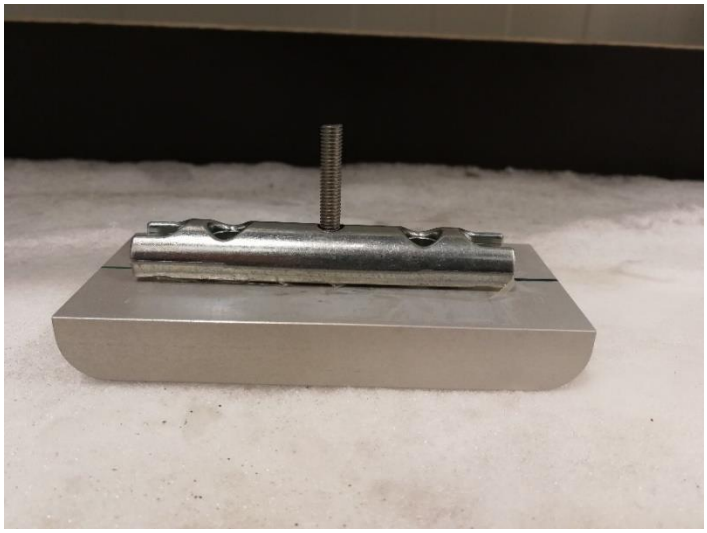

Appendix O: MATLAB code for determination of COF for all measurements

Note that this code is only given for one data set (AAO sample at -10 ºC and 2 m/s). The remaining three are similar, but with other variables.

```
clc; clear all; close all;
```

CONSTANTS

```
c=176; % Distance between point A and load cell [mm]
d=260; % Distance between point A and brakes [mm]
r_H=340; % Distance between center of wheel to snow base [mm]
r_B=313; % Distance between center of wheel to brakes [mm]
N=29.9; % Normal force [N]
```

COF (Note: First 8 lines of each Excel document is text)

```
files_in_this_folder_AA10 = dir;

number_of_files_AA10 = length(files_in_this_folder_AA10);

index_AA10 = 3;

C_AA10=zeros(600,40); % Preallocating space for COF matrix
T_AA10=zeros(600,40); % Preallocating space for time matrix
for index_AA10 = 3:number_of_files_AA10 % Looping files
filename_AA10 = files_in_this_folder_AA10(index_AA10).name;
if strcmpi(filename_AA10(end-4:end), '.xlsx') % Only Excel
  num_AA10 = xlsread(filename_AA10); % Reading Excel file

  % Checking which column, no. 2 or 3, the time vector is at
  if (num_AA10(12,2)~=8.9E-4) && (num_AA10(12,2)<1000)
      % I.e the Time vector is occupying column 2
    time_AA10=num_AA10(9:end,2);
  elseif (num_AA10(12,3)~=8.9E-4) && (num_AA10(12,3)<1000)
      % I.e the Time vector is at column 3
     time_AA10=num_AA10(9:end,3);
  end
```

```
  % Found the mean of the first five brake forces,
  % which becomes a zero point.
  % mean(zero_pointAA10(3:end))=56.5158.
  % Three first points are zero

  % Checking which column, no. 5 or 6, the brake force vector
  % is at zero_pointAA10(index_AA10)=mean(num_AA10(9:14,5))
   if num_AA10(12,5)<=1000 % I.e. Brake force is at column 5
       COF_AA10=(num_AA10(9:end,5)-
56.5158)*((c*r_B)/(d*r_H*N));
       % Subtracting the mean brake force of the first five
       % values to calculate COF
   else % I.e. the Brake force is at column 6
       COF_AA10=(num_AA10(9:end,6)-
56.5158)*((c*r_B)/(d*r_H*N));
   end

    figure(1); hold on % Plot all COFs(T)for entire track
    plot(time_AA10,COF_AA10);
    ylabel('Coefficient of fricton, μ');
    xlabel('Time [s]');
    title('COF for all runs in set for AAO sample at -10 °C
and 2 m/s');
    grid('on');
    grid('minor');
    yticks(-4:0.5:2);
    xticks(0:0.2:3);
    set(gca,'FontSize',20);
    set(gcf,'color','w');

    % Inserting COF vectors as columns in COF matrix
    C_AA10(1:length(COF_AA10),index_AA10-2)=COF_AA10;

    % Inserting Time vectors as columns in Time matrix
    T_AA10(1:length(time_AA10),index_AA10-2)=time_AA10;

    figure(2) % Plots a mean COF of all tests
    mean_C_AA10=mean(C_AA10(1:374,1:25),2); % Mean COF on each
row
```

```
    mean_T_AA10=mean(T_AA10(1:374,1:25),2); % Mean time on
each row
    plot(mean_T_AA10,mean_C_AA10);
    ylabel('Average coefficient of fricton, μ');
    xlabel('Average time [s]');
    title('Average coefficient of fricton, μ, for AAO at -10
°C and 2 m/s');
    grid('on');
    grid('minor');
    yticks(-0.15:0.05:0.2);
    xticks(0:0.2:2);
    set(gca,'FontSize',20);
    set(gcf,'color','w');
end
end

figure(3) % Plots the mean COF of all tests within 1.7-2 s
sel1=find(mean_T_AA10>1.7 & mean_T_AA10 < 2); % Velocity is
constantly 2 m/s
mean_T_AA10_sel=mean_T_AA10(sel1);
mean_C_AA10_sel=mean_C_AA10(sel1);
plot(mean_T_AA10_sel,mean_C_AA10_sel);
ylabel('Average coefficient of fricton, μ');
xlabel('Average time [s]');
title('Average coefficient of fricton, μ, for AAO at -10 C and
constant velocity 2 m/s');
legend('Experimental data');
grid('on');
grid('minor');
set(gca,'FontSize',20);
set(gcf,'color','w');
```

Appendix P: MATLAB code for statistical analysis and boxplot of COF

BOXPLOT

```
figure(13)

% Matrix with four columns; average COF values for each sample
between 1.7-2 s
x=[mean_C_AA10_sel,mean_C_REF10_sel,mean_C_AA27_sel,mean_C_REF
27_sel];
Sample_name={'AAO, -10 °C, 2 m/s';'REF, -10 °C, 2 m/s';'AAO, -
2.7 °C, 2 m/s';'REF, -2.7 °C, 2 m/s'};
boxplot(x,Sample_name,'Colors','rb');
ylabel('Coefficient of friction, μ');
title('Average coefficient of friction, μ, for all samples in
the time interval 1.7-2 s');
set(gca,'FontSize',20);
set(gcf,'color','w');
```

T-TEST

```
[h10,p10]=ttest2(mean_C_AA10_sel,mean_C_REF10_sel,'Vartype','u
nequal')
[h27,p27]=ttest2(mean_C_AA27_sel,mean_C_REF27_sel,'Vartype','u
nequal')
[hAA,pAA]=ttest2(mean_C_AA10_sel,mean_C_AA27_sel,'Vartype','un
equal')
[hREF,pREF]=ttest2(mean_C_REF10_sel,mean_C_REF27_sel,'Vartype'
,'unequal')
```

MEAN COFS AND STANDARD DEVIATIONS

```
% Mean and STD for AAO at - 10 C and 2 m/s
mean_mean_C_AA10_sel=mean(mean_C_AA10_sel)
std_mean_C_AA10_sel=std(mean_C_AA10_sel)

% Mean and STD for REF at - 10 C and 2 m/s
mean_mean_C_REF10_sel=mean(mean_C_REF10_sel)
std_mean_C_REF10_sel=std(mean_C_REF10_sel)
```

```
% Mean and STD for AAO at - 2.7 C and 2 m/s
mean_mean_C_AA27_sel=mean(mean_C_AA27_sel)
std_mean_C_AA27_sel=std(mean_C_AA27_sel)

% Mean and STD for REF at - 2.7 C and 2 m/s
mean_mean_C_REF27_sel=mean(mean_C_REF27_sel)
std_mean_C_REF27_sel=std(mean_C_REF27_sel)
```

Appendix Q: MATLAB code for COF values for first five and last five tests

Note that this code is only given for one data set (AAO sample at -10 ºC and 2 m/s), but the remaining three are similar, but with other variables.

```
clc; clear all; close all;
```

CONSTANTS

```
c=176; % Distance between point A and load cell [mm]
d=260; % Distance between point A and brakes [mm]
r_H=340; % Distance between center of wheel to snow base [mm]
r_B=313; % Distance between center of wheel to brakes [mm]
N=29.9; % Normal force [N]
```

COF (Note: First 8 lines of each Excel document is text)

```
files_in_this_folder_AA10 = dir; % Only analyzing files in the
same folder as this MATLAB script
number_of_files_AA10 = length(files_in_this_folder_AA10); %
Counting the total number of files in the folder
index_AA10 = 3;
C_AA10=zeros(600,40); % Preallocating space for COF matrix
T_AA10=zeros(600,40); % Preallocating space for time matrix

for index_AA10 = 3:number_of_files_AA10 % Looping through each
file
    filename_AA10 =
files_in_this_folder_AA10(index_AA10).name;
    if strcmpi(filename_AA10(end-4:end), '.xlsx') % Only
analyzing Excel files
          num_AA10 = xlsread(filename_AA10); % Reading the
data in the Excel file

  % Checking which column, no. 2 or 3, the time vector is at
  if (num_AA10(12,2)~=8.9E-4) && (num_AA10(12,2)<1000)
      % I.e the Time vector is at column 2
    time_AA10=num_AA10(9:end,2);
  elseif (num_AA10(12,3)~=8.9E-4) && (num_AA10(12,3)<1000)
```

```
      % I.e the Time vector is at column 3
     time_AA10=num_AA10(9:end,3);
  end

  % zero_pointAA10(index_AA10)=mean(num_AA10(9:14,5));
  % The mean of the first five brake forces, is zero point.
  % mean(zero_pointAA10(3:end))=56.5158.
  % Three first points are zero

  % Checking which column, 5 or 6, the brake force vector is
   if num_AA10(12,5)<=1000
       % I.e. the Brake force is at column 5
       COF_AA10=(num_AA10(9:end,5)-
56.5158)*((c*r_B)/(d*r_H*N));
       % Subtracting mean brake force of first five
   else % I.e. the Brake force is at column 6
       COF_AA10=(num_AA10(9:end,6)-
56.5158)*((c*r_B)/(d*r_H*N));
   end

    C_AA10(1:length(COF_AA10),index_AA10-2)=COF_AA10;
    % COF vectors as columns in COF matrix
    T_AA10(1:length(time_AA10),index_AA10-2)=time_AA10;
    % Time vectors as columns in Time matrix

    figure(1) % Plots a mean COF of first and last five tests
    mean_C_AA10_start=mean(C_AA10(1:374,1:5),2);
    % Mean of COF on each row of first five tests
    mean_T_AA10_start=mean(T_AA10(1:374,1:5),2);
    % Mean of time on each row of first five tests
    plot(mean_T_AA10_start,mean_C_AA10_start,'-r');
    hold on;

    mean_C_AA10_finish=mean(C_AA10(1:374,20:25),2);
    % Mean of COF on each row of last five tests
    mean_T_AA10_finish=mean(T_AA10(1:374,20:25),2);
    % Mean of time on each row of last five tests
    plot(mean_T_AA10_finish,mean_C_AA10_finish,'-b');
    hold off;
```

```
    legend('First five tests','Last five tests');
    ylabel('Average coefficient of fricton, μ');
    xlabel('Average time [s]');
    title('Average coefficient of fricton, μ, for AAO at -10
°C and 2 m/s');
    grid('on');
    grid('minor');
    set(gca,'FontSize',20);
    set(gcf,'color','w');

    end
end

figure(2) % Plots the mean COF of first and last five tests
within 1.7-2 s
sel1=find(mean_T_AA10_start>1.7 & mean_T_AA10_start < 2);
mean_T_AA10_sel_start=mean_T_AA10_start(sel1);
mean_C_AA10_sel_start=mean_C_AA10_start(sel1);
plot(mean_T_AA10_sel_start,mean_C_AA10_sel_start,'-r');
hold on;

mean_T_AA10_sel_finish=mean_T_AA10_finish(sel1);
mean_C_AA10_sel_finish=mean_C_AA10_finish(sel1);
plot(mean_T_AA10_sel_finish,mean_C_AA10_sel_finish,'-b');

ylabel('Average coefficient of fricton, μ');
xlabel('Average time [s]');
title('Average coefficient of fricton, μ, for AAO at -10 C and
constant velocity 2 m/s');
legend('First five tests','Last five tests');
grid('on');
grid('minor');
set(gca,'FontSize',20);
set(gcf,'color','w');
```

MEAN COFS AND STANDARD DEVIATIONS

```
% Mean and STD for first five tests for AAO at - 10 C and 2
m/s
```

```
mean_mean_C_AA10_sel_start=mean(mean_C_AA10_sel_start)
std_mean_C_AA10_sel_start=std(mean_C_AA10_sel_start)

% Mean and STD for last five tests for AAO at - 10 C and 2 m/s
mean_mean_C_AA10_sel_finish=mean(mean_C_AA10_sel_finish)
std_mean_C_AA10_sel_finish=std(mean_C_AA10_sel_finish)
```

T-TEST

```
[hAA10_abrade,pAA10_abrade]=ttest2(mean_C_AA10_sel_start,mean_
C_AA10_sel_finish,'Vartype','unequal')
```

Appendix R: COF plots

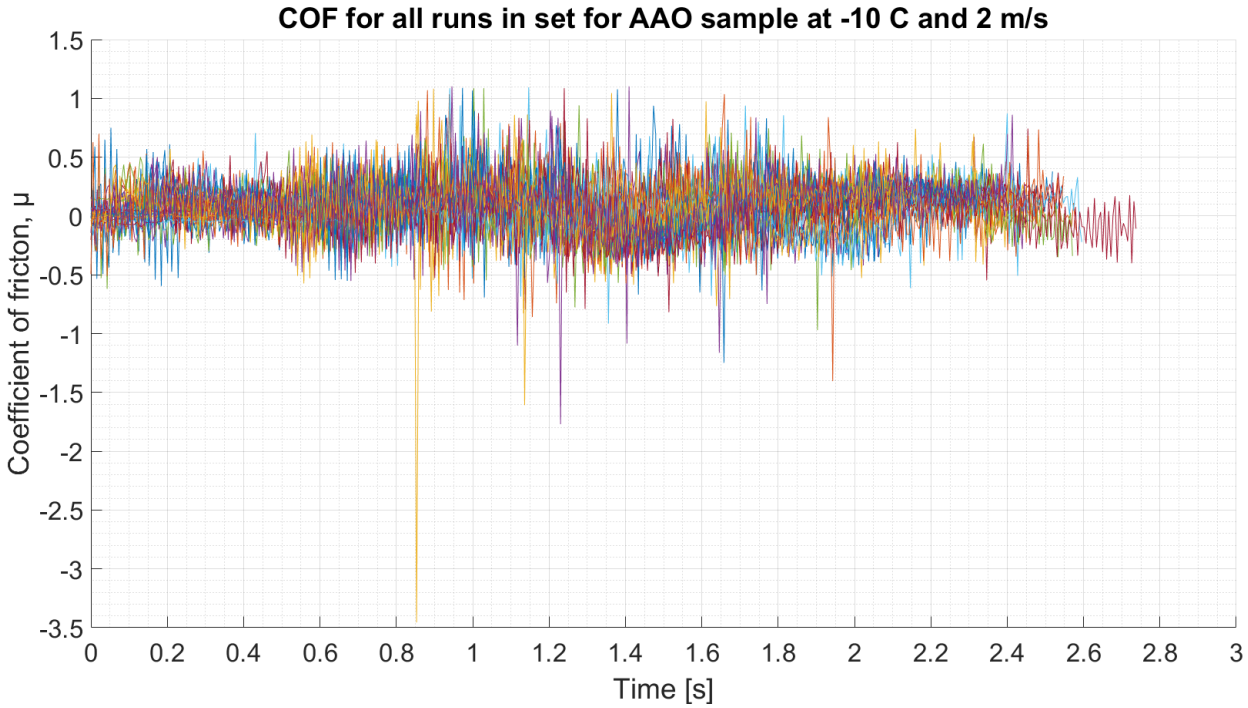

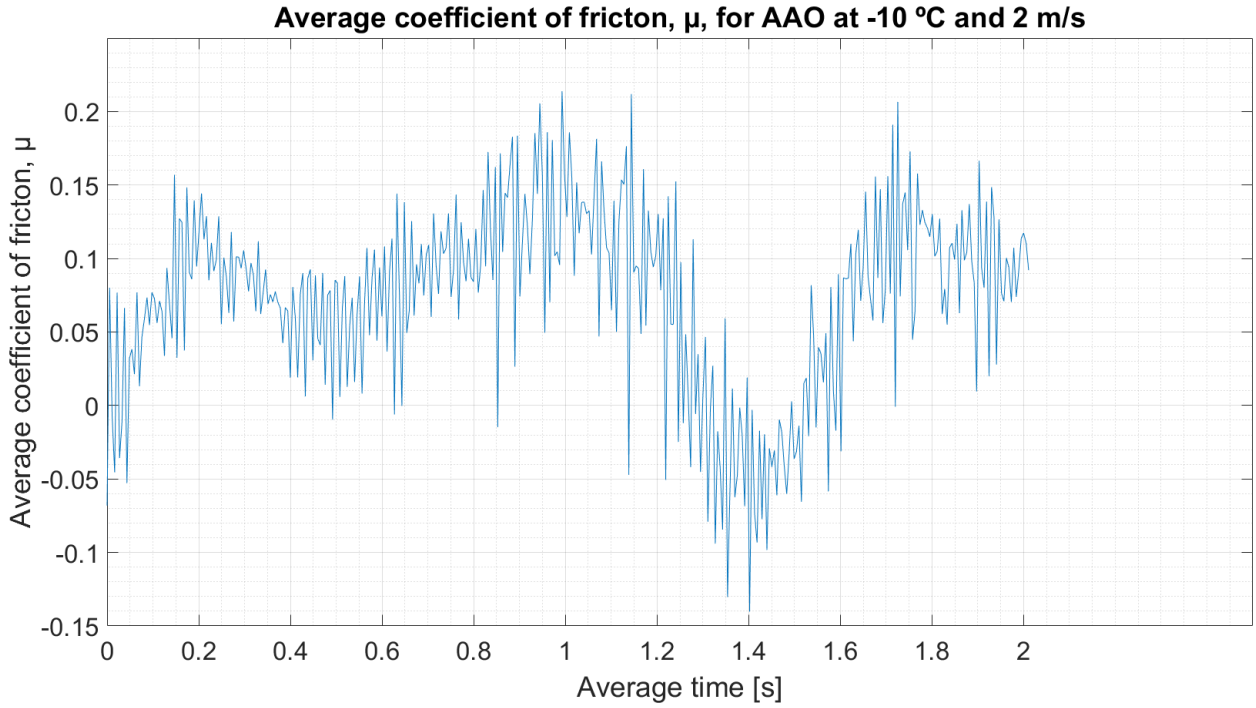

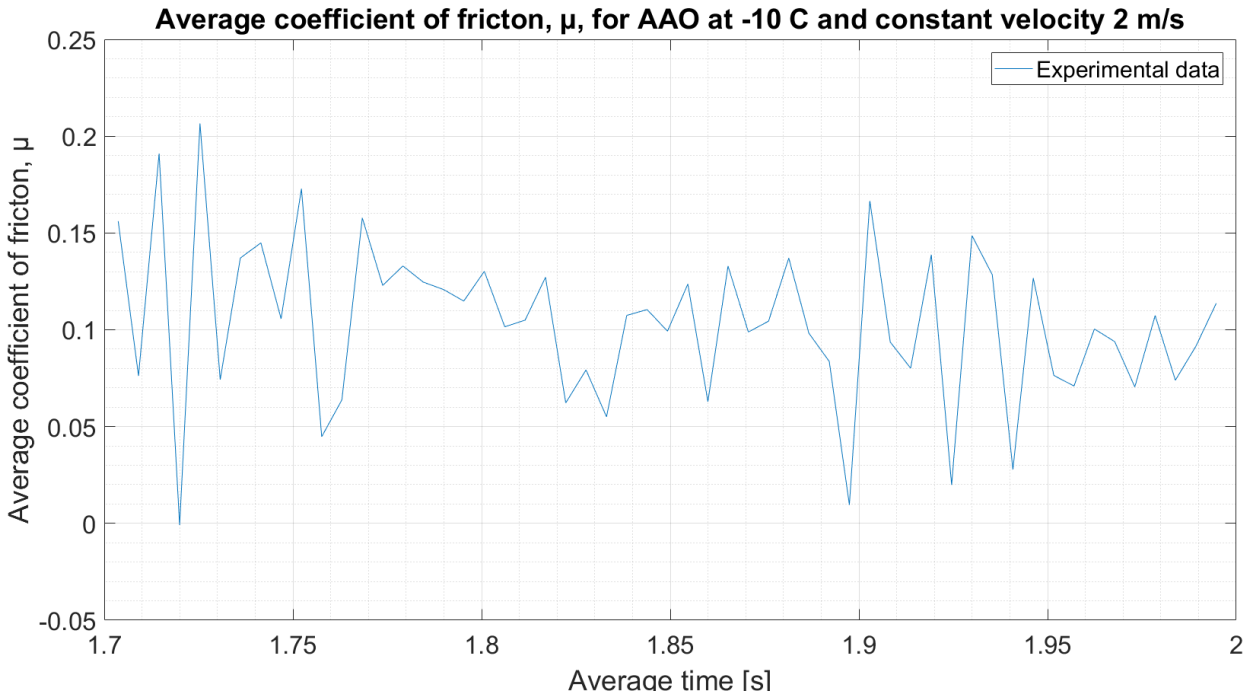
Average coefficient of fricton, μ, for AAO at -10 C and constant velocity 2 m/s
Experimental data
Average coefficient of fricton, μ
Average time [s]
0.25
0.2
0.15
0.1
0.05
0
-0.05
1.7
1.75
1.8
1.85
1.9
1.95
2

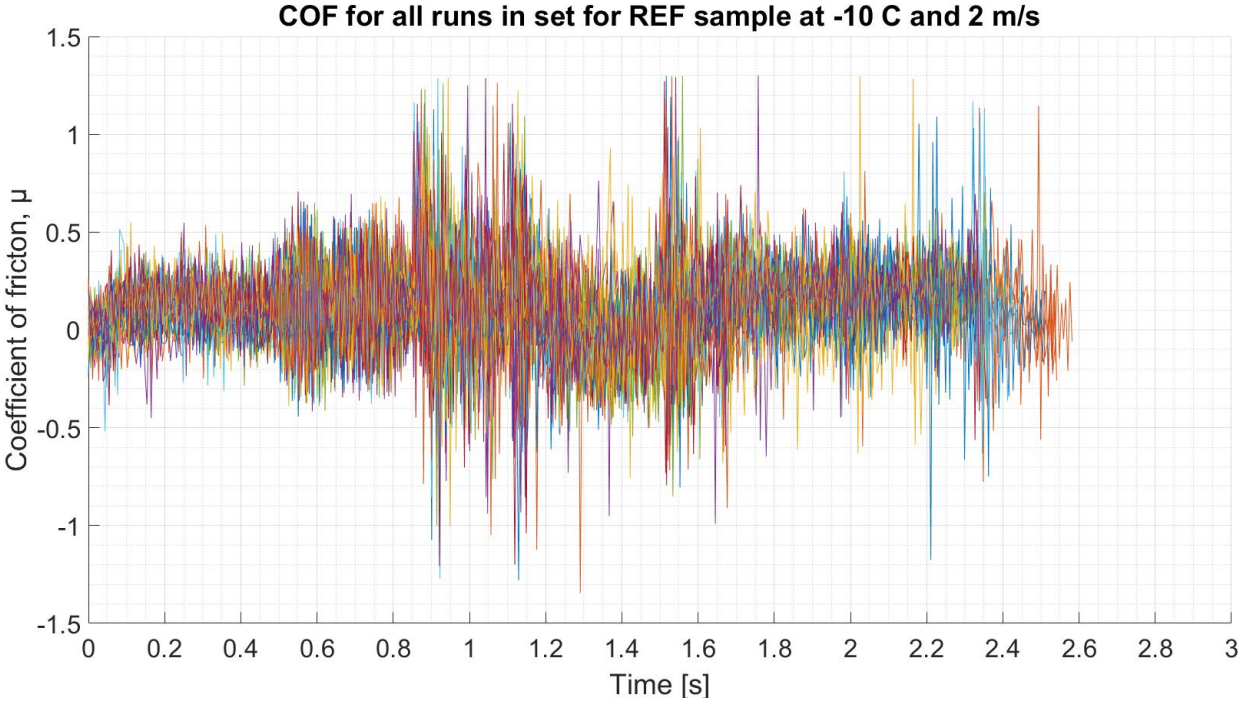
COF for all runs in set for REF sample at -10 C and 2 m/s
Coefficient of fricton, μ
Time [s]
1.5
1
0.5
0
-0.5
-1
-1.5
0
0.2
0.4
0.6
0.8
1
1.2
1.4
1.6
1.8
2
2.2
2.4
2.6
2.8
3

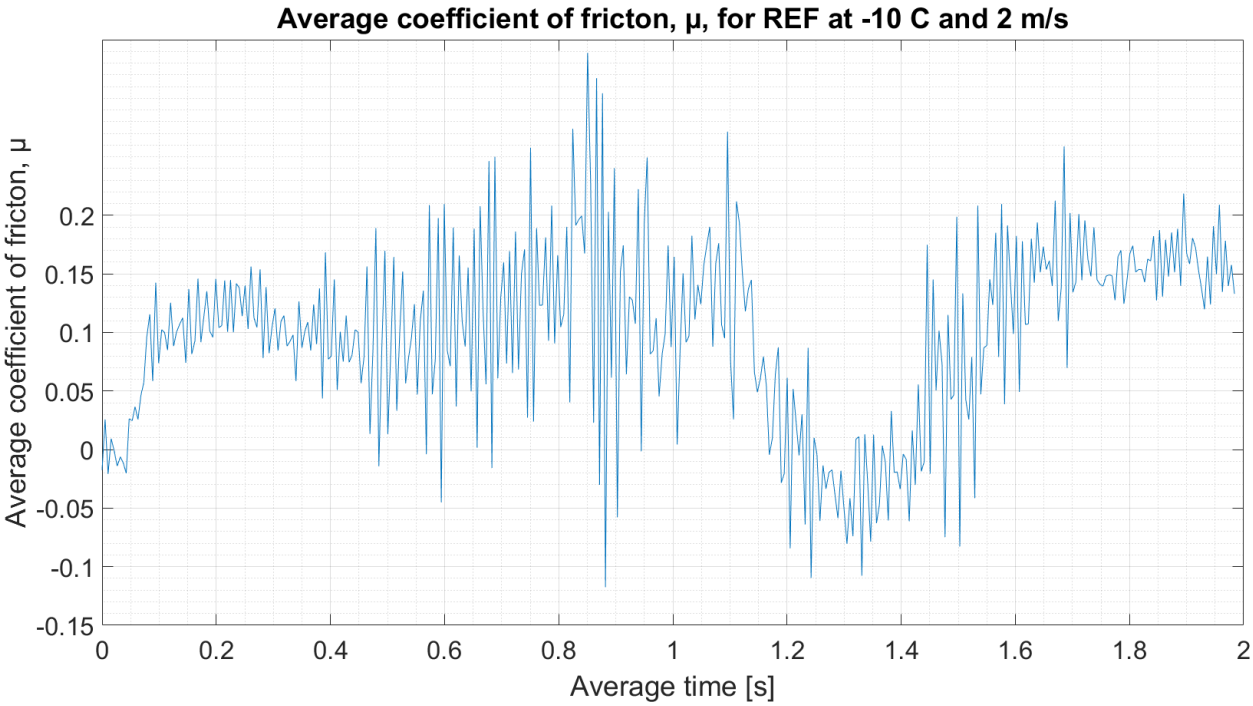
Average coefficient of fricton, μ, for REF at -10 C and 2 m/s
Average coefficient of fricton, μ
0.2
0.15
0.1
0.05
0
-0.05
-0.1
-0.15
0
0.2
0.4
0.6
0.8
1
1.2
1.4
1.6
1.8
2
Average time [s]

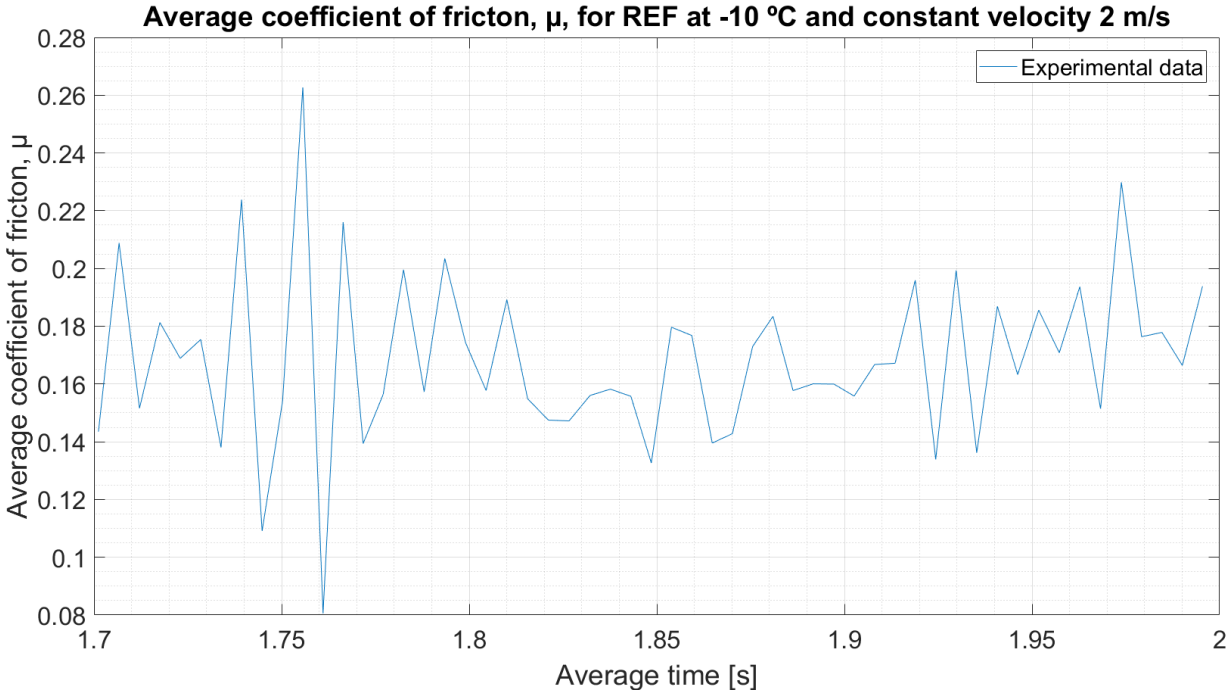
Average coefficient of fricton, μ, for REF at -10 ºC and constant velocity 2 m/s
Experimental data
Average coefficient of fricton, μ
0.28
0.26
0.24
0.22
0.2
0.18
0.16
0.14
0.12
0.1
0.08
1.7
1.75
1.8
1.85
1.9
1.95
2
Average time [s]

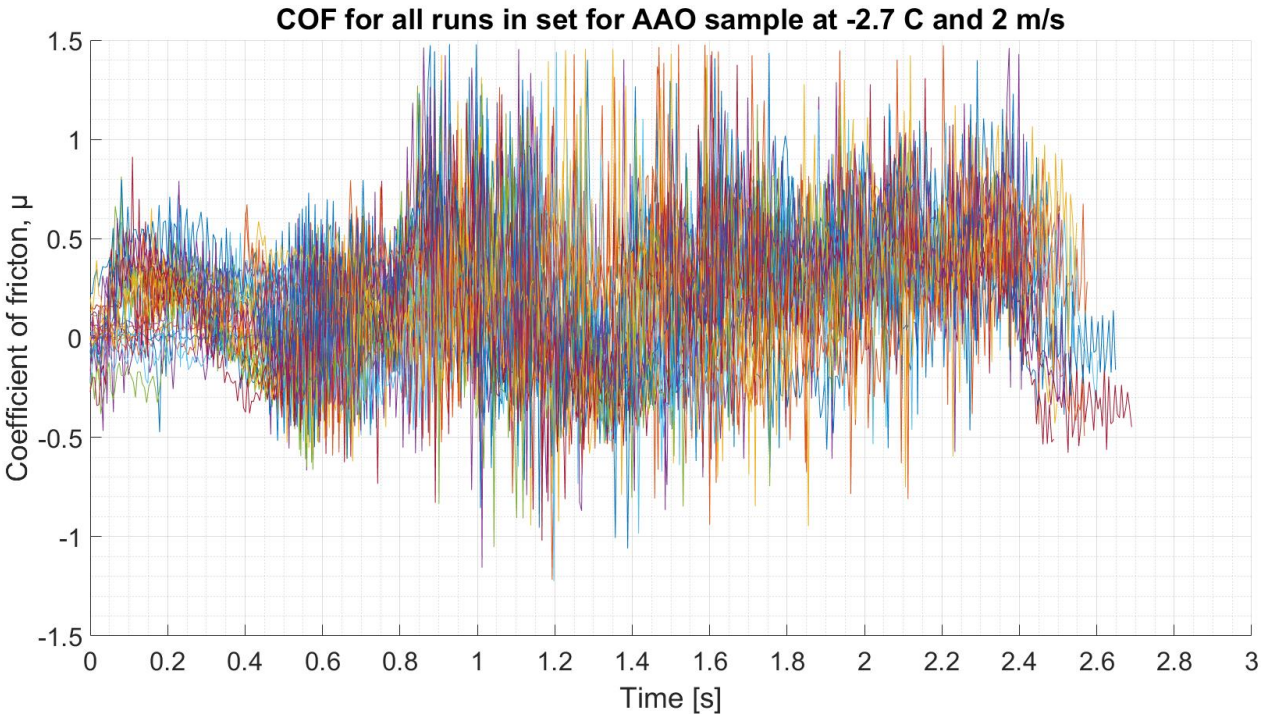
COF for all runs in set for AAO sample at -2.7 C and 2 m/s
Coefficient of fricton, μ
Time [s]
1.5
1
0.5
0
-0.5
-1
-1.5
0
0.2
0.4
0.6
0.8
1
1.2
1.4
1.6
1.8
2
2.2
2.4
2.6
2.8
3

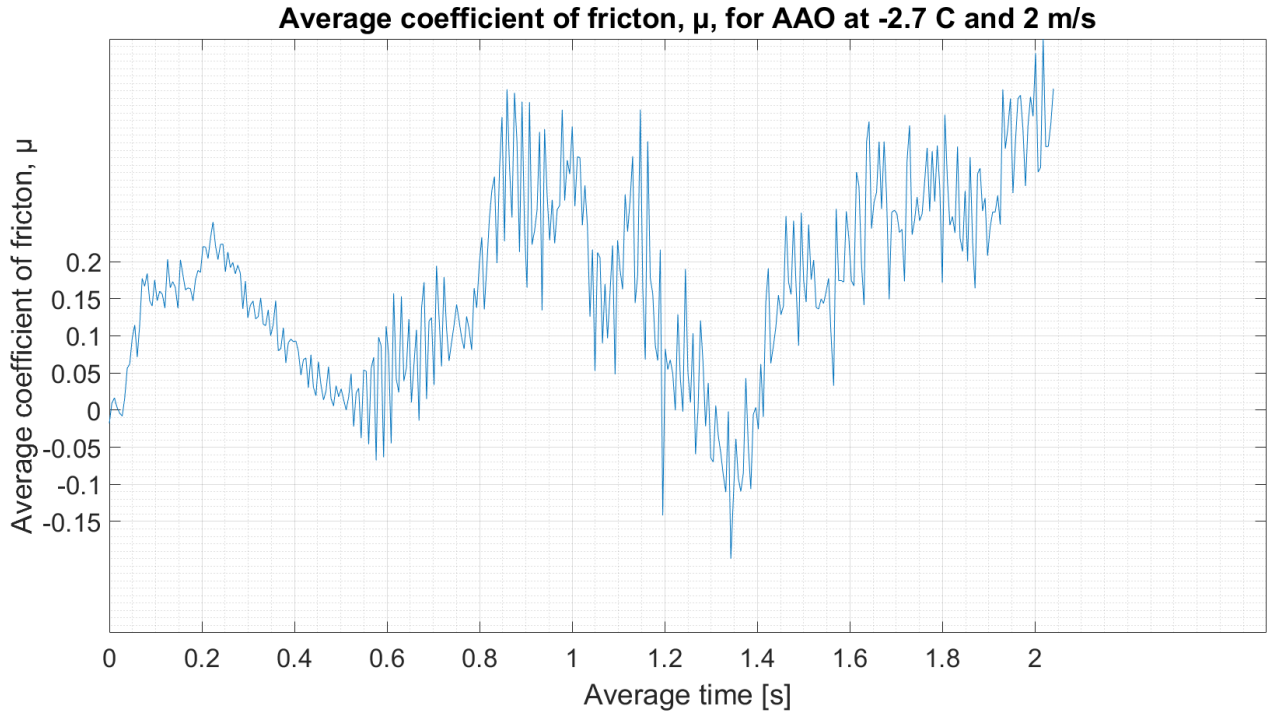
Average coefficient of fricton, μ, for AAO at -2.7 C and 2 m/s
Average coefficient of fricton, μ
Average time [s]
0.2
0.15
0.1
0.05
0
-0.05
-0.1
-0.15
0
0.2
0.4
0.6
0.8
1
1.2
1.4
1.6
1.8
2

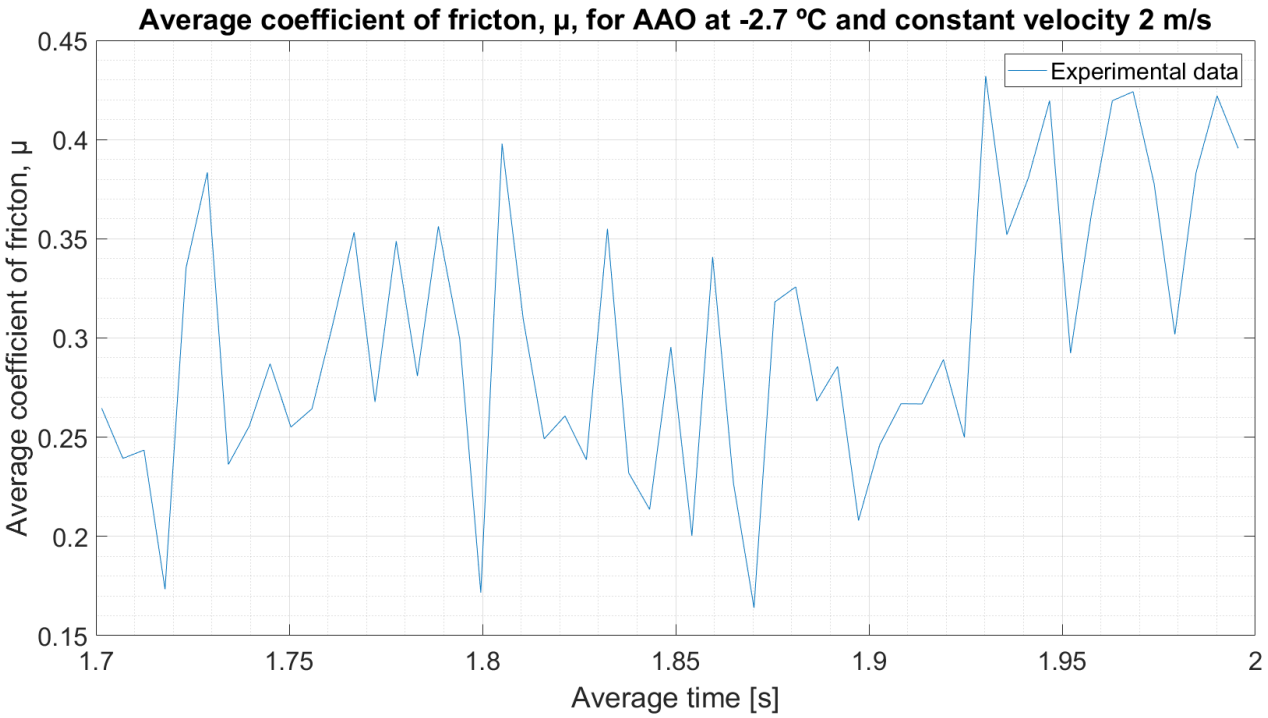
Average coefficient of fricton, μ, for AAO at -2.7 ºC and constant velocity 2 m/s
Experimental data
Average coefficient of fricton, μ
Average time [s]
0.45
0.4
0.35
0.3
0.25
0.2
0.15
1.7
1.75
1.8
1.85
1.9
1.95
2

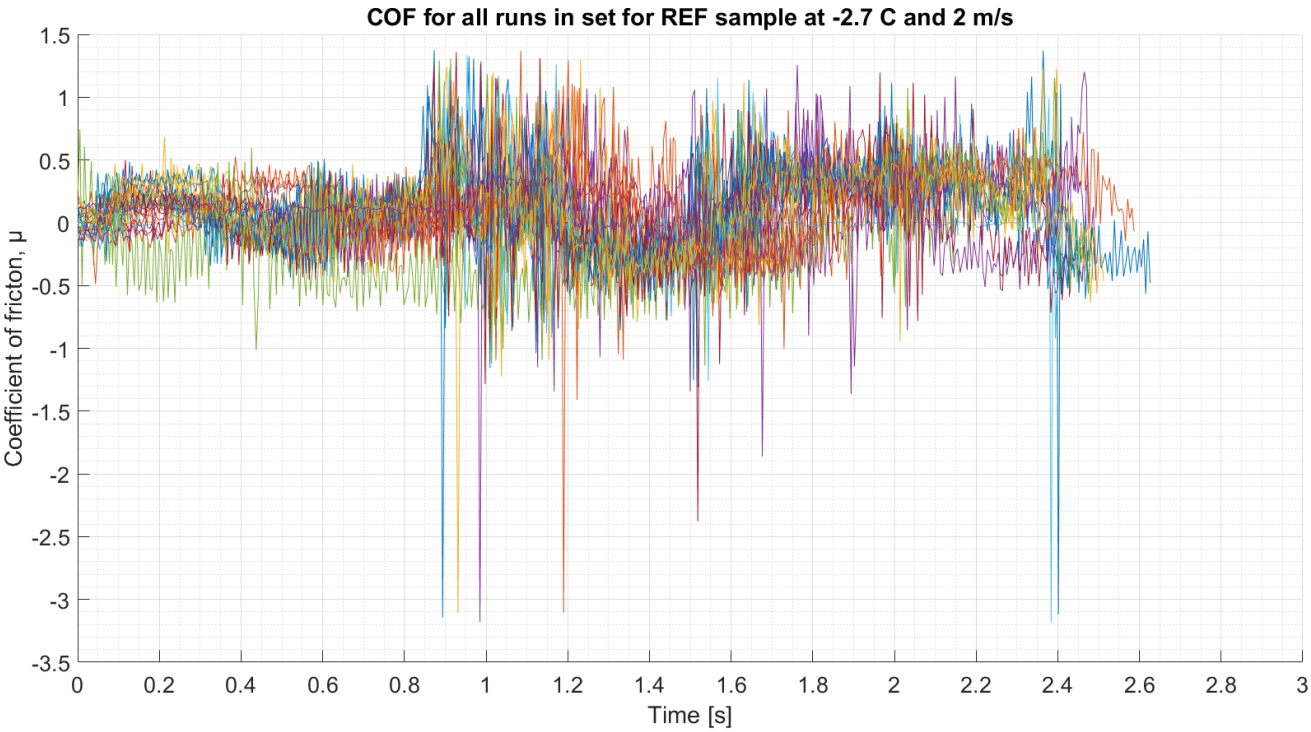
COF for all runs in set for REF sample at -2.7 C and 2 m/s
Coefficient of fricton, μ
Time [s]
1.5
1
0.5
0
-0.5
-1
-1.5
-2
-2.5
-3
-3.5
0
0.2
0.4
0.6
0.8
1
1.2
1.4
1.6
1.8
2
2.2
2.4
2.6
2.8
3

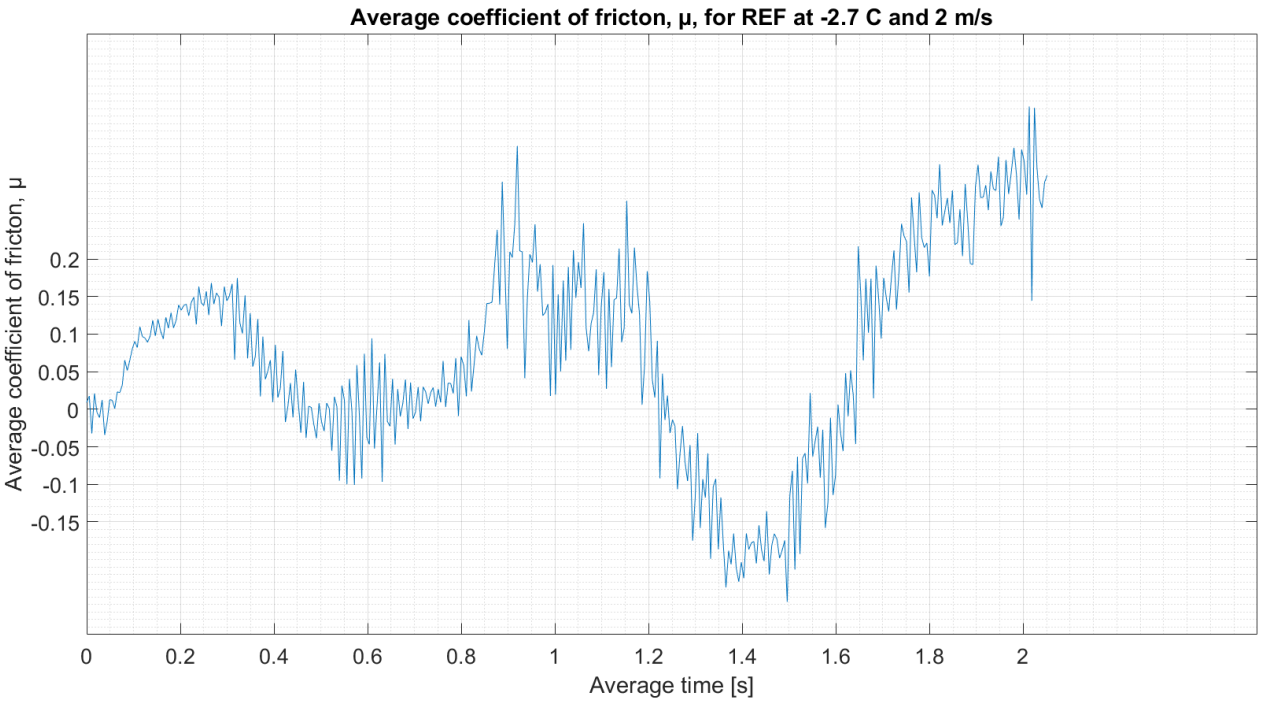
Average coefficient of fricton, μ, for REF at -2.7 C and 2 m/s
Average coefficient of fricton, μ
0.2
0.15
0.1
0.05
0
-0.05
-0.1
-0.15
0
0.2
0.4
0.6
0.8
1
1.2
1.4
1.6
1.8
2
Average time [s]

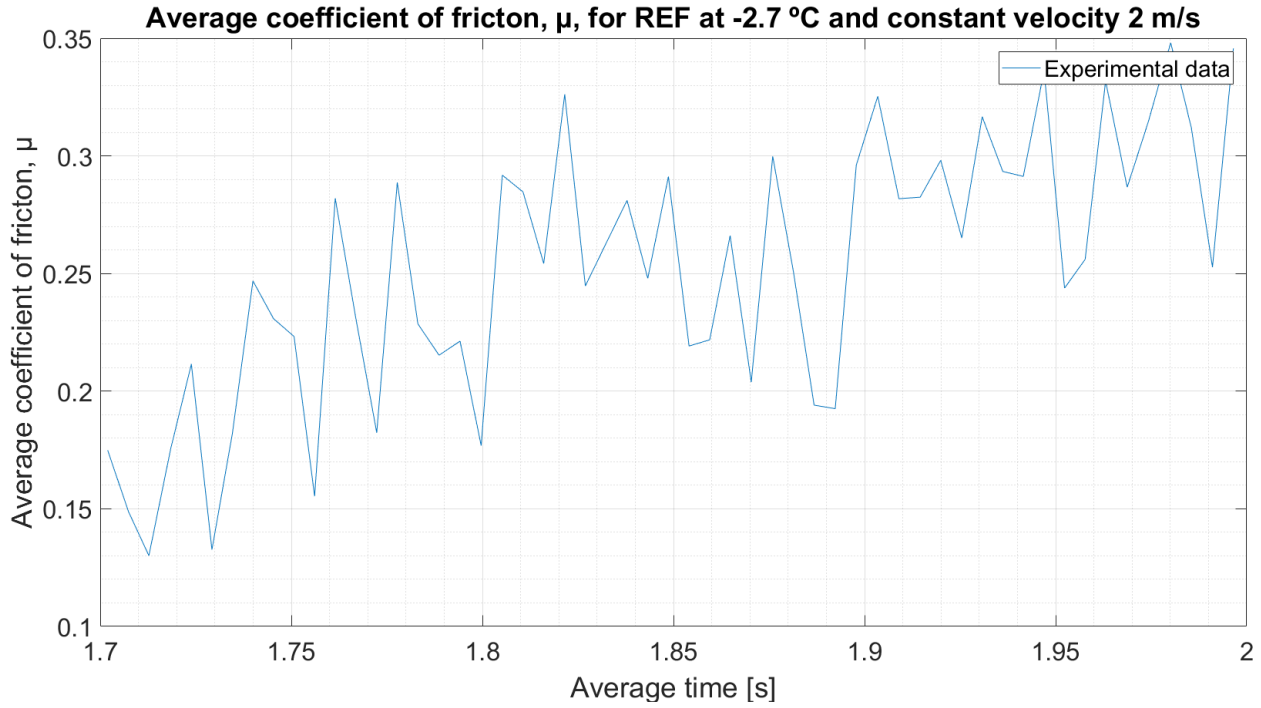
Average coefficient of fricton, μ, for REF at -2.7 ºC and constant velocity 2 m/s
Experimental data
Average coefficient of fricton, μ
0.35
0.3
0.25
0.2
0.15
0.1
1.7
1.75
1.8
1.85
1.9
1.95
2
Average time [s]

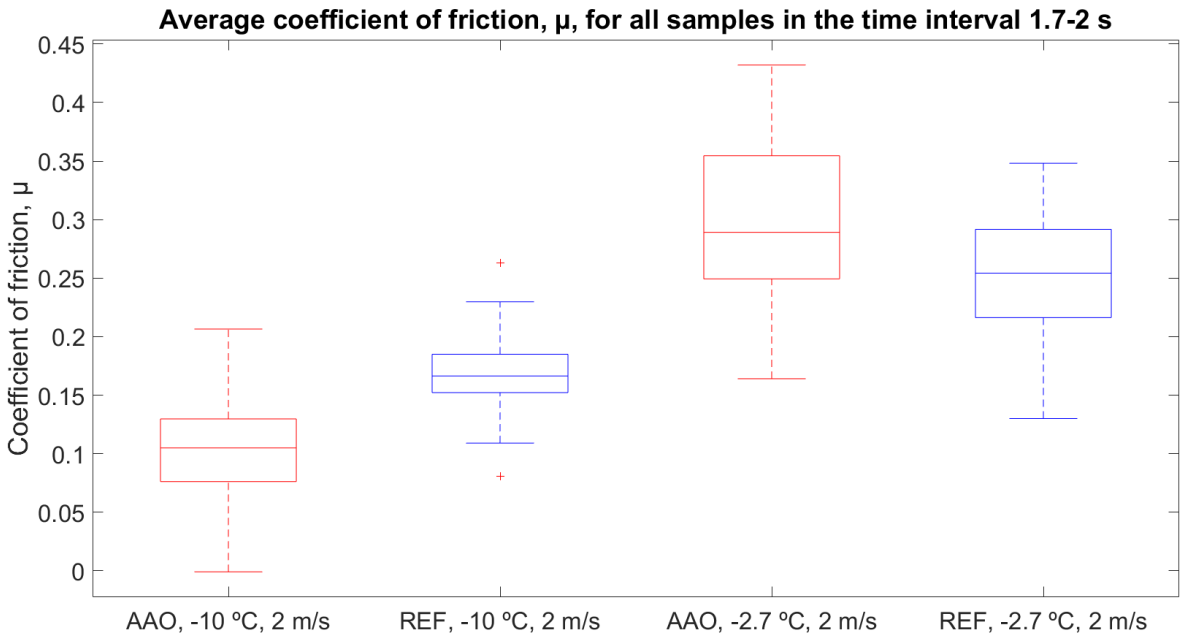
Average coefficient of friction, μ, for all samples in the time interval 1.7-2 s
Coefficient of friction, μ
0.45
0.4
0.35
0.3
0.25
0.2
0.15
0.1
0.05
0
AAO, -10 ºC, 2 m/s
REF, -10 ºC, 2 m/s
AAO, -2.7 ºC, 2 m/s
REF, -2.7 ºC, 2 m/s

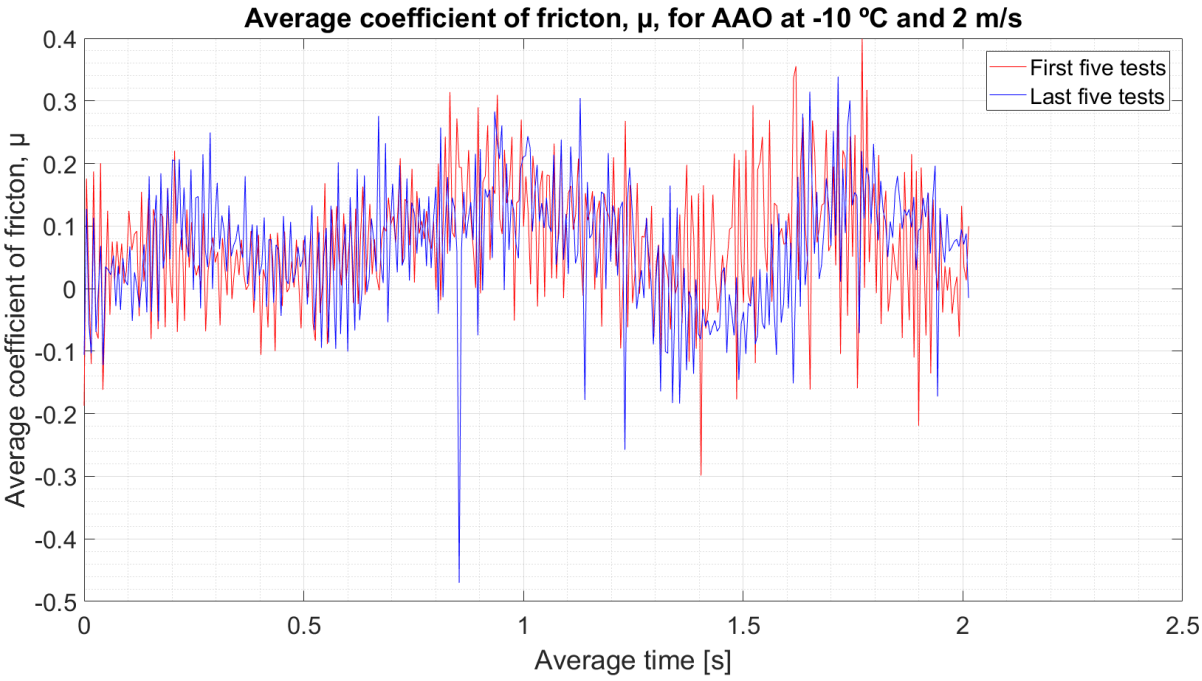
Average coefficient of fricton, μ, for AAO at -10 ºC and 2 m/s
Average coefficient of fricton, μ
First five tests
Last five tests
0.4
0.3
0.2
0.1
0
-0.1
-0.2
-0.3
-0.4
-0.5
0
0.5
1
1.5
2
2.5
Average time [s]

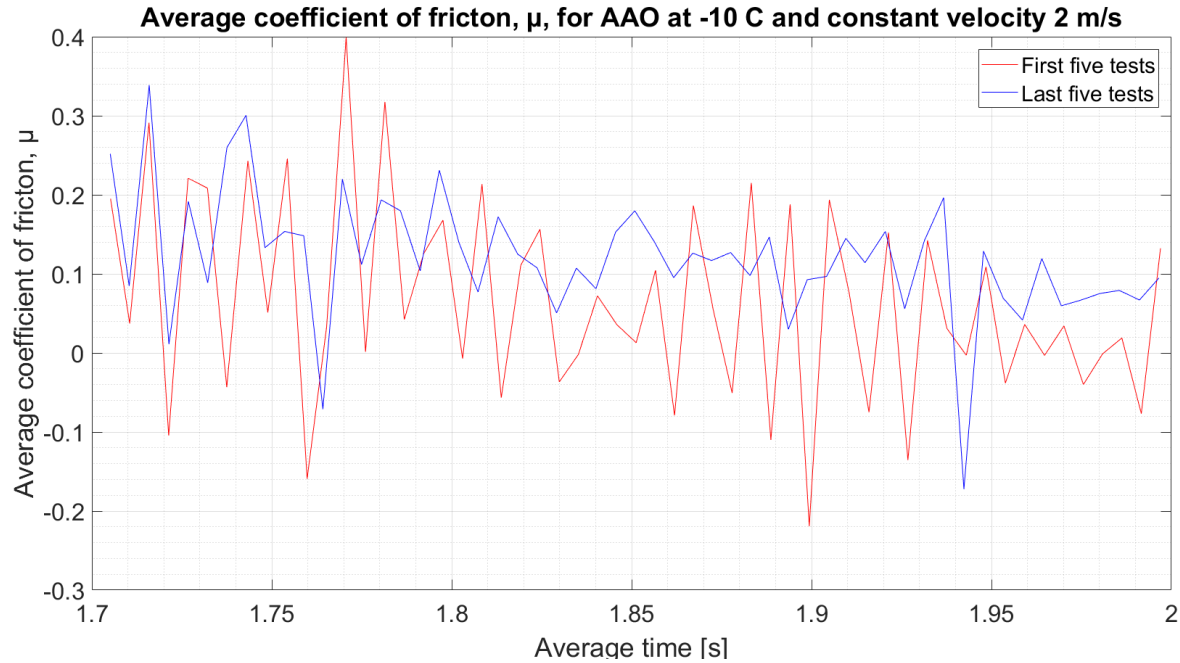
Average coefficient of fricton, μ, for AAO at -10 C and constant velocity 2 m/s
First five tests
Last five tests
Average coefficient of fricton, μ
Average time [s]
0.4
0.3
0.2
0.1
0
-0.1
-0.2
-0.3
1.7
1.75
1.8
1.85
1.9
1.95
2

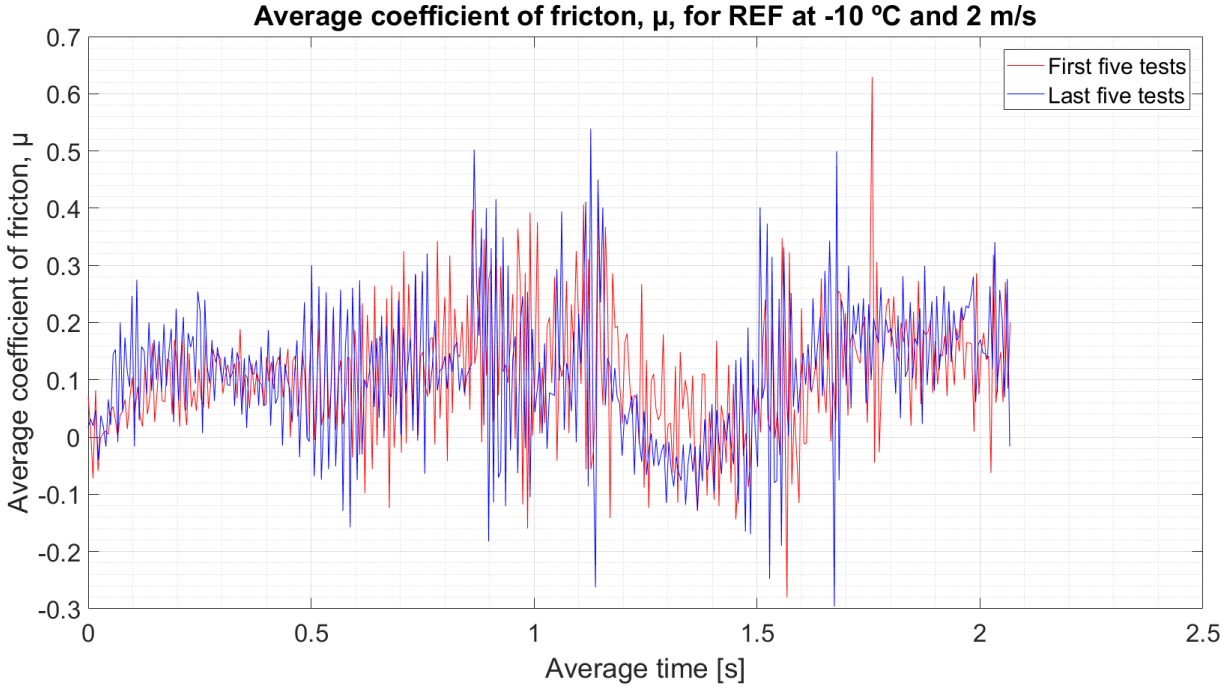
Average coefficient of fricton, μ, for REF at -10 ºC and 2 m/s
First five tests
Last five tests
Average coefficient of fricton, μ
Average time [s]
0.7
0.6
0.5
0.4
0.3
0.2
0.1
0
-0.1
-0.2
-0.3
0
0.5
1
1.5
2
2.5

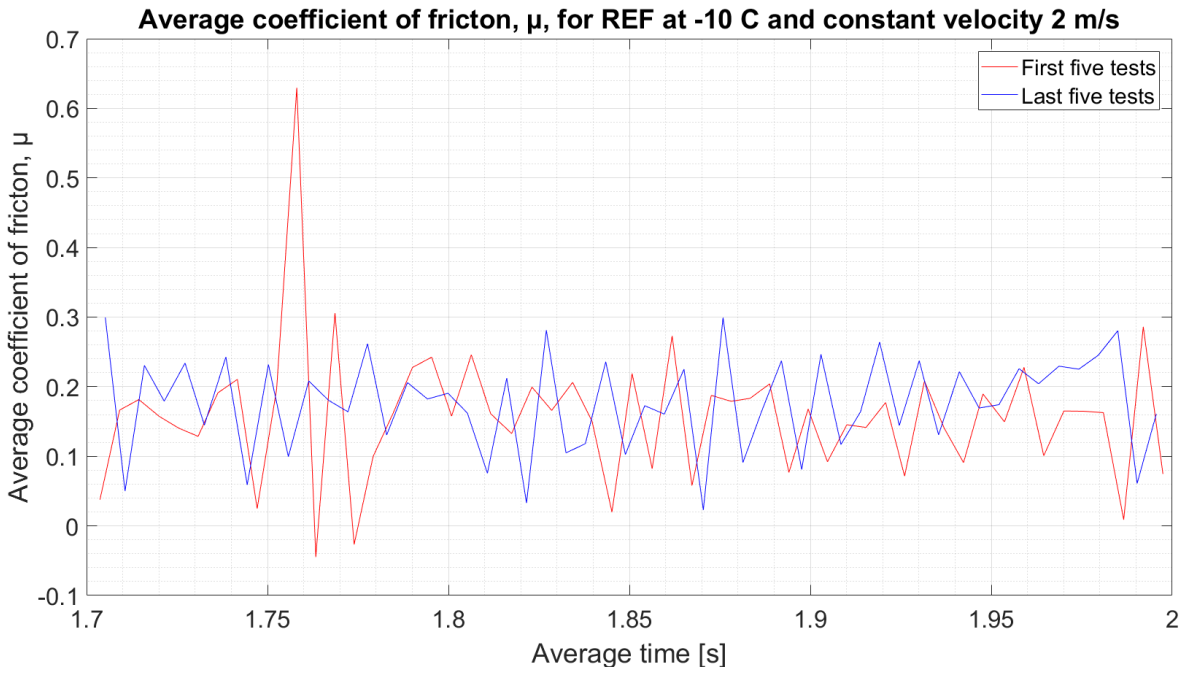
Average coefficient of fricton, μ, for REF at -10 C and constant velocity 2 m/s
First five tests
Last five tests
Average coefficient of fricton, μ
Average time [s]
0.7
0.6
0.5
0.4
0.3
0.2
0.1
0
-0.1
1.7
1.75
1.8
1.85
1.9
1.95
2

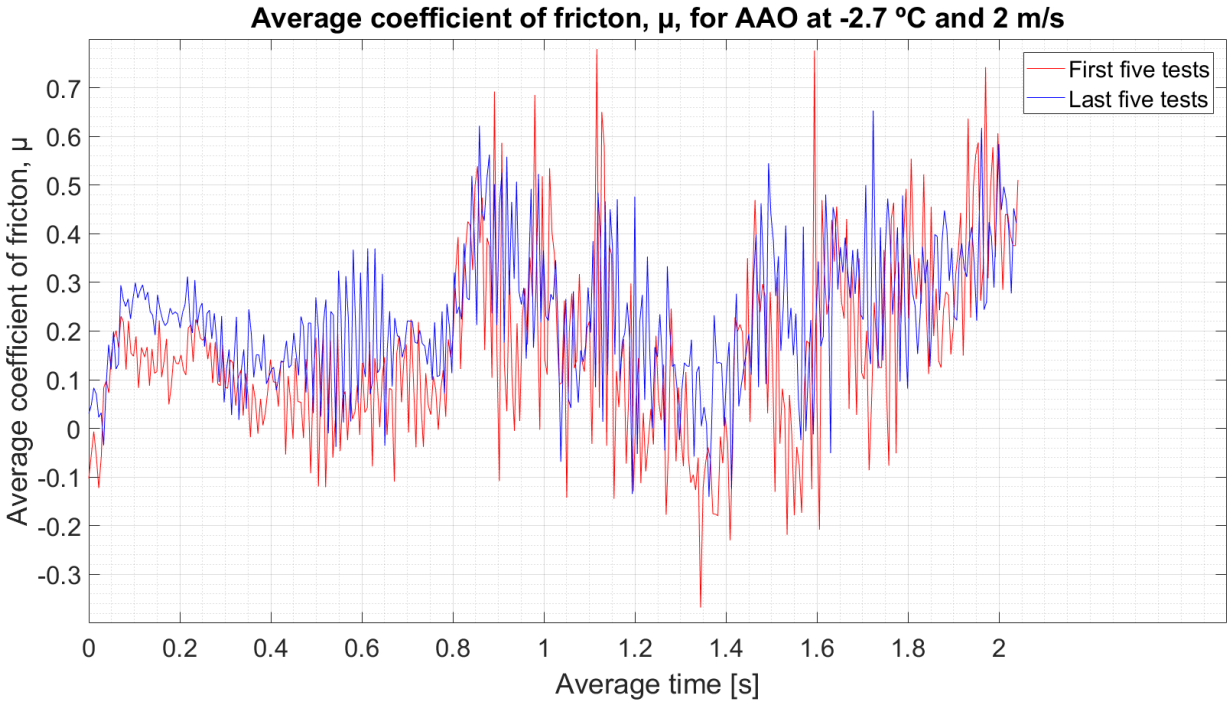
Average coefficient of fricton, μ, for AAO at -2.7 ºC and 2 m/s
First five tests
Last five tests
Average coefficient of fricton, μ
Average time [s]
0.7
0.6
0.5
0.4
0.3
0.2
0.1
0
-0.1
-0.2
-0.3
0
0.2
0.4
0.6
0.8
1
1.2
1.4
1.6
1.8
2

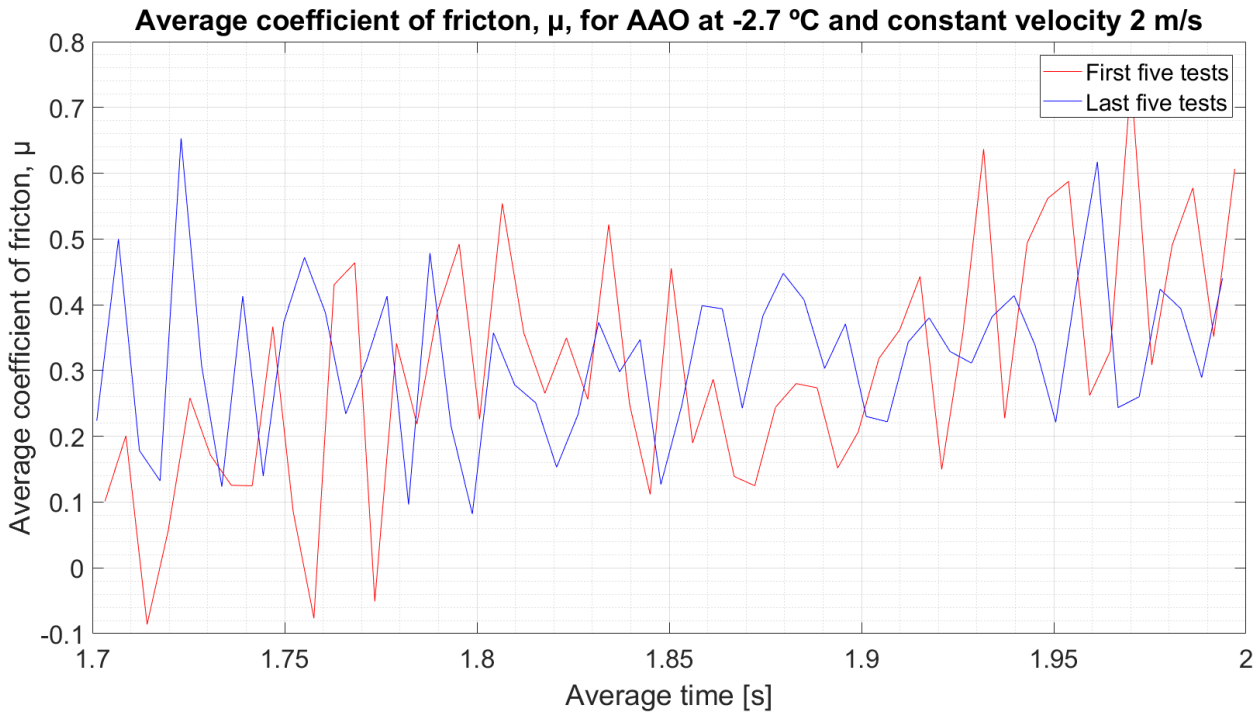
Average coefficient of fricton, μ, for AAO at -2.7 ºC and constant velocity 2 m/s
First five tests
Last five tests
Average coefficient of fricton, μ
Average time [s]
0.8
0.7
0.6
0.5
0.4
0.3
0.2
0.1
0
-0.1
1.7
1.75
1.8
1.85
1.9
1.95
2

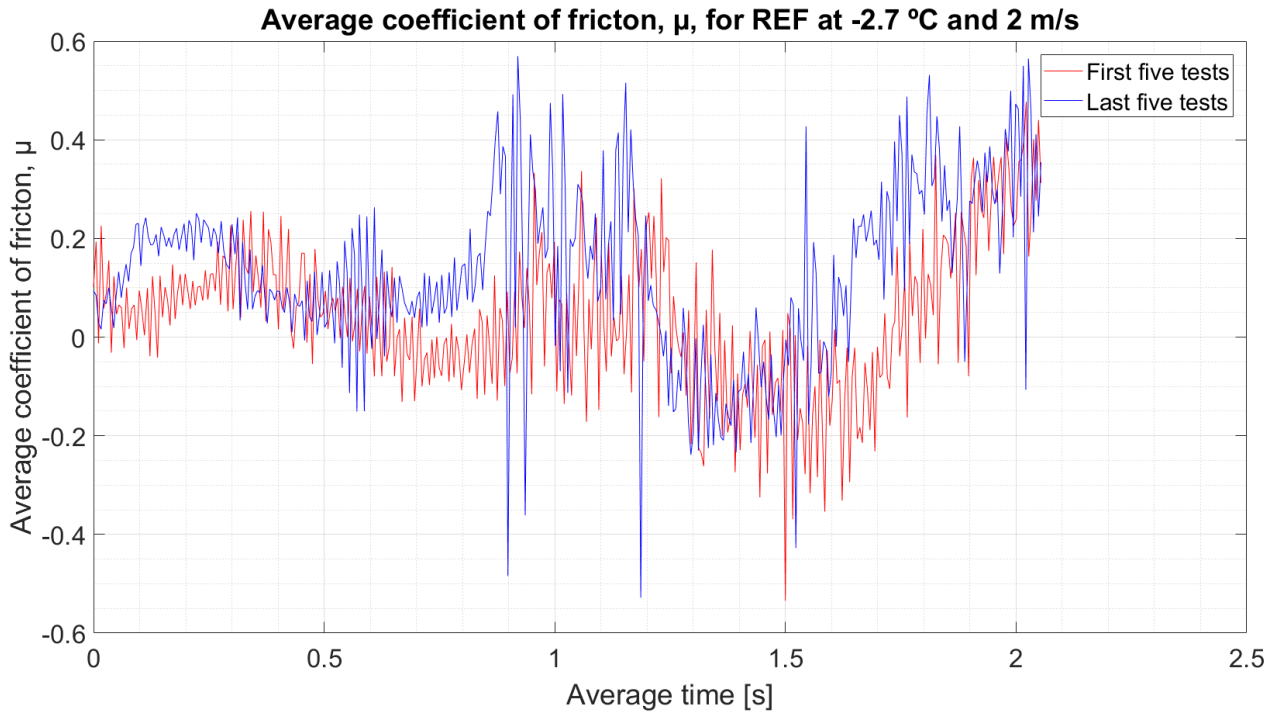
Average coefficient of fricton, μ, for REF at -2.7 ºC and 2 m/s
First five tests
Last five tests
Average coefficient of fricton, μ
Average time [s]
0.6
0.4
0.2
0
-0.2
-0.4
-0.6
0
0.5
1
1.5
2
2.5

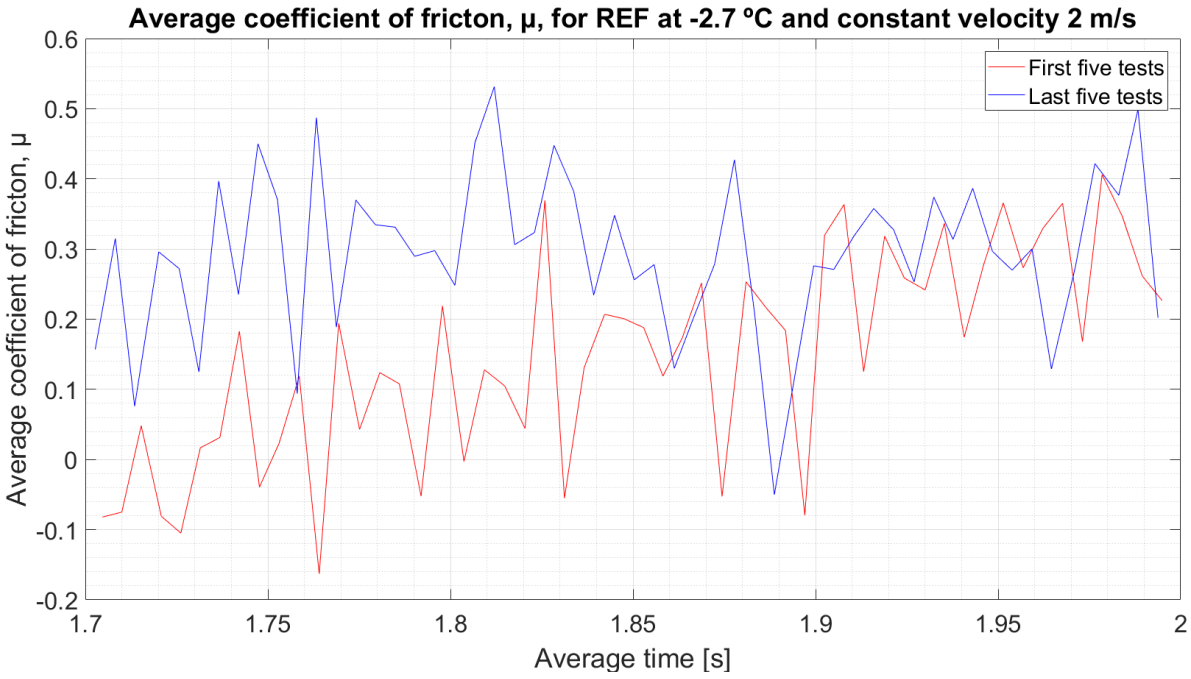
Average coefficient of fricton, μ, for REF at -2.7 ºC and constant velocity 2 m/s
First five tests
Last five tests
Average coefficient of fricton, μ
Average time [s]
0.6
0.5
0.4
0.3
0.2
0.1
0
-0.1
-0.2
1.7
1.75
1.8
1.85
1.9
1.95
2

Appendix S: Information retrieval

To collect information for this Master's thesis, several sources were utilized. Firstly, knowledge was gained from the specialization project reports and Master's theses of students previously participating in Olympiatoppen's Forsprang 2018 project, which were available at the institute. Secondly, NTNU's databases were employed, in which Google Scholar and Oria were most heavily used. These databases consist of enormous amounts of publications. For example, Google Scholar is estimated to contain 160 billion documents [127]. In searching for specific information, operators such as "AND", "OR" and "phrase" were used to find the most accurate information. Synonyms were used in cases were preferred information could not be found or to include different terms explaining the same phenomena. An example of the use of these operators is shown in the figure below in the search for published work on nanostructures in relation to ski- or ice friction. General Google searches were limited to certain searches, like material data sheets, product specifications, and some definitions. EndNote was used as a tool for efficient and correct referencing, with Numbered referencing style. Firsthand references were always used when available.